N72-26795
NASA CR-112066

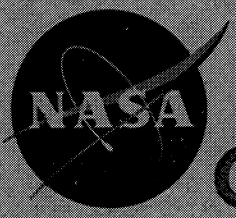

EXPERIMENTAL EVALUATION OF THREE LEAK DETECTION AND LOCATION CONCEPTS FOR SPACE STATIONS

M. V. SCHERB
G. P. KAZOKAS
J. A. ZELIK
J. R. MASTANDREA
D. C. MACKALLOR

June 1972

FINAL REPORT

Prepared under Contract NAS1-10840
McDonnell Douglas Astronautics Company
Huntington Beach, California
For
NATIONAL AERONAUTICS AND SPACE ADMINISTRATION

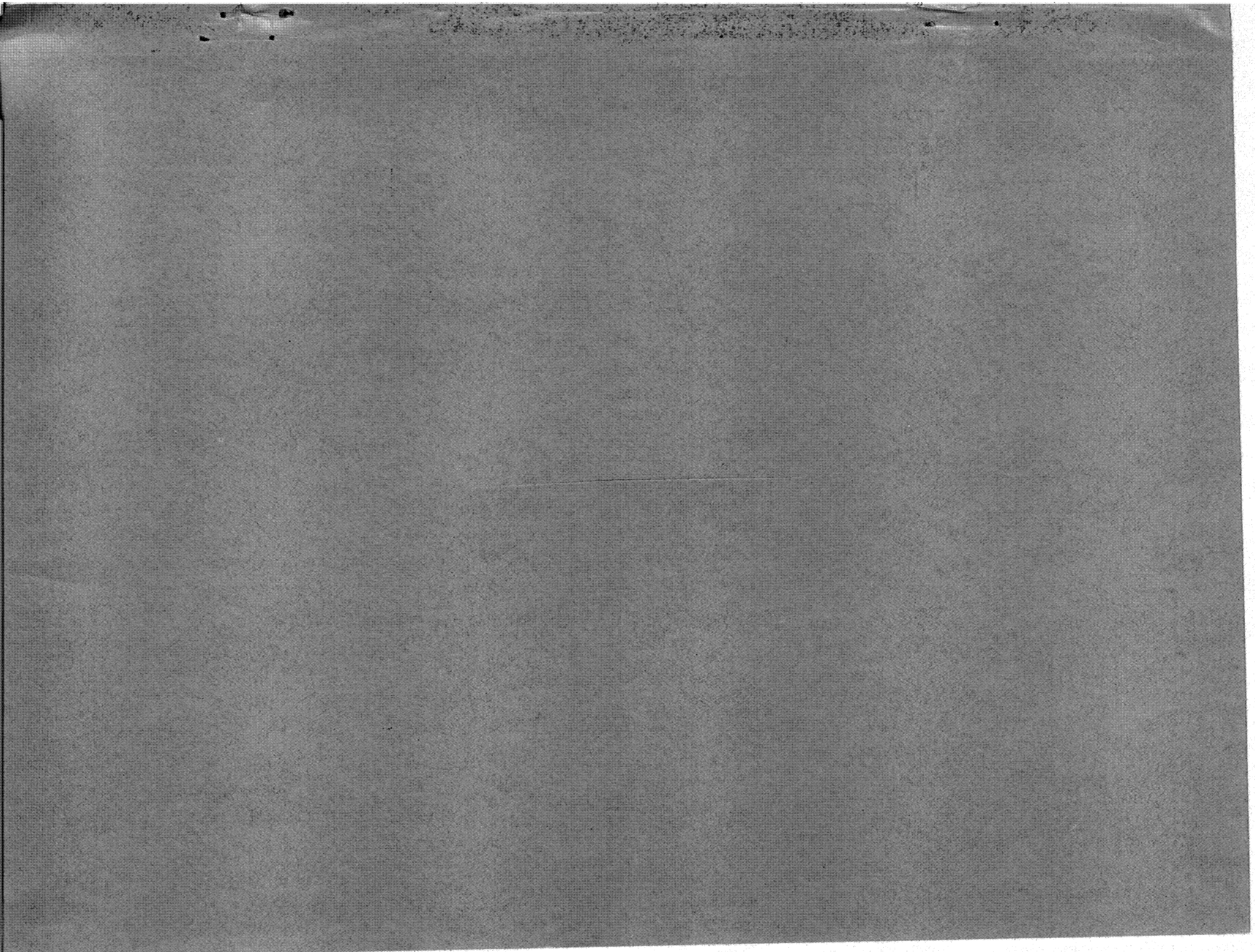

1. Report No.	2. Government Accession No.	3. Recipient's Catalog No.
Final Report		

4. Title and Subtitle	5. Report Date
Experimental Evaluation of Three Leak Detection and Location Concepts for Space Stations	June 1972
	6. Performing Organization Code
7. Author(s)	8. Performing Organization Report No.
M. V. Scherb, G. P. Kazokas, J. A. Zelik, J. R. Mastandrea, D. C. Mac Kallor, Jr.	MDC G2911
	10. Work Unit No.
9. Performing Organization Name and Address	11. Contract or Grant No.
McDonnell Douglas Astronautics Co. Huntington Beach, California. 92647	NAS1-10840
	13. Type of Report and Period Covered
12. Sponsoring Agency Name and Address	
NASA Langley Research Center Hampton, Virginia, 23365	14. Sponsoring Agency Code

15. Supplementary Notes

16. Abstract

Three leak (or precursor damage modes) detection and location concepts for space station overboard leakage were evaluated experimentally.

These techniques are:

A. Static and dynamic seal leak detector sensing of moisture or all gases in space cabin atmosphere
B. Active ultrasonic Lamb-wave detection of flaws or cracks in cabin wall
C. Impact gage detection of stress waves induced in cabin pressure wall by meteoroid or orbital debris impact.

The experimental results obtained in this program demonstrated that all three leak detection and location concepts are feasible. With further development, the methods can be integrated into an effective damage control system for advanced manned Earth-orbital systems.

17. Key Words (Suggested by Author(s))	18. Distribution Statement
Damage control Leak detection Seal leak detector Active ultrasonics - Lamb waves Impact gage - electrets	

19. Security Classif. (of this report)	20. Security Classif. (of this page)	21. No. of Pages	22. Price*

*For sale by the National Technical Information Service, Springfield, Virginia 22151

FOREWORD

This is the final report on the experimental evaluation of three leak-detection and -location concepts for space stations, which covers the work performed during the 12-month period from June 3, 1971 to June 3, 1972.

The experimental effort was directed toward determining the feasibility of three leak- (or precursor damage modes) detection and -location techniques for overboard cabin-atmosphere leakage that could be incorporated into an integrated damage-control system for advanced manned earth-orbital systems.

This project was carried out for the National Aeronautics and Space Administration, Langley Research Center, under the direction of Victor L. Vaughan, Jr. of the Structural Mechanics Branch, Structures Division.

The program was conducted by M. V. Scherb, principal investigator and study manager for the McDonnell Douglas Astronautics Company.

The work described in this report was performed by G. P. Kazokas, D. C. MacKallor, J. R. Mastandrea, W. W. Reinhardt, M. V. Scherb, R. N. Teng, and J. A. Zelik.

CONTENTS

FIGURES

TABLES

Section 1
INTRODUCTION AND SUMMARY

A study of damage control systems for both overboard and onboard leakage in space stations was carried out under NASA Contract NAS1-10184, Study of Damage Control Systems For Space Stations and Preliminary Design of a Space Station Simulator. The results of the study on damage control systems were published in NASA CR 111963, Study of Damage Control Systems For Space Station, October 1971 (Reference 1).

Three leak detection (or precursor modes) and location techniques for overboard leakage were identified as showing promise for use in an integrated damage control system for manned Earth-orbital systems and future space stations.

The three methods are:

A. Static and dynamic seal leak detector – moisture or gas thermal conductivity sensing.

B. Active ultrasonics – Lamb-wave propagation/reflection from flaws or cracks.

C. Impact gage – passive detection of stress waves induced in a target by the impact of a meteoroid or of orbital debris.

The purpose of this study was to carry out an experimental investigation to determine whether the methods were feasible. In addition, the concept of dual-function ultrasonic transducers was investigated.

Experimental results obtained in this program indicate that all three techniques are feasible for integration into a damage control system for space stations.

For seal leak detection, the thermal conductivity sensor using thermistors proved to be the only method capable of meeting the objective of a detection sensitivity of 10^{-4} standard cubic centimeters per second (scc/s) or greater. The thermistor detector exhibited a sensitivity of 10^{-8} scc/s. Therefore, this method can measure the normal permeation of cabin atmosphere through a seal and provide a baseline continuous signal if desired. Thermistor sensors are small, rugged, low in power requirements, and can readily be integrated into a damage control system. For the test program evaluation, a breadboard system was fabricated which featured a direct digital readout of leak rate coupled with an audio alarm.

The capacitance sensor for sensing moisture leaking past a seal did not achieve the necessary sensitivity in its present state of development. However, the concept does have potential for significant improvement and could be applied to the detection of both overboard and onboard seal leaks.

The active ultrasonics program concentrated on a parametric investigation of Lamb-wave technology applied to the detection of flaws, cracks, and holes in plain and integrally stiffened ribbed aluminum sheets representative of the pressure wall of a modular space station. It was demonstrated that Lamb waves are sensitive to small-sized flaws and can be propagated past ribs of a pressure wall structure. Transmit-receive techniques are more useful than pulse-echo methods for remote leak detection and location in integrally stiffened structures.

Overall, the results of this investigation indicate that Lamb-wave technology is feasible for detecting and locating leaks (or precursor flaws) in realistic space cabin structures featuring ribs, rivets, and feed-throughs.

Miniature prototype impact gages were fabricated and successfully tested for ballistic and hypervelocity impacts on simulated space station pressure walls.

Impact signals from internal impacts within a space cabin can readily be discriminated against.

Both standard ceramic (lead zirconate titanate) and polymer (fluorocarbon electrets) transducers demonstrated excellent response for a wide spectrum of impact conditions. In particular, the plastic electrets, polyfluoroethylene-propylene (FEP) and polytetrafluoroethylene (TFE), offer great potential as a new class of impact transducers.

Triangulation techniques using a transducer array and measuring the shock wave time-of-arrival from the point of impact to each transducer successfully predicted the point of impact within a few centimeters for plain aluminum sheets and integrally ribbed large-area sheets.

A breadboard impact gage signal processing subsystem was completed which demonstrated that the subsystem was capable of providing by multiplexing techniques the output signals necessary for impact location calculations.

Acoustic emission signals from a dynamic flaw were detected with the miniature impact gages. Impact and acoustic emission signals can be processed with electronic subsystems having a frequency response of 50 to 800 kHz. It was demonstrated that the impact signals and acoustic emission signals can be multiplexed by two different techniques.

Based on the results obtained in this program, the dual-function passive ultrasonic (impact-acoustic emission) gage is feasible.

Section 2
SEAL LEAK DETECTOR

2.1 INTRODUCTION

The objective of this task was to develop and evaluate experimental sensors for the detection of overboard leaks past static and dynamic seals with a minimum detection efficiency of 1×10^{-4} scc/s for cabin atmosphere pressures ranging from 3.4×10^{4} N/m^2 to 1.01×10^{5} N/m^2.*

Aboard manned spacecraft there are many throughputs which penetrate the pressure shell. These include pressurized gas/liquid lines, electrical connections, dump valves, hatches, etc. All of these are potential leak sources, especially seals, which are exercised frequently such as hatches, airlocks, and dump/disposal valves. Sensitive leak sensors strategically placed would reduce the possibility of large quantities of gas reserves being lost with possible compromise of mission duration and crew safety.

This consideration is of paramount importance for long-duration missions.

In a previous study program carried out under Contract NAS1-10184 (Reference 1) the following three sensor concepts were identified as showing promise for experimental evaluation:

A. Electrolytic hygrometry to measure primarily moisture
B. Capacitance to measure primarily moisture
C. Thermal conductivity to measure all gases and vapors.

The three concepts are displayed in Figures 2-1, 2-2, and 2-3.

---

*5 psia to 14.7 psia

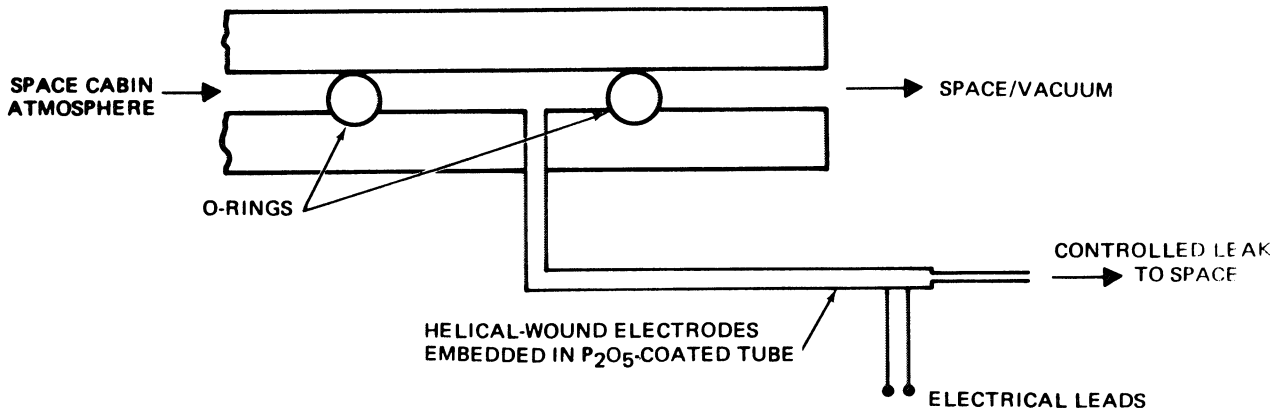

(a) ELECTROLYTIC HYGROMETRY

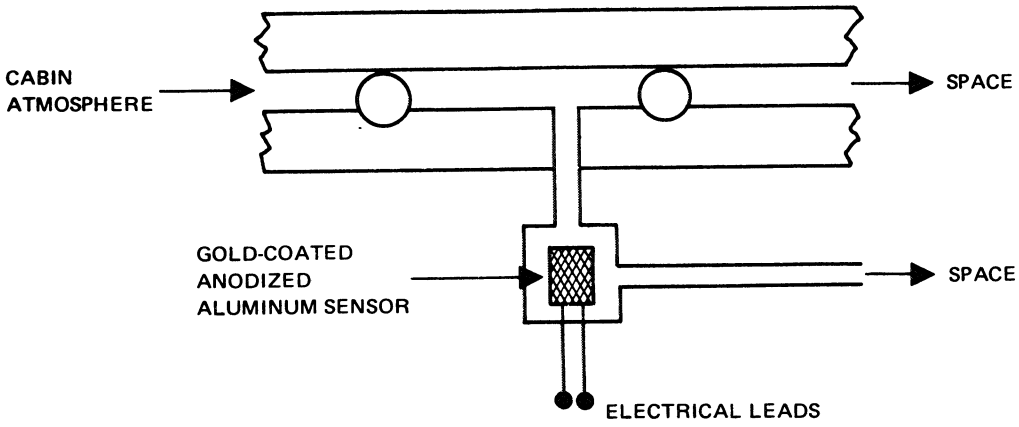

(b) CAPACITANCE-IMPEDANCE HYGROMETRY

Figure 2-1. Moisture Measurement Hygrometry

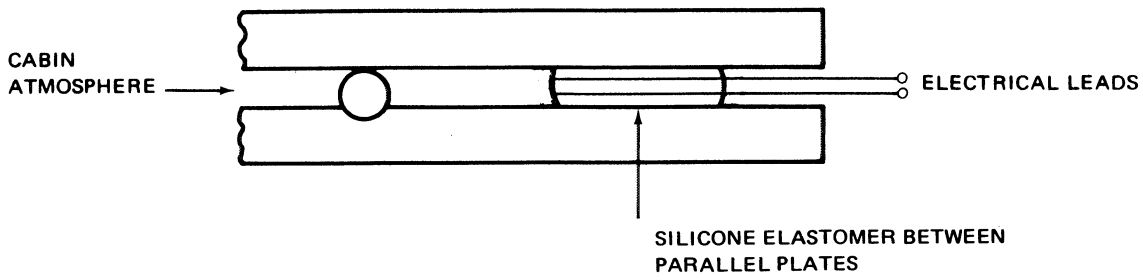

Figure 2-2. Gases/Vapors/Moisture Measurement – Silicone Elastomer Capacitor

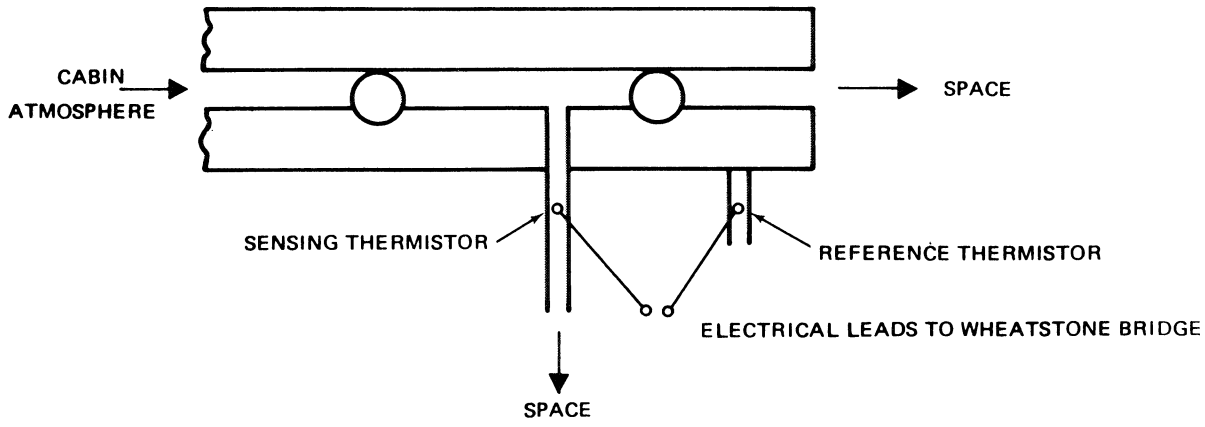

Figure 2-3. Gases/Vapors Measurement - Thermal Conductivity Detector

The composition of the cabin atmosphere consists mainly of oxygen and nitrogen with small amounts of carbon dioxide and water vapor plus trace amounts of many other gases. Each or all of these constituents can be considered as tracers if the initial concentration is known and if the detector is sensitive enough to meet the minimum objective. Concepts A and B sense primarily water vapor which is normally present in the cabin atmosphere of concentrations up to several thousand ppm. Water vapor is monitored continuously aboard manned spacecraft. Concept C, which senses all gases, primarily will respond to oxygen and nitrogen which comprise the bulk of the cabin atmosphere.

A basic distinction must be made between permeation and a leak past a seal. Permeation of gases through an elastomer seal is a normal process and as such represents a very small amount of gas lost per linear centimeter per second.

Typical permeation values are in the range of 10^{-4} to 10^{-8} scc/s/cm. Detection of the initial stages of a leak, assuming a gradual deterioration of the seal will depend on the sensitivity of the technique. In general, detection sensitivity should be great enough to sense normal permeation. This capability would have two advantages: (1) a leak could be detected in its earliest stages and (2) detection of permeation would provide a convenient test of the sensor.

To accurately measure the leakage rate and to increase the sensitivity of detection, all of the escaping gases are temporarily confined and passed through the sensor as shown in Figures 2-1, 2-2, and 2-3. The secondary barrier downstream from the primary seal may be an O-ring, gasket, or lip seal. In all cases, the temporarily confined gases are ultimately allowed to escape to vacuum.

In the evaluation of the three concepts, commercially available components and sensors were used as much as possible to expedite the study. All measurements of leak detection sensitivity are given in scc/s to yield the basic sensitivity range for each sensor concept independent of cabin atmospheric pressure.

2.2 ELECTROLYTIC HYGROMETRY

The basic principle involved in this detection technique is the electrolysis of water vapor leaking past the primary seal into the sensor. Electrolysis of the water vapor results in an electric current that is proportional to the amount of water vapor.

A block diagram of the experimental setup used to evaluate the electrolytic hygrometry concept is shown in Figure 2-4. Ambient air at 1.01×10^5 N/m^2 pressure was passed into a controlled relative humidity (RH) chamber of approximately 50 percent RH. This conditioned air passed through the shutoff valve (V_1) and through the calibrated micrometering valve (V_2) into the evacuated electrolytic cell (2). After the moisture became electrolyzed, the products, H_2 and O_2, passed through the downstream shutoff valve (V_5) to vacuum. The electrolytic cell bypass valve (V_3) was used to facilitate system equilibrium prior to the test and was usually closed during the tests. The micrometering valve (V_4) was used only to determine the effect of controlled bleeding to vacuum of the H_2 and O_2 during the recombination experiment; i.e., the shutoff valve (V5) was closed and the H_2 and O_2 leaked to vacuum at a reduced rate.

Moisture which passed through the electrolyte was absorbed by the phosphorus pentoxide (P_2O_5) coating. The P_2O_5 was ionized by the moisture, which caused a current to flow between two helically wound electrodes embedded in the P_2O_5 coating that lined the inner wall of the nonconductive glass tubing. The current flow electrolyzed the moisture to H_2 and O_2, which were vented to vacuum. The resulting current flow between the helically wound electrodes was proportional to the moisture present and, in turn, was related to the leak rate (flow) through the system. Figures 2-5 and 2-6 present photographic details of the test system.

The system was leak checked with a helium mass spectrometer leak detector which also served as the vacuum source during the test . Data obtained in a representative run are shown in Figure 2-7 and indicate a minimum detectable leak rate of about 2×10^{-3} scc/s.

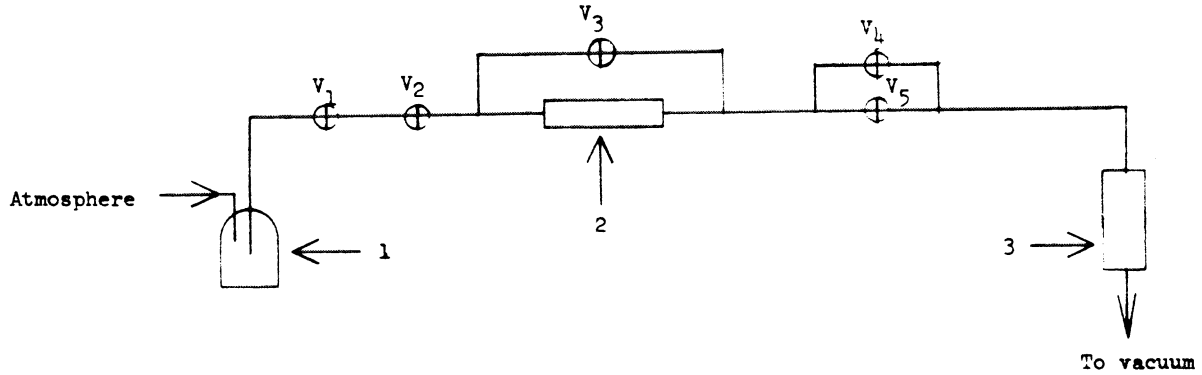

1 – $Mg(NO_3)_2 \cdot 6H_2O$, Saturated Solution, approx. 50% relative humidity
2 - Electrolytic cell
3 - Molecular Sieve (Type 5A) Trap
V_1 - Shut-off valve
V_2 - Calibrated micrometering valve
V_3 - Shut-off valve
V_4 - Micrometering valve
V_5 - Shut-off valve

Figure 2-4. Electrolytic Hygrometry Concept Experimental Setup

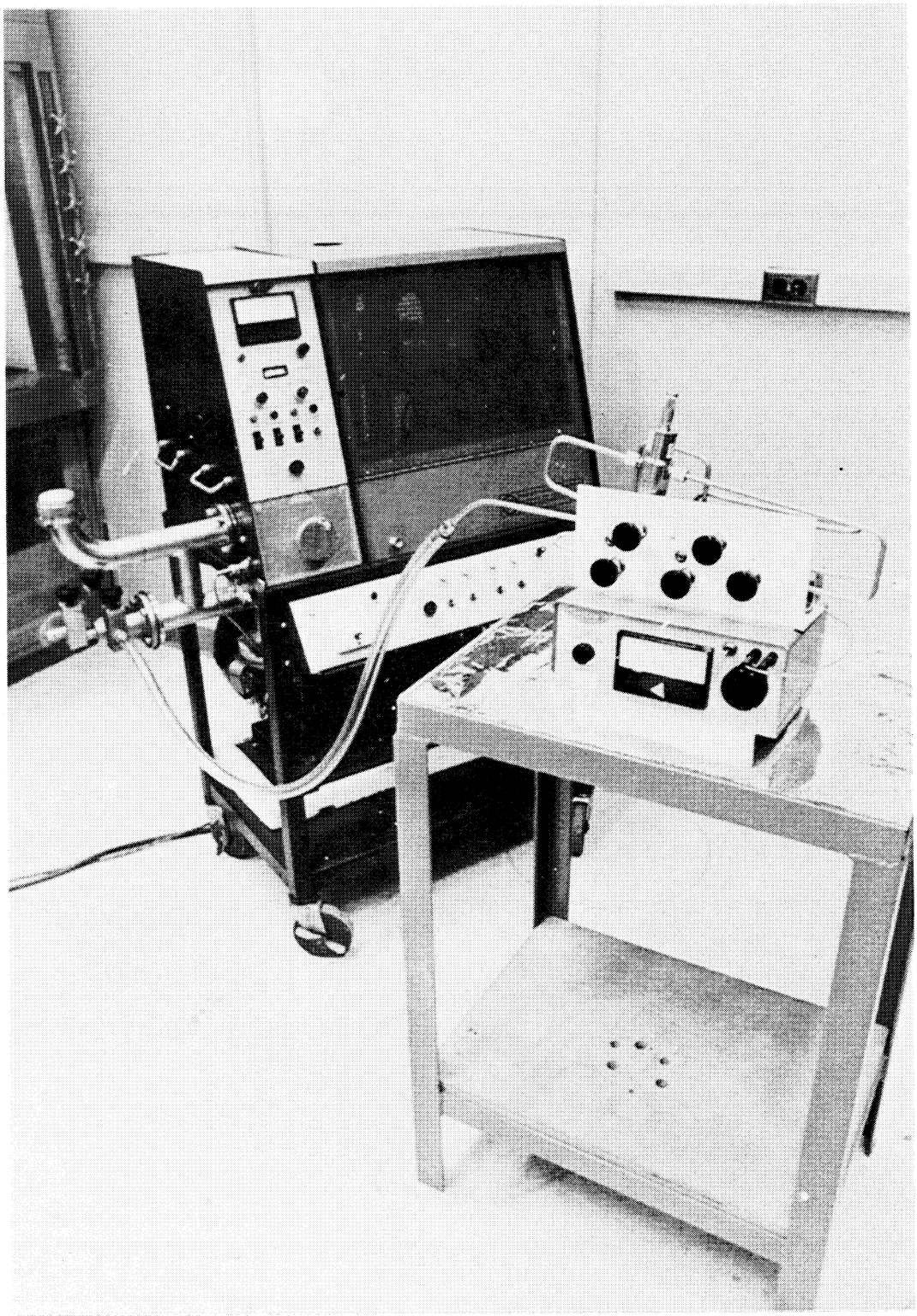

Figure 2-5. Experimental System for Evaluation of Seal Leak Detector Concept

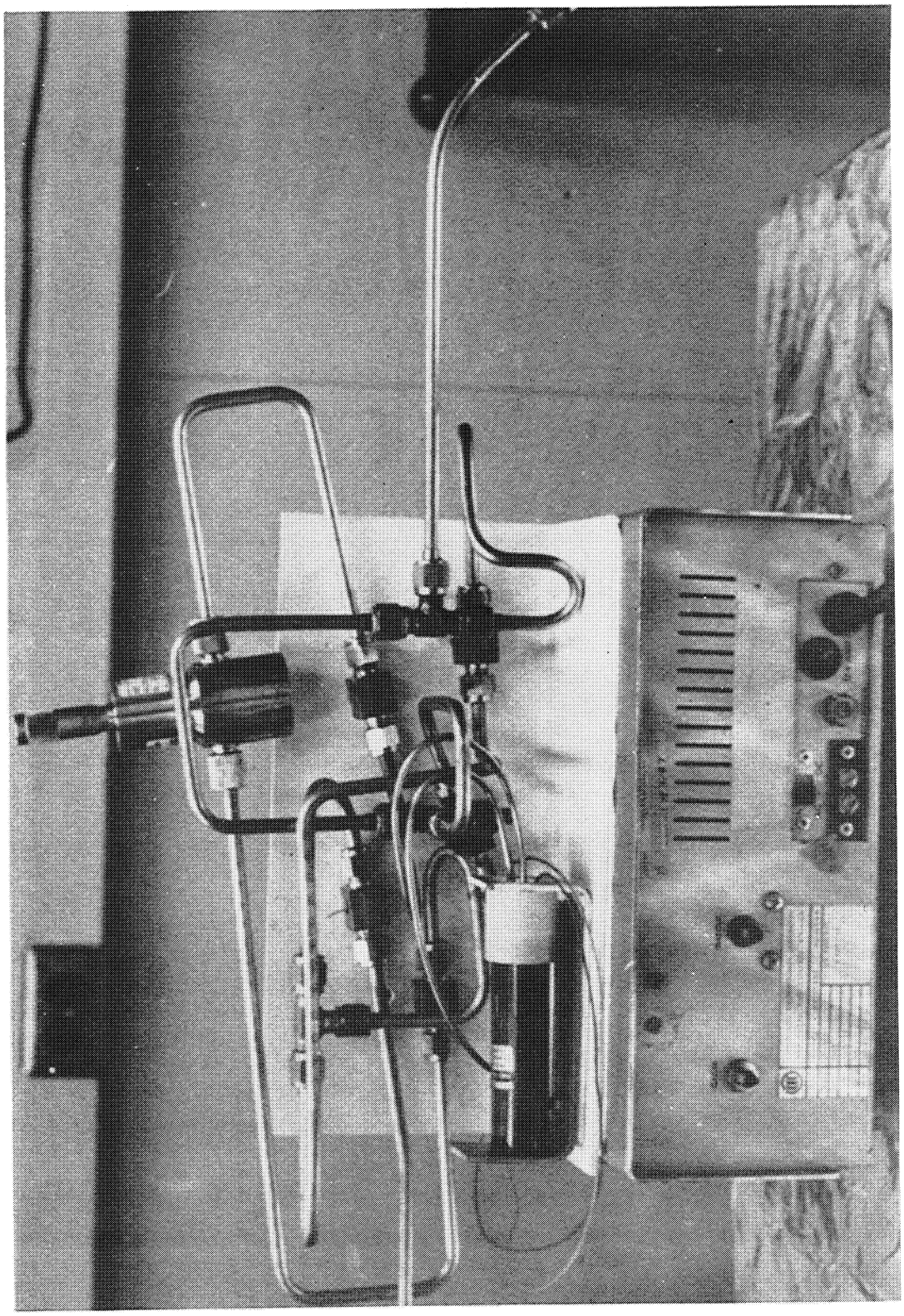

Figure 2-6. Electrolytic Hygrometry Concept Experimental Setup —— Rear View

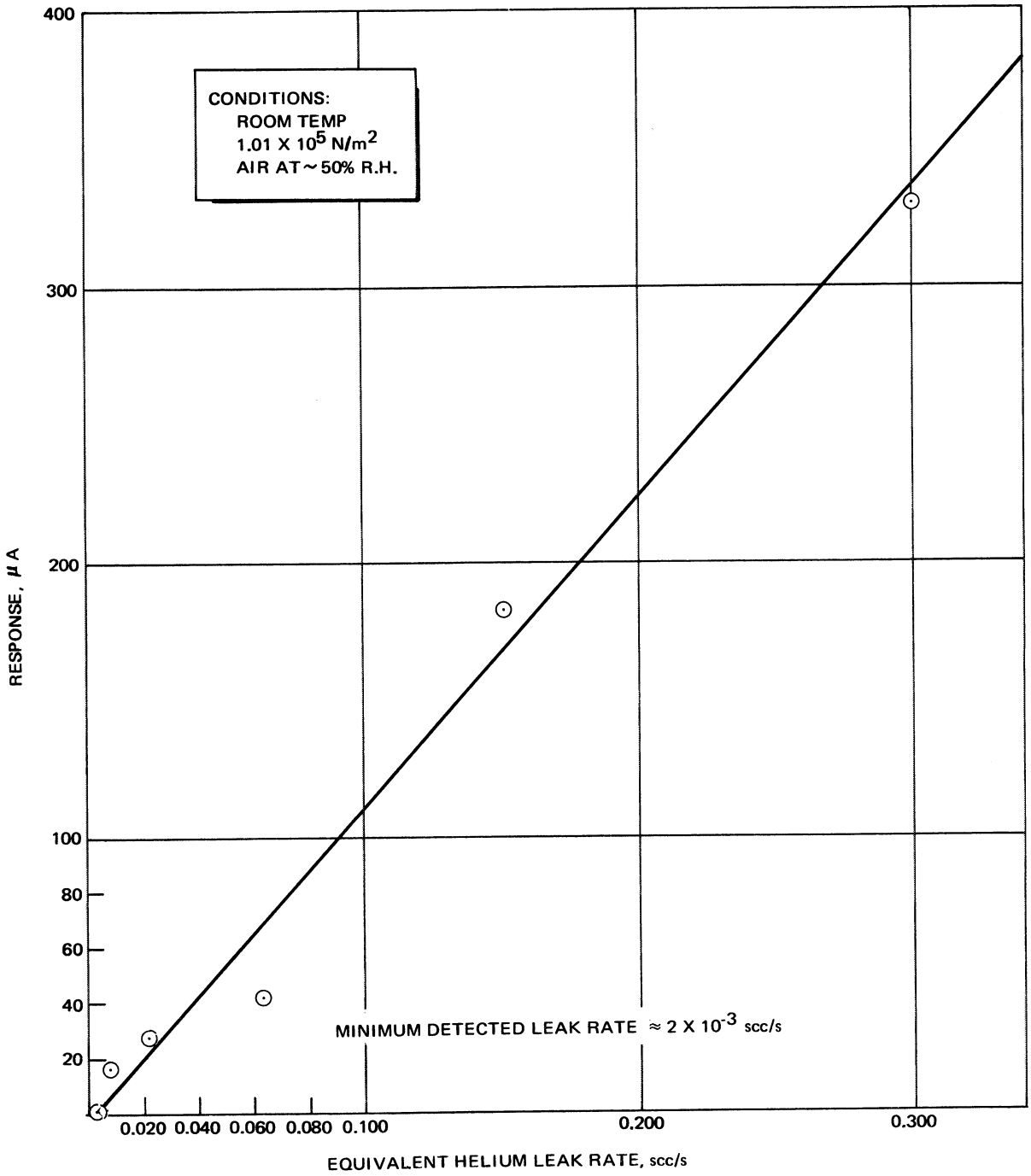

Figure 2-7. Electrolytic Hygrometry Concept: Response Versus Leak Rate

In an attempt to increase the sensitivity of the technique, controlled throttling of the gases on the downstream side of the electrolytic cell was tried to increase residence time of H_2 and O_2 in the electrolytic cell and promote recombination.

This approach did not prove successful.

2.3 CAPACITANCE DETECTION OF WATER VAPOR

2.3.1 Impedance-Capacitance Technique

To provide a guideline for detection sensitivity for capacitance techniques, an initial evaluation was carried out with a commercial instrument. The instrument uses a sensor which consists of a porous oxide layer made by anodizing aluminum with a permeable but conductive gold film overlaying the aluminum oxide surface. Water vapor which passes through the gold film is absorbed on the oxide, changing both the impedance and capacitance in a complex manner which can be related to the moisture present.

The experimental setup used to evaluate the instrument was essentially the same as shown in Figure 2-4; Figure 2-8 is a photograph of the equipment.

The test results shown in Figure 2-9 illustrate that the instrument has about the same detection sensitivity as the electrolytic-hygrometry concept previously evaluated. The minimum detectable leak obtained with this apparatus was 1.5×10^{-3} scc/s.

2.3.2 Silicone Elastomer Capacitance Technique

Water which is present in the cabin atmosphere has a dielectric constant of about 80 as compared to a dielectric constant of about 1 for O_2, N_2, and CO_2. Dimethylsilicone (DMS) elastomer has a dielectric constant of slightly less than 2 and possesses the unusual property of being highly permeable to O_2, N_2, CO_2, and H_2O. These gases and water vapor permeating a capacitor using DMS as the dielectric would have a marked effect on the dielectric constant of the elastomer and increase the capacitance of the sensing unit.

Initial tests were carried out on the capacitance properties of DMS film exposed to a controlled atmosphere. A 5-cm-dia DMS film, 0.0025 cm

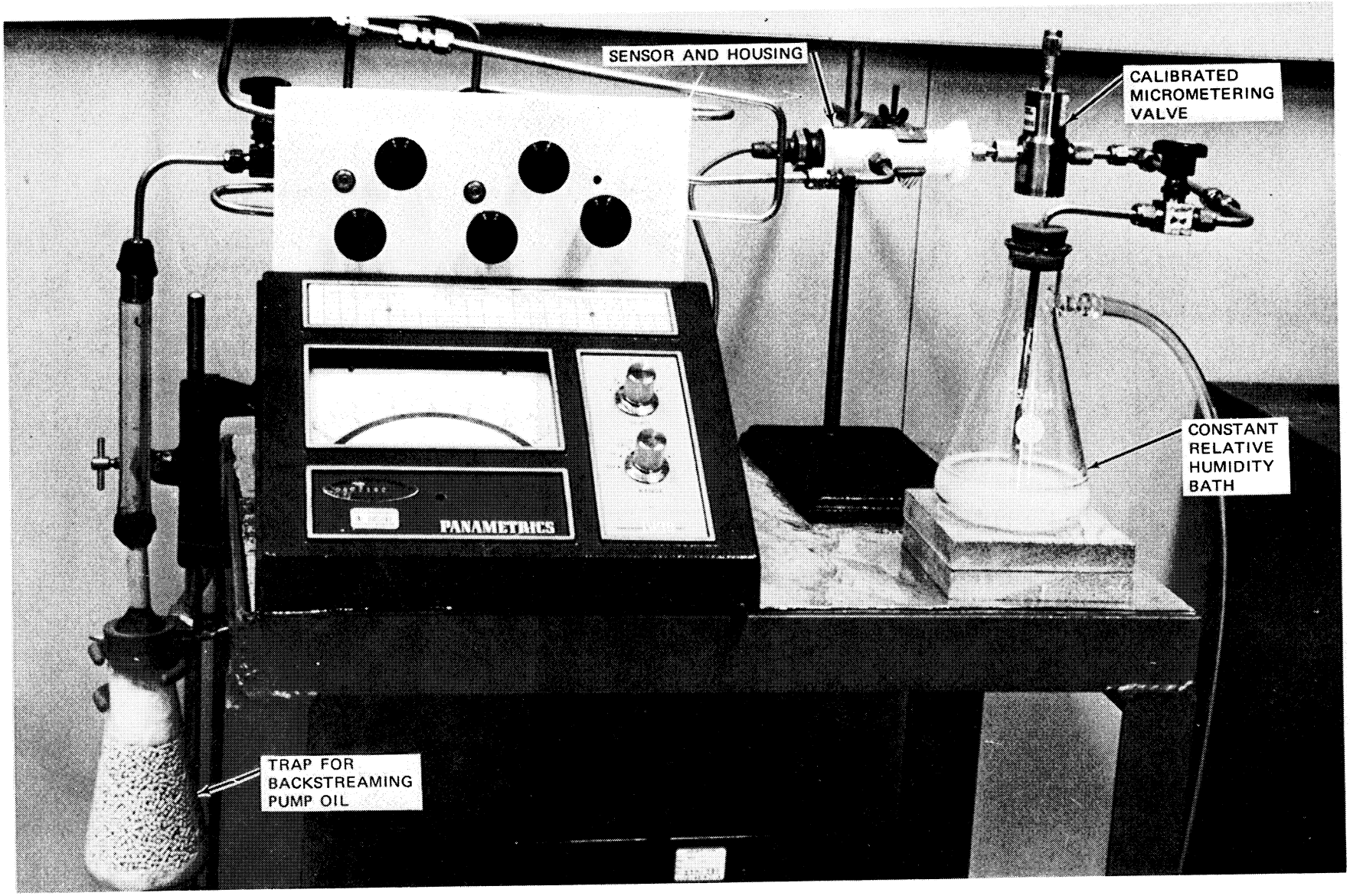

Figure 2-8. Experimental Test Setup —— Capacitance Detection of Water Vapor

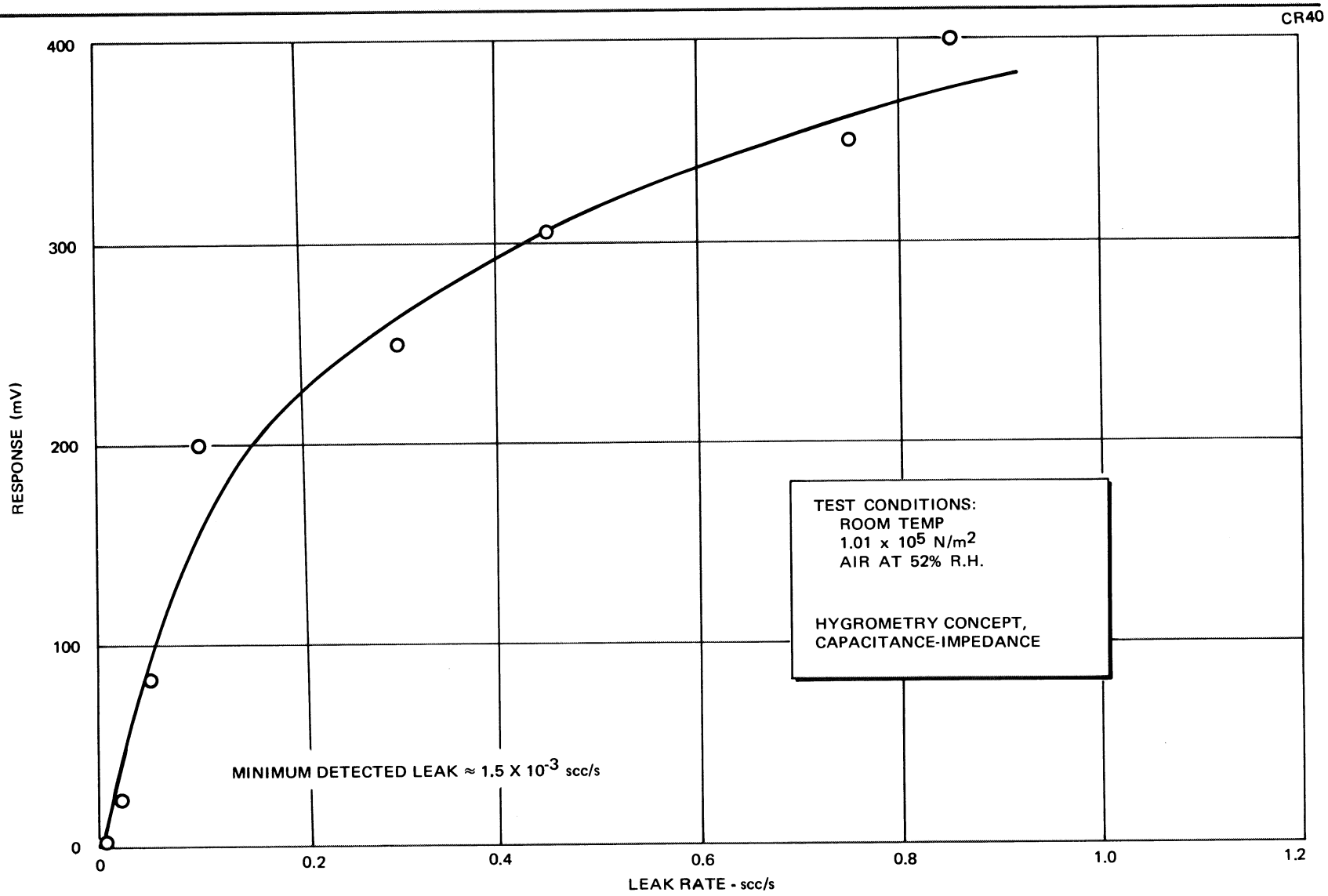

Figure 2-9. Capacitance-Impedance Detection of Water Vapor

thick, was inserted in a dielectric sample holder and measurements taken with a capacitance bridge. Upon initial outgassing of the film in a vacuum, the film displayed an 8 percent decrease in capacitance. After outgassing, the film was exposed to ambient laboratory air at 21°C and 34 percent relative humidity and capacitance was measured as a function of frequency with a capacitance bridge. Test results obtained are listed in Table 2-1 which shows the effects of various frequencies on the capacitance of the DMS film. Since no significant differences were noted as a function of frequency, a frequency of 1 kHz was chosen as the baseline. During these tests, long equilibration times ($\geq$12 hours) were required. Therefore, the sensors designed for evaluation in the test jig had a porous backing applied to the DMS film to facilitate faster equilibration times. Tests disclosed that the backing provided two advantages: (1) the simulated leaking atmosphere dynamically equilibrated quickly with the DMS and (2) the backing prevented a pressure buildup upstream of the sensor which could compromise the sensor accuracy.

Two variations of the capacitance sensor with a Dacron backing were studied in the test jig. As shown in Figure 2-10, common to both were outer Teflon-film insulators and copper-foil electrodes with the DMS in the center. One

Table 2-1

CAPACITANCE CONCEPT – EFFECT OF FREQUENCY ON CAPACITANCE
Dimethylsilicone, 0.0025 cm thick, (1 mil); 20.25-cm^2 area Between Parallel Copper Disks

Frequency (Hz)	Capacitance (pF)
	34% RH, Air
100	1135.00
200	1130.00
400	1127.00
500	1126.00
1,000	1123.36
2,000	1121.20
5,000	1118.29
10,000	1116.12

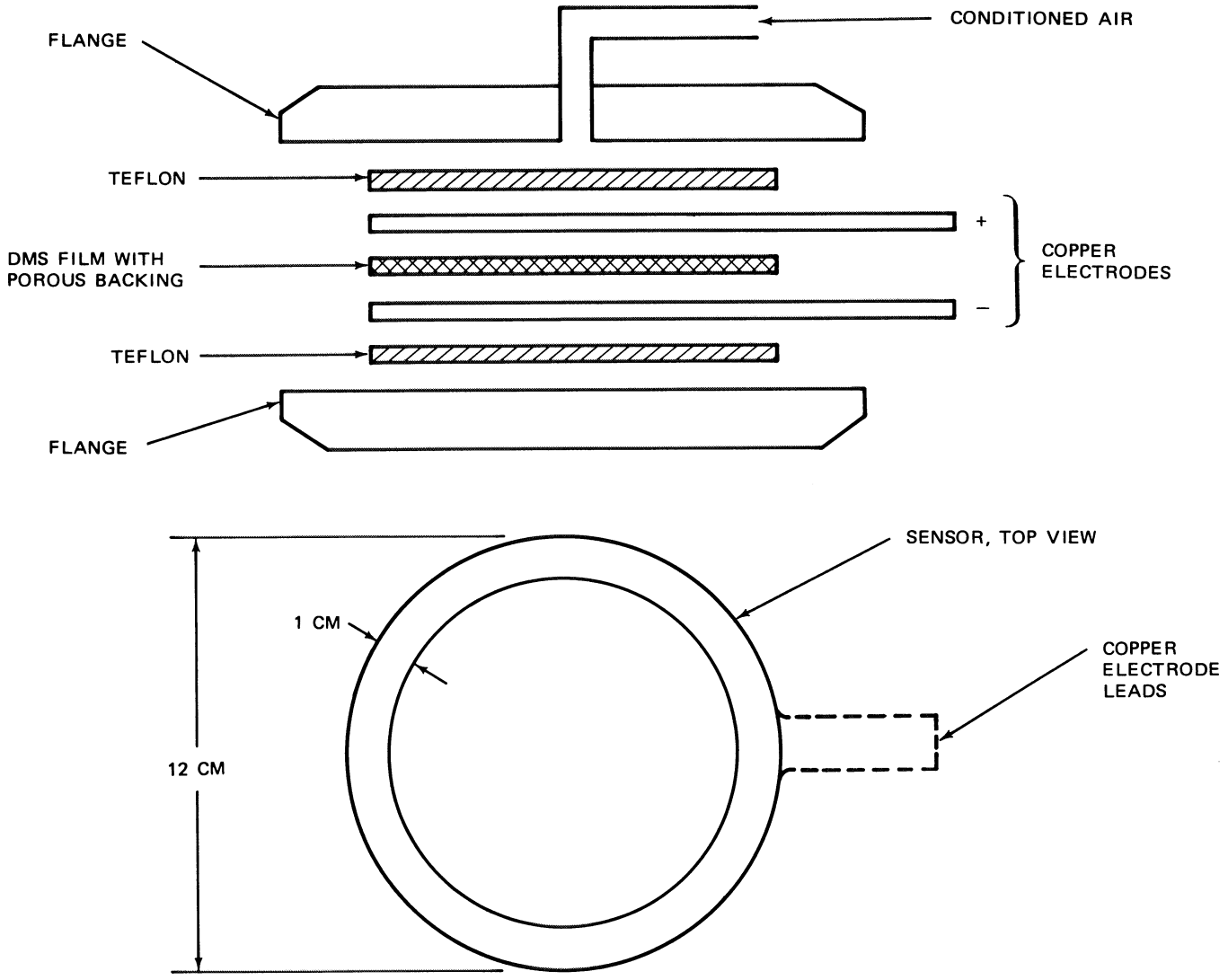

Figure 2-10. Capacitance Concept –– Sensor Construction and Placement in Test Jig

setup used a single 0.0025-cm-thick DMS film backed by 0.005-cm-thick Dacron matting. The other setup used the same Dacron matting between two DMS films.

Figure 2-11 displays the essential elements of the capacitance sensor (matting not shown). Figure 2-12 shows the assembled capacitance sensor applied to the 15.2-cm-dia flange set.

A block diagram of the complete experimental setup is shown in Figure 2-13. Figure 2-14 shows the assembled 15.2-cm-dia flange containing the capacitance sensor as mounted in the bell-jar assembly. Figure 2-15 shows photographic details of the complete experimental setup.

During the test runs with both sensor types, it was determined that the response time was fairly rapid, usually on the order of several minutes.

Test results for the two sensor types are shown in Figure 2-16. Over the range of calibrated leaks examined, the single-layer DMS film arrangement displayed greater sensitivity. The minimum detectable leak rate was measured as 2×10^{-2} scc/s at 52 percent R.H.

Compared to previously measured equilibrium values of capacitance change for plain DMS film, tests on the film with Dacron mat backing indicate an effect only about 22 percent as great. That is, the penalty paid for faster equilibration was about a 78 percent smaller response in capacitance change.

The capacitance sensor concept has the potential for greater sensitivity than the results indicate. Necessary design improvements can yield significant improvements in performance.

2.4 THERMISTOR SENSOR - THERMAL CONDUCTIVITY

2.4.1 Seal Leak Detector

Thermistors exhibit large changes in resistance with small temperature changes. This property can be used to great advantage in sensing gases leaking past a seal. A heated thermistor exhibits the property of a semiconductor with a negative coefficient of resistance. Gas passing over the thermistor that is at some equilibrium temperature in a vacuum will produce

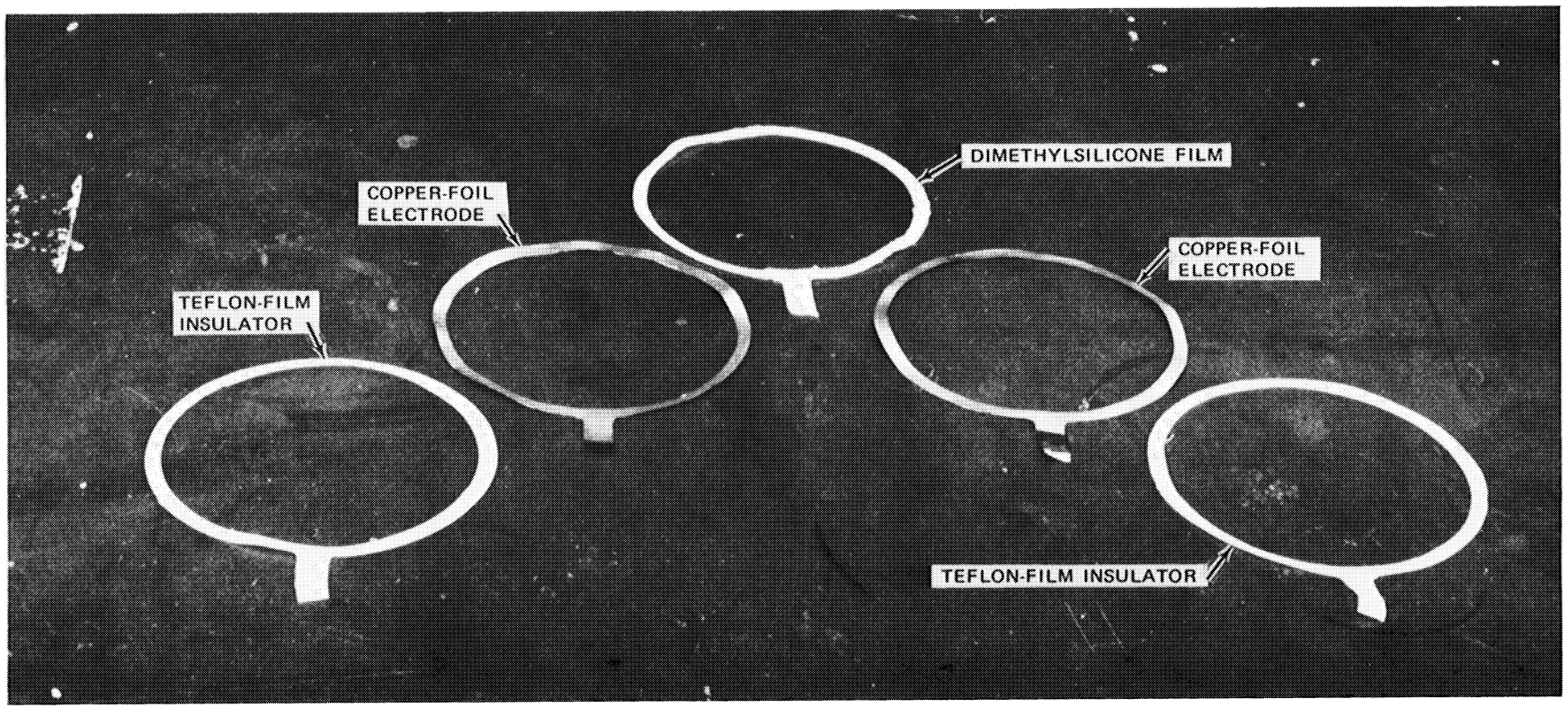

Figure 2-11. Seal-Leak Detector – Capacitance Sensor for Moisture Measurement (Components)

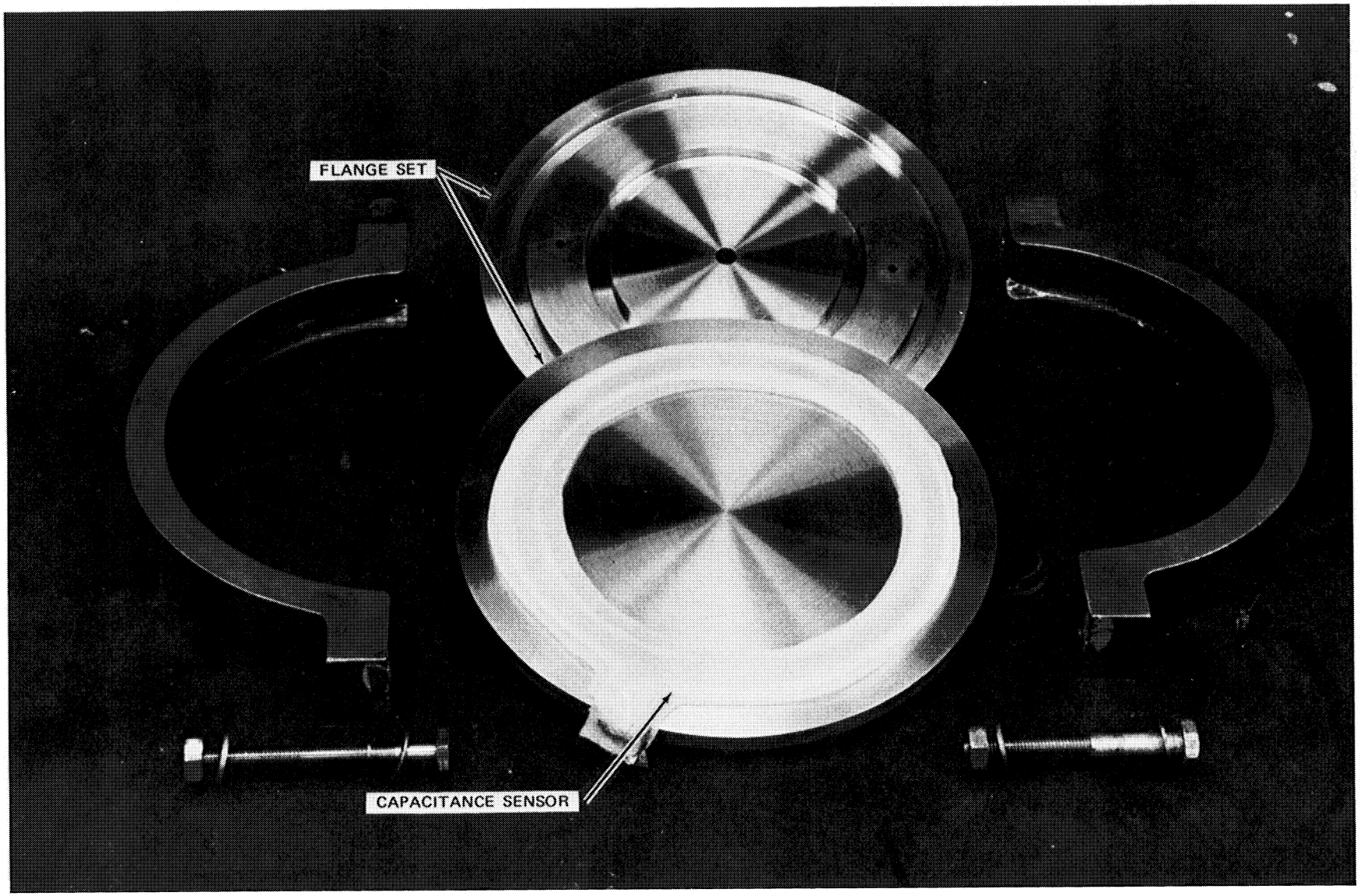

Figure 2-12. Capacitance Sensor Installed in 15.2-cm Seal Leak Detector Flange Set

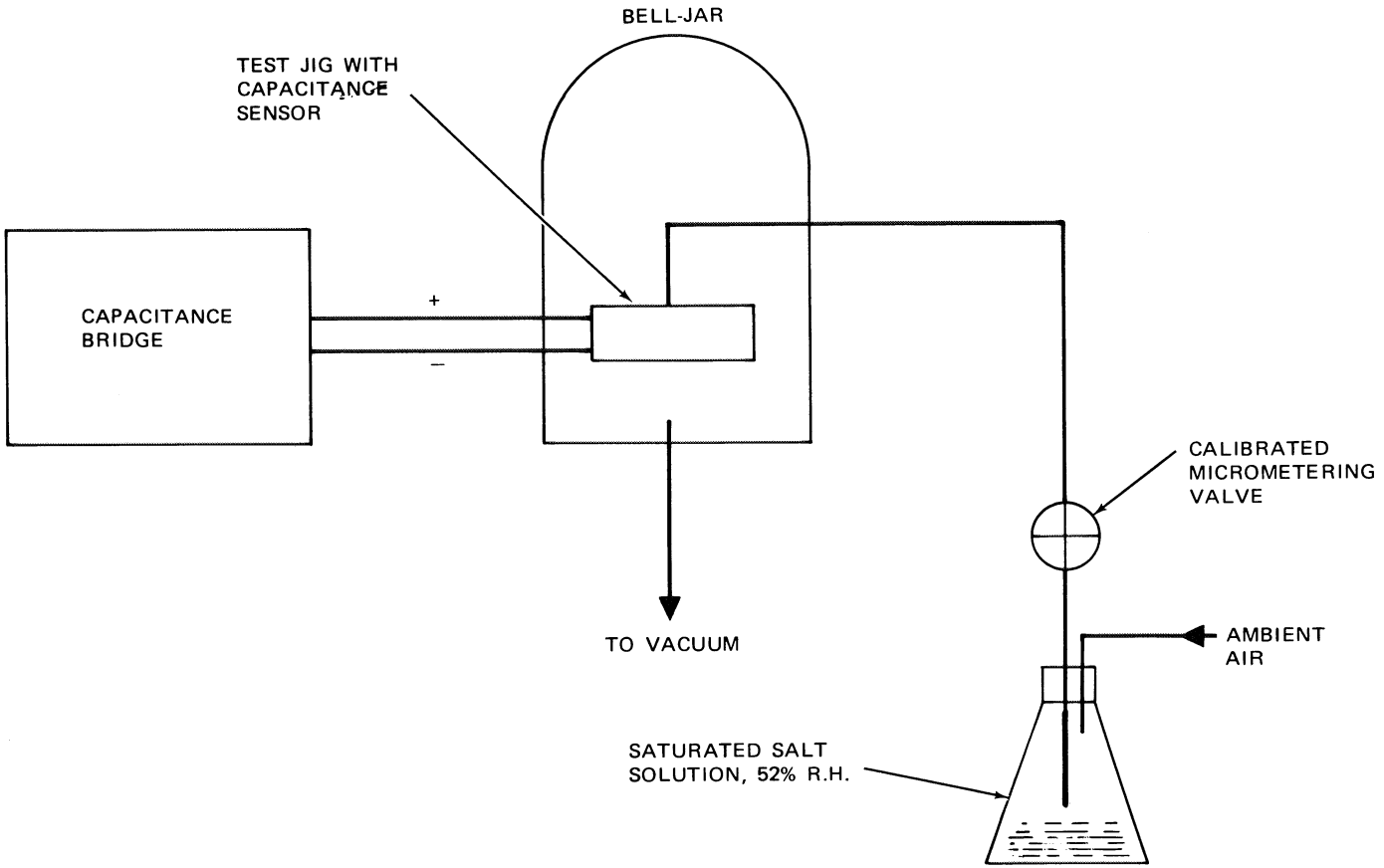

Figure 2-13. Capacitance Concept –– Experimental Setup

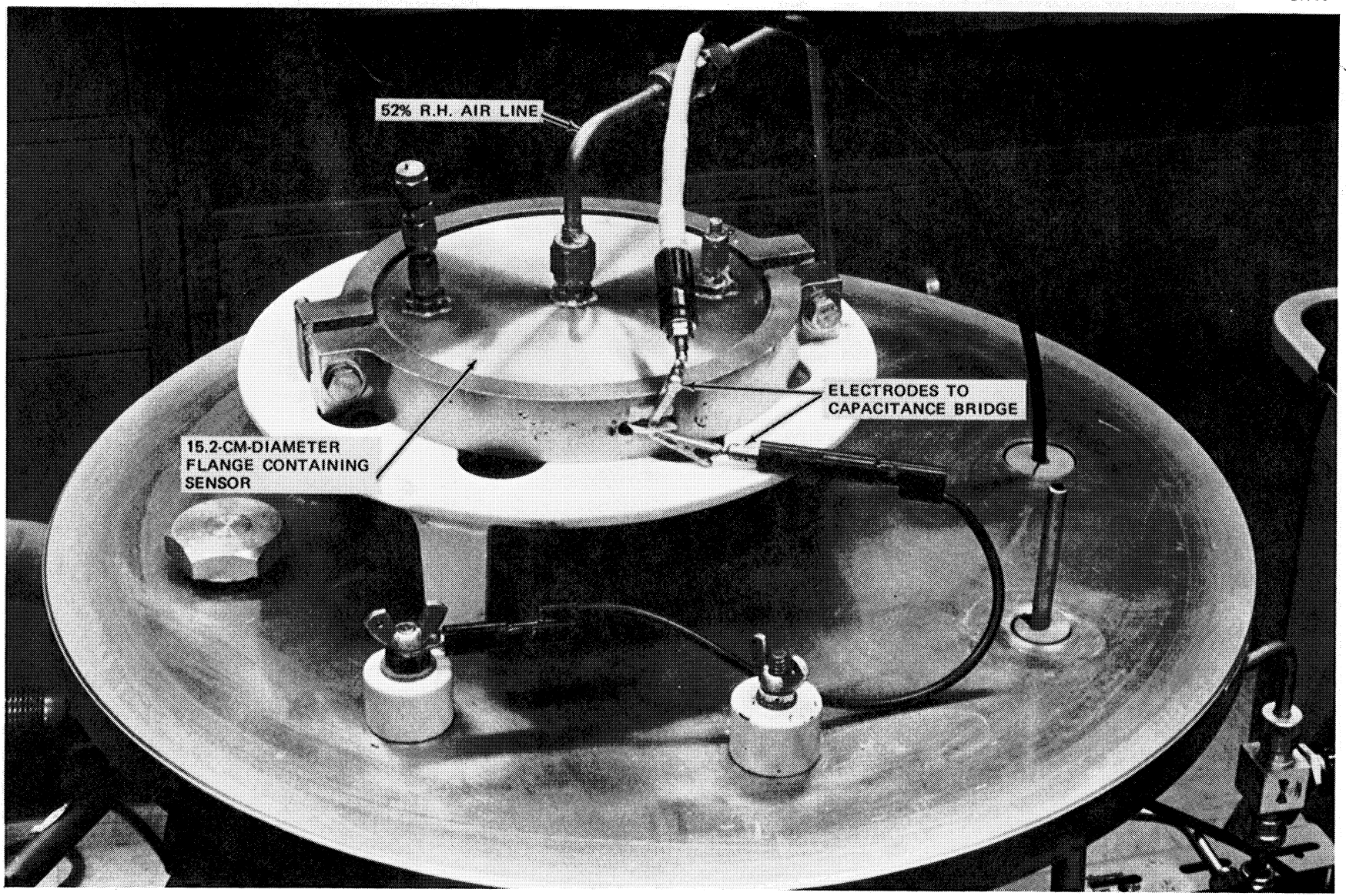

Figure 2-14. Capacitance Sensor —– Test Jig

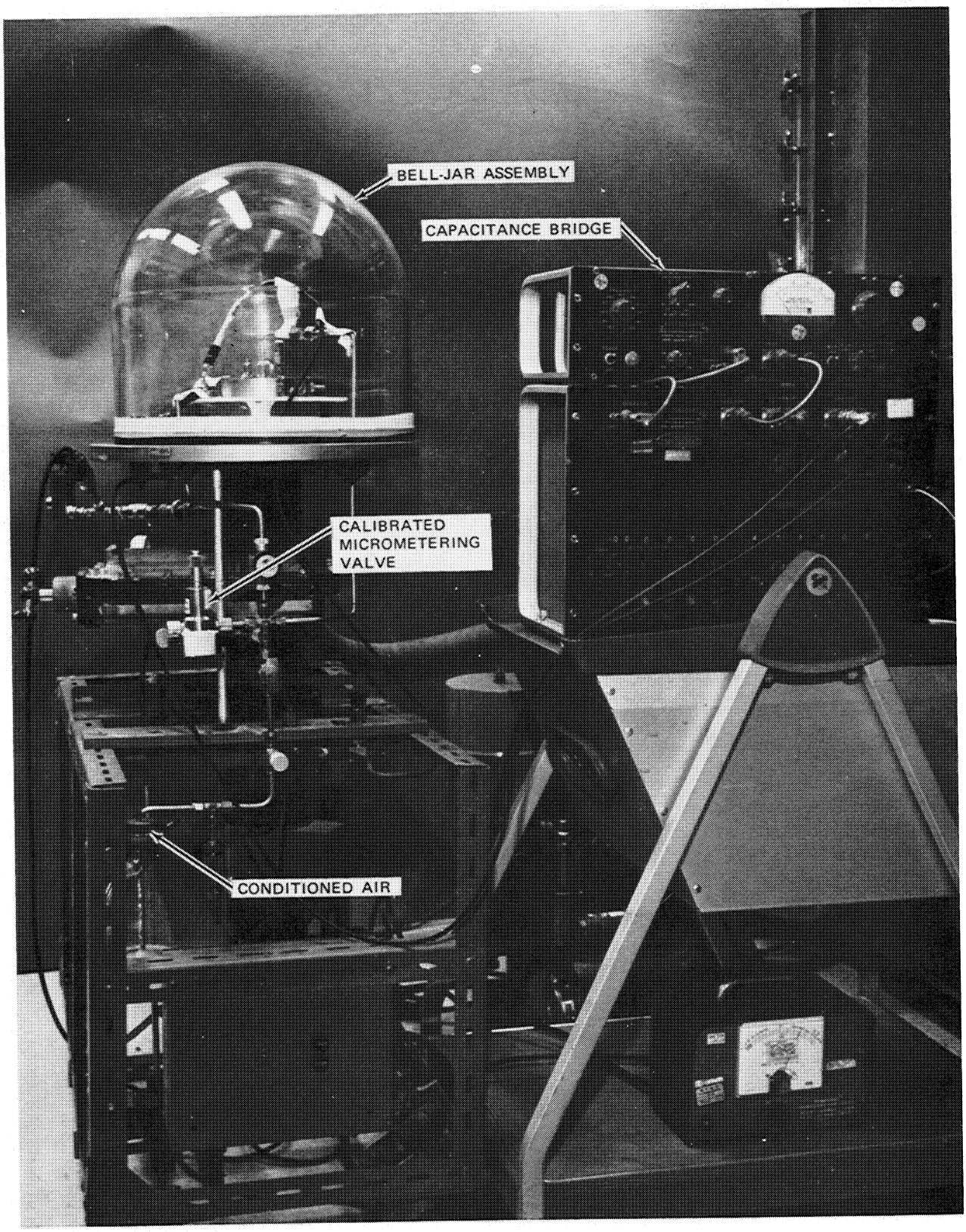

Figure 2-15. Capacitance Sensor Test Setup

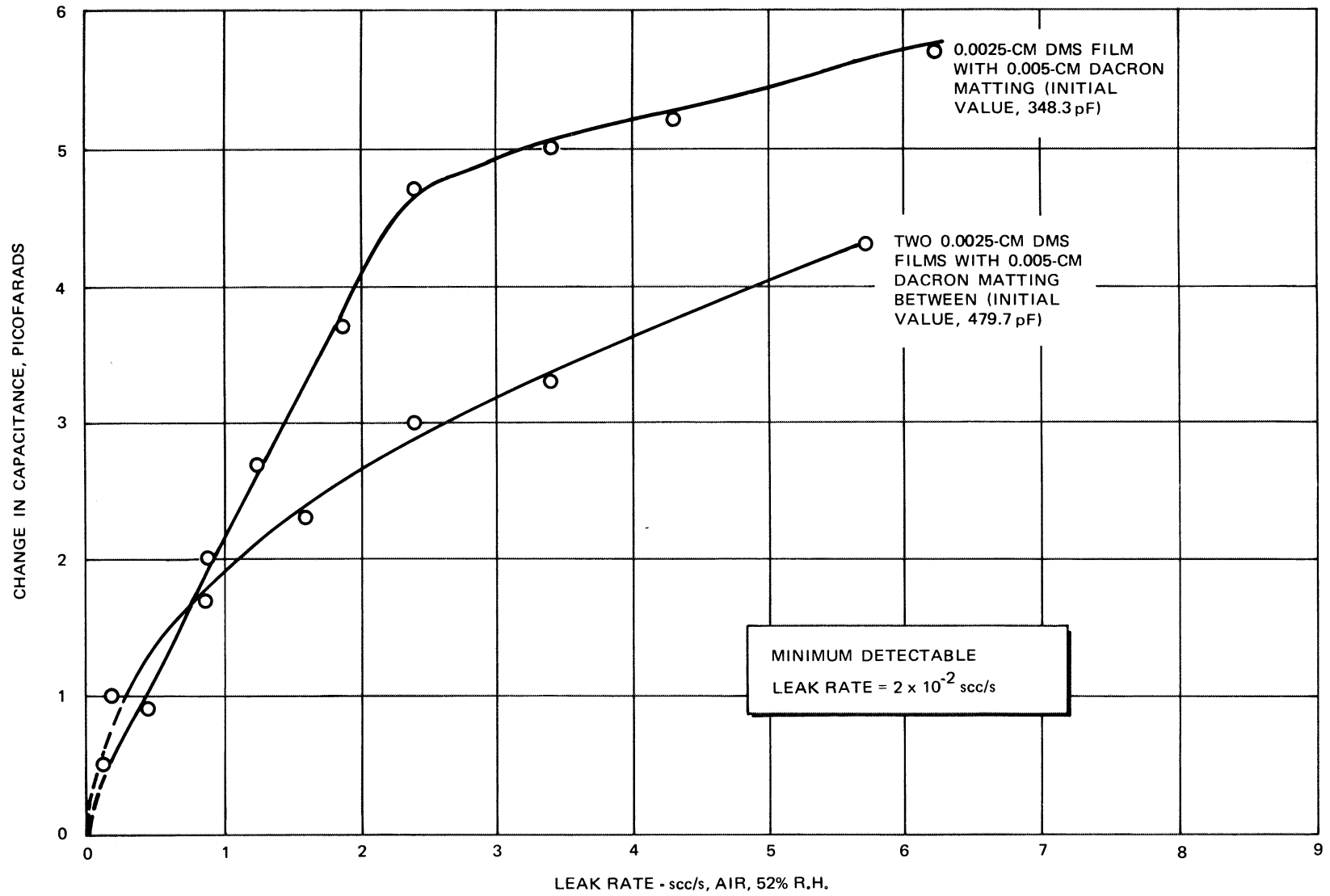

Figure 2-16. Capacitance Sensor Response —— Change in Picofarads as Function of Leak Rate

a cooling effect thereby changing the resistance. By using two thermistors (see Figure 2-3), one sensing and the other as a reference, as two legs of a Wheatstone bridge, any change in resistance registers as a voltage change. Figure 2-17 displays the concept as applied to a critical hatch seal. Any gases, including normal permeation, leaking past the hatch seal can readily be sensed, thereby allowing corrective action to be taken if the hatch has not been properly secured.

A block diagram of the experimental setup for determining the detection sensitivity of thermistor sensors is shown in Figure 2-18.

The following procedure was followed in making measurements.

The entire system was first evacuated with both mechanical and diffusion pumps. The system was then leak-checked down to a maximum leak rate of 10^{-10} scc/s using a helium leak detector. When the system was tight, the Wheatstone bridge circuit was balanced, i.e., zeroed. The mechanical pump was then isolated and the test gas (helium or nitrogen) was introduced upstream of a glass capillary standard leak as shown in Figure 2-19. Gas leaks through the capillary at known rates based on upstream pressure and is sensed by the thermistor within a thermal conductivity cell. Figure 2-20 shows photographic detail of measurement equipment.

Typical test results obtained are shown in Figure 2-21. The minimum detectable leak rate is approximately 10^{-8} scc/s, based on nitrogen gas, which is representative of the main constituents of a space cabin atmosphere.

At the high-leak end, the response saturated. However, the upper range could probably be extended by varying the geometry of the thermal conductivity cell and the thermistor characteristics.

Figures 2-12 and 2-22 display the essential elements of a compact laboratory breadboard for evaluating seal leak detection concepts. Figure 2-22 shows a

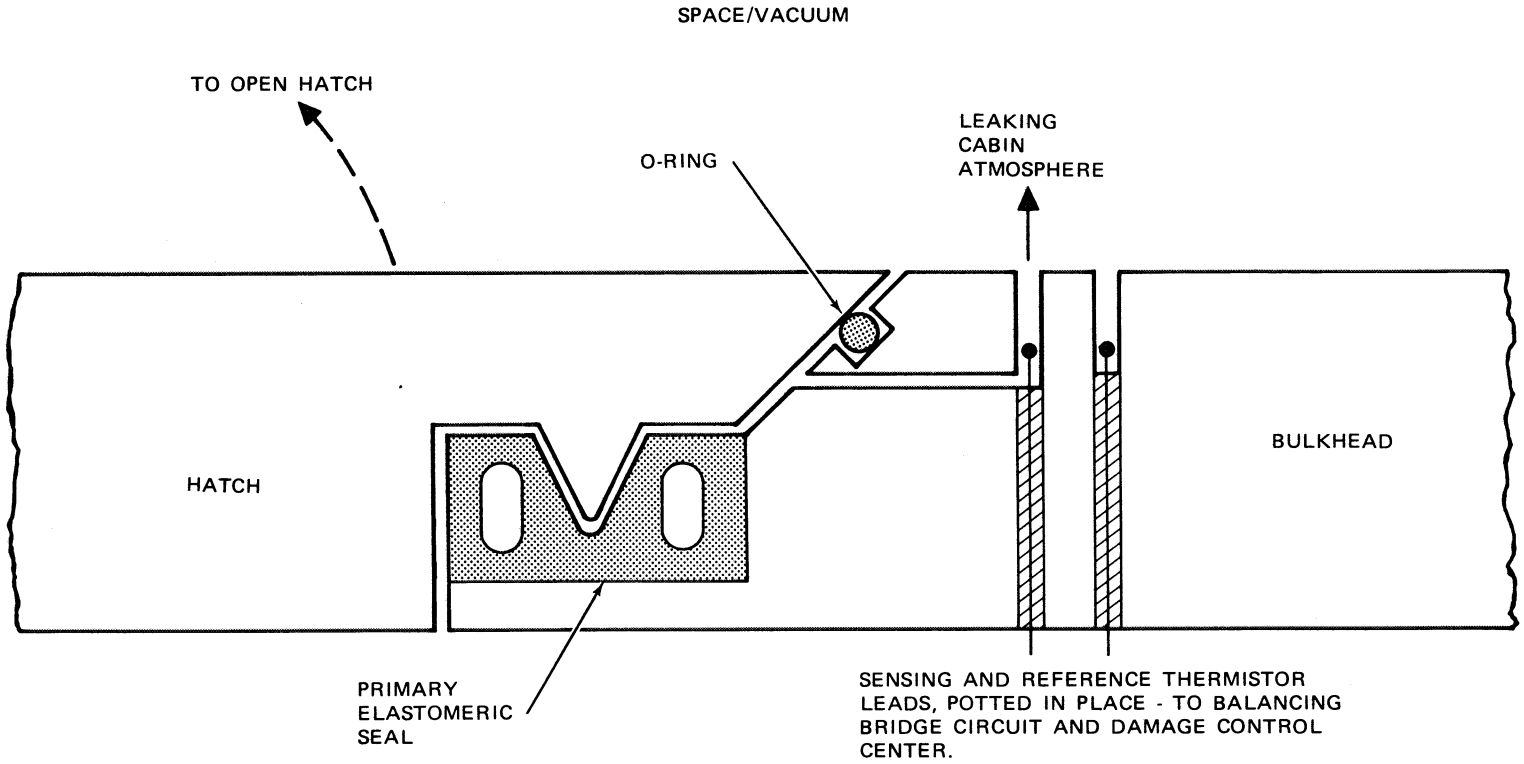

CABIN ATMOSPHERE, LEAKING PAST STRIKER PLATE/PRIMARY SEAL IS TEMPORARILY CONTAINED BY THE O-RING AND VENTED TO SPACE VIA A DRILLED PASSAGE CONTAINING A SENSING THERMISTOR. A REFERENCE THERMISTOR COMPENSATES FOR TEMPERATURE VARIATIONS AND FORMS ONE LEG OF A BALANCING BRIDGE CIRCUIT.

Figure 2-17. Location of Sensors Used to Detect Hatch Seal Leaks

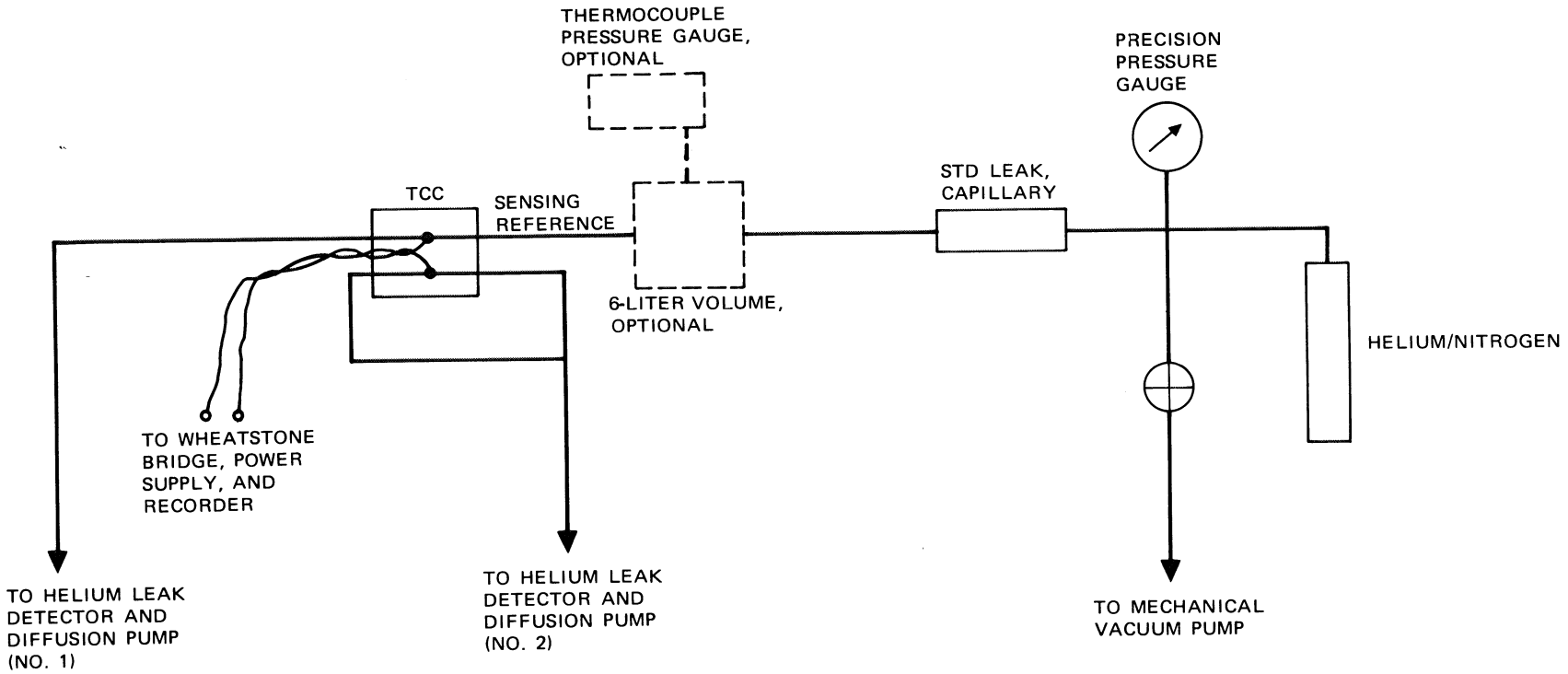

Figure 2-18. Thermal Conductivity – Experimental Setup

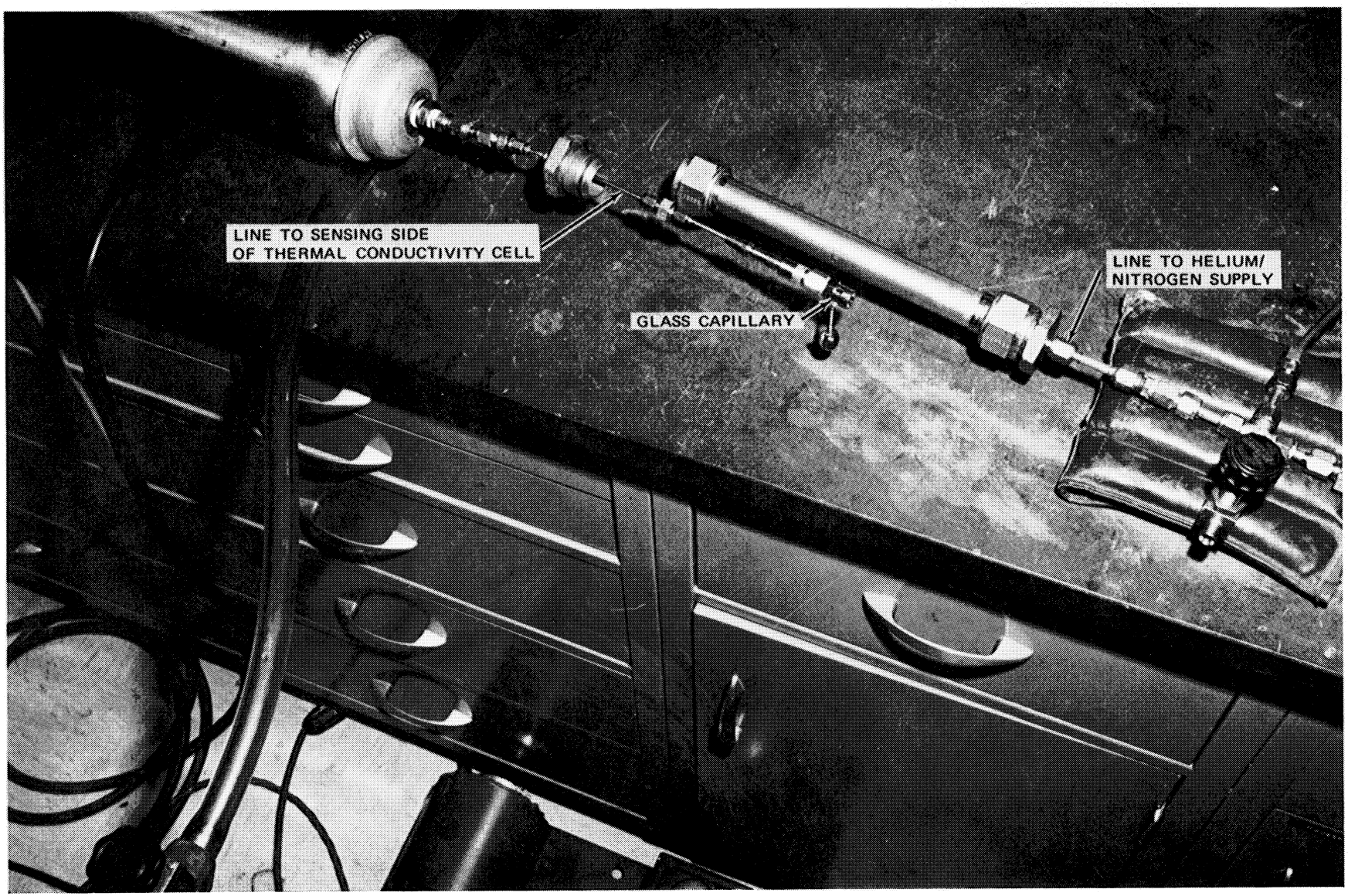

Figure 2-19. Thermal Conductivity —– View of Exposed Glass Capillary Standard Leak

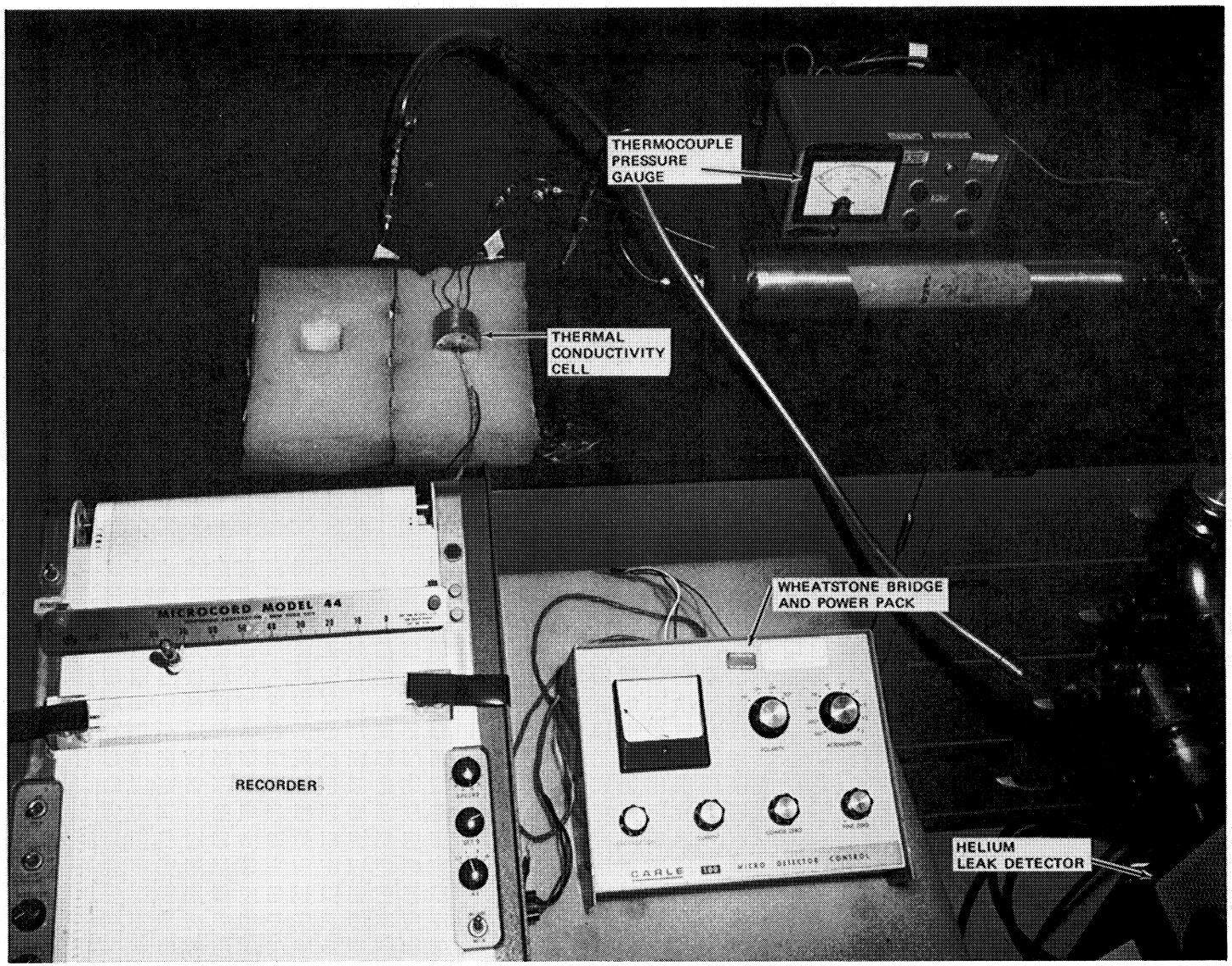

Figure 2-20. Thermal Conductivity —— View of Measurement Equipment Test Setup

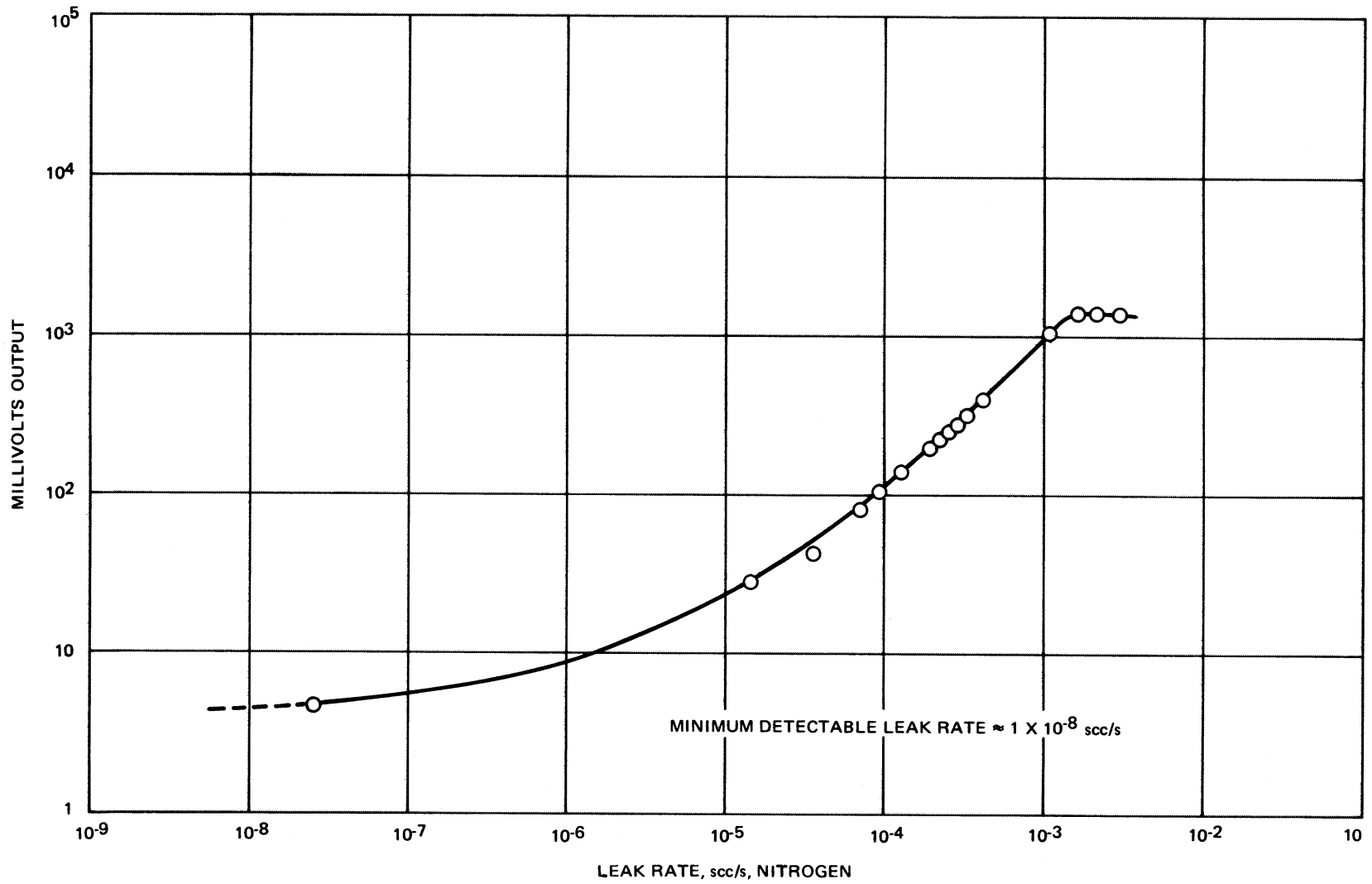

Figure 2-21. Thermal Conductivity — Thermister Response vs Leak Rate

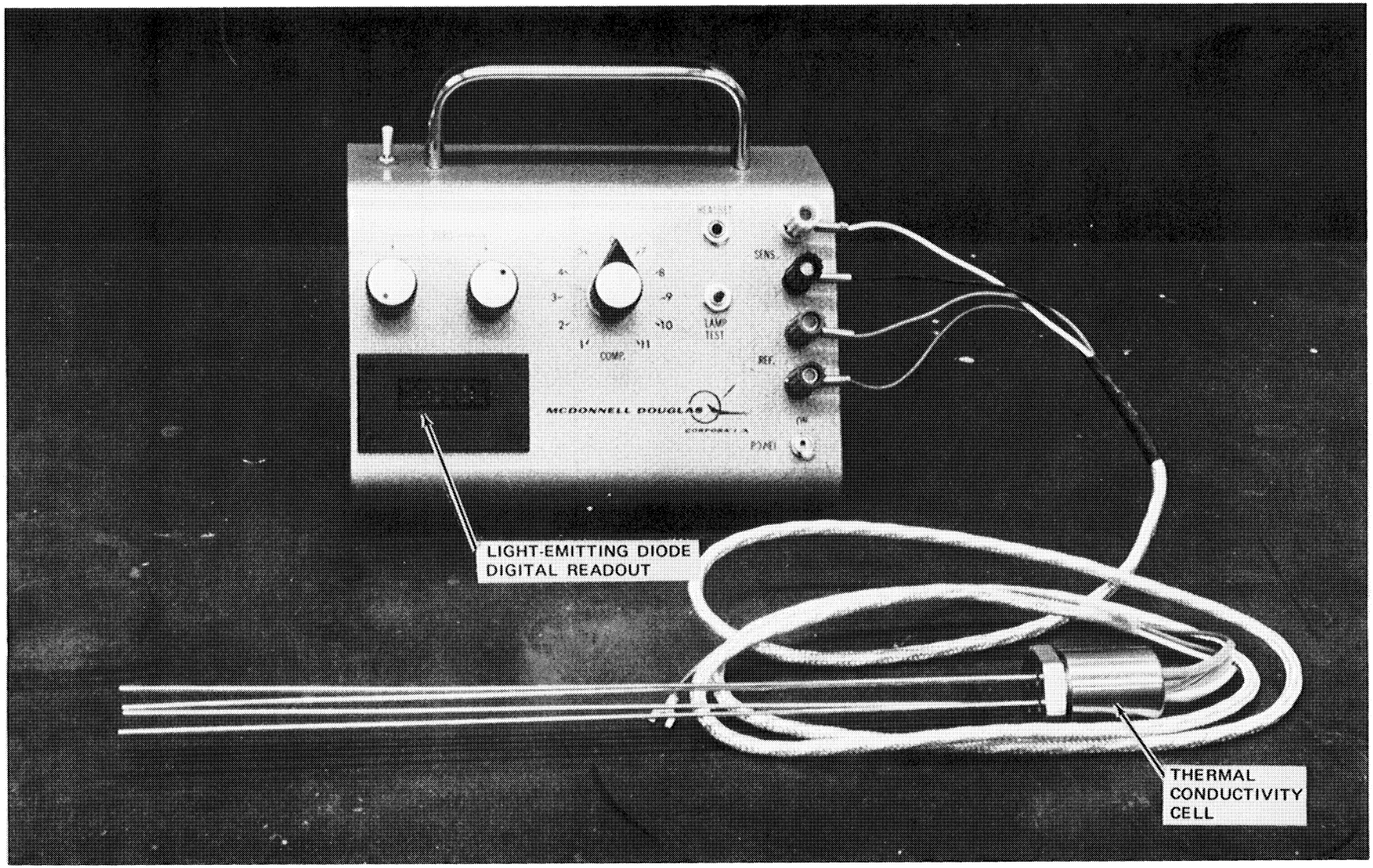

Figure 2-22. Prototype Thermal Conductivity Seal Leak Detector

version of a prototype portable compact signal conditioning - readout display system. Millivolt output reads out direct in a digital light-emitting diode (L. E. D.) display. An audio output is also provided to trigger at an arbitrary level.

2.4.2 Space Station Pressure Shell Overboard Leakage

In a review of concepts for detecting overboard leaks through the pressure shell of a manned space cabin (Reference 2), Withey suggested the use of an ionization gage for detecting gas escaping through the leak into the compartment formed by the pressure wall and the meteoroid bumper. As part of the experimental study on thermistor sensing of gas leaks past seals, the feasibility of applying thermistor sensing to overboard leaks in the pressure shell was also explored.

To simulate gas leaking through a spacecraft pressure shell into the volume defined by the shell and meteoroid bumper, a 6-liter volume was placed before the thermal conductivity cell but after the standard leak in the test setup (Figure 2-18). As expected, there was no change in the response because the leak was totally confined before passing through the thermal conductivity cell. The more general case is where the confined volume has one or more holes in the surface representing the meteoroid bumper. Over a period of time, a meteoroid bumper can expect to have a number of penetrations even though the main wall is not necessarily penetrated. In the case of a leak in the main wall and holes in the bumper cabin, gas escaping through the leak in the main wall expands rapidly, some passing through the hole(s) in the bumper and some filling the space between the walls.

This condition was simulated in the test setup shown in Figure 2-23. Test results are shown in Figure 2-24. In this case the thermal conductivity cell acts as a thermistor pressure gage which would provide a measure of the leakage rate.

2.5 COMPARISON OF SEAL LEAK DETECTOR CONCEPTS

Comparison of the test results obtained for all three concepts are shown in Table 2-2.

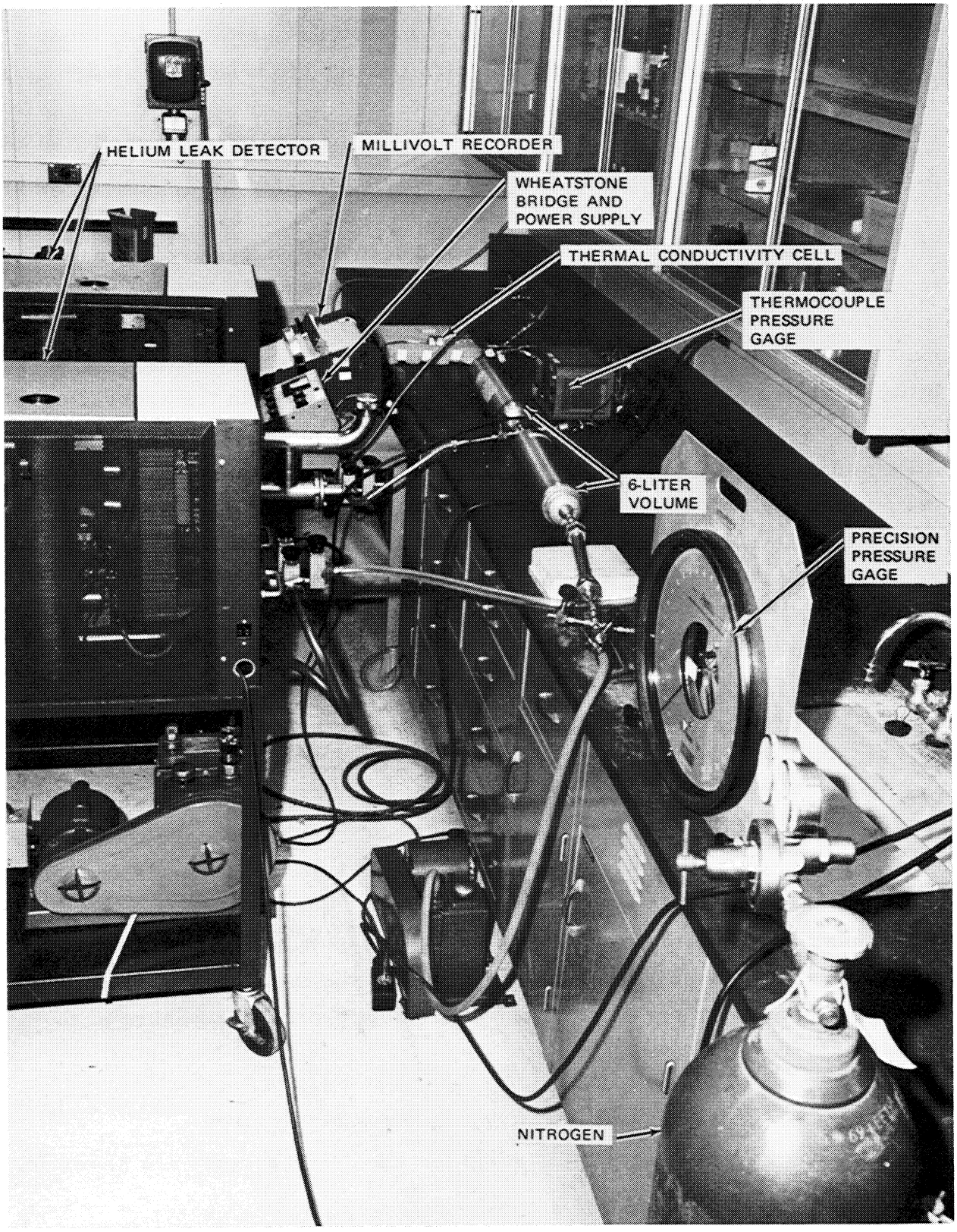

Figure 2-23. Thermistor Static Pressure Sensor Test Setup

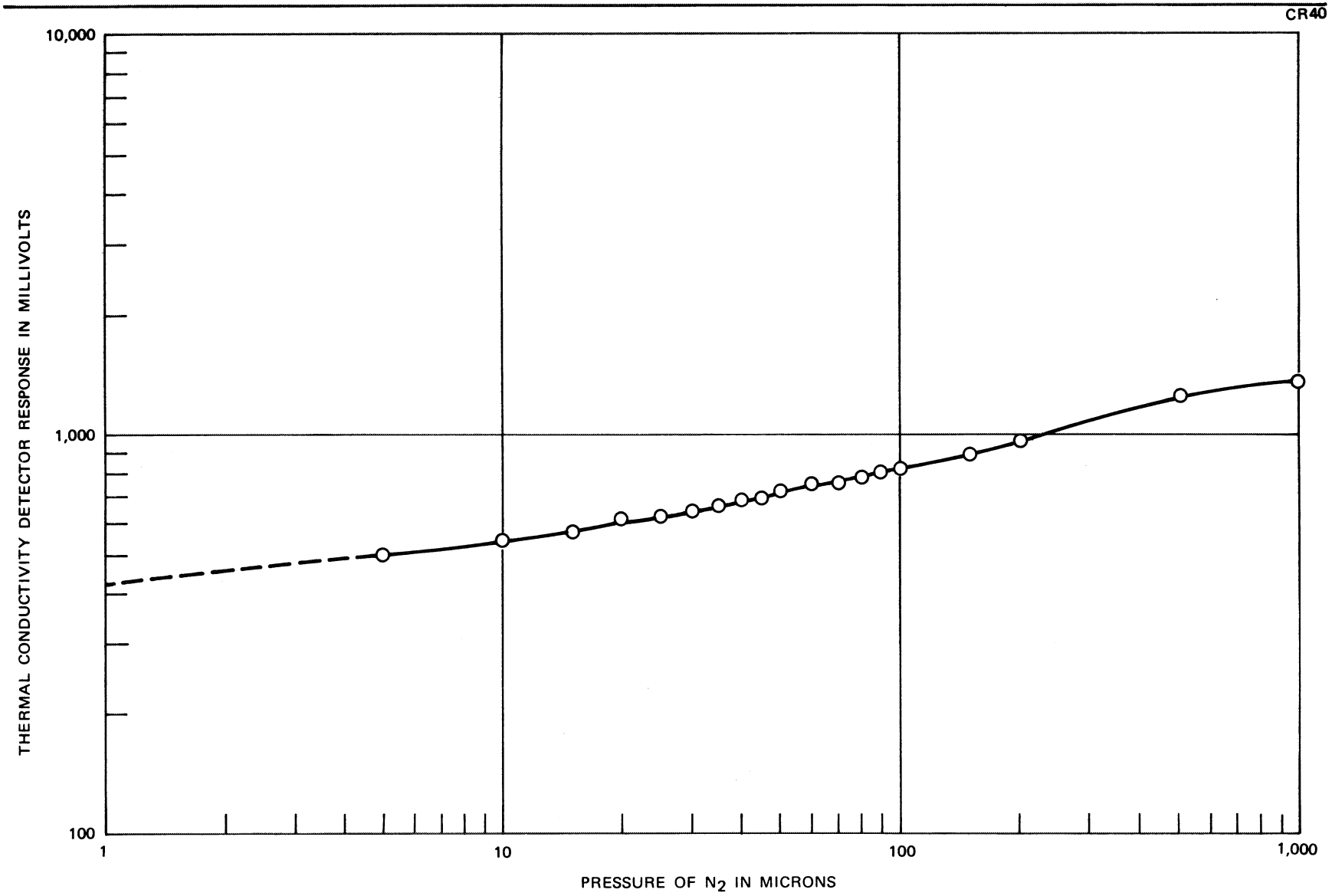

Figure 2-24. Thermistor Thermal Conductivity Cell Response to Static Pressures

Table 2-2

SUMMARY OF SENSOR LIMITS FOR LEAK DETECTION (scc/s)

Method	Detection Range	
	Lower	Upper
1. Hygrometry		
-Electrolytic	2×10^{-3}	>1
-Impedance-Capacitance	1.5×10^{-3}	>1
-Capacitance-Dimethylsilicone Film	2×10^{-2}	>1
2. Thermal Conductivity	$<1 \times 10^{-8}$	$\sim 1 \times 10^{-3}$

From the experimental data, it is apparent that the thermal conductivity technique employing thermistors is the only method which met the stated detection sensitivity objective of 10^{-4} scc/s or better.

The electrolytic and impedance-capacitance concepts represent well developed state-of-the-art systems and promise little further potential in increased sensitivity. Although the DMS capacitor film displayed relatively low detection sensitivity in the current tests, the method is believed to have considerable potential for significant improvements in detection efficiency. Such film systems are flexible and can readily be adapted to flanges with minimal design changes. Further, such film sensors are adaptable to both gas and fluid leaks for onboard leak detection.

Overall, the thermal conductivity technique using thermistors is the recommended method based on the tests carried out. This method can monitor normal permeation of cabin atmosphere past a seal and thereby provide a continuous check of successful operation as well as give a warning of malfunction at any arbitrary level of leakage beyond normal permeation. Thermistor systems are small, rugged, lightweight, and can readily be integrated into a damage control system.

Section 3
ACTIVE ULTRASONICS

3.1 INTRODUCTION

Ultrasonic Lamb-wave techniques have been considered for application in a damage-control system to locate leaks in a space cabin wall because these waves propagate within plate-like structures, are sensitive to small defects, and can propagate past ribs on integrally stiffened panels. To determine the feasibility of using ultrasonic Lamb-wave techniques for remote leak location and detection on space station-type structures, the following program was conducted. First, Lamb-wave modes were selected for use with the material of interest (1.60-mm-thick aluminum). These modes were then screened for their applicability to leak location by determining their sensitivity for remotely detecting simulated flaws in aluminum sheets. Then the relative ability of each mode to traverse an integral reinforcement rib was investigated to further narrow selection of the Lamb-wave modes to be used in a final breadboard demonstration of leak location. In conjunction with the mode selection studies, more detailed flaw detection investigations were carried out on partial and through-the-thickness simulated flaws such as notches and holes. Also, the effects on flaw detectability of obstructions like a fastener or a feedthrough were investigated when the obstruction was located between the transducer and the flaw. Finally, flaw detection on the ribbed panel was investigated, and Lamb-wave operating conditions were selected for use on the breadboard leak-location system. Based on the results of this study, conclusions and recommendations are given for future research and development studies on damage-control applications of Lamb-wave ultrasonic techniques.

3.2 LAMB-WAVE PROPAGATION

Ultrasonic techniques are widely used in nondestructive testing to detect cracks and flaws in materials. The types of ultrasonic waves that are most commonly used are longitudinal, shear or transverse, surface or Rayleigh,

and Lamb or plate waves. A longitudinal wave is so called because the particles in the medium through which it propagates vibrate back and forth along the direction of propagation of the wave. In shear waves, the particles vibrate perpendicular to the direction of propagation of the wave. The surface waves as their name implies have their vibrational energy concentrated at the surface of the medium in which they propagate. At a distance of one wavelength below the surface, their amplitude decreases to about 10 percent of that at the surface. Lamb or plate waves are ultrasonic waves that propagate in elastic plates of uniform thickness. There are two classes of Lamb waves, symmetrical and asymmetrical, so named for the way in which the wave disturbance distorts the cross section of the plate. These distortions of the plate cross section are shown in Figure 3-1 (Reference 3). The symmetrical wave motion resembles a series of bulges propagating along the plate, whereas the asymmetrical wave motion resembles that of a flag waving in the wind. These disturbances propagate along the plate with a velocity that depends on the frequency of the wave and the thickness of the plate. The disturbance is felt throughout the plate and on both its surfaces, so that these waves can be used to detect flaws on both plate surfaces as well

CR40

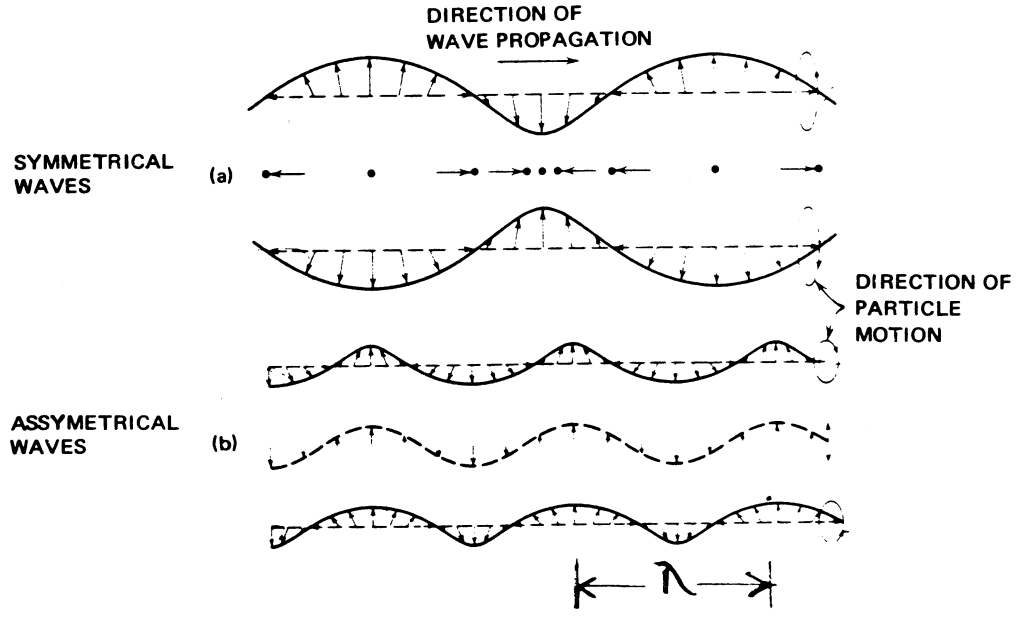

(AFTER KRAUTKRÄMER)

Figure 3-1. Distortion of Plate Cross Section Caused by Lamb Waves

as within the plate. Lamb waves are frequently used to inspect tubing and sheet metals.

In the general case of a Lamb wave propagating in a plate, the wave motion can be thought of as composed of longitudinal and shear wave components reflecting back and forth between the surfaces of the plate, as indicated in Figure 3-2 (Reference 4). Each time a longitudinal or a shear wave is reflected at a boundary, mode conversion occurs where some of the longitudinal wave energy is converted into a shear wave component and some of the shear wave energy is converted into a longitudinal wave component, with the result that extra shear and longitudinal components are produced. The energy is best propagated along the plate under those conditions where the various reflected components combine in and out of phase at regular intervals. The disturbances of these components combine in their effects on the motion of the plate to produce the symmetrical and asymmetrical Lamb-wave modes. For other conditions of excitation, energy is propagated along the plate in a random manner, and no Lamb-wave mode is obtained.

CR40

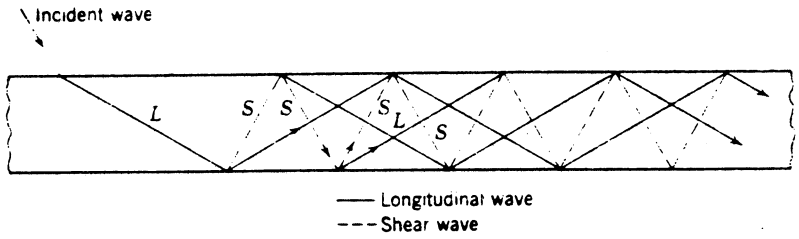

Figure 3-2. Longitudinal and Shear Components of Lamb Wave in a Plate

The relationship between Lamb-wave phase velocity and frequency and plate thickness is shown in Figure 3-3 (Reference 5) for Lamb waves in aluminum. Lamb-wave velocity is plotted as a function of the product of the frequency and the plate thickness (f x d product). The phase velocity is the characteristic velocity of a continuous sinusoidal wave propagating in a plate of thickness d, and gives the rate at which the plate cross-section distortions (Figure 3-1) travel along the plate. The velocity curves show that several different Lamb waves or wave modes of different velocities can exist for a given frequency and plate thickness. For the application of Lamb waves in nondestructive inspection, it is desirable to work with only one wave mode at a time.

Lamb waves can be generated using an experimental setup as shown in Figure 3-4. In this setup, a longitudinal ultrasonic wave is obliquely incident on the surface of a plate such that the angle between the incident wave front and the surface of the plate is θ. This angle will be subsequently referred to as the transducer wedge angle. The line of intersection of the incident wave front with the plate sweeps along the surface of the plate with a velocity, v, which is related to the velocity of the incident longitudinal wave, v_ℓ, by the equation:

$$v = v_\ell / \sin \theta .$$

When the angle, θ, is chosen so that the intersection velocity, v, is equal to the velocity of a possible Lamb-wave mode in the plate having the same frequency as the incident longitudinal wave, that Lamb-wave mode is generated in the plate. Working at a fixed frequency in a given plate thickness, i.e., a given f x d product, different Lamb-wave modes are generated by varying the angle of incidence of the longitudinal wave.

The velocity at which short-duration pulses of Lamb waves travel within the plate is given by the group velocity. A pulse of waves is composed of a superposition of Fourier component waves with frequencies centered around the pulse frequency. The width of the distribution of frequencies is inversely proportional to the number of wavelengths in the pulse. For waves whose phase velocity in a medium strongly depends on the frequency of the wave, the velocities of the various components are different and the group velocity,

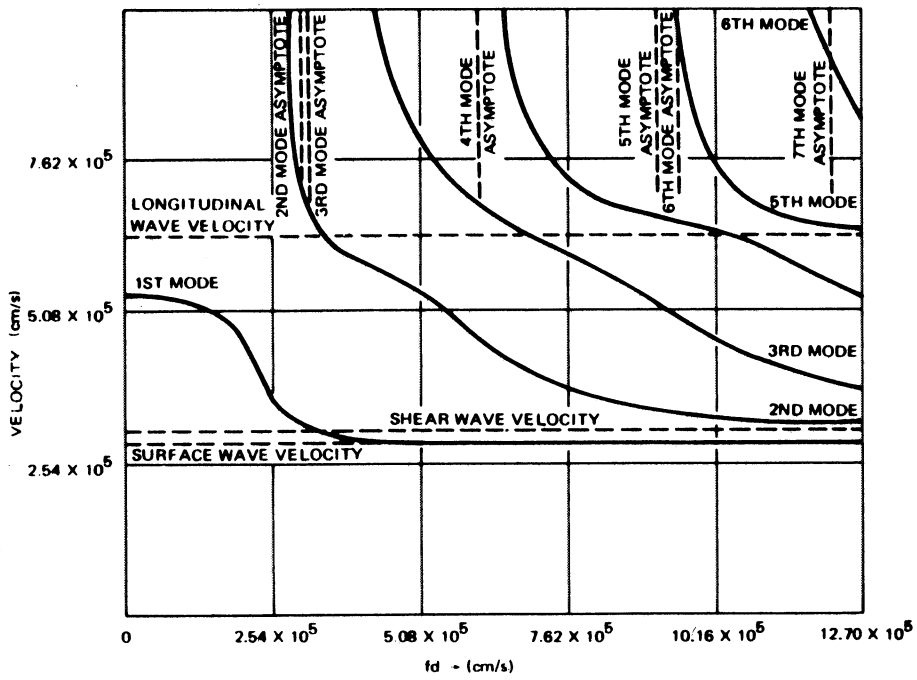

SYMMETRICAL WAVES

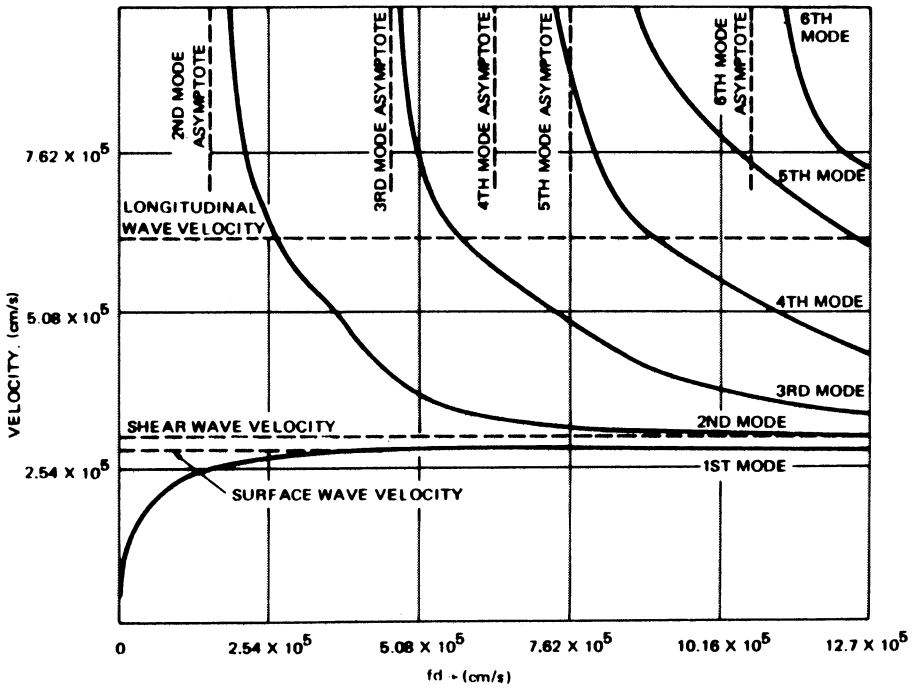

ASYMMETRICAL WAVES

Figure 3-3. Lamb-Wave Phase Velocity in an Aluminum Plate

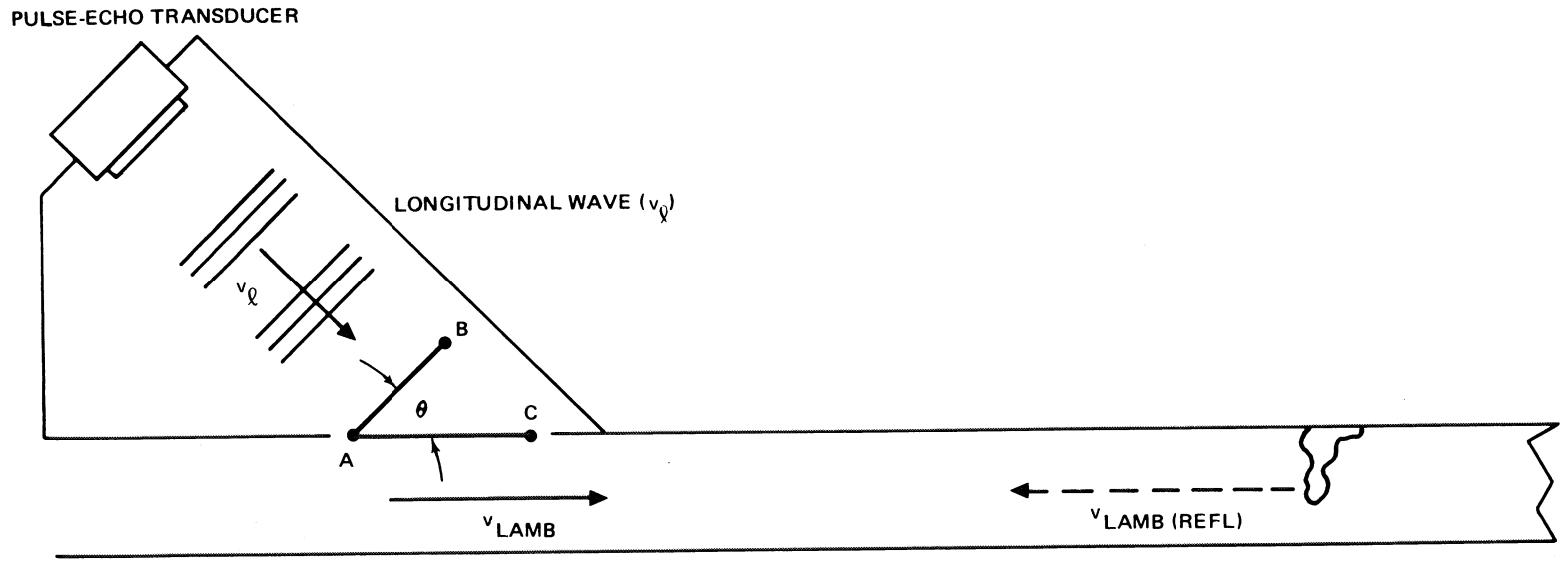

$$v_{LAMB} = v_\ell / \sin \theta$$

Figure 3-4. Pulse-Echo Experimental Arrangement for Generating and Detecting Lamb Waves in Plates

or velocity of the pulse, can differ markedly from the phase velocity. The group velocities of the first six symmetric and asymmetric Lamb-wave modes in aluminum are shown in Figure 3-5 (Reference 6). It is the group velocity which is involved in making triangulation calculations to locate flaws remotely by using Lamb waves.

Lamb waves can be detected by using a second transducer oriented with respect to the surface with an equal but opposite angle to that used to generate the waves. Reflection of the waves from flaws or discontinuities in the plate can also be detected by using only the transmitter transducer in the pulse-echo configuration as shown in Figure 3-5. In the present experimental program, both transducer configurations have been used to study remote flaw detection in aluminum.

3.3 LAMB-WAVE MODE SELECTION MEASUREMENTS

For the initial flaw detection studies, 1.60-mm-thick aluminum alloy sheet (type 2219-T37) was selected. This type sheet and thickness is representative of the pressure wall of the modular space station (Figure 3-6) recently studied at MDAC.

3.3.1 Test Setup

The setup used in these experiments is shown schematically in Figure 3-7. Fixed angle transducer wedges were used in conjunction with broad band piezoelectric transducer elements with center frequencies at 2.25, 5.0, and 10.0 MHz. A pulsed oscillator and receiver system was used to drive the transducers and to amplify and rectify the received signal. This system has the capability to adjust the transducer input pulse width, frequency, amplitude, and repetition rate. The complete system provided the flexibility needed in generating ultrasonic Lamb waves and in selecting the optimum working parameters for a given material and thickness.

3.3.2 Generation of Lamb-Wave Modes and Initial Mode Selection

The Lamb-wave modes that were expected to be generated in the 1.60-mm-thick aluminum test panel were determined from the Lamb-wave velocity curves in aluminum. The existences of the wave modes were experimentally verified and their relative signal strengths recorded.

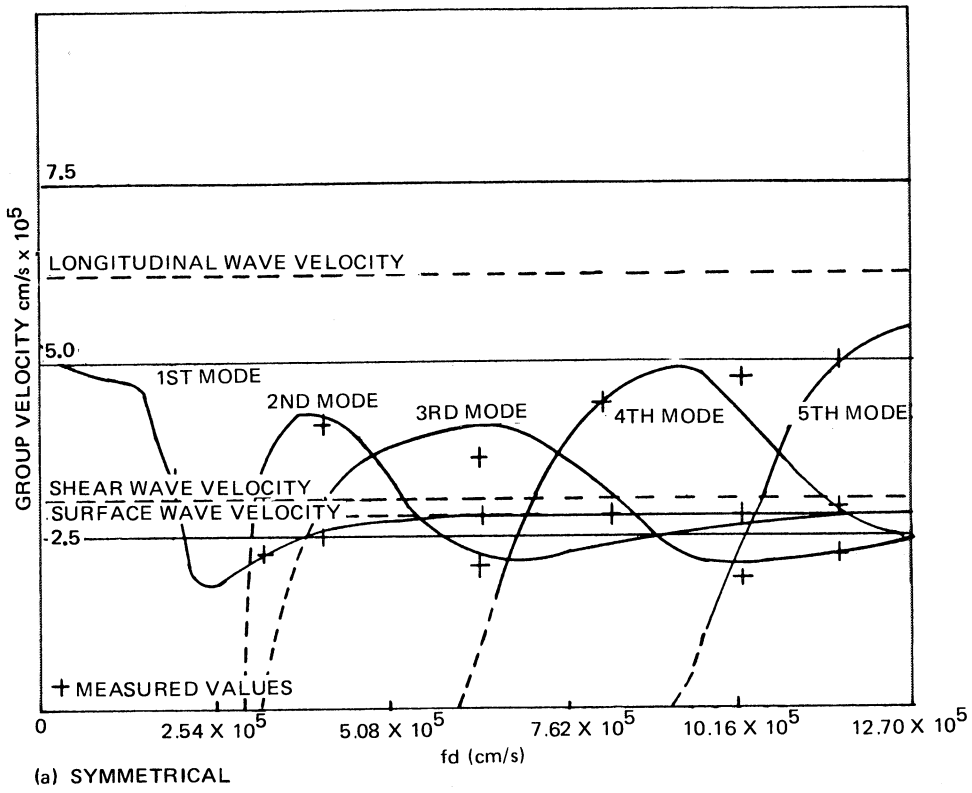

(a) SYMMETRICAL

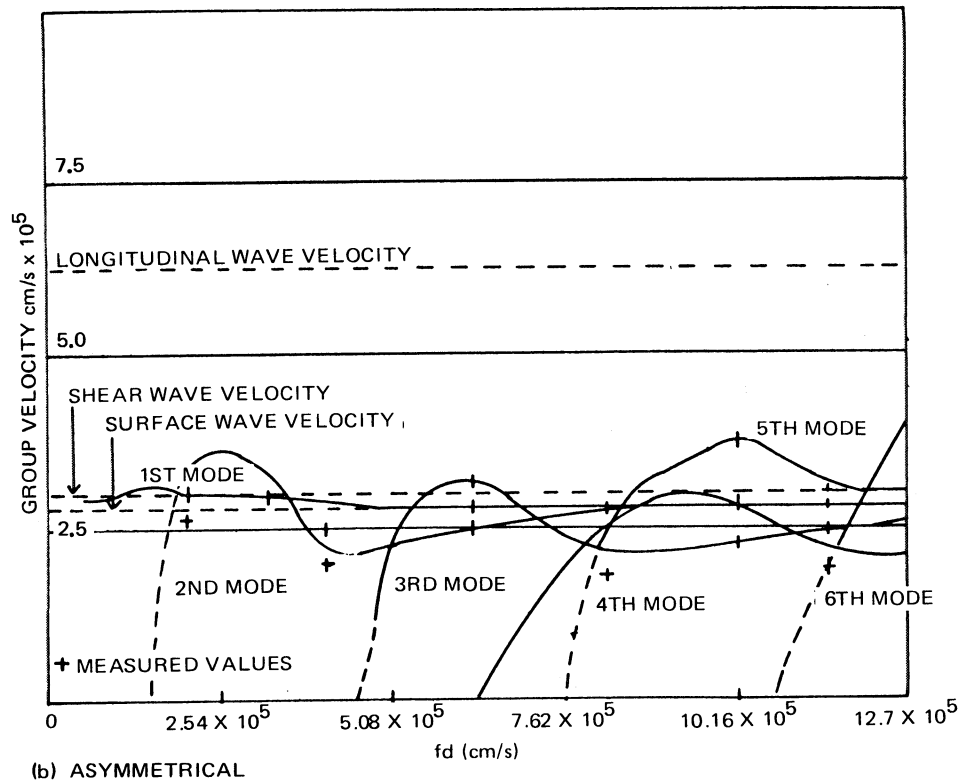

(b) ASYMMETRICAL

Figure 3-5. Lamb-Wave Group Velocity in an Aluminum Plate

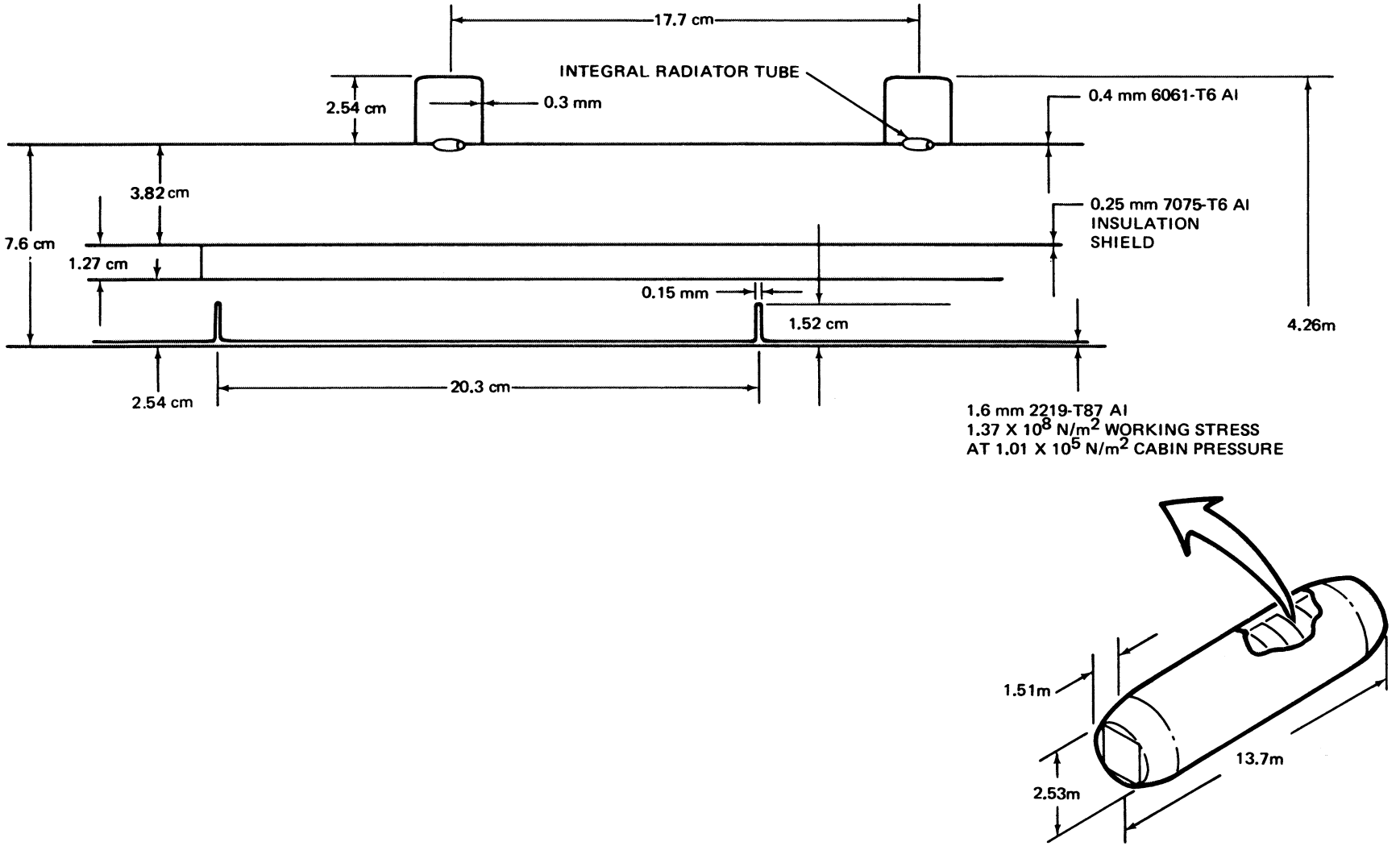

Figure 3-6. Space Station Module Candidate Structural Concept

In making predictions from the velocity curves, a frequency range of about 1.2 to 12 MHz was considered. In this range, by using fixed wedge-angle transducers, a total of 18 different Lamb-wave modes potentially can be generated within the test plate. Experimentally, 13 modes were generated. The waves were studied by using a single transducer operating in the pulse-echo mode. Reflected signals from the edge of a 2219-T37 test plate were observed with an oscilloscope. The path length which the wave traversed before being detected was approximately 96.5 cm.

The results indicate that an optimal frequency range for wave generation in 1.60-mm-thick aluminum is about 2.0 to 5.0 MHz using 20- to 40-deg transducer wedge angles. At higher frequencies, the aluminum begins to strongly attenuate the waves. At frequencies lower than about 2.0 MHz and with a 10-deg transducer wedge angle, many low-amplitude modes were generated in addition to the primary mode being investigated, giving rise to an undesirable amount of interference with the primary mode.

3.3.3 Flaw Detection Using Lamb Waves

The test specimen used in the flaw detection measurements was a 1.60-mm-thick 2219-T37 aluminum plate, 0.61 m wide x 1.22 m long (Figure 3-8). The flaws were circular holes machined into the plate using twist drills and were of the approximate sizes as shown in Table 3-1.

Table 3-1

FLAW SIZES IN TEST SPECIMEN

Diameter (mm)	Drill Number
1.02	60
0.787	68
0.635	72
0.508	76
0.406	78
0.356	80

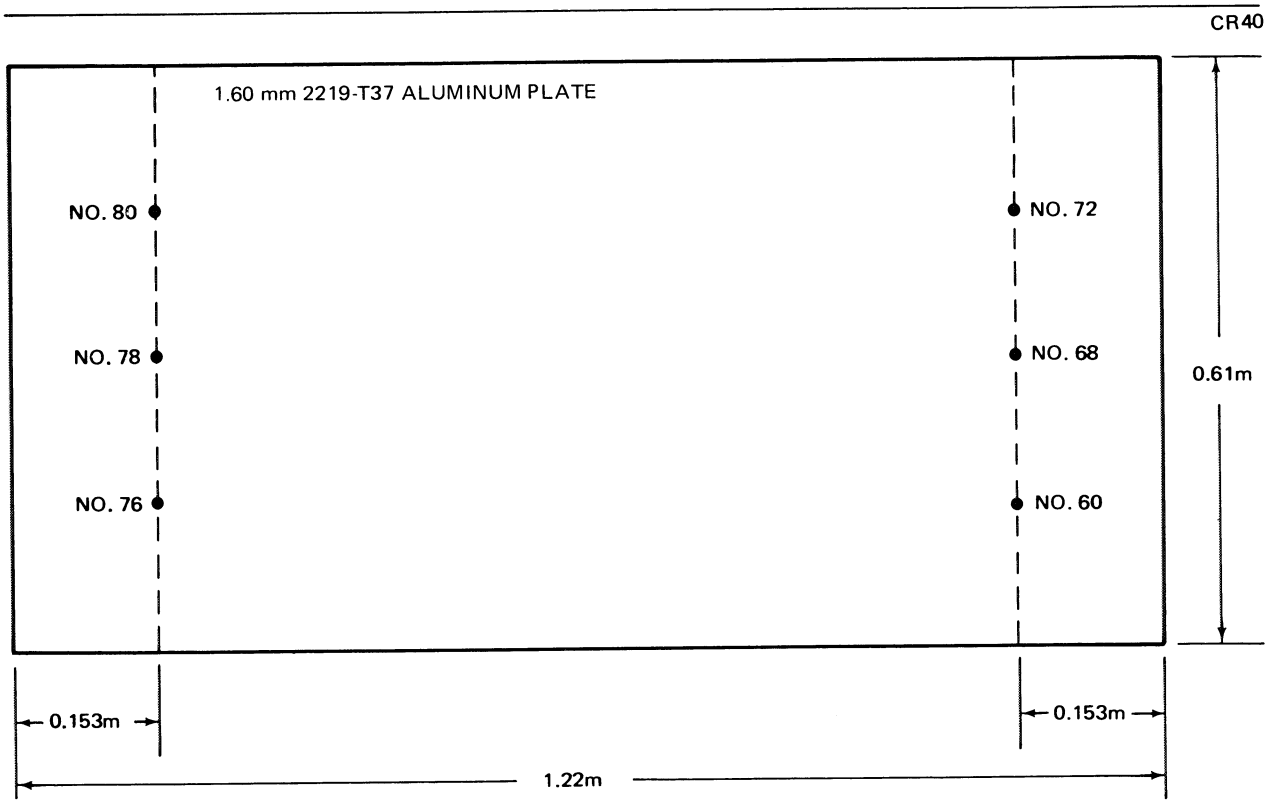

Figure 3-8. Test Setup for Lamb-Wave Flaw Detection Measurements

The Lamb-wave modes and experimental conditions (transducer wedge angle and ultrasonic frequency) were those which gave the strongest signal-to-noise ratio when reflections from the edge of the test plate were observed. The wave modes selected for the flaw detection study are listed in Table 3-2 in terms of transducer wedge angle, usual mode classification ascribed to the various wave modes by Horace Lamb (who theoretically predicted the wave motion), and frequency used to generate the waves. The numbers are labels to identify the wave modes as used in this investigation.

Lamb waves that did not give a strong reflection from the edges of the test plate would not be expected to be sensitive to small flaws and therefore were not investigated in the flaw detection work.

In taking the flaw detection measurements, echo signals were recorded with the transducer placed at 15, 30, and 60 cm from the flaw for each flaw studied. In the initial detection measurements, all the holes in the plate were investigated by using the S_1 Lamb-wave mode generated with a 50-deg transducer

Table 3-2

SELECTED WAVE MODES

Mode Identification Number	Transducer Wedge Angle (deg)	Lamb-Wave Mode Number	Ultrasonic Frequency (MHz)
1	50	S_1	2.35
2	40	S_1	1.57
3	40	A_2	3.50
4	40	S_2	5.37
5	30	S_1	1.27
6	30	A_2	2.51
7	30	S_2	3.83
8	30	A_3	5.30
9	20	A_2	1.70
10	20	S_2	2.30
11	20	A_3	3.65
12	20	A_4S_4	5.37
13	10	S_3	2.40
14	10	S_4	4.20

wedge angle and an ultrasonic frequency of 2.35 MHz. For all subsequent measurements, only the Nos. 60 and 80 drilled holes were studied. The reflections from the largest and the smallest holes were assumed to provide sufficient information for selecting the most promising wave modes and for optimizing operating conditions for flaw detection. Data were recorded by displaying the signal received by the transducer on an oscilloscope and making photographic records of the scope trace. The input signal to the transducer was adjusted so that the amplitude of the displayed echo signal on the oscilloscope was 6 V for each data point. This signal level was obtained by using a variable attenuator between the transmitter oscillator output

(operating at maximum output level) and the transducer. Also, small adjustments in the width of the pulse used to drive the transducer were made for each mode to maximize the observed signal. (The pulse width was usually about 5 to 10μs.)

In evaluating the data, two factors were considered: the signal-to-noise ratio of the received signal, and the relative amplitude of the signal. The signal-to-noise ratio is important, as it indicates how well the signal is distinguishable from the noise background and consequently determines the detectability of the signal. The observed noise was partially generated in the preamplifiers of the detector circuits, and was also in part derived from the transducer and the test specimen, i.e., internal reflections inside the transducer, grain boundary noise, and generation of additional weak wave modes in addition to the primary wave being studied. The amplitude of the signal gives an indication of how strongly the waves are reflected from the flaw, and consequently, their suitability for remote flaw detection. The amplitude of the signal and also that of the ultrasonic noise contribution depend on the reflectivity of the flaw and the attenuation of the test material, as well as the quality of the coupling of the transducer to the test specimen. In these flaw detection measurements, a liquid couplant was used. A liquid couplant makes positioning the transducer easy; however, the efficiency of the liquid coupling can vary from measurement to measurement due to variations in the thickness of the couplant layer or the presence of small bubbles in the couplant. It is difficult to consistently maintain uniform coupling with a liquid couplant. Some of the variations between signals received using the same wave mode but with different flaw sizes or flaw-transducer spacings can be attributed to this coupling problem. In these measurements, the coupling was good enough that the variations in the amplitude and the quality of the received signals for different wave modes were small and were primarily due to the differences in the interaction of the various modes with the test specimen.

In analyzing the data, an attempt was made to graphically indicate the relative ability of the various wave modes to detect the flaws by considering both the relative amplitude of the ultrasonic signal and the signal-to-noise

ratio of the signal. The relative amplitude of the signal was determined from the amount of attenuation (in dB) required to give a signal of approximately 6-V amplitude on the oscilloscope trace. The amount of attenuation in dB was taken as the relative amplitude of the ultrasonic signals. The signal-to-noise ratio for each signal was determined from the photographed scope traces and was then normalized to a signal-to-noise ratio of 10, by dividing the signal-to-noise ratio by 10. The normal signal-to-noise ratio of 10 was arbitrarily chosen and represents a signal condition that would be adequate for flaw detection. The relative signal amplitude was multiplied by the normalized signal-to-noise ratio to give an adjusted signal amplitude that will be taken to be representative of the utility of the particular wave mode for use in flaw detection.

All the wave modes listed in Table 3-2 were investigated for their flaw detection capability. Figure 3-9 shows an example of the detected ultrasonic signals for the No. 7 mode using a 30-deg wedge angle at 3.83 MHz with the relevant experimental parameters. Figure 3-10 shows graphically the adjusted amplitudes derived from the data. The general results are shown in Table 3-3, where the various modes are listed in order of their capability to find the flaws at a 60-cm-flaw-transducer separation based on the average adjusted amplitude of the signals from the Nos. 60 and 80 drilled holes. The Nos. 11, 12, 9, and 6 modes showed the best characteristics. The No. 2 mode (40-deg wedge, 1.57 MHz) was unable to find any of the flaws.

3.3.4. Remote Flaw Detection

The ability of selected Lamb-wave modes to remotely detect a 1.02-mm-dia hole and a 0.35-mm-dia hole in 1.60-mm-thick aluminum plate was investigated employing the following wave modes as shown in Table 3-4.

The A_4 and S_4 modes occur together in the 1.60-mm-thick sheet at 5.37 MHz using a 20-deg wedge angle to generate the waves. The A_3 mode and the A_4S_4 "double mode" showed good sensitivity to the 0.35- and 1.02-mm-dia holes at distances up to 1.00 m. An additional 1.60-mm-thick specimen was subsequently obtained with 0.356-mm, 0.635-mm, and 1.02-mm holes which enabled larger flaw-transducer separation to be investigated. This specimen is seen in Figure 3-11.

ULTRASONIC SIGNALS RECEIVED FROM NO. 60 HOLE. THE CENTRAL PEAK IS THE ECHO FROM THE FLAW, THE FIRST LARGE PEAK IS PICKUP FROM THE TRANSMITTER PULSE, THE SECOND OFF-SCALE PEAK IS THE REFLECTION FROM THE EDGE OF THE TEST PLATE'

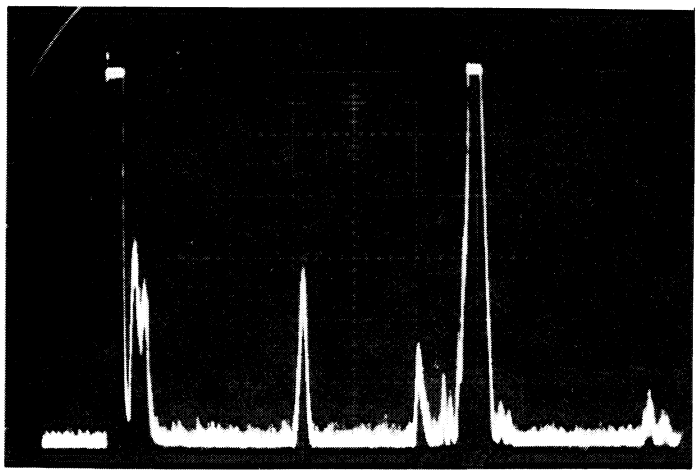

(a)
DISTANCE FROM HOLE: 15 cm
ATTENUATION: 40 dB
SIGNAL/NOISE: 8.7
ADJUSTED AMPLITUDE: 34.8

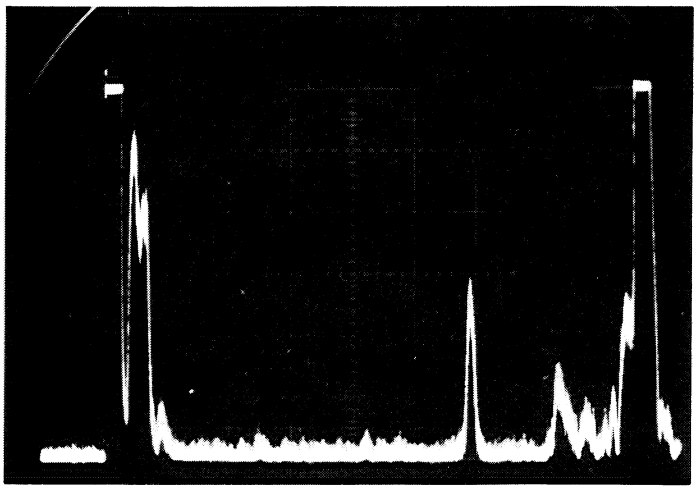

(b)
DISTANCE FROM HOLE: 38 cm
ATTENUATION: 35 dB
SIGNAL/NOISE: 9.0
ADJUSTED AMPLITUDE: 31.5

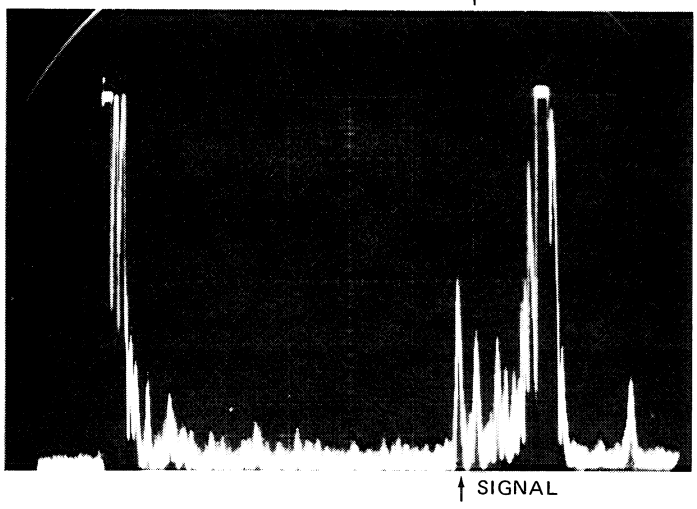

(c)
DISTANCE FROM HOLE: 76 cm
ATTENUATION: 29 dB
SIGNAL/NOISE: 7.0
ADJUSTED AMPLITUDE: 20.3

Figure 3-9. No. 7 Lamb-Wave Mode Detection of 0.356-mm-Diameter Hole (30-Deg Wedge Angle, 3.83 MHz)

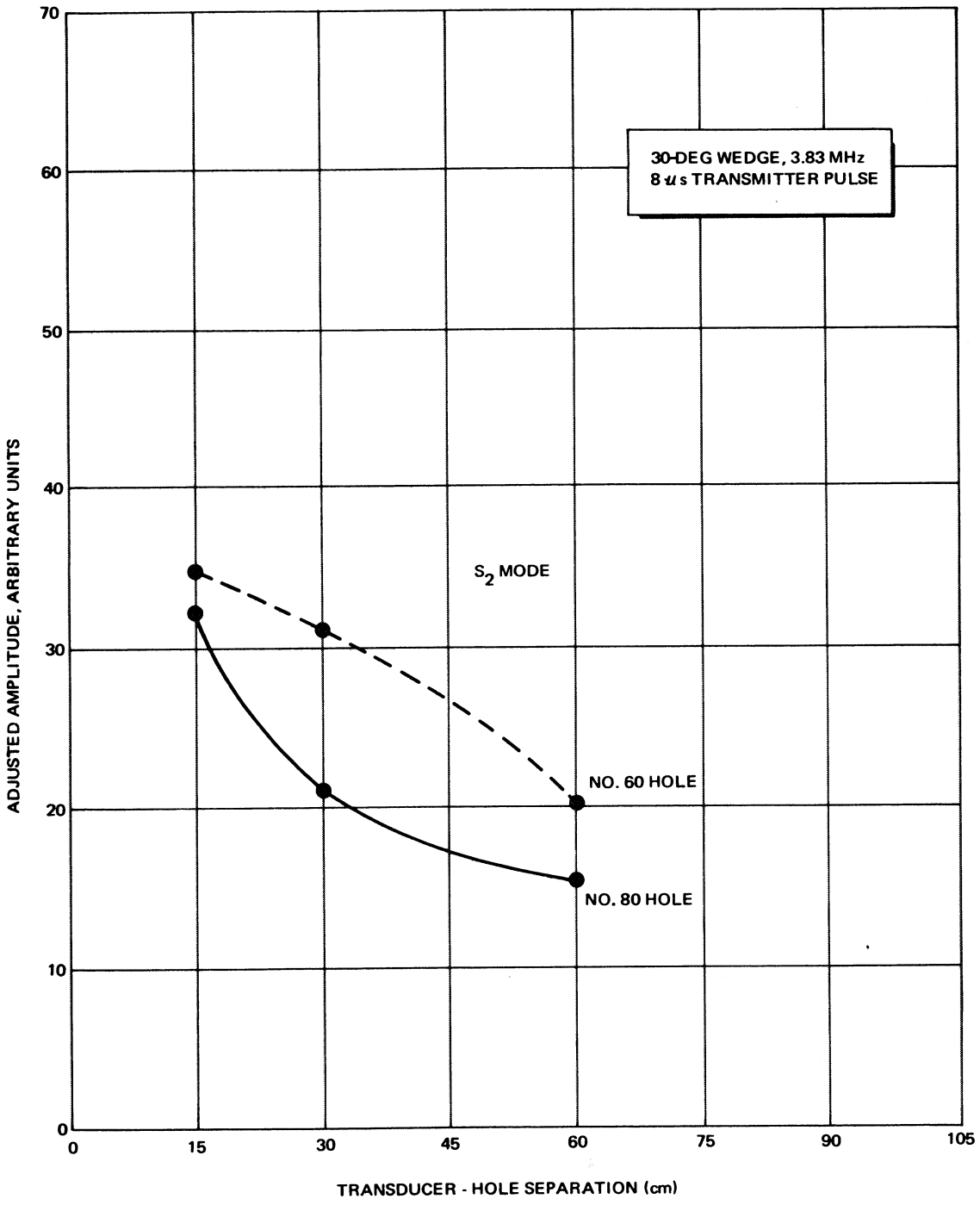

Figure 3-10. Flaw Detection by Lamb-Wave Pulse-Echo Response

Table 3-3

WAVE-MODE FLAW-DETECTION CAPABILITIES

Order of Utility	Mode Identification Number	Average Adjusted Amplitude (arbitrary units)
1	11	43
2	12	41
3	9	40
4	6	37
5	14	22
6	10	20
7	7	18
8	8	10
9	3	6.3
10	1	6.0
11	4	5.5
12	13	4.0
13	2	0
14	5	0

Table 3-4

WAVE MODES USED

Lamb Wave Mode Number	Order of Utility	Transducer Wedge Angle (deg)	Ultrasonic Frequency (MHz)
A_3	1	20	3.60
A_4, S_4	2	20	5.37
S_2	7	30	3.83

Using the A_4 S_4 "double mode" above, the 0.35-mm-dia hole could be detected at 3.05 m from the pulse-echo transducer. Figure 3-12 shows an example of the ultrasonic signal received from the hole. The hole was located approximately 38 cm from the edge of the test plate. The A_3 mode

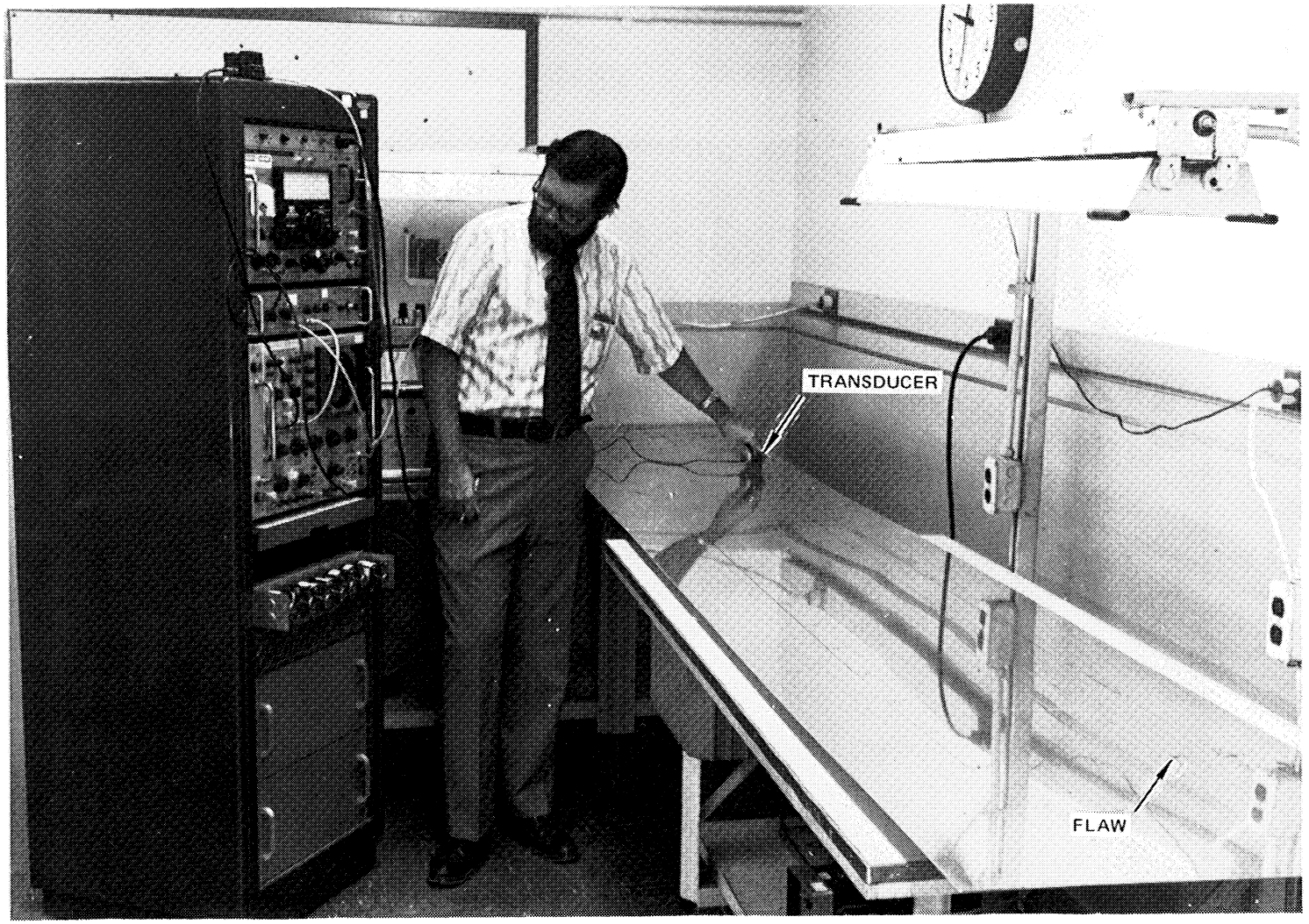

Figure 3-11. Flaw Detection with 3.05-m Flaw Transducer Separation

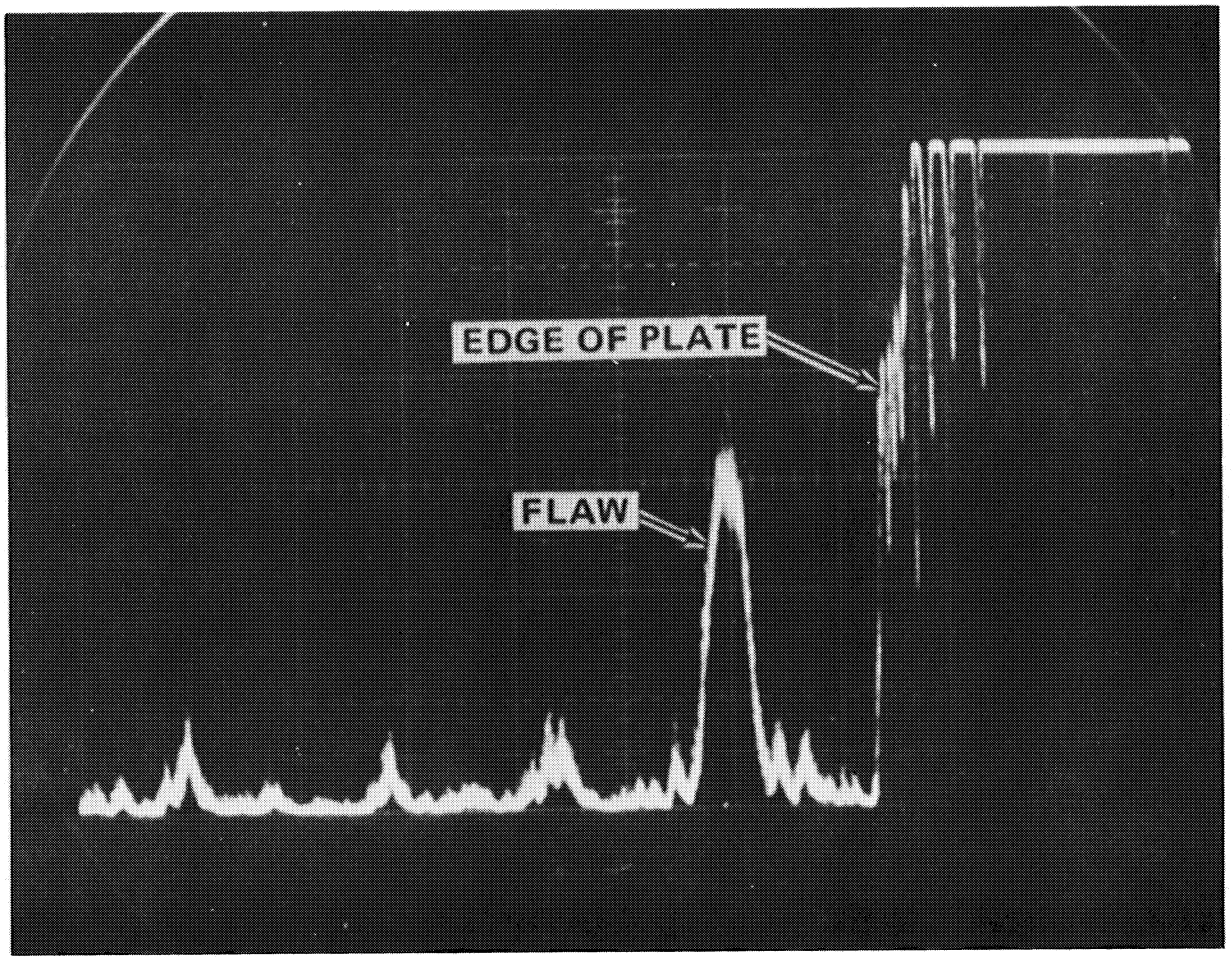

Figure 3-12. Active Ultrasonic-Flaw Detection for Modular Space Station (Transducer-Flaw Separation = 3.05 m)

gave a slightly cleaner signal (better signal to noise) but had a 2-dB weaker signal amplitude. An additional mode was tried, the S_2 mode generated at 3.83 MHz using a 30-deg wedge angle. The S_2 mode gave a signal which was of still lower amplitude and was more noisy than that received using the other two modes. No other modes were used for detecting the 0.35-mm-diam hole at a 3.05-m transducer-flaw separation.

3.4 LAMB-WAVE PROPAGATION IN INTEGRALLY REINFORCED RIBBED STRUCTURES

The propagation of Lamb waves past structural reinforcements was investigated to determine the degree of interference by the ribs on the propagation of the waves. It is necessary to understand rib effects in order to determine the ultimate feasibility of detecting flaws in this type of structure.

3.4.1 Initial Measurements

Initial tests were conducted on an integrally stiffened panel of aluminum with a 1.15-mm membrane thickness and with ribs 1.15 mm wide and 12.7 mm high. The test configuration is shown in Figure 3-13. The transducer was located so as to send the Lamb waves past two ribs to the edge of the panel, and then to receive the reflected wave from the edge of the plate, after it had again traversed the two ribs. This particular test specimen was cut from a larger panel which had been formed, so the test panel was not flat. The curvature sometimes made it difficult to obtain good coupling on the test panel. Several Lamb wave modes were tried with varying degrees of success.

Figure 3-14(a) shows the results using the A_2 Lamb wave mode (10-deg wedge angle, 1.57 MHz). Strong reflections are received from the ribs, and other smaller interference reflections are present after the reflection from the edge of the panel is received. Since the edge reflection does not exceed the rib signals and since the edge represents a very large effective cross section flaw, this mode would not be useful in flaw detection in this test panel. Figure 3-14(b) shows the received signal using the S_1 mode (40-deg wedge angle, 2.17 MHz). Here again, the first rib gives a large reflection, and a lot of interference with the edge reflection is present. This also is not a useful mode for flaw detection in the test panel. Figures 3-14(c) and 3-14(d)

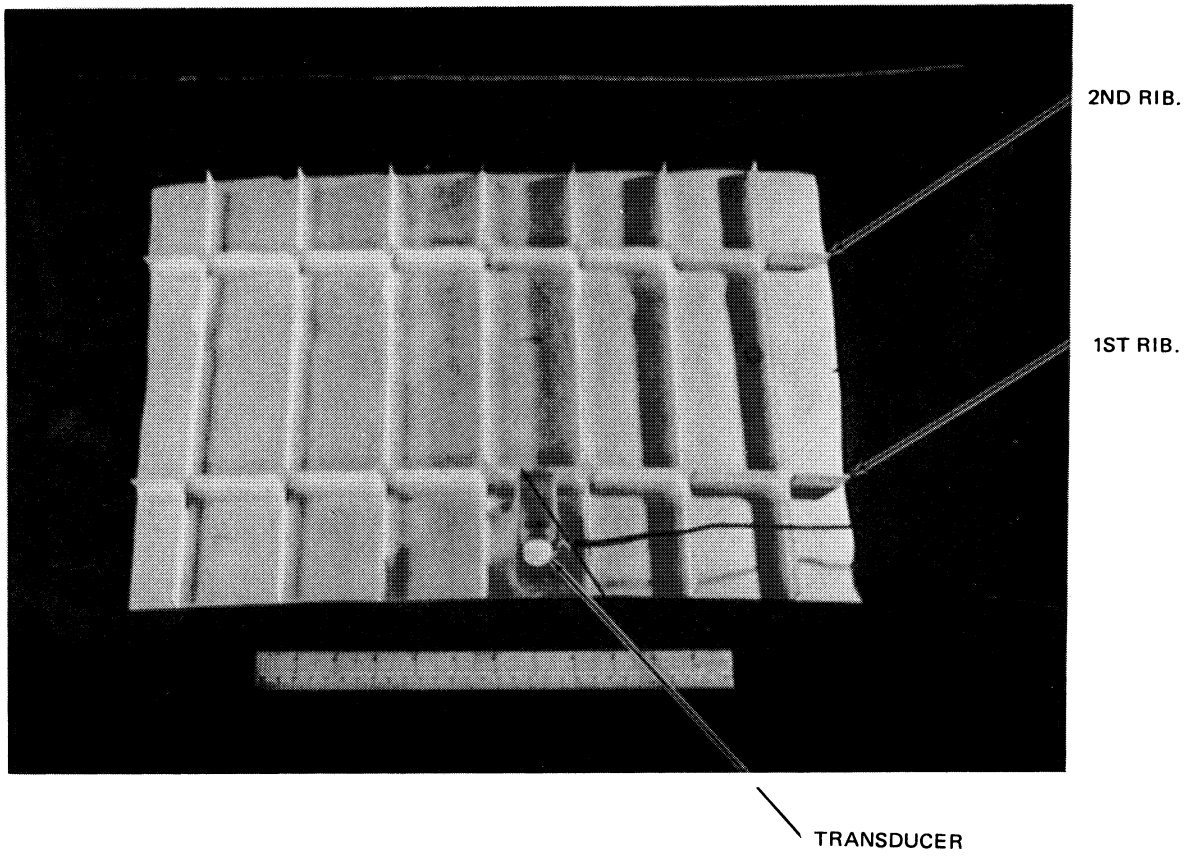

Figure 3-13. Test Setup for Lamb-Wave Propagation in Integrally Stiffened Structure Panel

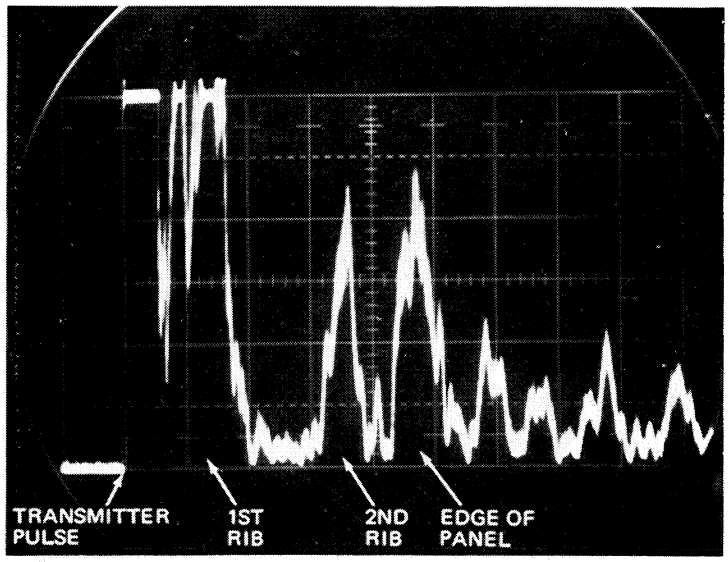

(a) A_2 LAMB WAVE MODE
10-DEG WEDGE ANGLE - 1.57 MHz

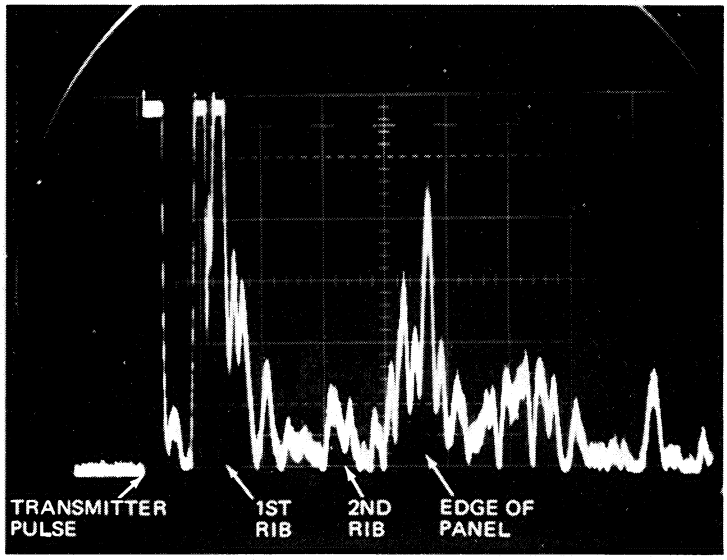

(b) S_1 LAMB WAVE MODE
40-DEG WEDGE ANGLE - 2.17 MHz

Figure 3-14. Lamb-Wave Propagation Past Integral Structural Ribs (Page 1 of 2)

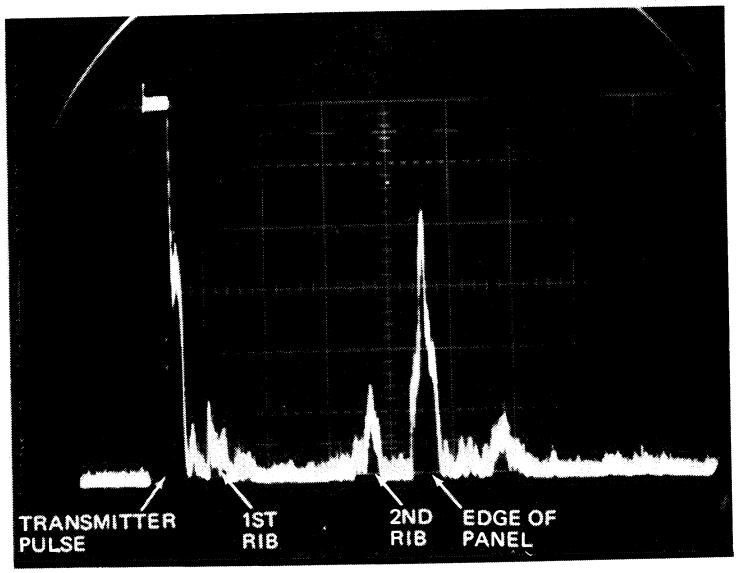

(c) S_1 LAMB WAVE MODE
50-DEG WEDGE ANGLE - 3.32 MHz

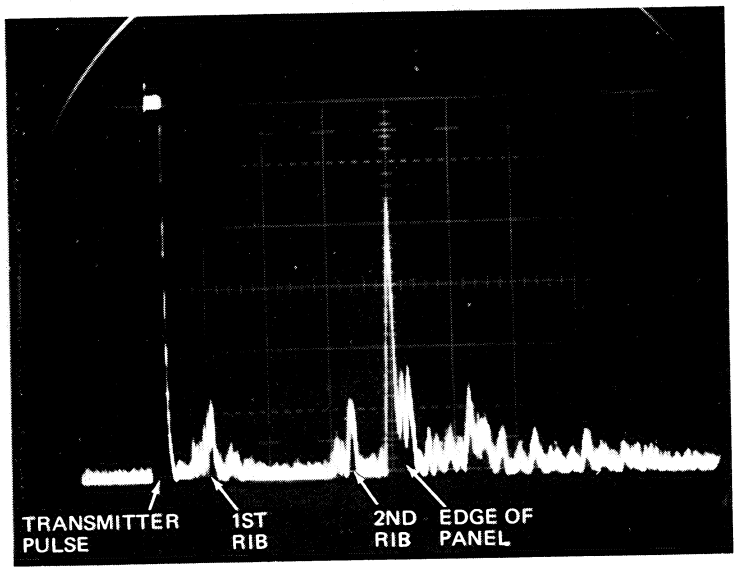

(d) A_1 LAMB WAVE MODE
60-DEG WEDGE ANGLE - 1.84 MHz

Figure 3-14. Lamb-Wave Propagation Past Integral Structural Ribs (Page 2 of 2)

show test results using the S_1 mode (50-deg wedge angle, 3.32 MHz) and A_1 mode (60-deg wedge angle, 1.84 MHz), respectively. These scope traces show strong edge reflections with weak reflections from the ribs and little interference from spurious received signals. Both these modes show promise for flaw detection in this test panel.

3.4.2 Measurements on a Single Rib Panel

To more thoroughly study transmission of Lamb waves past an integral stiffener and to establish optimal operating parameters for use with 1.60-mm-thick aluminum, a test specimen with a single integral rib was used. The panel was machined from 2.54-cm-thick aluminum alloy plate and had dimensions: 61 cm wide by 122 cm long x 0.152 cm average thickness. The central rib (see Figure 3-15) was 2.38 cm high with a rib root radius of curvature of 0.635 cm. Due to the size and nature of the panel, the thickness varied somewhat over the panels, but was within about ±0.013 cm over most of the specimen.

3.4.2.1 Measurements of Transmitted Signal Amplitude

Two sets of rib interference measurements were conducted. One set used two transducers to compare the amplitude of the signal transmitted past the rib to the amplitude of the same signal when no rib was traversed. The second was a set of pulse-echo measurements to detect the reflection from the edge of the panel, with the rib between the transducer and the edge.

In the first series of measurements, ultrasonic signals were received with the two transducers widely separated on a single ribbed panel with no intervening rib and with a rib between the transducers. The transducer positions are shown in Figure 3-15. For the direct transmission measurements, the transducers were spaced 48.3 cm apart on one side of the panel. For the rib interference measurements, the transducer separation was 88.9 cm. The difference in separations used is estimated to account for about 1 dB of the decrease in the received signal strength when the Lamb waves were sent past the rib. For some of the measurements, dissimilar wedge angle transducers were used since two each of all of the various wedge angles as used in the pulse echo measurements were not available in the NDT Laboratory. The results of the measurements are listed in Table 3-5. The dB loss column shows the decrease in the received single strength due to interference of the

T = TRANSMITTER TRANSDUCER POSITION
1 = RECEIVER TRANSDUCER POSITION – NO INTERVENING RIB
2 = RECEIVER TRANSDUCER POSITION – TO DETERMINE RIB INTERFERENCE

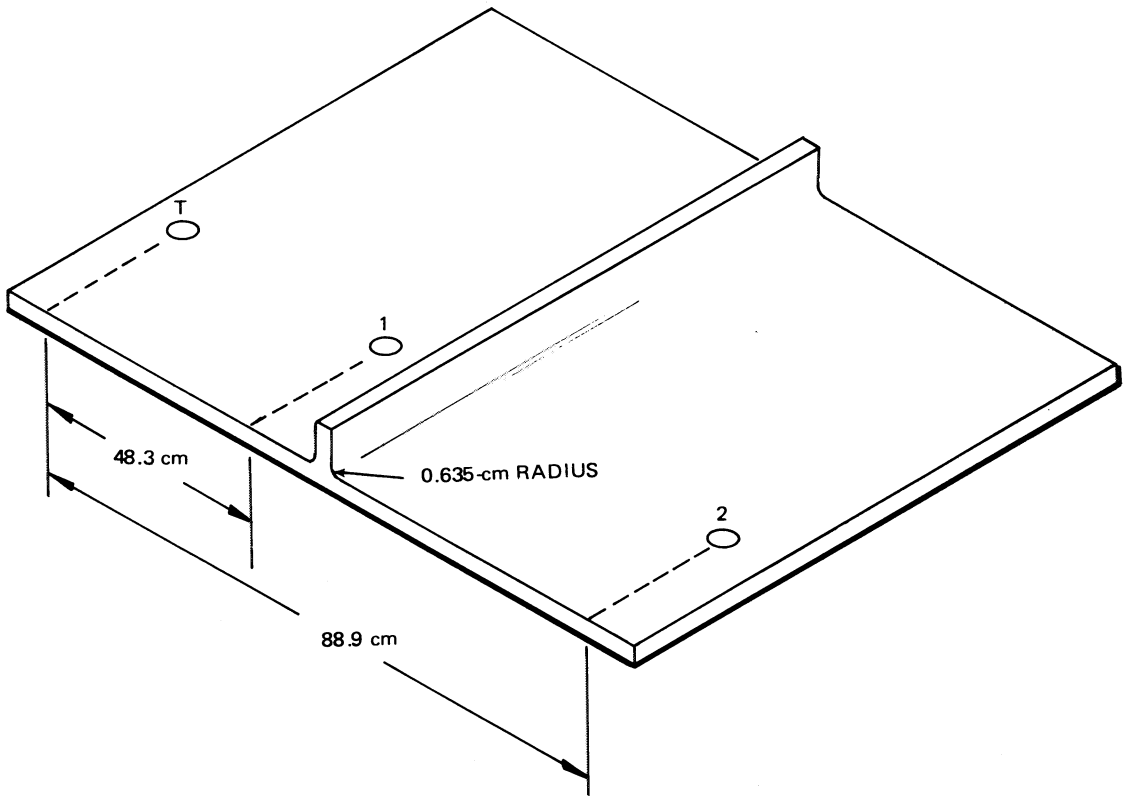

Figure 3-15. Panel with Single Integral Stiffener (Lamb-Wave Propagation Study)

Table 3-5

ATTENUATION OF LAMB WAVES PAST SINGLE INTEGRAL STIFFENED RIB

Transducer Wedge Angles (deg)		Frequency	dB Loss Past Rib	Lamb-Wave Mode
Transmitter	Receiver			
21.5	21.5	1.80	4	A_2
21.5	21.5	2.67	16	S_2
21.5	21.5	3.75	17	A_3
21.5	21.5	5.8	14	A_4
20	21.5	1.7	7	A_2
20	21.5	2.3	10	S_2
20	21.5	3.65	18	A_3
20	21.5	5.37	13	A_4, S_4
30	30	1.22	2	S_1
30	30	2.59	19	A_2
30	30	3.90	19	S_2
30	30	5.3	30	A_3
50	60	2.29	13	S_1

rib with 1 dB due to increased attenuation by the aluminum because of the wider separation of the transducer for the rib measurements. It can be seen from Table 3-5 that several modes suffered a small loss in amplitude when traversing the rib.

The frequencies in Table 3-5 differ in some cases from those listed for similar modes and wedge angles in Table 3-2 due to the difference in thickness of the machined panel. Also, a new wedge angle of 21.5 deg was included in these measurements. For the wedge material used, this wedge angle

enables generation of a Lamb-wave phase velocity equal to the longitudinal velocity in aluminum. Any symmetric or asymmetric mode which has this velocity will not vibrate the plate surface along its normal direction (Reference 7). This operating condition appeared favorable in a series of tests on a thicker integrally stiffened aluminum panel (MDAC-IRAD program) and so it was also incorporated into the current studies.

3.4.2.2 Pulse-Echo Edge Reflection Measurements

The second set of rib interference measurements were performed with the pulse-echo transducer placed 111.8 cm from the edge of the panel. The same operating conditions (modes, wedge angles, and frequencies) were used for these measurements as were used in the above-mentioned transmission measurements. It was observed that the pulse-echo signals generally contained a lot of interference which was attributable to mode conversion at the rib due to the large rib root radius of curvature giving rise to many additional Lamb-wave modes being generated in the panel.

3.5 MEASUREMENTS ON RIBBED PANEL WITH REDUCED RIB ROOT RADIUS

To assess the possibility of excessive interference due to the large rib root radius, a second single-rib panel was procured, identical to the original panel but with a rib root radius of curvature of 0.079 cm. On this panel, a series of transmit-receive transmission and pulse-echo edge reflection measurements were performed using the same modes as used previously (Table 3-5). The operating frequency and transmitter pulse duration were optimized while observing the transmitted signal. The receiver transducer with its couplant was then removed and the edge reflection was observed using the transmitter transducer in the pulse-echo mode. For the transmission measurements, the transmitter and receiver transducers were placed 42 cm on either side of the rib as shown in Figure 3-16. The total distance between transducers was 84 cm. For the pulse-echo measurements, the distance from the transducer to the edge of the panel was 102.9 cm. For each measurement, the output pulse from the pulsed oscillator was set at 150 V (0-peak) since it was found that the output pulse amplitude changed slightly with frequency and with the amount of attenuation for levels below about 20 dB. For each mode, the velocities of the transmission signal and the pulse echo signal were measured. In some instances the velocity of the pulse-echo

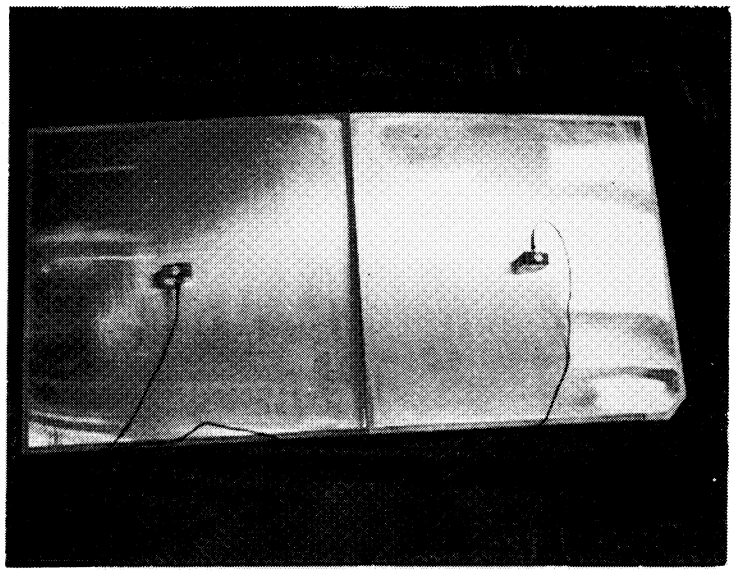

Figure 3-16. Single Rib Test Panel for Rib Transmission Measurements

signal did not correlate with that of the transmission signal so that these modes do not appear useful for a remote leak location system which incorporates pulse-echo operation. In calculating the velocities, the following measured delay time were used to correct for the time that the signal spent traversing the transducer elements and wedges. The delays were measured for the various transducer combinations by butting two transducers together on an aluminum plate and measuring the transit time of a short pulse. The delays used are listed in Table 3-6.

Based on these measurements, six modes were selected as potentially useful for detecting a hole in the ribbed panel. The modes are listed in Table 3-7.

Figures 3-17, 3-18, 3-19, show representative examples of these results for both transmission and pulse-echo measurements for the A_3, S_3, and A_4 modes respectively. In the A_2 mode, pulse-echo measurement (Figure 3-20) the reflected signal from the edge of the panel is lost in the hash and a

Table 3-6

MEASURED DELAY TIMES

Transducer Wedges Angles (deg)		Delay Time (μs)
Transmitter	Receiver	
20	21.5	19
21.5	21.5	19
30	30	23
50	60	33

Table 3-7

MODES POTENTIALLY USEFUL FOR HOLE DETECTION

	Mode	Transmitter Wedge Angle (deg)	Frequency (MHz)	Velocity (cm/μs)	
				Transmission	Pulse-echo
1.	A3	20	3.58	0.407	0.411
2.	A_4-S_4	20	4.92	0.466	0.477
3.	A_2	21.5	1.62	0.348	0.285
4.	S_3	21.5	4.95	0.476	0.480
5.	A_4	21.5	6.37	0.490	0.489
6.	S_1	50	2.27	0.294	0.295

low-velocity component gives the predominant signal. This mode was not found useful for pulse-echo measurements on the ribbed panels, but was sensitive to flaws when used only in the transmit-receive mode on a ribbed test panel. Figures 3-21 and 3-22 show examples of echo signals where there is strong interference from the rib and probably additional strong mode conversion at the edge of the plate.

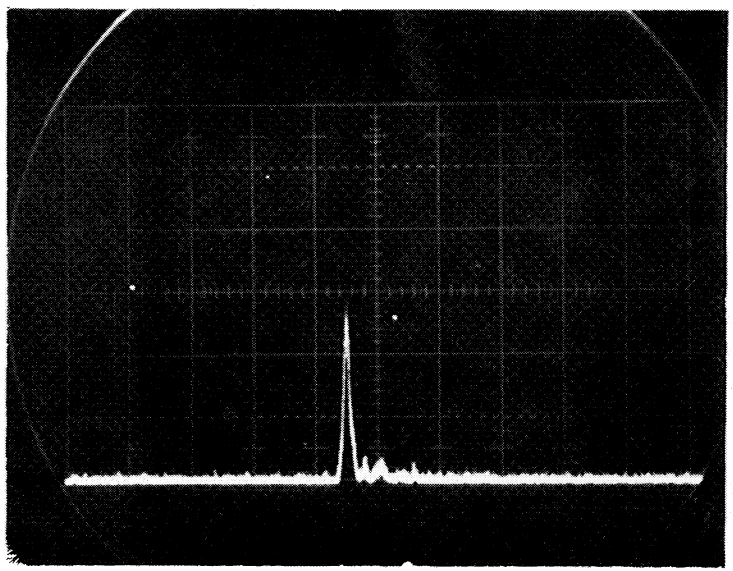

SIGNAL TRANSMITTED PAST RIB

50-μs/cm SWEEP
42-dB ATTENUATION

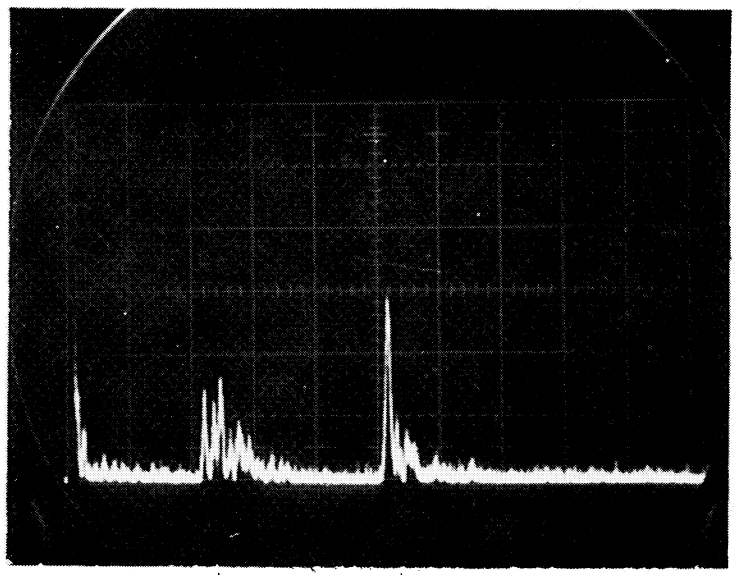

PULSE-ECHO SIGNAL FROM EDGE
OF PANEL

100-μs/cm SWEEP
37-dB ATTENUATION

Figure 3-17. A_3 Mode (20-Deg Transmitter Wedge, 3.58 MHz)

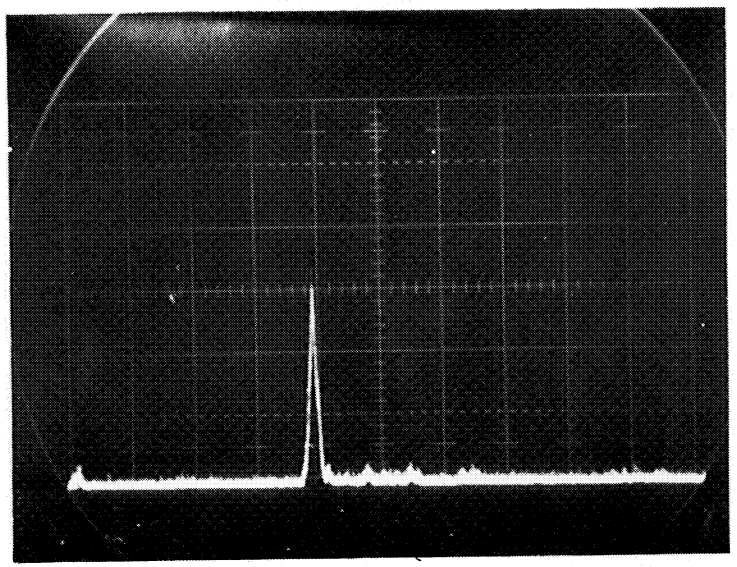

SIGNAL TRANSMITTED PAST RIB

50-μs/cm SWEEP
40-dB ATTENUATION

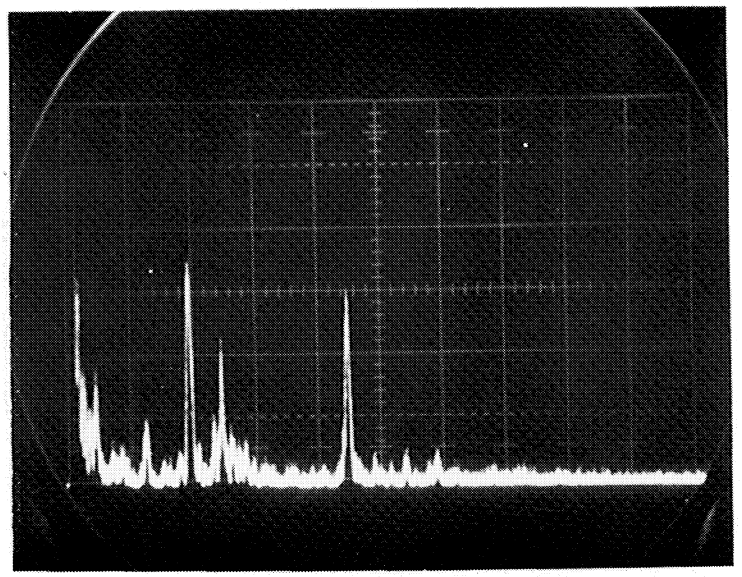

PULSE-ECHO SIGNAL FROM EDGE OF PANEL

100-μs/cm SWEEP
31-dB ATTENUATION

Figure 3-18. S_3 Mode (21.5-Deg Transmitter Wedge, 4.95 MHz)

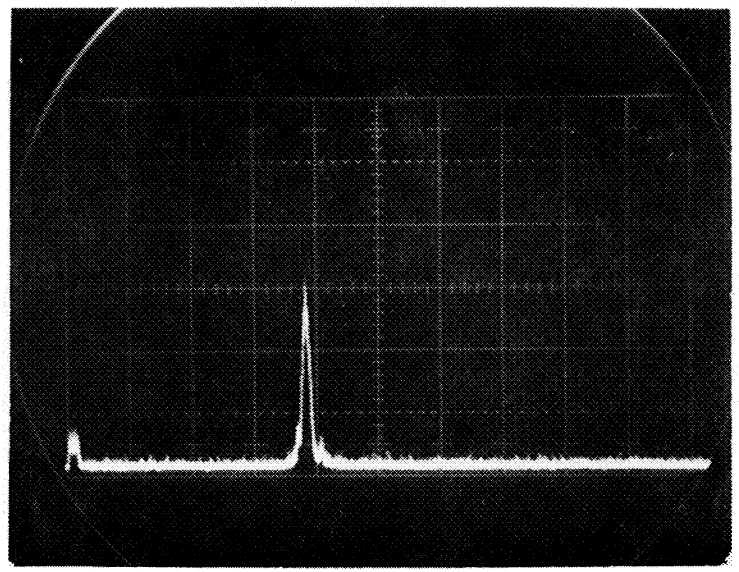

SIGNAL TRANSMITTED PAST RIB

50-μs/cm SWEEP
32-dB ATTENUATION

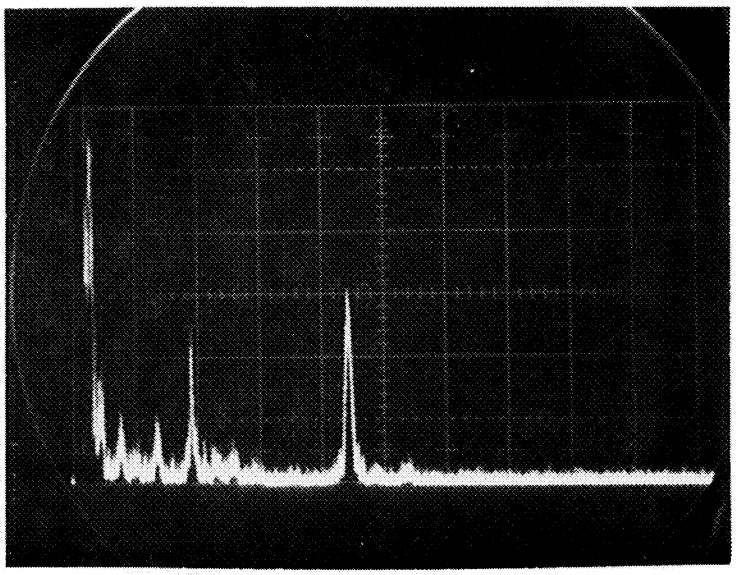

PULSE-ECHO SIGNAL FROM
EDGE OF PANEL

100-μs/cm SWEEP
16-dB ATTENUATION

Figure 3-19. A_4 Mode (21.5-Deg Transmitter Wedge, 6.37 MHz)

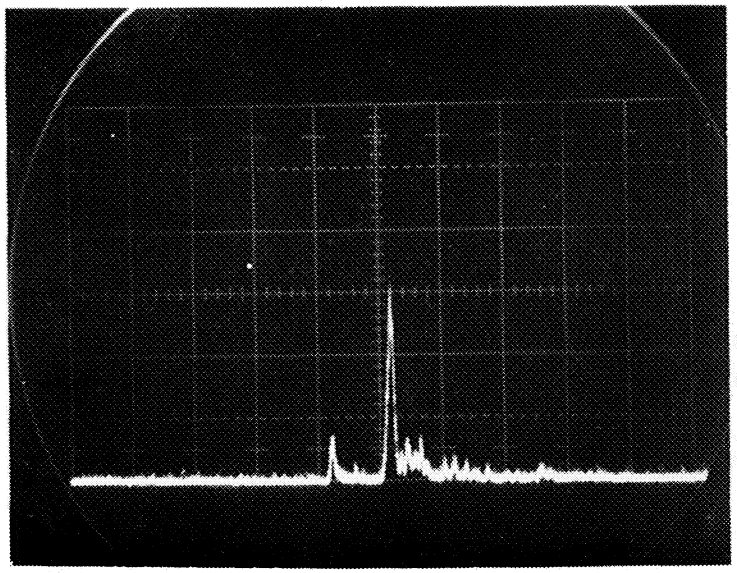

SIGNAL TRANSMITTED PAST RIB

50-μs/cm SWEEP
28-dB ATTENUATION

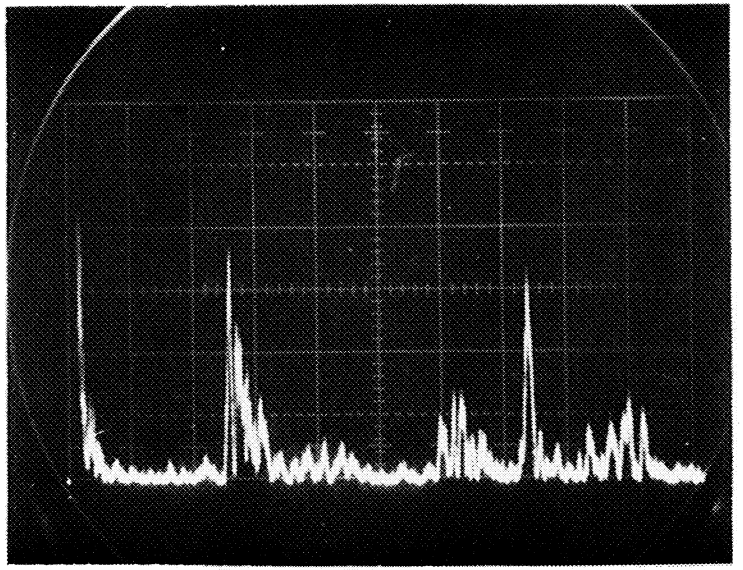

PULSE-ECHO SIGNAL FROM
EDGE OF PANEL

100-μs/cm SWEEP
17-dB ATTENUATION

Figure 3-20. A_2 Mode (21.5-Deg Transmitter Wedge, 1.62 MHz)

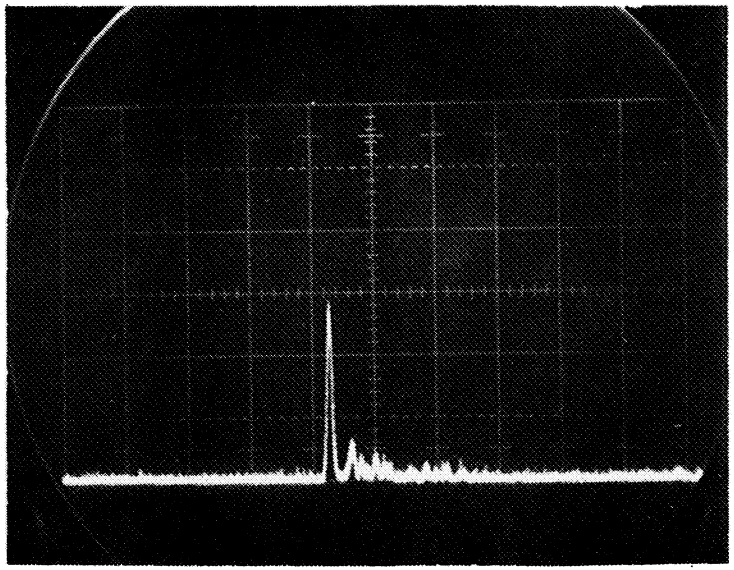

SIGNAL TRANSMITTED
PAST RIB

50-μs/cm SWEEP
42-dB ATTENUATION

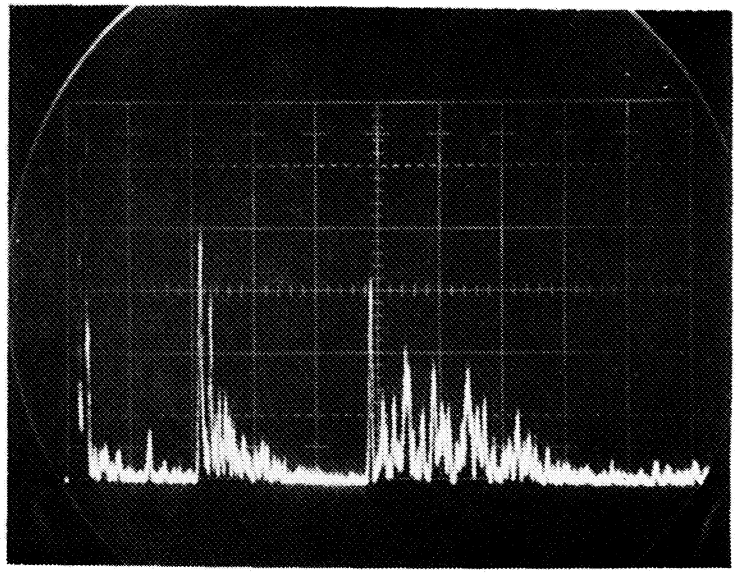

PULSE-ECHO SIGNAL

100-μ s/cm SWEEP
14-dB ATTENUATION

Figure 3-21. S_2 Mode (20-Deg Transmitter Wedge, 2.33 MHz)

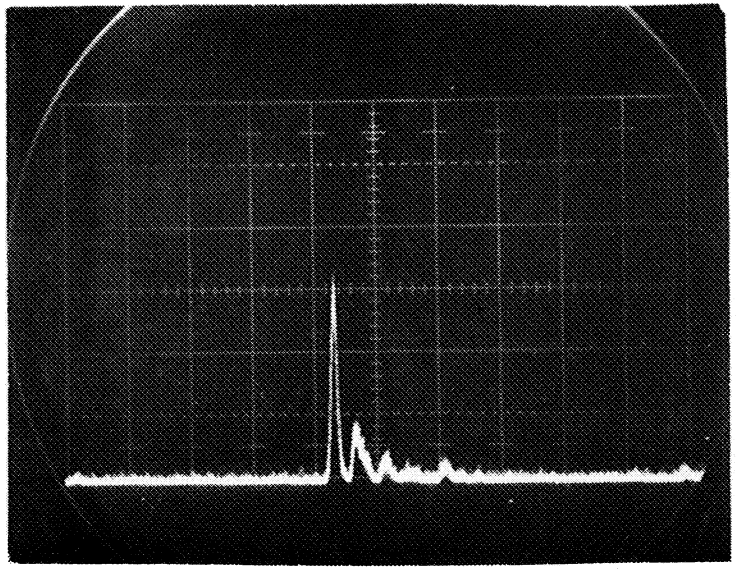

SIGNAL TRANSMITTED PAST RIB

50-μs/cm SWEEP
45-dB ATTENUATION

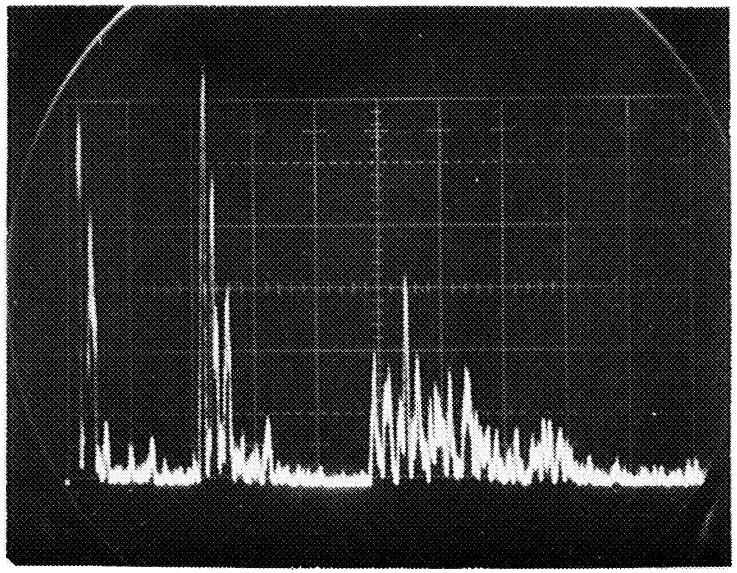

100-μs/cm SWEEP
19-dB ATTENUATION

Figure 3-22. S_2 Mode (21.5-Deg Transmitter Wedge, 2.42 MHz)

The pulse-echo measurements on the 0.079-cm rib root radius panel tended to give cleaner signals than those recorded on the panel with a 0.635-cm rib root radius. Figure 3-23 compares the pulse-echo signals received on the 0.079- and the 0.635-cm radius panels respectively for the S_3 mode using a 21.5-deg wedge angle. Figure 3-24 compares the pulse-echo signals for the A_3 mode using the 20-deg wedge angle.

3.6 INVESTIGATION OF DETECTABILITY OF SEVERAL FLAW TYPES

In addition to the study of circular cross-sectional holes extending through the thickness of a 1.60-mm-thick plate of aluminum, other flaw types in 1.60-mm-thick plate were investigated to assess their detectability using Lamb waves. Additional flaw types investigated were a rectangular cross-sectional slot extending through the plate, a rectangular cross-sectional slot extending part way through the plate, and a circular cross-sectional hole extending partially through the plate. Also investigated were the detection of a small through hole blocked by small obstructions in the form of an open hole and a hole with a bolt fastened through it, the detection of circular cross-sectional through holes using a transmit-receive configuration of the transducers, and the detection of a part through notch in a 1.27-cm-thick plate of aluminum.

3.6.1 Flaw Orientation Measurements

3.6.1.1 Through-Thickness Rectangular Slot

The pulse-echo signal from a rectangular slot (0.51 mm long x 0.13 mm wide and extending through the thickness of the 1.60 mm-thick aluminum test plate) was recorded at various angular orientations between the normal to the length of the notch and the direction of the ultrasonic beam of the transducer using seven different Lamb wave modes. The separation between the transducer and the notch was 45.7 cm. The experimental set-up is shown in Figure 3-25. Measurements were taken at ten degree increments over the range of orientation angles between 100 and 350-deg (110-deg range) with the flaw oriented such that the length was along the 0-deg direction and the normal to the length of the flaw was along the 90-deg direction. In general

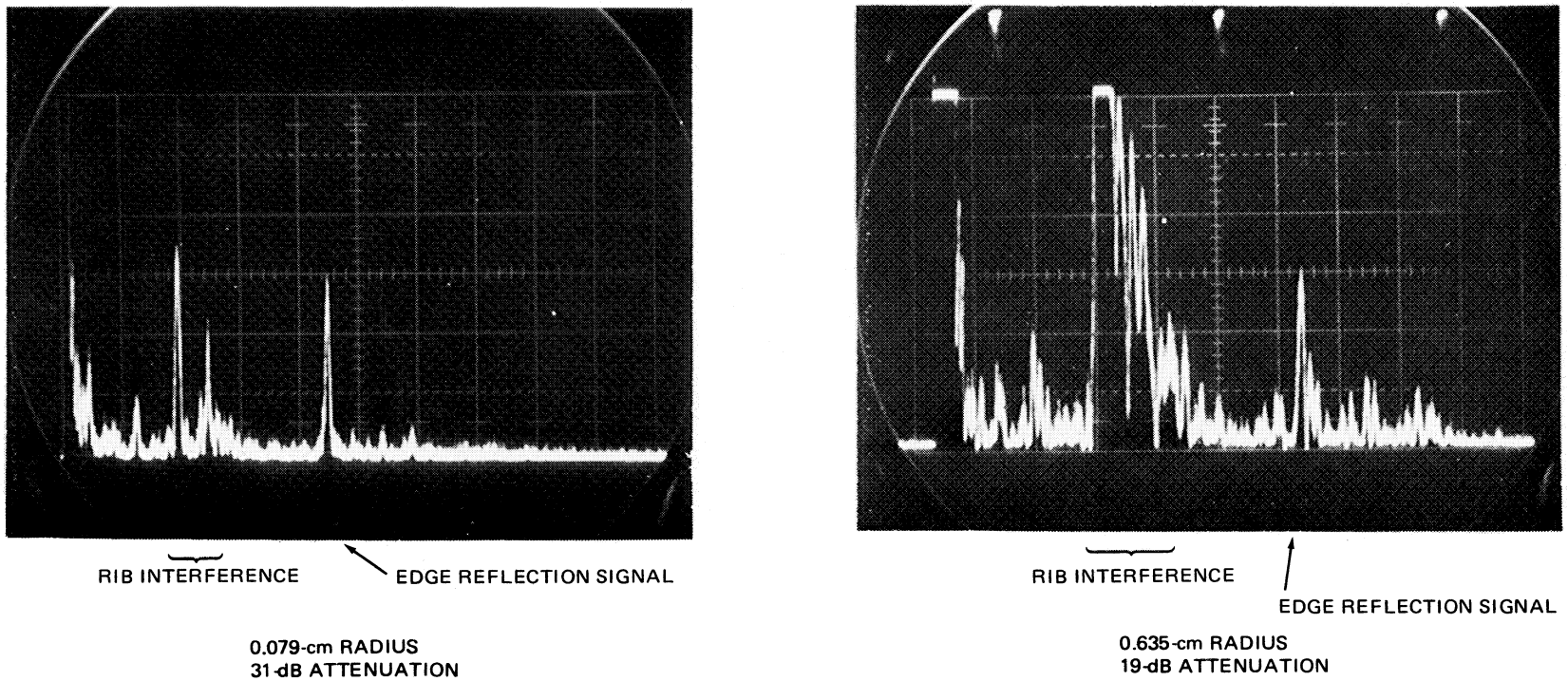

PULSE-ECHO SIGNALS ON SINGLE RIB PANEL FOR 0.079-cm AND 0.635-cm RIB ROOT RADIUS

Figure 3-23. S_3 Mode (21.5-Deg Wedge, 4.95 MHz)

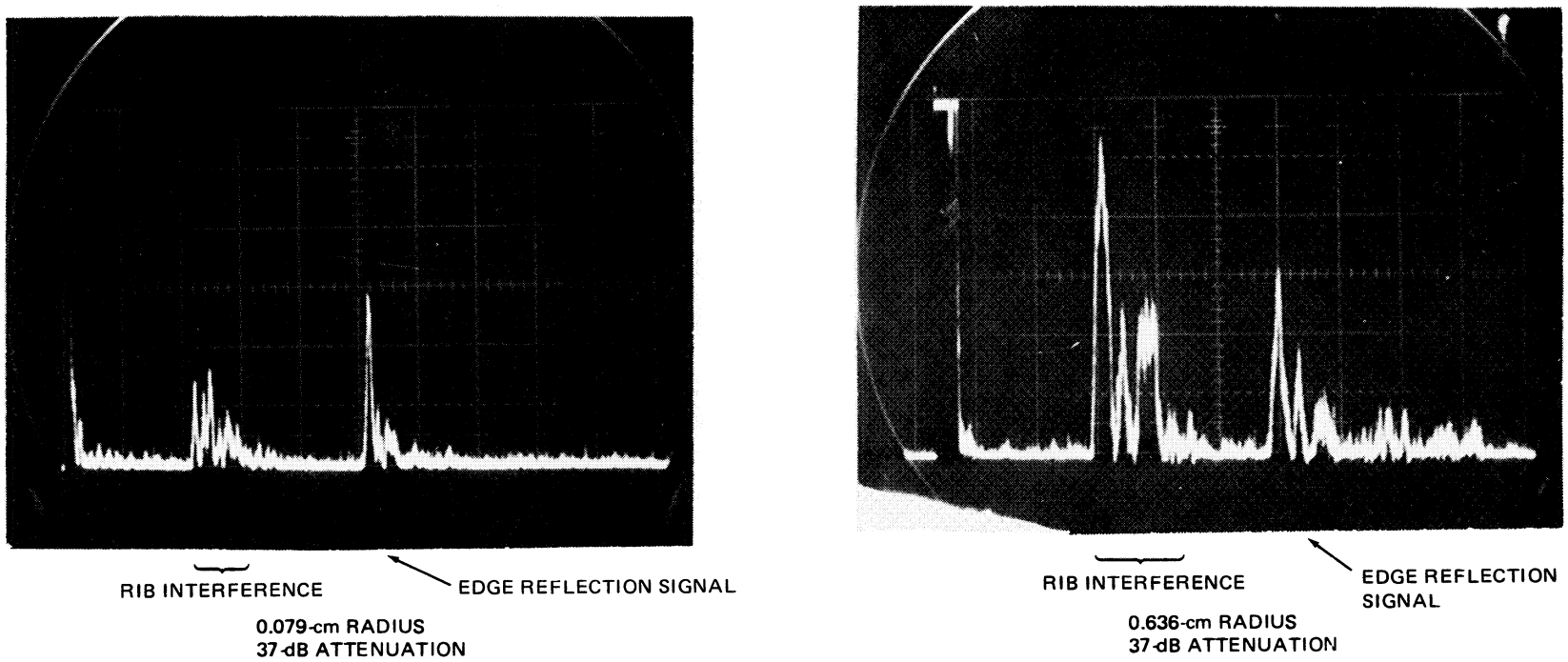

PULSE-ECHO SIGNALS ON SINGLE RIB PANEL FOR 0.079-cm AND 0.635-cm RIB FOOT RADIUS OF CURVATURE

Figure 3-24. A_3 Mode (20-Deg Wedge, 3.58 MHz)

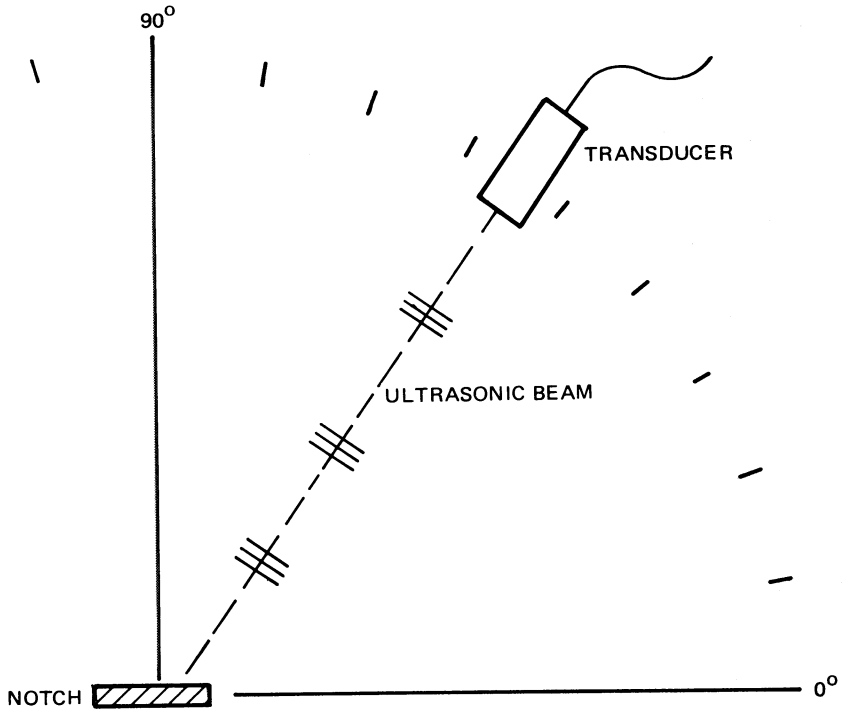

Figure 3-25. Experimental Configuration Used for Measurements of the Dependence of Pulse-Echo Signal Amplitude on Flaw Orientation

the results indicated that the higher frequency modes gave good reflected amplitudes along the 0° direction. The ability of a mode to detect a rectangular flaw end-on is a desirable property, especially if the amplitude of the reflected signal does not strongly vary with the flaw-transducer orientation. The results are shown in Figures 3-26 to 3-32 respectively, where the reflected amplitude from the rectangular flaw is plotted as a function of transducer orientation about the flaw. The amplitude in the graphs is the number of dB of attenuation of the transmitter output that was required to maintain a constant signal amplitude of 6 V displayed on an oscilloscope. For two of the modes studied, the A_4-S_4 (Figure 3-28) and the S_5 (Figure 3-29), the 0-deg direction signal was strong and the angular dependence of the reflected signal was weak. The S_2 mode (Figure 3-31) and the A_4 mode (Figure 3-32) also gave strong reflections in the 0-deg direction, but showed a large amplitude variation with orientation changes. The overall results of the experiments are summarized in Table 3-8.

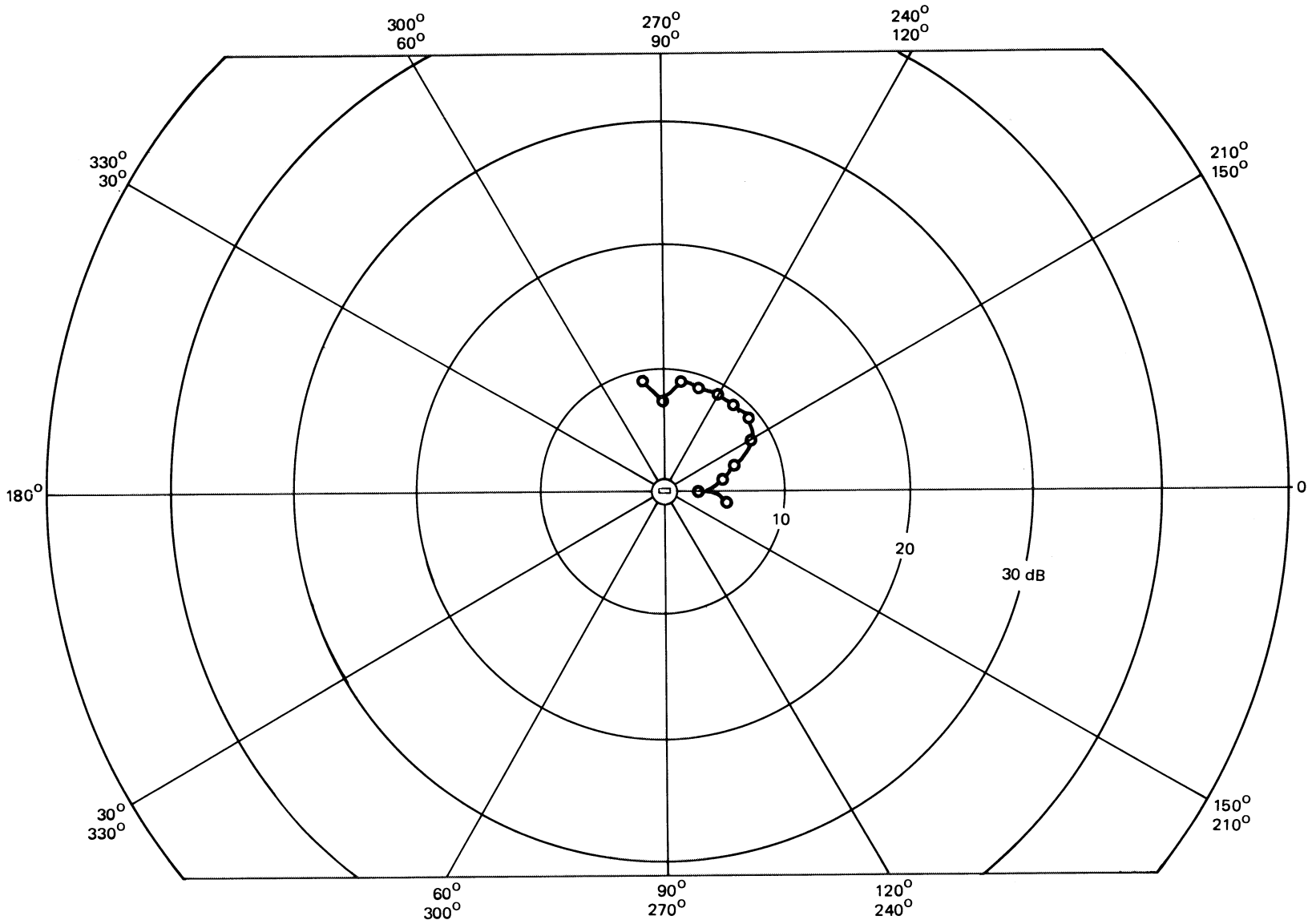

Figure 3-26. Pulse-Echo Amplitude vs Flaw Orientation (S_2 Mode; 20-Deg Wedge, 2.30 MHz)

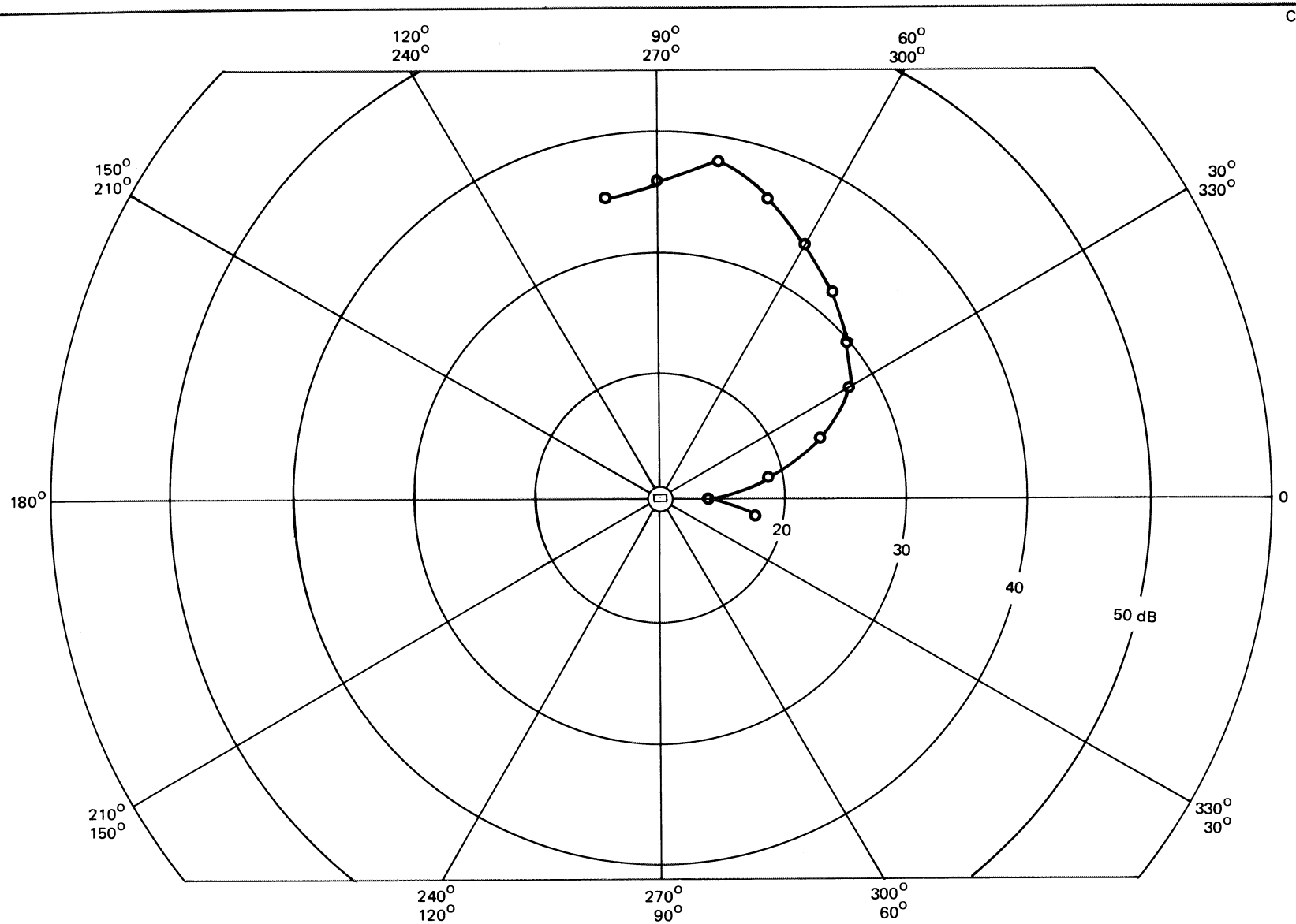

Figure 3-27. Pulse-Echo Amplitude vs Flaw Orientation (A_3 Mode; 20-Deg Wedge, 3.65 MHz)

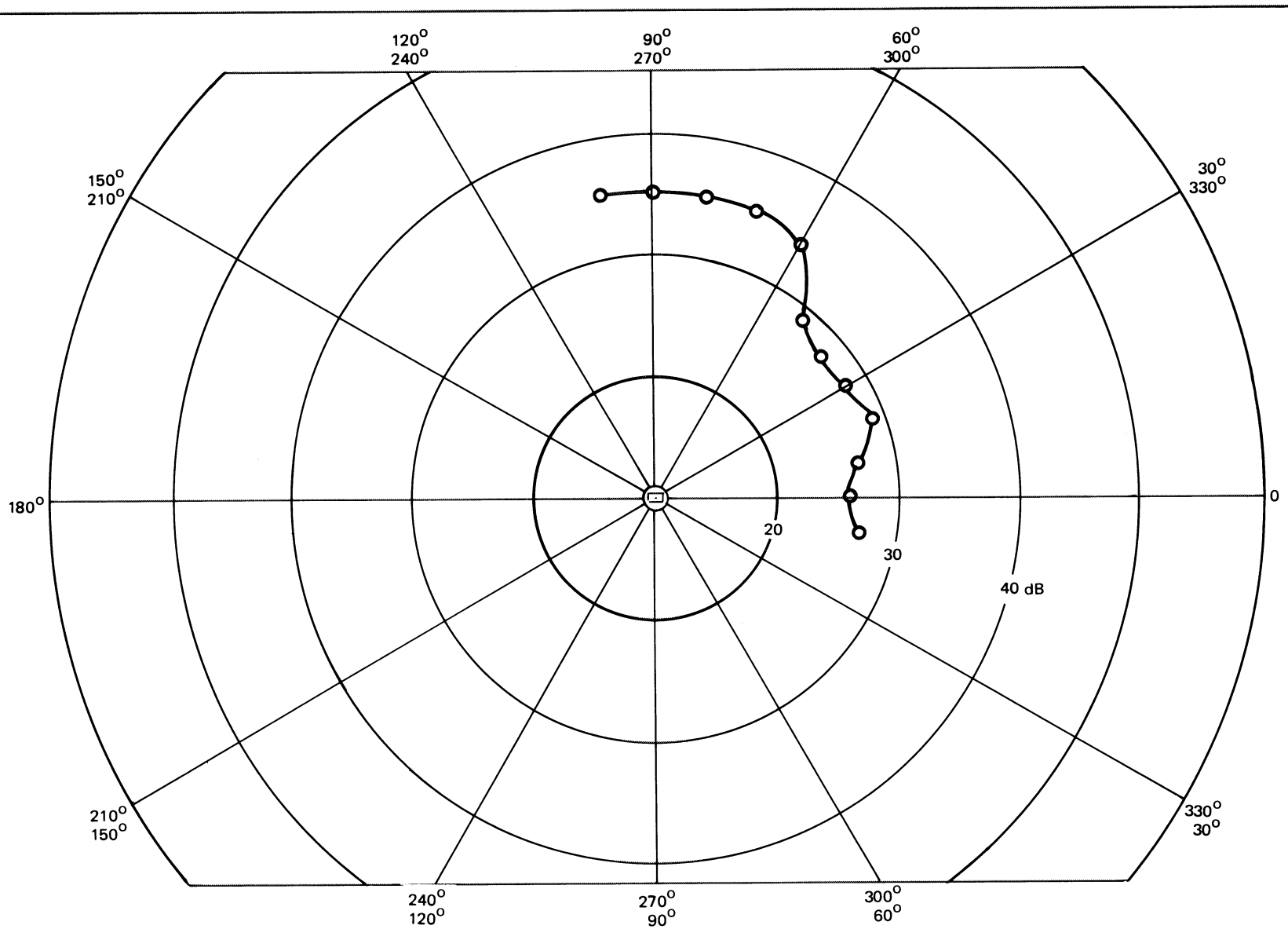

Figure 3-28. Pulse-Echo Amplitude vs Flaw Orientation (A_4 - S_4 Mode; 20-Deg Wedge, 5.37 MHz)

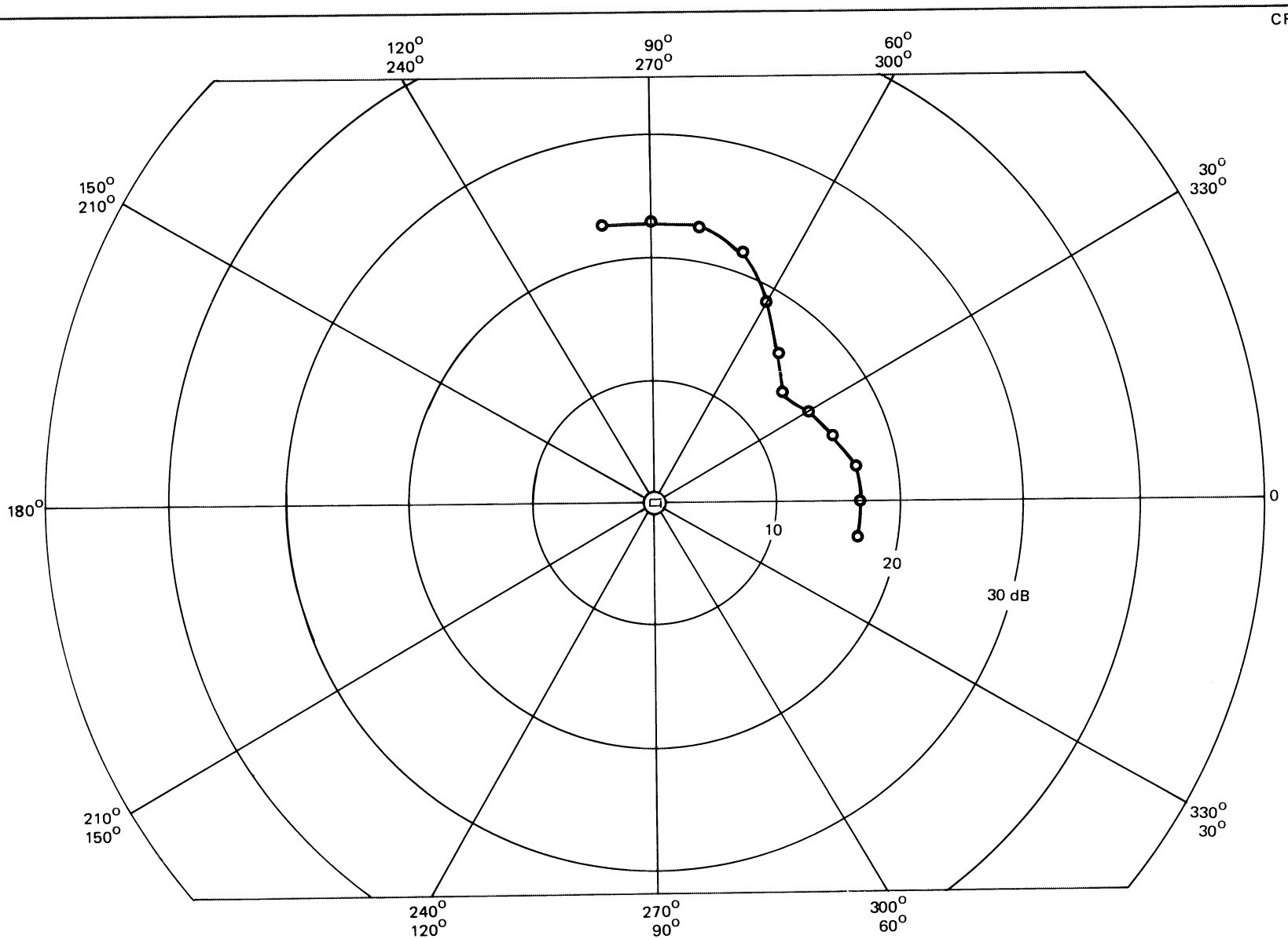

Figure 3-29. Pulse-Echo Amplitude vs Flaw Orientation (S_5 Mode; 20-Deg Wedge, 6.80 MHz)

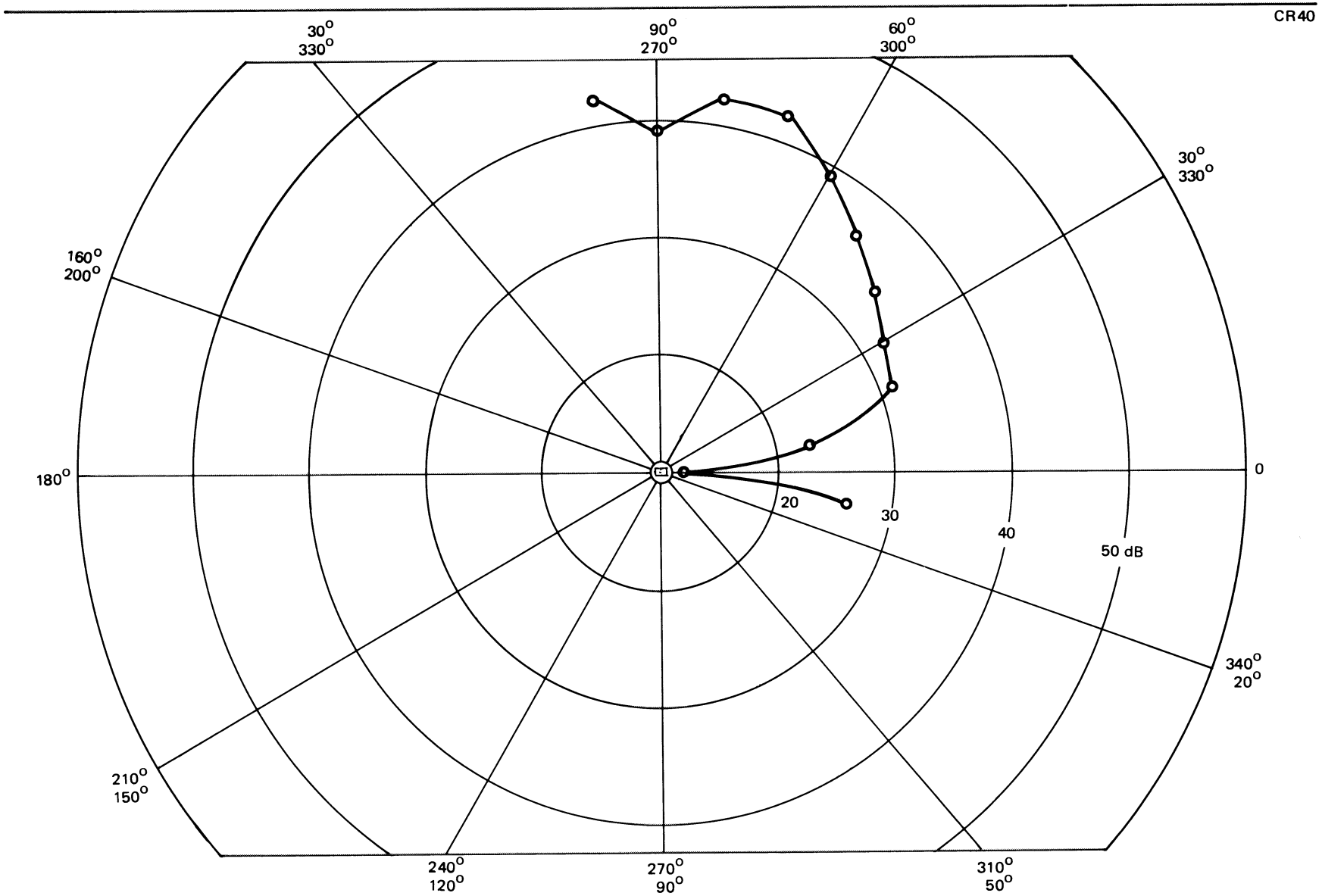

Figure 3-30. Pulse-Echo Amplitude vs Flaw Orientation (A_2 Mode; 30-Deg Wedge, 2.51 MHz)

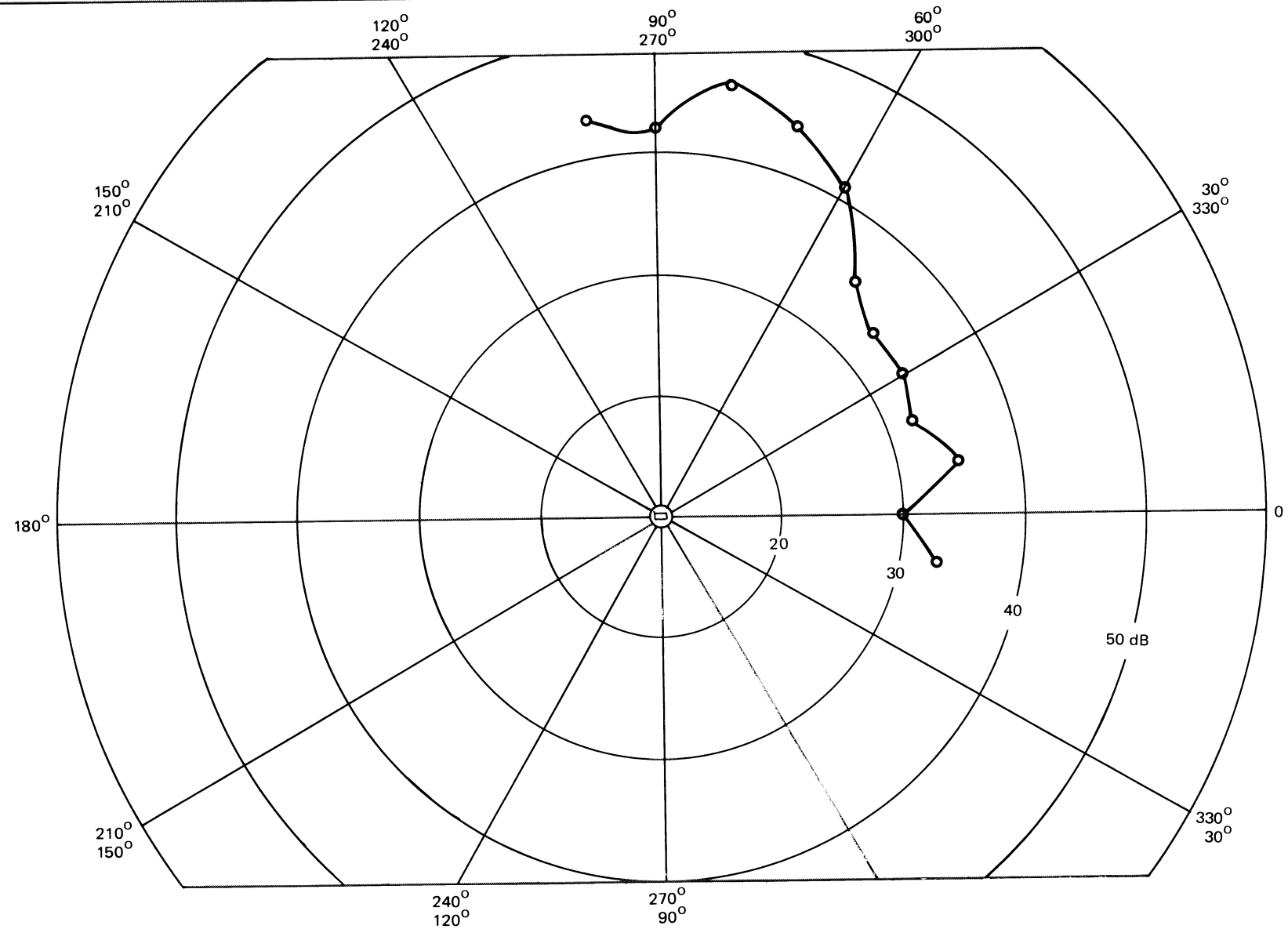

Figure 3-31. Pulse-Echo Amplitude vs Flaw Orientation (S_2 Mode; 30-Deg Wedge, 3.81 MHz)

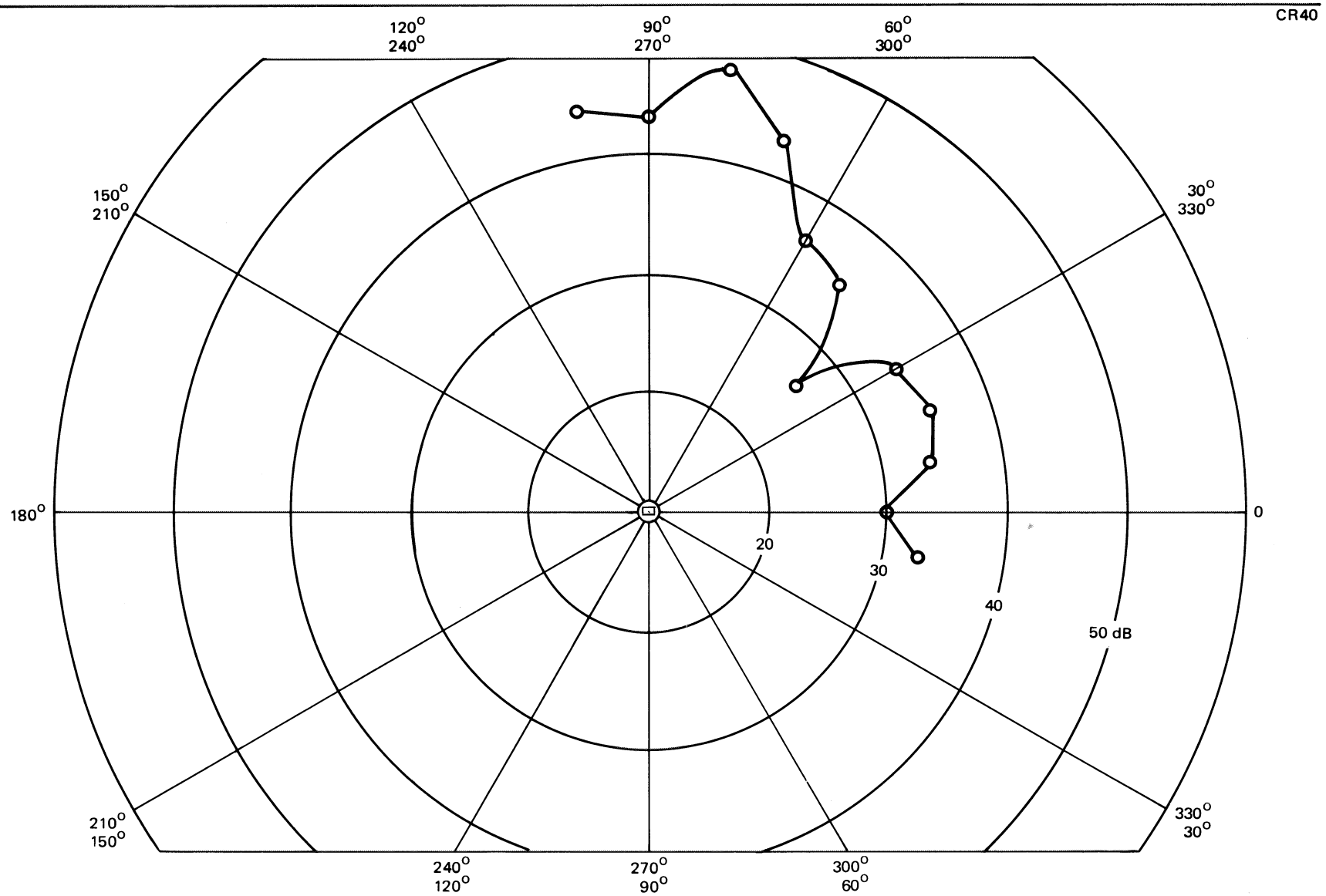

Figure 3-32. Pulse-Echo Amplitude vs Flaw Orientation (A_3 Mode; 30-Deg Wedge, 5.30 MHz)

Table 3-8

THROUGH-THICKNESS RECTANGULAR-SLOT EXPERIMENT RESULTS

Lamb-Wave Mode	Maximum Amplitude (dB)	Minimum Amplitude (dB)	0-deg Reflection (dB)	Orientation Dependence of Amplitude
S_2	9	3	3	strong
A_3	38	14	14	strong
A_4-S_4	35	26	26	weak
S_5	23	14	17	weak
A_2	42	11	11	strong
S_2	46	30	30	strong
A_3	52	26	30	strong

3.6.1.2 Part-Through Notch Measurements Pulse-echo Detection

The pulse-echo signal from a rectangular cross-sectional slot (0.51 mm long x 0.18 mm wide x 0.51 mm deep) in the center of a 1.60-mm thick aluminum plate 1.22 m square was recorded for various orientations between the slot and the transducer using the A_4-S_4 mode (20-deg wedge, 5.12 MHz). The A_4-S_4 mode was used since it gave a relatively uniform reflected signal as a function of angle in the through-thickness slot measurements, and it transmits well past ribs. The test configuration was identical with that shown in Figure 3-25 with a 46-cm separation between the transducer and the slot. Measurements were taken at 10-degree intervals over a 110-degree range of transducer orientation angles between 100 and 350 degrees with the slot oriented such that its length was along the 0-degree direction. The reflected signal as a function of orientation is shown in Figure 3-33. Although the amplitude of the signal is weaker than that for a through slot (Figure 3-28), the form of the amplitude curve is similar to that obtained using the A_4-S_4 mode on a through slot.

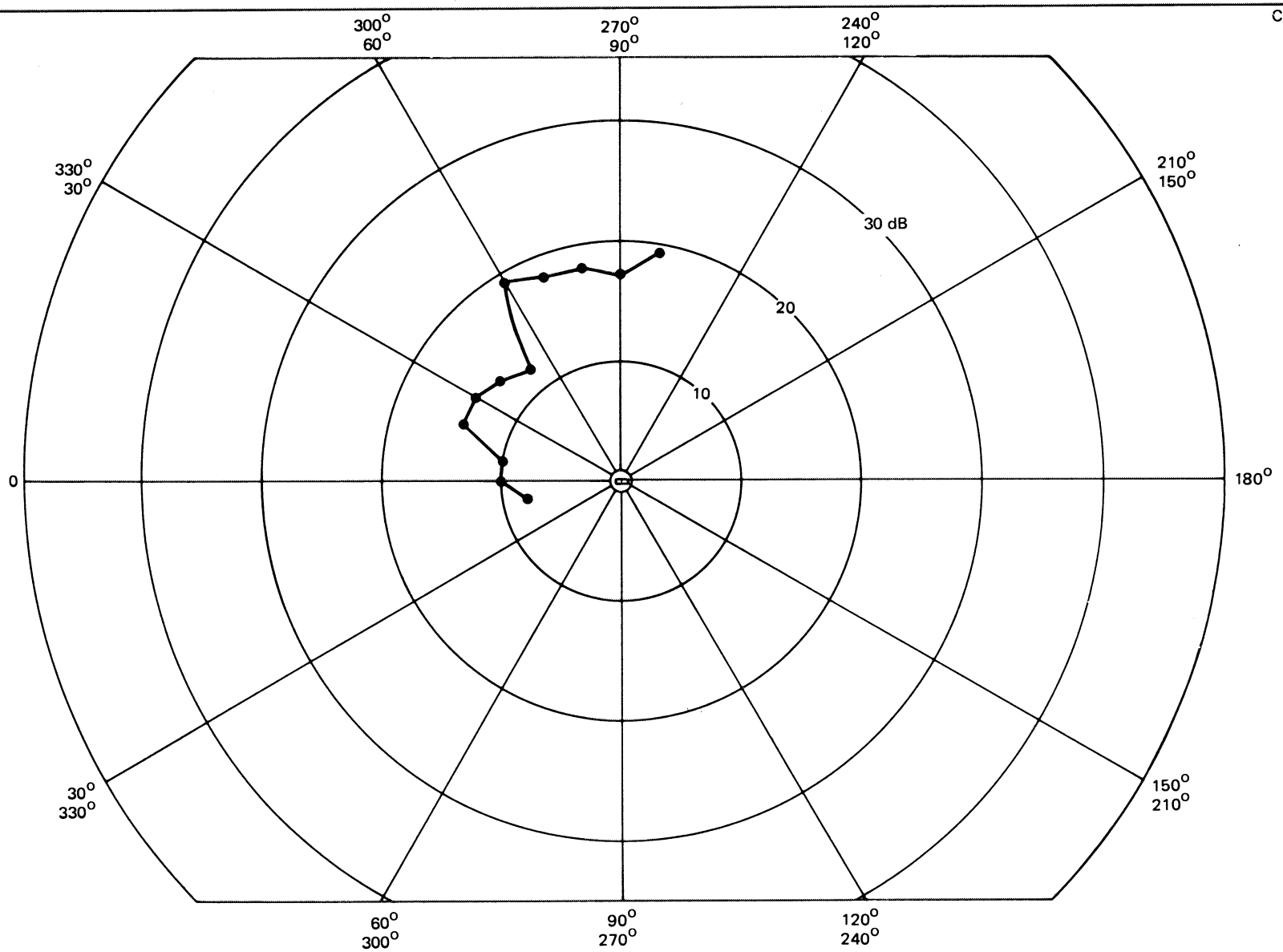

Figure 3-33. Pulse-Echo Amplitude vs Flaw Orientation (A_4 - S_4 Mode; 20-Deg Wedge, 5.12 MHz)

3.6.1.3 Transmit-Receive Detection

Some transmit-receive measurements were also carried out using the A_4-S_4 mode to detect the part-through slot. For these measurements, the same orientation convention was used as that for the above pulse-echo measurements, with the transducers separated 46 cm from the slot. Signals were recorded for the transmitter at 10-deg and the receiver at 50-deg, and for the transmitter at 90 deg and the receiver at 50 and at 0 deg. The test results are shown in Figure 3-34. For the transmitter at 10 deg and receiver at 50-deg, the signal was relatively weak compared to the background noise in the plate. For the other measurements the signal was stronger as would be expected due to the 90-deg orientation of the slot to the transducer. The peaks which appear on the scope traces after the initial peak are due to edge reflections in the plate reaching the transducer after the signal reflected from the slot is detected.

3.6.2 Part-Through Hole Measurements

A study of the received signal from a circular cross-sectional part-through hole was carried out to assess the ability of Lamb waves to detect this flaw with the transducer placed on the hole side of the test plate and on the smooth side of the plate. Since Lamb waves propagate within the thickness of the plate, they are expected to be useful to detect part-through flaws open on either side of the plate. Two examples of Lamb wave detection of a 0.36-mm diameter hole extending 0.51 mm into a 1.60 mm-thick plate are shown in Figures 3-35 and 3-36. Each figure shows the received signals for the transducer placed on the hole side of the plate and on the smooth side of the plate. The separation between the transducer and the flaw was 17.8 cm. Figure 3-35 shows results using the A_4-S_4 mode (20-deg wedge angle at 5.37 MHz). The flaw is detectable from both sides of the test plate, but the signal is somewhat noisy. Figure 3-36 shows the same flaw using the A_3 mode (20-deg wedge angle at 3.65 MHz). Here the signal from the flaw is sharp and easily discernable from the low level background noise.

3.6.3 Detection Past Obstructions

In addition to integral stiffener ribs, a Space Station wall could have feedthroughs, rivets or bolts located such that they intersect the line between a

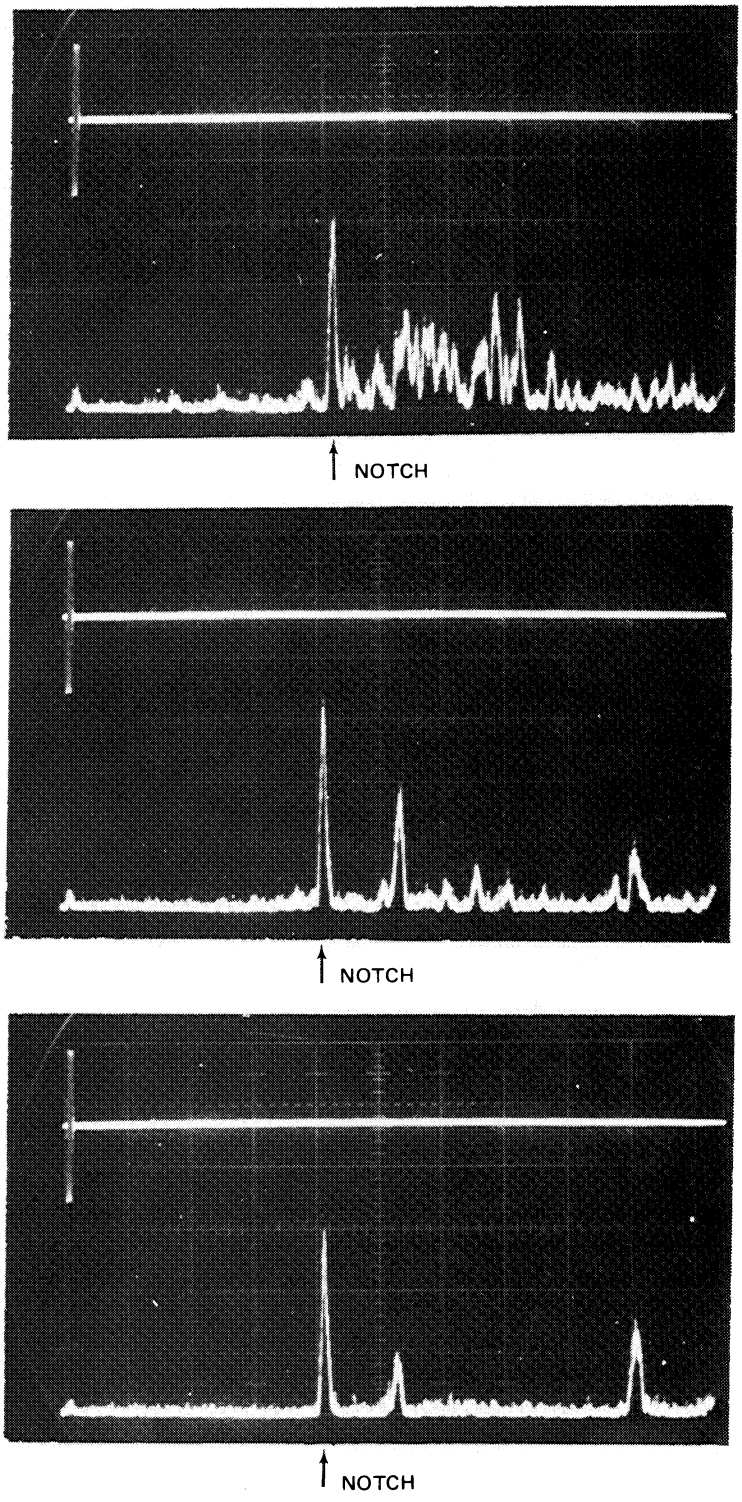

Figure 3-34. Transmit - Receive Detection of Part-Through Notch

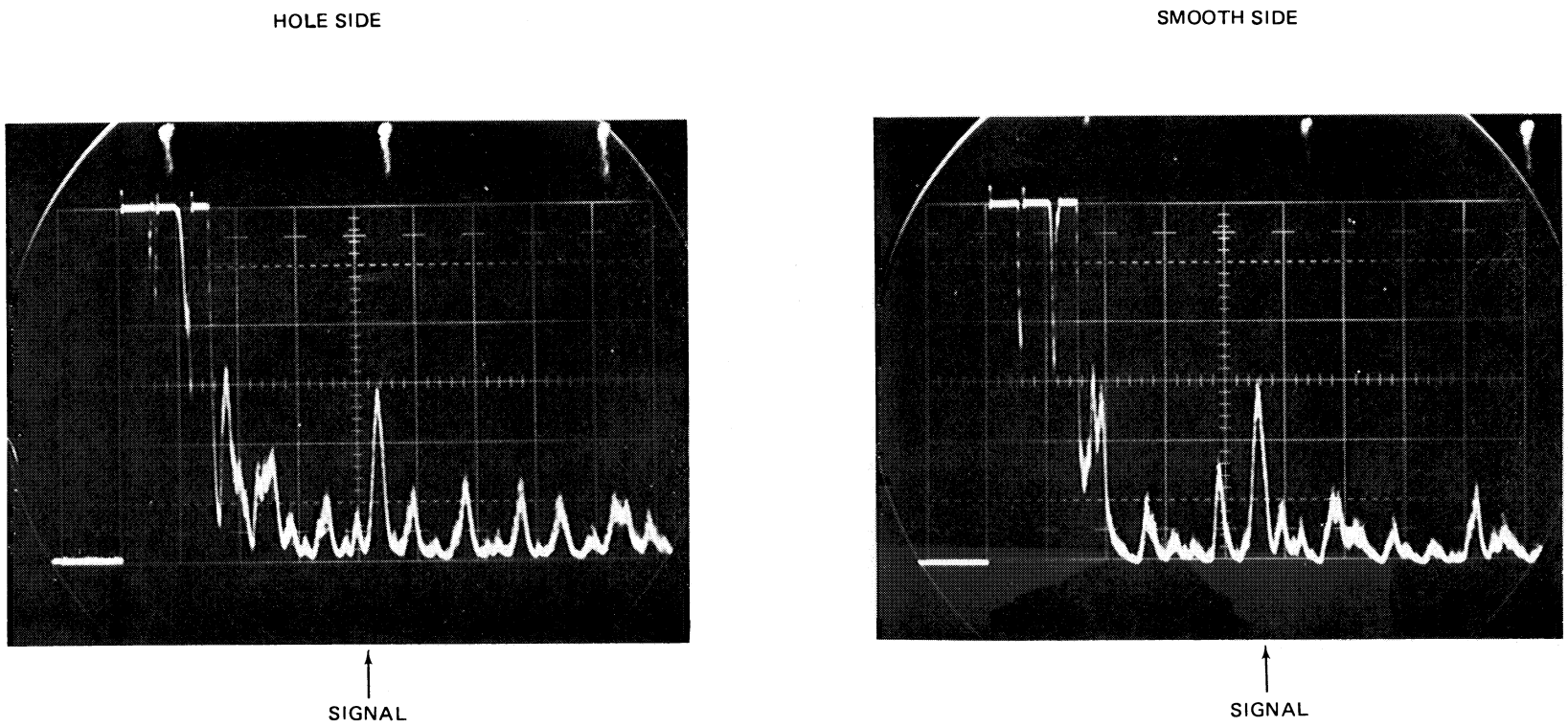

Figure 3-35. Detection of a 0.36 mm - Diameter Hole, 0.51 mm Deep, in a 1.60 mm - Thick Aluminum Plate (A_4 - S_4 Mode)

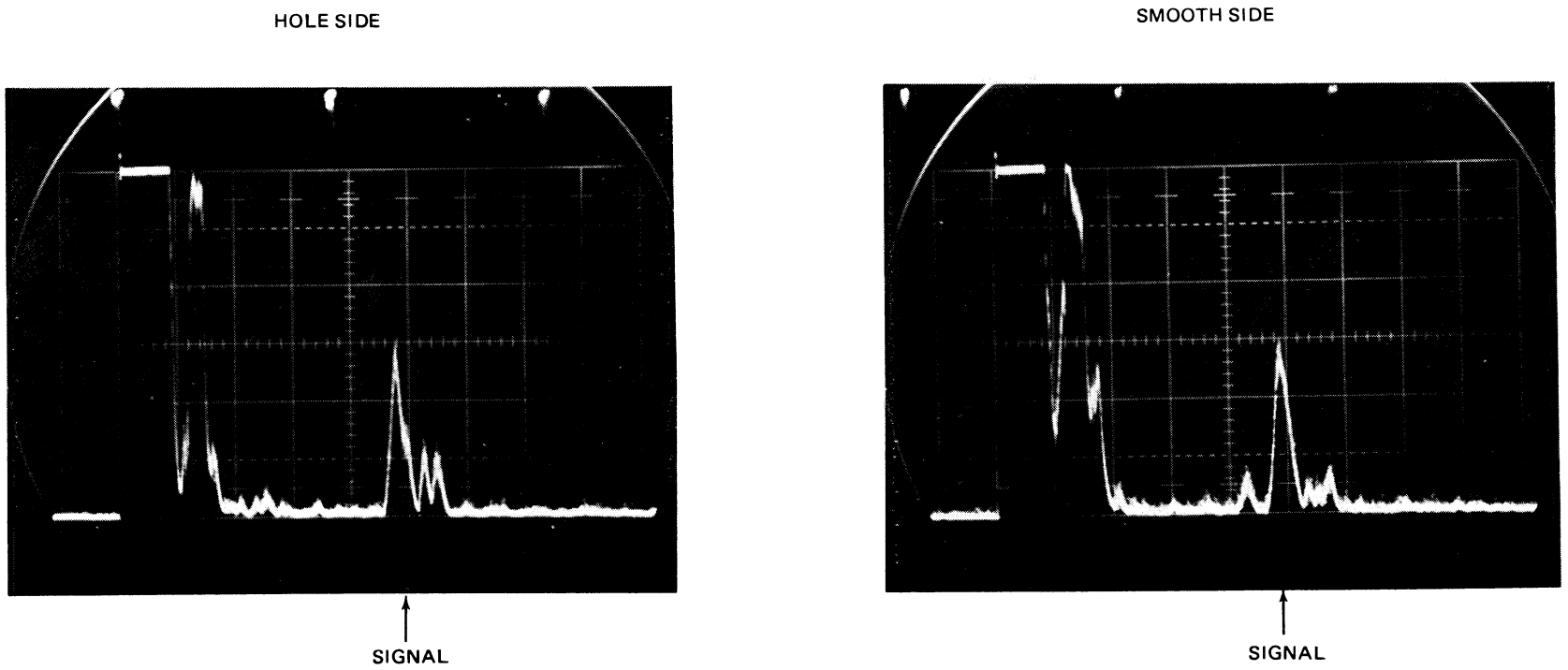

Figure 3-36. Detection of a 0.36 mm-Diameter Hole, 0.51 mm Deep, in a 1.60 mm-Thick Aluminum Plate (A_3 Mode)

transducer mounted on the wall and a flaw. An investigation was done on the detection of a small hole past a bolt hole to determine the degree of interference such an obstacle presents to Lamb wave flaw detection. The flaw investigated was a No. 68 drilled hole (0.79 mm) in a 1.60 mm-thick aluminum plate. The No. 68 hole was located 15.2 cm from the hole and an obstacle hole was drilled on the line between the transducer and flaw 30.5 cm from the No. 68 hole. This pulse-echo configuration is shown in Figure 3-37.

The first obstacle hole used was a No. 28 drilled hole (0.58 mm in diameter). The Lamb wave mode used for all the measurements was the A_3 mode at 3.65 MHz using a 20 deg wedge angle. This mode was previously found to have high sensitivity for detecting small flaws remotely. Using the A_3 mode, the No. 68 hole could be detected past the No. 28 hole as shown in Figure 3-38(a). Sufficient attenuation was used on the input to the scope to maintain the signal pulse at 6-V on the scope face. The attenuation was adjusted for each subsequent measurement to maintain the 6-V flaw signal level, and the amount of attenuation used was taken as the relative signal amplitude. The signal level from the No. 68 hole past the No. 28 hole was 25 dB. Next a 6-32 screw was inserted through the No. 28 hole and tightly fastened with a nut. The No. 68 hole still gave an easily detectable signal of 28 dB amplitude. This signal is shown in Figure 3-38(b).

The experiments were repeated with the obstacle hole enlarged to a No. 12 drilled hole (4.80 mm dia.) and the measurements were repeated with and with without a body fit screw tightly fastened through the No. 12 hole. The No. 68 hole was detectable once again with signal strength of 29 dB without the screw, and a signal strength of 28 dB with the screw inserted. These results are shown in Figures 3-39(a) and (b). The No. 12 hole was further enlarged to 0.635 cm diameter and the measurements were again repeated. The No. 68 hole was again detectable past the obstacle with a 17-dB amplitude for the open 0.635-cm hole and with a 19-dB amplitude when a 1/4-24 screw was tightly fastened through the hole. These results are shown in Figures 3-40(a) and (b) respectively.

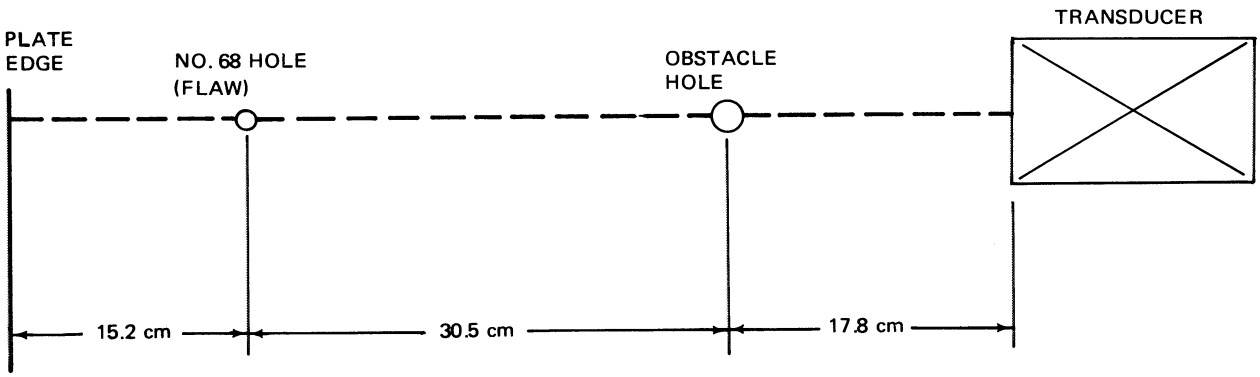

Figure 3-37. Pulse-Echo Configuration

3.6.4 Transmit-Receive Detection of Circular Holes.

Some measurements in the transmit-receive configuration using a 90-deg angular orientation between the transducers were made to detect the reflected signal from a 1.02-mm diameter and a 0.36-mm-diameter hole on the test panel of Figure 3-8.

Both transducers were spaced 30.5 cm from the holes. Various modes used were found to have different sensitivities to the holes. The modes investigated are listed in Table 3-9.

Of these, only the A_4 mode could not detect the 0.36-mm-diameter hole. All the remaining modes could detect both holes; however, the A_2 mode gave very noisy signals.

Examples of the received signals are shown in Figures 3-41 and 3-42 for the A_4S_4 mode and the A_3 mode respectively. In Figure 3-42, the additional signals following the main reflected signal are edge reflections.

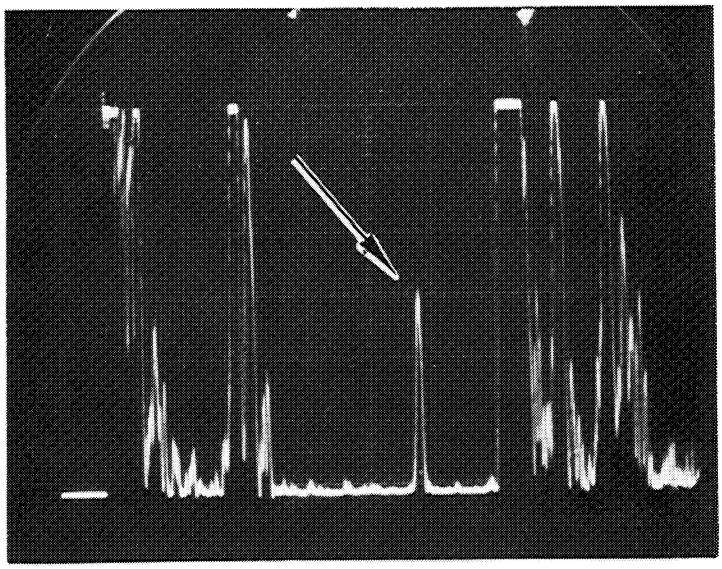

(a) OPEN 3.58-mm-DIAMETER HOLE

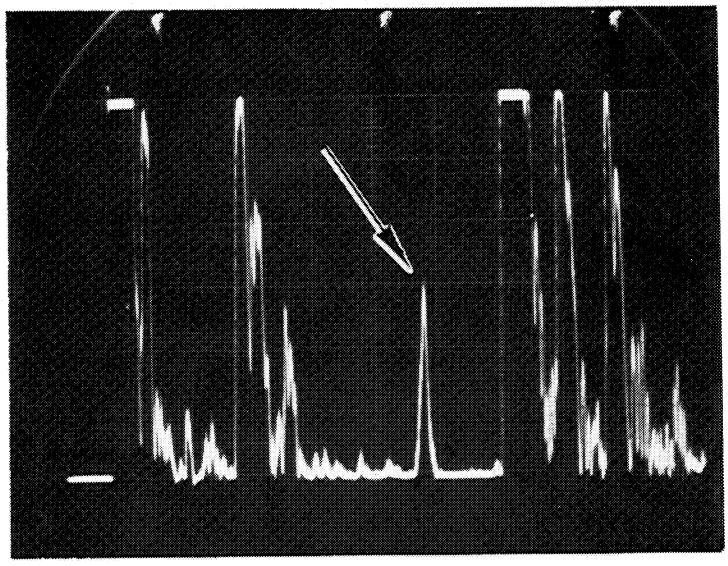

(b) 3.58-mm HOLE WITH SCREW INSERTED

THE ARROW INDICATES THE SIGNAL FROM THE NO. 68 HOLE. THE FIRST LARGE SIGNAL AT THE LEFT IS THE TRANSMITTER OUTPUT PULSE. THE SECOND SIGNAL AT THE LEFT IS THE REFLECTION FROM THE 3.58-mm DIA HOLE, THE LARGE SIGNALS IN THE RIGHT ARE THE REFLECTIONS FROM THE EDGE OF THE TEST PLATE

Figure 3-38. Detection of No. 68 Hole Past a 3.58-mm Diameter Hole

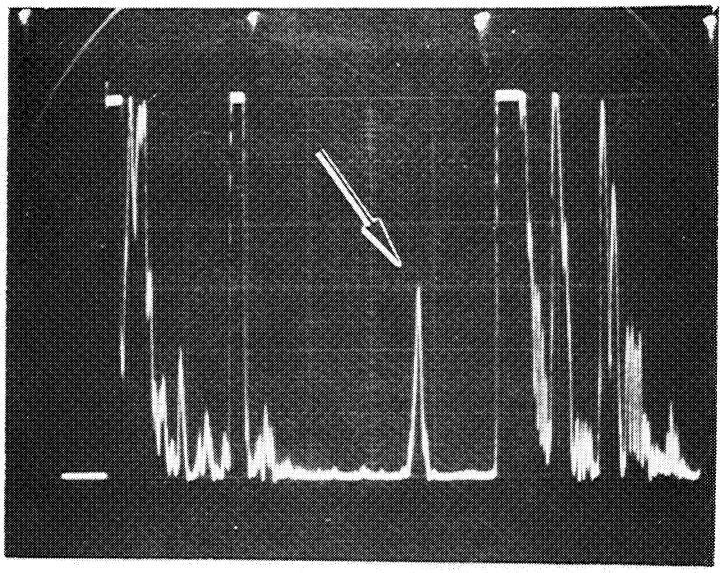

(a) OPEN 4.80-mm-DIAMETER HOLE

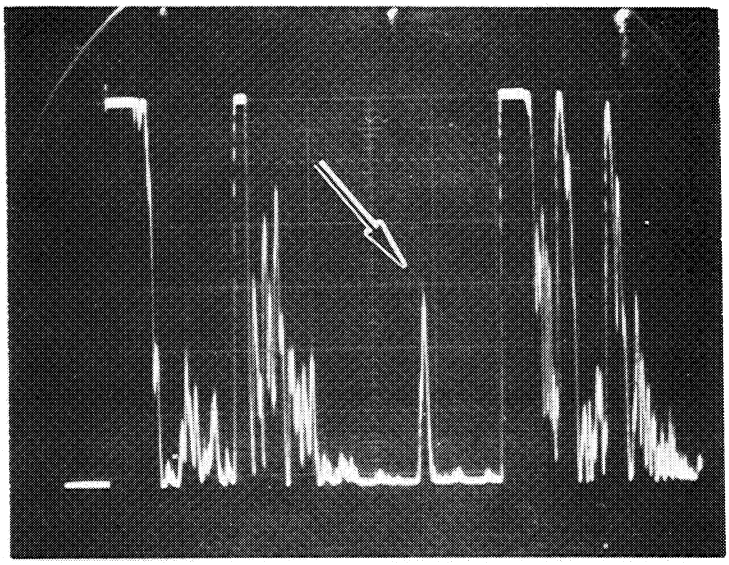

(b) 4.80-mm HOLE WITH SCREW INSERTED

THE ARROW INDICATES THE SIGNAL FROM THE NO. 68 HOLE

Figure 3-39. Detection of a No. 68 Hole Past a 4.80-mm Diameter Hole

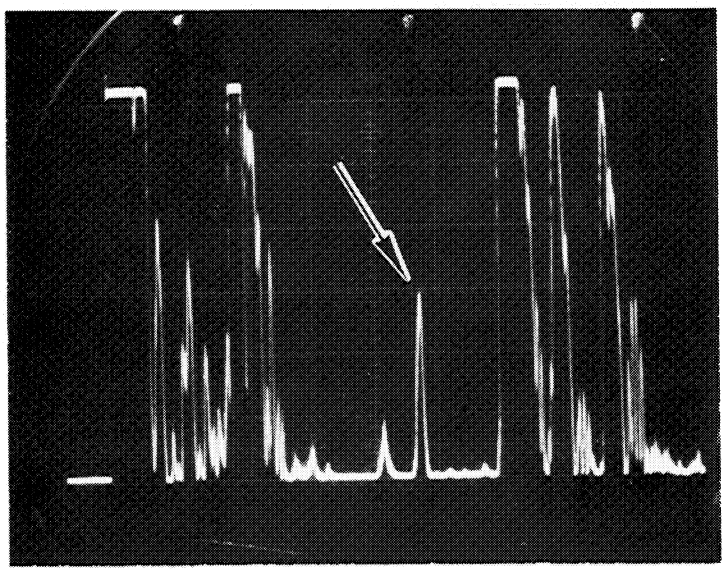

(a) OPEN 6.35-mm-DIAMETER HOLE

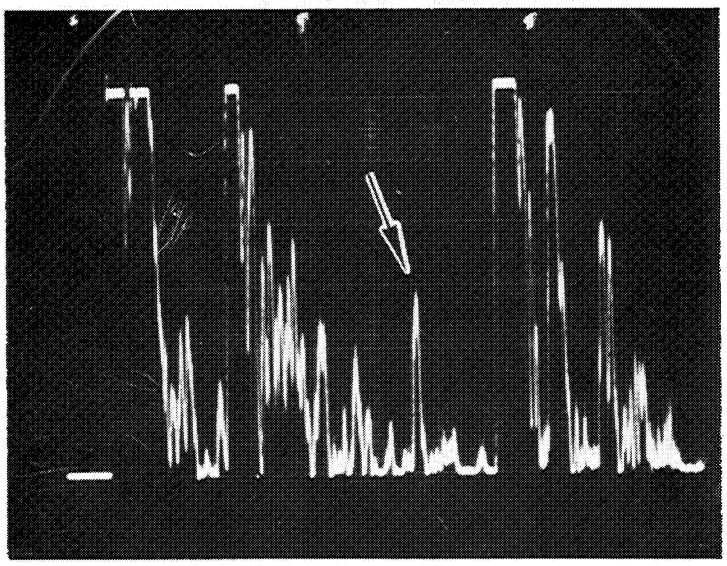

(b) 6.35-mm HOLE WITH SCREW INSERTED

THE ARROW INDICATES THE SIGNAL FROM THE NO. 68 HOLE

Figure 3-40. Detection of a No. 68 Hole Past a 6.35mm-Diameter Hole

Table 3-9

MODES INVESTIGATED FOR CIRCULAR-HOLE DETECTION

	Mode	Transmitter Wedge Angle (deg)	Frequency (MHz)
1.	A_2	21.5	1.80
2.	S_2	21.5	2.59
3.	A_3	21.5	3.75
4.	A_4	21.5	5.80
5.	S_2	20	2.35
6.	A_3	20	3.65
7.	A_4-S_4	20	5.37

3.6.5 Thick-Plate Flaw Detection Measurement

A limited study of flaw detection in a thicker aluminum specimen was performed using a 1.27-cm-thick aluminum plate. A rectangular cross-sectional part-through notch was machined into the plate with dimensions of 1.27 mm long by 0.13 mm wide by 3.18 mm deep. The signal received from this notch with the transducer placed 61 cm from the notch is displayed in Figure 3-43. For this measurement, the operating conditions were 50 deg wedge angle and 2.46 MHz. This result demonstrates that Lamb-wave techniques are applicable to thick plates or to thick areas of platelike structures, such as in the weldment areas of a pressure vessel.

3.7 FLAW DETECTION ON A RIBBED PANEL: LEAK LOCATION BREADBOARD

Modes used for this study are those identified in Table 3-7. All have demonstrated the ability to traverse a reinforcement rib and to detect flaws on 1.60 mm-thick aluminum plate. These flaw detection measurements on a ribbed panel provide a further screening of modes for use in flaw detecting and locating on an integrally reinforced panel as well as providing data for flaw location on a damage control breadboard.

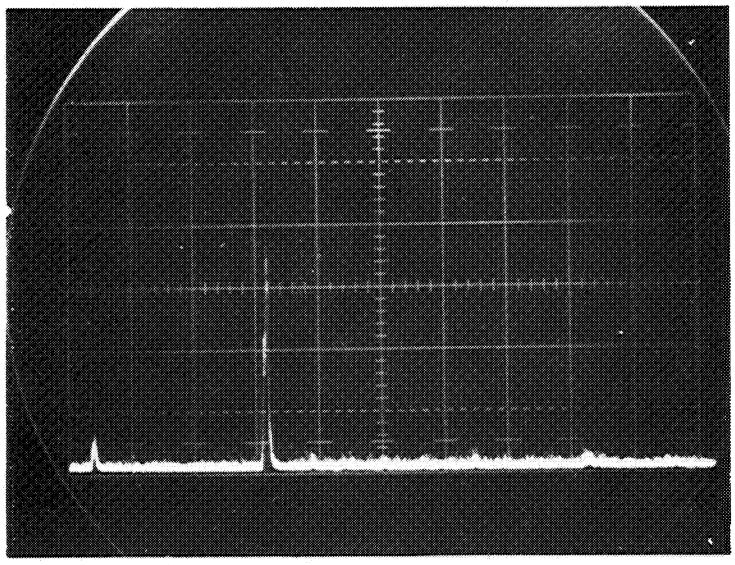

NO. 60 HOLE

14-dB ATTENUATION

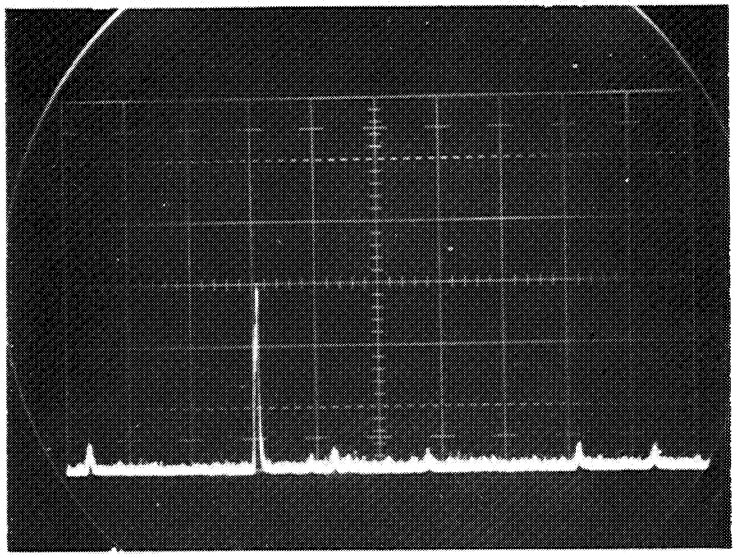

NO. 80 HOLE

13-dB ATTENUATION

Figure 3-41. Transmit-Receive Detection of No. 60 and 68 Holes Using the A_4 - S_4 Mode (20-Deg Wedge, 5.37 MHz)

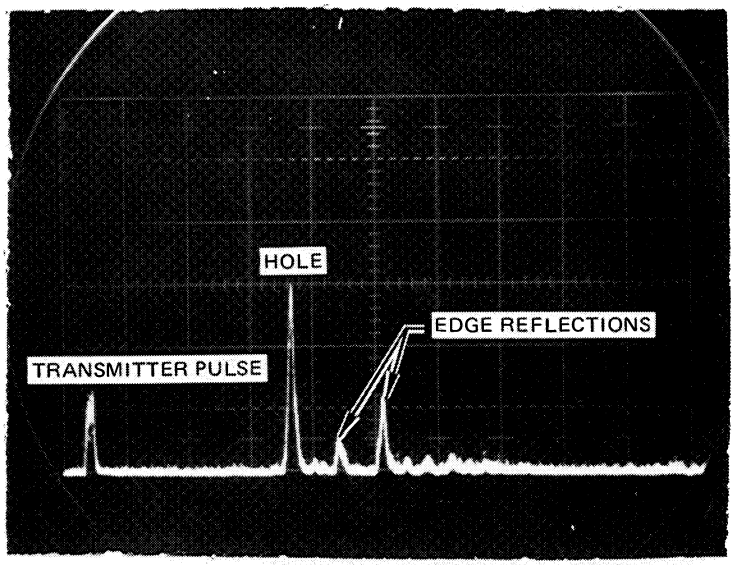

NO. 60 HOLE

21-dB ATTENUATION

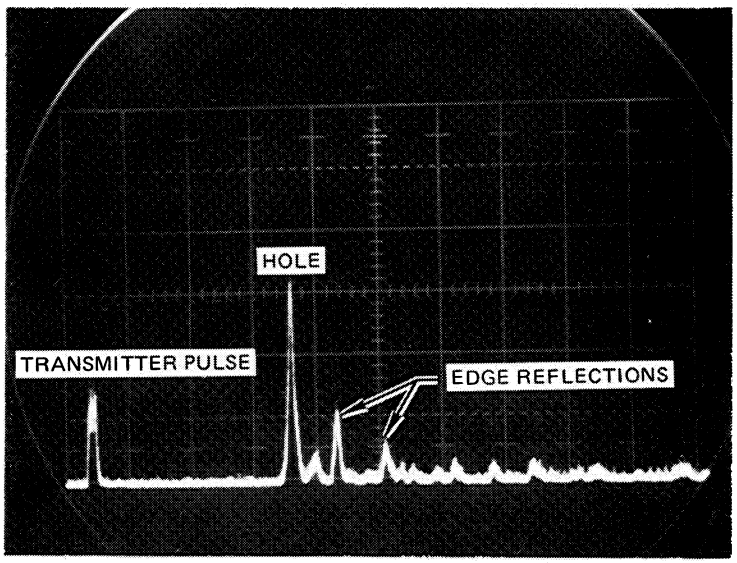

NO. 80 HOLE

20-dB ATTENUATION

Figure 3-42. Transmit-Receive Detection of No. 60 and 80 Holes Using the A_3 Mode (20-Deg Wedge, 3.65 MHz)

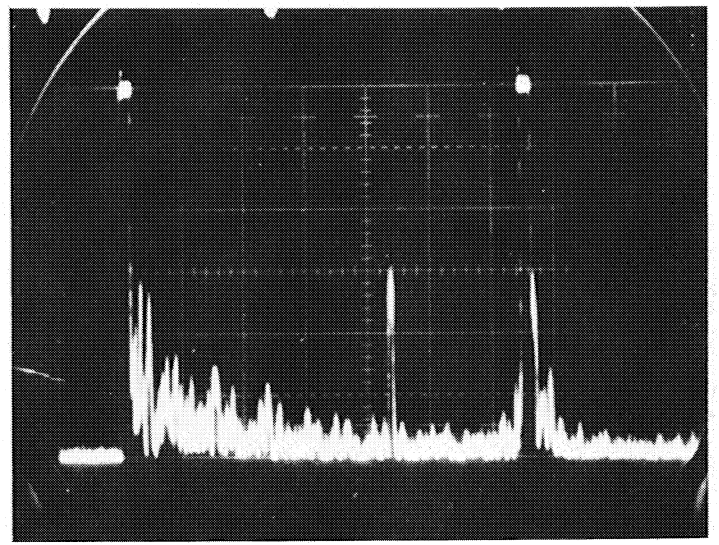

SIGNAL

TRANSDUCER SEPARATED 61 cm
FROM THE NOTCH. A 50-DEG WEDGE
ANGLE TRANSDUCER WAS USED
OPERATING AT 2.46 MHz

Figure 3-43. Pulse-Echo Signal from Notch (1.27 mm Long by 0.13 mm Wide by 3.18 mm Deep) in 1.27 cm Thick Aluminum

The initial measurements involved the detection of a 1.02 mm diameter through hole in a single rib panel of aluminum (7075 alloy) with an average thickness of 1.52 mm. For the flaw detection measurements, three transducer positions on the panel were used as shown in Figure 3-44. The three positions allowed a total of nine different measurements as follows:

Three pulse echo measurements with the transducers in positions 1, 2, and 3 respectively. Position 1 provided flaw detection with no intervening rib between the transducer and the hole. Position 2 provided detection past the rib with oblique incidence of the sound beam with respect to the rib. Position 3 provided detection past a rib with normal incidence of the sound beam to the rib.

Six transmit-receive measurements provided at least one traversal of the rib by the ultrasonic signal before it was detected. These measurement positions gave three variations in the position of the rib in the signal path and three different angular orientations between the transmitter and receiver transducers of 30, 60, and 90 deg.

CR40

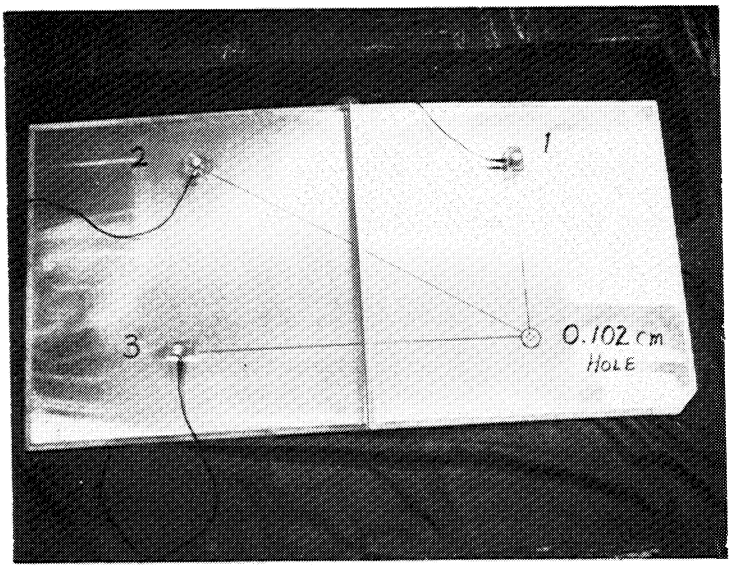

DISTANCES:

1 TO HOLE = 30.5 cm
2 TO HOLE = 66 cm
3 TO HOLE = 61 cm

Figure 3-44. Transducer Placement on Single Rib Panel

None of the pulse-echo measurements were successful in detecting the hole past the rib. With the transducer in Position 1, the pulse-echo measurements with no intervening rib yielded signals with considerable interference from the material. These signals were much weaker than those recorded using the rolled sheet of 1.60 mm thickness.

In one instance, using the S_3 mode, the echo signal was almost obscured by the background noise. With the A_4 mode, the echo signal was not discernable in the noise background. This behavior was first attributed to the roughness of the machined surface of the ribbed panel. The surface of the panel was sanded to remove the machining ridges, but the smoothed surface did not improve the quality of the pulse-echo signals. In an attempt to understand this behavior, metallographic specimens were taken to observe the grain structure of the two single-ribbed panels, and of the 1.60 mm-thick aluminum sheet of Figure 3-8 on which the initial flaw detection measurements were taken in the pulse-echo mode. Because the ribbed panels were milled from 2.54-cm-thick plate, it was expected that their grain size would be larger than that in the 1.60-mm-thick rolled sheet which had been worked more. The metallographic results are presented in Figure 3-45. The grain structure in the 1.60-mm-thick sheet appeared the same for samples take along (longitudinal specimen) and across (transverse specimen) the sheet. The grain structure in the ribbed panels differed in the longitudinal and the transverse directions, showing a longer grain size in the longitudinal direction. As can be seen from Figure 3-45, the grain structure in the ribbed panels was much larger than that in the rolled sheet. The larger grain size yields strong attenuation of the Lamb-wave beam caused by scattering of ultrasonic energy at the grain boundaries. The effects of grain structure on the absorption of Lamb waves has been investigated in brass and mild steel (Reference 8). It was found that the attenuation in brass and steel increased as the grain size increased. While it appears that the grain structure on the ribbed panels interfered strongly with the pulse-echo measurements, the transmit-receive measurements showed positive results. The interference by the grain structure on the ribbed panels should be less severe if lower Lamb wave frequencies are used; however, this possibility has not yet been experimentally investigated.

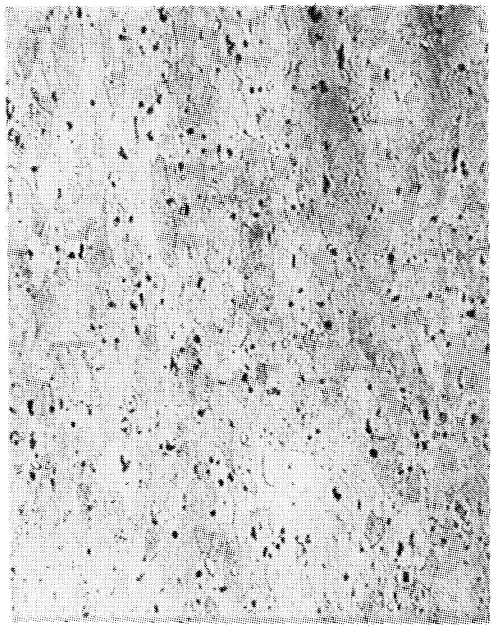

1.60 mm 2219-T37
ALUMINUM SHEET

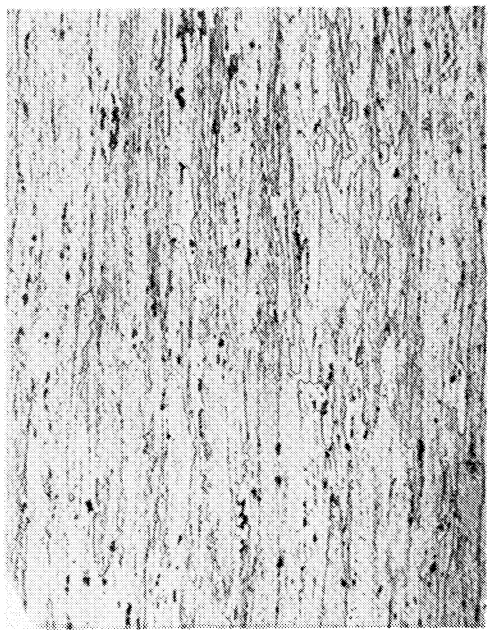

1.52 mm 7075 ALUMINUM
(RIBBED PANEL)
TRANSVERSE SECTION

1.52 mm 7075 ALUMINUM
(RIBBED PANEL)
LONGITUDINAL SECTION

Figure 3-45. Grain Structure of Test Panels

For the transmit-receive measurements, four of the six modes were successful in detecting the hole on the ribbed panel. The A_4 S_4 and S_3 modes could detect the hole for all configurations of the transducers. The A_3 and A_2 modes could not detect the hole when two transversals of the rib were made. The A_4 mode was unable to detect the hole in any configuration of the transducers. This lack of success with the A_4 mode was probably due to the grain structure interference. The S_1 mode was not used because in the previous transmission past rib measurement, it gave an edge reflection echo signal which was composed of two closely spaced peaks and was somewhat noisy. As a result, the S_1 mode was not expected to perform better than the modes tested above. The results were also analyzed for the velocities of the received signal pulse. The velocity was found in all the measurements to remain constant for each mode in all the various transducer configurations, indicating no strong mode conversion into modes of other velocities was occurring at the flaw or the rib. In as much as the velocity remained constant, these modes could be used to locate the hole by triangulation based upon the time of arrival of the signal pulse into the detector system. The A_4 S_4 and the S_3 modes showed the greatest promise for location by triangulation since they could detect the hole for all the transducer positions. To maintain a 6-V oscilloscope signal amplitude for the A_4 S_4 mode measurements, between 6 and 13 dB of attenuation were required. For the S_3 mode, 2 to 3 dB of attenuation were used to maintain a 6-V signal.

3.8 APPLICATION TO A BREADBOARD LEAK LOCATOR

The results using the A_4 S_4 mode are shown in Figure 3-46. The velocity calculated from these signals is 0.457 cm/μsec. Since the velocity for the A_4 S_4 mode in the ribbed panel is known, it can be used to triangulate to locate the position of the flaw. The velocity is used to determine the distance a pulsed signal traveled in the panel before reaching the receiver transducer. The distance traveled is given by the expression:

$$d = v\,(t - t_o)$$

where:

v = velocity of the Lamb-wave pulse

t = time delay between generation of pulse and detection of signal.

t_o = time interval signal spends traversing the transducer wedges.

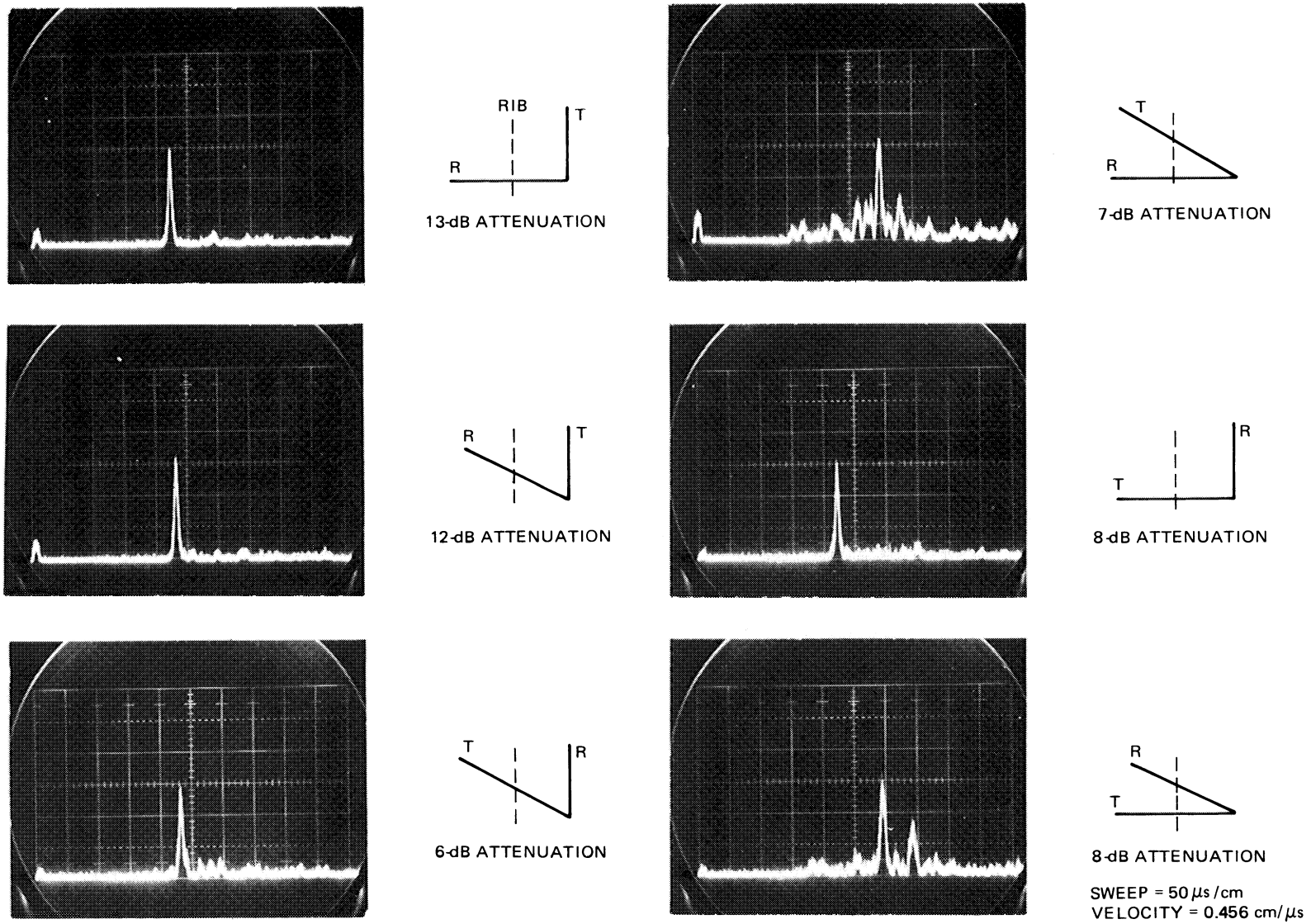

Figure 3-46. Flaw Detection Measurements on Ribbed Panel (A_4 S_4 Mode; 20-Deg Wedge, 4.85 MHz)

The total distance d can be used to construct an ellipse on the panel containing the flaw position on its circumference with the transmitter and the receiver transducer positions as its foci, and the sum of its radii equal to d. Taking three separate groups of two transducers at a time, three intersecting ellipses can be generated, each containing the location of the flaw. The common intersection point of the ellipses is the location of the flaw. The intersection of the ellipses can be determined using computer analysis, or more simply by using graphical methods.

Section 4
IMPACT GAGE

4.1 INTRODUCTION

In a prior study (Reference 1), the need for a meteoroid/orbital debris-impact gage was identified for space station. Triangulation techniques are necessary to locate the region of impact. This can be provided by a transducer array mounted on the pressure wall of space station. Two sensing methods were considered: (1) locating the point of impact by measuring the time-of-arrival of the impact-generated shock wave at a minimum of three separate locations, and (2) determining the direction vector of the shock wave at a minimum of two locations. The point of intersection of the two vectors located the point of impact. Since the shock-wave time-of-arrival method had been proved feasible in a McDonnell Douglas Astronautics Company IRAD program in 1970, this technique was chosen for further study.

4.2 DUAL-FUNCTION IMPACT GAGE

The concept of a dual-function impact gage was studied in this program and influenced the design of the electronics and signal conditioning equipment associated with an impact-gage triangulation system.

Two approaches which merited consideration were: (1) impact gage/active ultrasonics and (2) impact gage/acoustic emission.

The signal generated by the impact of meteoroid debris on a pressure wall is likely to be large for a significant impulse. It is probable that an ultrasonic transducer basically designed for Lamb-wave flaw detection will respond to a meteroid impact. Requirements for sensing meteoroid impact (50 kHz to 1 MHz) are compatible with the operating frequencies for active ultrasonic transducers. Inasmuch as the impact gage is a passive detector, there would be no conflict in operation. Similar considerations apply to signal processing requirements.

The dual-function impact gage – acoustic emission monitor was also considered feasible. Except for signal sensitivity requirements, both sensors are similar and could be incorporated within a single transducer covering a frequency range from 50 kHz to about 1 MHz. Since acoustic emission stress waves come in discrete packets generally at amplitudes less than 10mV, signal conditioning requirements would be different.

The meteoroid/bumper debris impulse (beyond a given magnitude) imparted to a pressure wall is likely to bulge the wall and produce cracks. Therefore, in real time, a dual-function transducer could sense a large-amplitude pulse (meteoroid debris) followed by trains of small pulses (acoustic emission) derived from crack growth induced by the impact. Subsequent crack growth (if any) could also be monitored on a long-term basis by the dual-function transducer.

4.3 PIEZOELECTRIC TRANSDUCERS FOR IMPACT GAGE

The standard transducer material for the impact gage program was PZT-5A (lead zirconate titanate). This piezoelectric ceramic is widely used for ultrasonic wave measurements. In addition to PZT-5A, the prototype impact gages were designed to allow evaluation of other candidate piezoelectric materials.

4.3.1 Piezoelectric Polymer Transducers

Plastic transducers were evaluated for the meteoroid impact gage. Such a transducer, potentially, could be attractive because of its low cost and would lend itself to a wide variety of applications. Even if the plastic exhibited relatively low piezoelectric activity compared to conventional ceramic types such as PZT, its response could be adequate when the signal generated in an aluminum wall is large, as would be the case under meteoroid impact. Polymers under consideration included polyvinylchloride (PVC), polyvinylfluoride (PVF), polyvinylidene fluoride (PVF_2), Mylar, and others.

In recent years, there has been considerable activity in studying the properties of piezoelectric polymers and polymer electrets, which are permanently

polarized dielectrics (Reference 9). Room and Halkaides (Reference 10) described a variety of plastics which will detect mechanical vibrations. Allison and Hauver (Reference 11) demonstrated that many polar polymers under explosive shock-induced polarization yielded large transient signal outputs. Recently, Champion (Reference 12) observed similar effects for PTFE and polyethylene.

Fluorocarbons are among the most promising polymer piezoelectric transducers (Reference 13). The U. S. National Bureau of Standards, Bell Laboratories (Reference 14), and Japanese researchers have been studying the pyroelectric and piezoelectric properties of fluorocarbon systems. Cohen and Edelmen (References 15 to 18) have demonstrated large piezoelectric effects in plastics which approach the activity in quartz. In general, the following two methods (or a combination) enhanced the piezoelectric activity of polymers: (1) chain ordering by stretch processing, and (2) poling techniques which induce dipole ordering by heating the plastic to a transition temperature and allowing it to cool under the influence of an electric field. This second method induces the permanently polarized electret state in the polymer film. PVF and PVF_2 appear to offer particular promise for high-performance piezoelectric transducers. Fukada and Nishiyama (Reference 19) recently made detailed measurements on PVF while Kawai (Reference 20) demonstrated that PVF_2 was significantly superior to all other polymers tested including PVF.

4.4 PROTOTYPE IMPACT-GAGE TEST RESULTS

Four prototype meteroid impact gages were designed and fabricated. The active element holder was constructed so that materials other than PZT-5A could be tested. To facilitate evaluation of less sensitive materials than PZT-5A without requiring simulated meteoroid impact at hypervelocities, a preamplifier was incorporated into the unit. The preamp circuit was packaged on a printed circuit for uniformity. The preamp allowed detection of low-amplitude, high-frequency signals which could be easily generated in the laboratory. Thus attenuation, triangulation, and signal processing experiments could be performed prior to testing with a light-gas gun that did not require a preamp because of the large signals generated by simulated meteoroid impact.

The test setup to study the frequency response and signal output of candidate piezoelectric materials to various acoustical signals is shown in Figure 4-1 and the block diagram in Figure 4-2. The four prototype impact gages and one "in-house" McDonnell Douglas Aerophysics Laboratory (MDAL) shock detector were mounted in a row 8.25 cm from one end of a 73.8-cm x 1.12-m aluminum sheet 1.60 mm thick. This type of sheet was representative of the pressure wall of the modular space station recently studied at MDAC. High-speed impacts from lead shot fired from a pellet gun or low-speed impacts from various-sized spheres dropped one at a time could be employed to obtain acoustical signatures. For these tests, only low-speed impacts from 1.9-cm-dia aluminum spheres dropped one at a time on a sheet were used to obtain acoustical signatures. All drop impacts were made along a line 29.2 cm from one edge of the aluminum sheet and dropped a distance of 30.0 cm. A second portable MDAL shock detector was placed on the aluminum sheet some centimeters from the location of the sphere impacts on the sheet. This shock detector was used to determine the time each impact occurred. For most drop tests, a different transducer gage material was installed in each of the impact gages for each impact on the sheet. This allowed simultaneous testing of as many as four different gage elements and the shock detector. Impact gage outputs and the shock detector output were connected to three dual-beam oscilloscope inputs, using low-noise cables. The output of the time-zero shock detector was also connected to one of the oscilloscope inputs and was used only as a trigger to start the sweeps of the oscilloscopes. Approximately 80-μs time delay occurred between the time when the sphere impacted on the sheet and the time when the acoustical signal reached the stationary impact gages and shock detector. The oscilloscope sensitivity ranged from 0.1 mV/cm to 2V/cm. Signal levels as low as 0.1 mV could easily be observed.

4.4.1 Impact Gage Sensing Elements Tested

The following list shows all the transducer sensing element materials which were installed in the prototype impact gage and then tested.

A. Crystals
   1. Ceramic PZT-5A
   2. Quartz

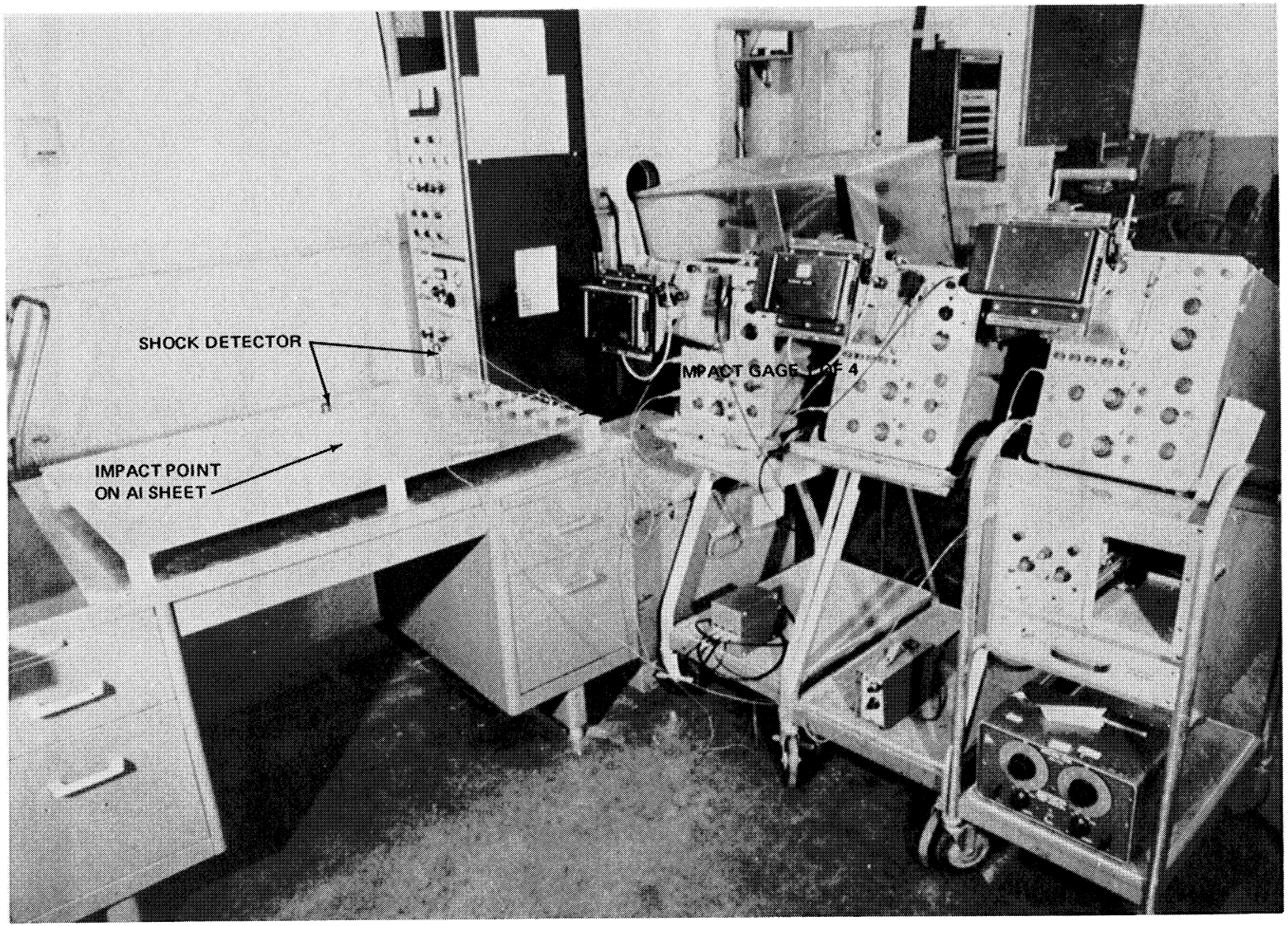

Figure 4-1. Impact Gage Test Setup —— Drop Tests

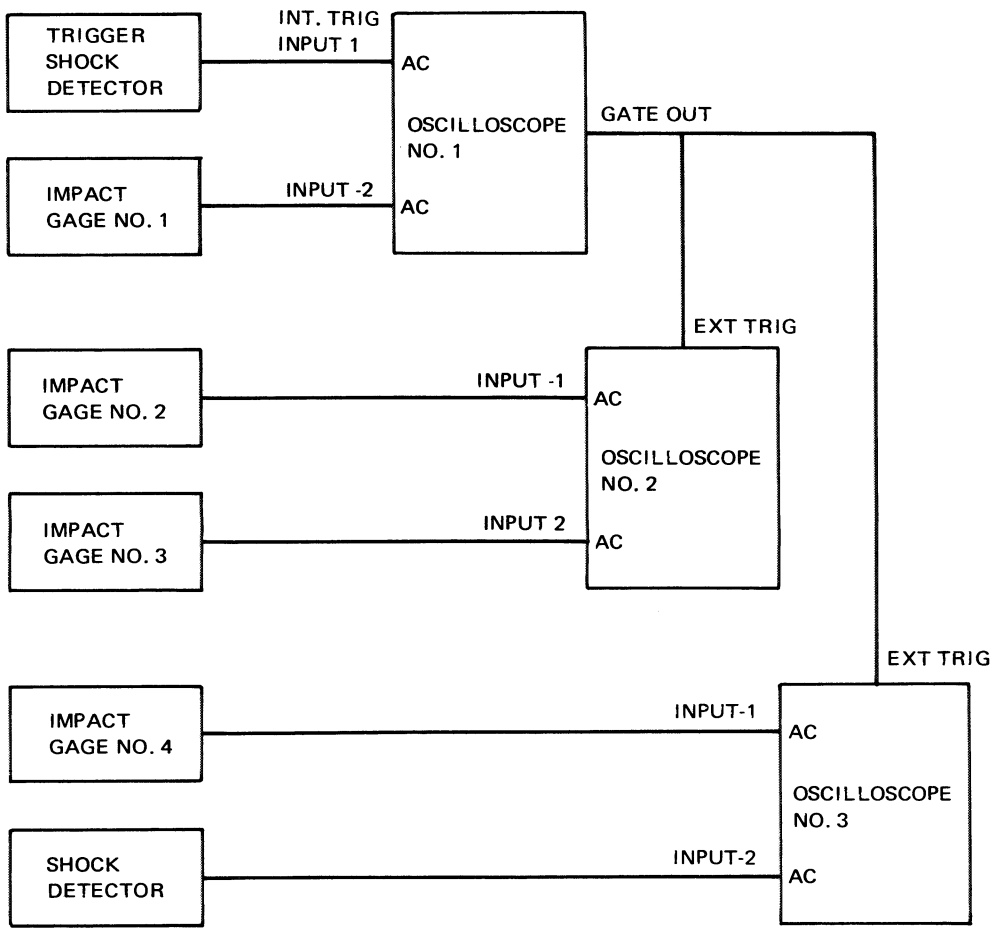

Figure 4-2. Impact Gage Instrumentation Setup for Drop Tests

B. Plastics

1. Electret – electron-beam-bombarded 0.0254-mm (1-mil) FEP foils, aluminum-coated on one side (this was an experimental sample obtained from Bell Laboratories)
2. Electret – Corona-charged 0.0254-mm (1-mil) strip of aluminum-coated TFE Teflon (this was an experimental sample obtained from Northern Electric Research Labs, Ottawa, Canada)
3. Kapton
4. Mylar
5. Mylar pressure-sensitive tape (DPM 895)
6. Polyethylene
7. Polyvinylfluoride (PVF)
8. Polyvinylchloride (PVC)
9. Saran Wrap
10. Scotch Tape (clear)
11. Shrink tape (PVC)
12. Teflon
13. Vinyl plastic tape (DPM 868)

C. Others

1. Mica
2. Paper
3. Scotchply

The dimensions and pertinent electrical characteristics of the materials tested are given in Table 4-1.

Figure 4-3 shows the sensing element by itself. Note that the open-circuit output for an acoustical input is $E_{SE\ (OC)}$. The next two circuits are the equivalent circuits for the sensing element by itself. The charge output of the sensing element (Q_{SE}) is equal to the product of the $E_{SE\ (OC)}$ and the capacitance of the sensing element (C_{SE}).

Table 4-1

PERTINENT GAGE AND SENSING ELEMENT CHARACTERISTICS

	Diameter (cm)	Thickness (mm)	Cap. Sensing Element (pF) - calc.	Cap. Sensing Element (pF) - meas.	Total Gage Cap. (pF) - meas.	Dielectric Constant
Air	0.635	0.025	11.02	–		1.0
Celulose Acetate[1]	0.635	0.40	3.78	≈10	45	3.5 to 7.5
FEP	0.635	0.025	23.1	≈21	62	2.1
Kapton	0.635	0.10	10.1	≈6	42	3.7
Mica	0.635	0.24	12.8	–		7
Paper	0.635	0.20	7.7	–		3.5
Mylar	0.635	0.20	6.5	≈5	40	3.0
PVC[1]	0.635	0.32	7.16	≈3.5	37	2.3 to 9.0
PVF	0.635	0.05	41.25	–	52	7.5
PVF	0.635	0.025	82.5	≈6	61	7.5
Polyethylene	0.635	0.037	16.5	–	54	2.26
Polyethylene (sheet)[2]	0.635	0.037		2	2	2.26
Polyethylene (sandwich)[2]	–	0.075	7,000	8,000	8,000	2.26
PZT-5A	0.318	0.063	165	≈170	200	1,500
Quartz	0.238	0.75	0.21	≈3.5	37	4.5
Teflon	0.635	0.029	0.21	≈5.5	39	2.1
TFE	0.635	0.025	23.1	≈21	63	2.1
Cage (air insulator)	0.845	0.025	19.4	–		1.0
Gage Curved Surface	MICA[3]	0.125	≈33.5	–		≈3.14
	AIR	0.23	33.5			
Gage Flat Surface	Excludes Sensing Material[4]	0.025	≈8.38			

NOTE: Cable capacitance approximately 150 pF and oscilloscope capacitance 15 pF.

1. Dielectric constant is a function of material processing.
2. 30.2 cm long by 30.2 cm wide.
3. 0.127 mm MICA, 0.203 mm AIR-thickness; curved surface area - 4.3 cm^2.
4. Excluded area for sensing element - 0.025 mm thick, 0.635 cm dia.

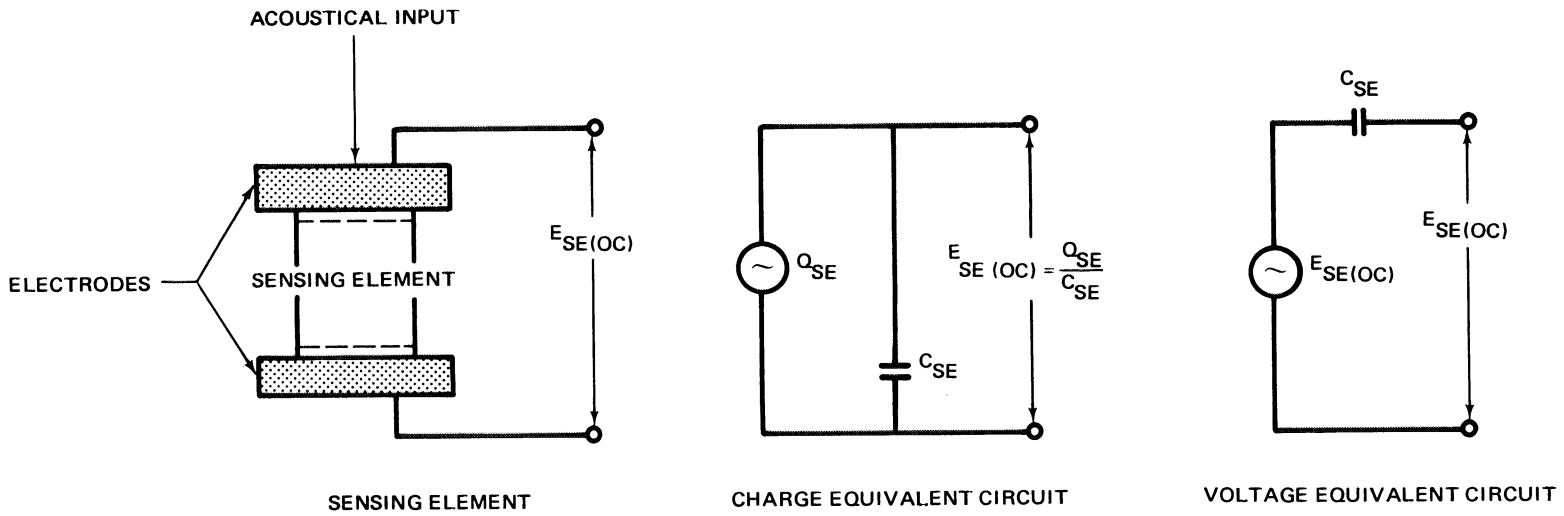

SENSING ELEMENT

CHARGE EQUIVALENT CIRCUIT

VOLTAGE EQUIVALENT CIRCUIT

$Q_{SE} = KF$ (1)

$Q_{SE} = (C_{SE})\ E_{SE\ (OC)}$ (2)

WHERE

K = PIEZOELECTRIC CONSTANT

F = ACOUSTICAL INPUT

Q_{SE} = CHARGE OUTPUT OF SENSING ELEMENT

$E_{SE(OC)}$ = VOLTAGE OUTPUT OF SENSING ELEMENT FOR OPEN CIRCUIT CONDITION

C_{SE} = CAPACITANCE OF SENSING ELEMENT

Figure 4-3. Piezoelectric Sensing Element and Equivalent Circuits

4.4.2 Experimental Results

Data from the acoustical tests are tabulated in Table 4-2. Initial experimental data showed that spray cleaning some of the plastic materials with Freon prior to installation in the impact gages produced a lower output and frequency response than for the same materials when they were not so cleaned. Mylar and Teflon were significantly affected by the Freon. The Freon may have dissolved a portion of the test material, or residue from the Freon on the gage sensing material could have resulted in attenuation of the acoustical signal.

Before discussing additional experimental results, the equivalent electrical circuits and corresponding equations for the sensing element alone and for the sensing element installed in the impact gage with the electrical setup will be described.

Figure 4-4 shows the simplified equivalent circuit of a sensing element installed in the impact gage with the electrical setup. This was basically the setup used for most of the tests. From the equations with the figure, it can be seen that the voltage recorded at the oscilloscope input (E_R) is not the true output of the gage sensing element but a voltage which was attenuated by the capacitance external to the sensing element (C_H, C_C, C_O). If these capacitances were all zero, then the voltage output recorded by the oscilloscope would be equal to the open-circuit output of the sensing element.

Because $E_{SE(OC)}$ is inversely proportional to the capacitance of the sensing element, an accurate measurement of C_{SE} is required for an accurate result for $E_{SE(OC)}$. A tabulation of the capacitance of the impact gages and sensing elements is given in Table 4-1. The measured capacitance of the cabling and the oscilloscope input agree with manufacturer specifications within 5 percent. The measured capacitance of the sensing element material was obtained by measuring the capacitance of the gage with the sensing element installed and then subtracting the computed capacitance of the gage with the area of the sensing element material excluded. Many measurements did not agree within 10 percent of the calculated value of the capacitance of the sensing element. This disagreement was probably due to the 10-percent uncertainty of the computed value of the capacitance of the impact gage, excluding

Table 4-2

EXPERIMENTAL IMPACT GAGE DATA

Impact No.	Gage Loc	Gage Sensing Element: Material	Output: Peak to Peak (A) (mV)	Output: Peak to Peak (B) (mV)	Frequency kHz (A)	Frequency kHz (B)
12[1]		Sandwich (PVC)[2]	3	15	-	-
13	3	Electret - FEP	2.8	12	100	50
13	2	Quartz	3.5	18	100	50
14	1	Cellulose Acetate	0.08	0.4	100	50
14	2	Electret - TFE	2	14	100	50
14	3	Electret - FEP	1	6	100	50
14	4	PZT-5A	200	600	100	50
15	1	Cellulose Acetate	0.08	0.6	100	50
15	2	Electret - TFE	2	10	100	50
15	3	FEP	1.5	2	100	50
15	4	PZT-5A	200	800	100	50
16	1	Mylar (0.38 mm)	0.1	1.8	100	50
16	2	Electret - TFE	2	6	100	50
16	3	Mylar (0.38 mm)	0.08	0.4	100	50
16	4	PZT-5A	400	700	100	50
17	1	Mylar (0.38 mm)	0.08	0.8	100	50
17	2	Electret - TFE	2	8	100	50
17	3	Teflon	0.5	1.5	100	50
17	4	PZT-5A	200	600	100	50
18	1	Mylar (0.38 mm)[6]	<0.02	0.8	100	50
18	2	Electret - TFE	2	10	100	50
18	3	Teflon	0.1	1.5	100	50
18	4	PZT-5A	300	600	100	50
19	1	Mylar (0.127 mm)	<0.02	3	100	50
20	2	Polyethylene	0.8	6	100	50
20	3	PZT-5A	300	1,500	100	50
21	2	Shrink Tube - PVC	0.1	2	100	50
21	3	PZT-5A	300	1,200	100	50
22[2]	3	PZT-5A	2	4	100	50
23	2	Cellulose Acetate	0.15	5	100	50
23	3	PZT-5A	300	1,500	100	50
24	2	Cellulose Acetate[6]	0.12	0.6	100	50
24	3	PZT-5A	400	1,200	100	50
25	2	Teflon	0.3	1.8	100	50
26	2	Cellulose Acetate[6]	0.1	0.8	100	50
27	2	Kapton[6]	0.06	1.0	100	50
28	2	PZT-5A	300	1,000	100	50
29	2	Mylar (0.38 mm)	0.03	0.3	100	50
30	2	PVC[6]	<0.02	0.1	100	50
31	2	Electret - TFE	3	10	100	50

Table 4-2

EXPERIMENTAL IMPACT GAGE DATA (Continued)

Impact No.	Gage Loc	Gage Sensing Element Material	Output Peak to Peak (A) (mV)	Output Peak to Peak (B) (mV)	Frequency kHz (A)	Frequency kHz (B)
32	2	Mylar (0.38)[6]	0.03	1		
33[1]	-	Sandwich (Polyethylene)	150	150	5	-
33[1]	-	MDAL Shock[5] Detector	3,000	3,000	5, 20	
34[3]	-	Polyethylene Sheet (30.4 cm x 30.4 cm)	58		0.33	
35[4]	-	Polyethylene Sheet (30.4 cm x 30.4 cm)	65			
37	2	PVF (0.0508 mm)	0.05	0.4	100	50
38	2	PVF (0.0254 mm)	0.06	0.5		
39	2	PVC	0.02	0.3		
39	3	PZT-5A	250	1,000		
40	2	Kapton	0.1	0.25		
40	3	PZT-5A	250	1,000		
41	2	Cellulose Acetate	0.12	0.6		
41	3	PZT-5A	250	1,000		

NOTE:

(A) Transducer output from 0 to 80 μs after acoustical signal reaches transducer.

(B) Transducer output from 80 to 500 μs after acoustical signal reaches transducer.

1 1.91 cm diameter aluminum sphere dropped a distance of 30 cm and impacting on the center of the sandwich.

2 0.1 μF capacitor put in parallel with the gage.

3 1.91 cm diameter aluminum sphere dropped a distance of 30 cm and impacting on the center of the polyethylene sheet.

4 1.91 cm diameter aluminum sphere dropped a distance of 30 cm and impacting on the center edge of the polyethylene sheet.

5 MDAL shock detector was installed on the sandwich front face.

6 Sensing element cleaning material was Freon.

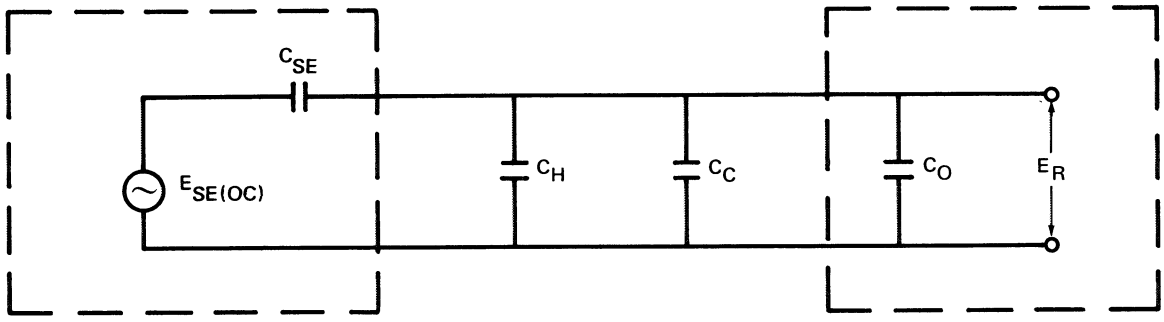

$$E_R = \frac{C_{SE}\, E_{SE(OC)}}{C_{SE} + C_H + C_C + C_O} \qquad (3)$$

$$E_{SE(OC)} = \frac{E_R\,(C_{SE} + C_H + C_C + C_O)}{C_{SE}} \qquad (4)$$

$$Q_{SE} = (C_{SE} + C_H + C_C + C_O)\,(E_R) = C_{SE(OC)}\,(E_{SE(OC)}) \qquad (5)$$

WHERE

E_R = VOLTAGE OUTPUT RECORDED BY OSCILLOSCOPE

C_H = CAPACITANCE OF IMPACT GAGE WITHOUT SENSING ELEMENT ($\approx$ 35 pF)

C_C = CAPACITANCE OF CABLE ($\approx$ 150 pF)

C_O = CAPACITANCE OF THE OSCILLOSCOPE INPUT ($\approx$ 15 pF)

Figure 4-4. Simplified Equivalent Circuit of Sensing Element in Impact Gage

the area of the sensing element and the 1-pF resolution of the capacitance bridge. Because of these uncertainties, the data in Table 4-3 are based upon the computed capacitance of the impact gage sensing element.

The results of the most promising of the tested sensing element materials are tabulated in Table 4-3. Typical oscilloscope traces are shown in Figure 4-5. Neither the output voltage E_R recorded at the oscilloscope nor the open-circuit output voltage $E_{SE(OC)}$ should be used for comparison of the true relative outputs of the sensing element materials. The output voltage E_R for the impact gage using PZT-5A as the sensing element was more than a hundred times higher than it was for the other sensing elements. This result is misleading because E_R is not corrected for equivalent sensing element dimensions and for the capacitive loading effects. Since the capacitance of PZT-5A is very high compared to the other sensing elements, its output is attenuated much less by external capacitance. Equation 4 was used to compute $E_{SE(OC)}$ for the sensing element materials. Although Equation 4 corrects for capacitive loading of the sensing element outputs, it does not correct for equivalent sensing element dimensions.

Comparison of the piezoelectric activity of the sensing elements can be made by using the remaining characteristics* (g_{33}, $E_{SE(OCC)}$, Q) in Table 4-3. The experimental piezoelectric g_{33} constant is the most useful of these three characteristics. This has been defined as the open-circuit electric field developed for a given applied stress. (Equation 6)

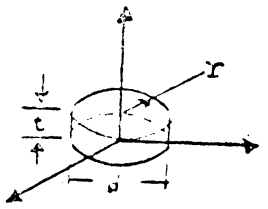

$$g_{33} = \frac{\text{Electric Field}}{\text{Stress}} = \frac{\frac{E_{SE(OC)}}{t}}{\frac{F}{\pi r^2}} \quad (6)$$

*The PZT-5A sensing element dimensions and output were used as references.

Table 4-3

SENSING-ELEMENT CHARACTERISTICS

Sensing Material	Element Cap. - C_{SE}	Output[1] Recorded E_r	$E_{SE(CC)}$ [2]	$E_{SE(OCC)}$ [3]	g_{33} [4]	$C_{SE(OCC)}$ [5]	Q [6] (coulombs)
	(pf)	(mv P. P.)	(mv P. P.)	mv/in. per force/in.	V/m per N/m^2	(pf)	
PZT-5A	165	500	1,106	1,106	24.4×10^{-3}	165	182×10^{-12}
Quartz	0.21	3.5	3,300	1,600	35.4×10^{-3}	0.44	0.68×10^{-12}
Electret (TFE)	23	3	30	3,000	66×10^{-3}	0.23	0.63×10^{-12}
Electret (FEP)	23	2.8	28	2,800	62×10^{-3}	0.23	0.58×10^{-12}
Mylar Tape	5.9	2	59	1,060	23.5×10^{-3}	0.33	0.41×10^{-12}
Polyethylene	16.5	0.8	10.5	700	15.4×10^{-3}	0.25	0.178×10^{-12}
Teflon	0.21	0.5	450	410	9×10^{-3}	0.21	0.097×10^{-12}
Mylar (15 mil)	2.14	0.4	9.5	63	1.36×10^{-3}	0.3	0.08×10^{-12}
Mylar (5 mil)	6.5	< 0.02	< 6.2	<125	$<2.75 \times 10^{-3}$	0.32	$<0.04 \times 10^{-12}$
PVC	7.78	0.2	5.28	66	1.45×10^{-3}	0.63	0.04×10^{-12}
PVF	41.5	0.05	0.24	12	0.26×10^{-3}	0.83	0.01×10^{-12}

NOTE: (1) Maximum output of gage recorded by oscilloscope.
(2) Maximum open-circuit output of sensing element.
(3) Maximum open-circuit output of sensing element corrected for a surface area and thickness equivalent to reference sensing element PZT-5A.
(4) Theoretical piezoelectric coefficient (g_{33} = Electric Field Thickness/Stress) referenced to equivalent dimensions and the open-circuit output of PZT-5A. $g_{33} = 24.4 \times 10^{-3}$ for PZT-5A and $\approx 50 \times 10^{-3}$ for quartz.
(5) Capacitance of sensing element corrected for a surface area and a thickness equivalent to reference element PZT-5A.
(6) Maximum charge output (coulombs) of sensing element computed from $Q = (E_r)(C_{SE} + C_H + C_C + C_O)$. Theoretical open-circuit charge output based upon the charge output of the sensing element PZT-5A as a reference. $Q_{THEO} = 182 \times 10^{-12}$ for PZT-5A and 1.1×10^{-12} for quartz.

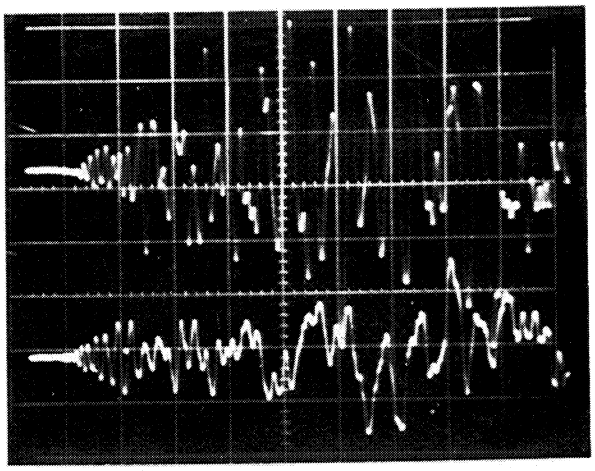

RECORD RATE 100 μs/cm

UPPER TRACE - IMPACT GAGE (POLYETHYLENE) - 1 mV/cm

LOWER TRACE - IMPACT GAGE (PZT-5A) - 500 mV/cm

(a) IMPACT TEST NO. 20

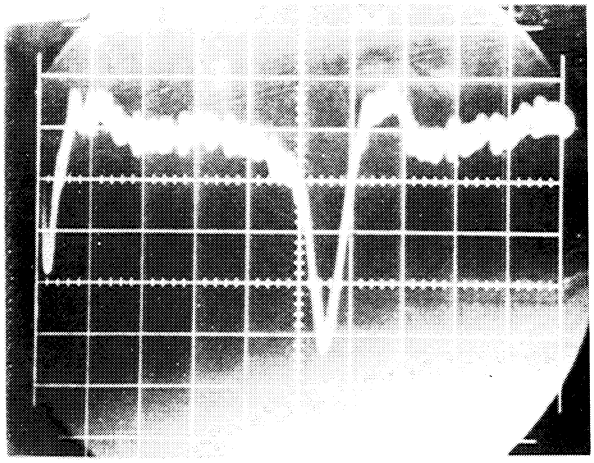

RECORD RATE 5 ms/cm
POLYETHYLENE SHEET - 20 mV/cm

(b) IMPACT TEST NO. 34

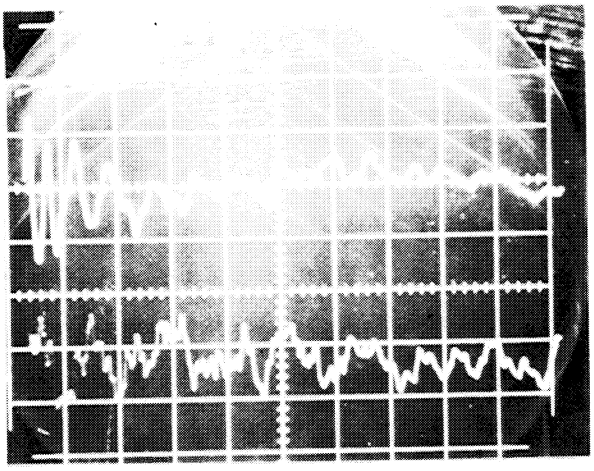

RECORD RATE 0.5 ms/cm
UPPER TRACE - POLYETHYLENE SANDWICH 50 mV/cm
LOWER TRACE - SHOCK DETECTOR 2,000 mV/cm

(c) IMPACT TEST NO. 33

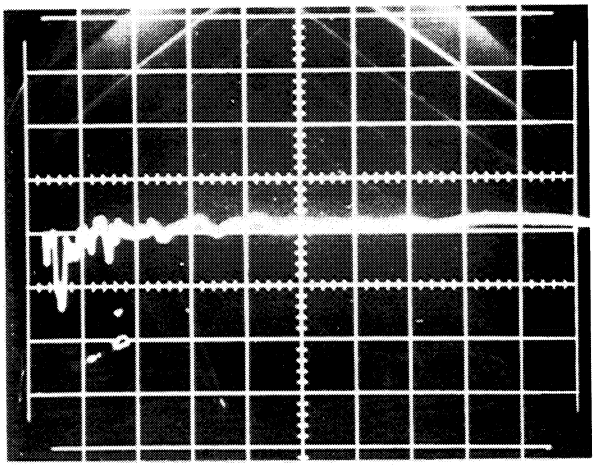

RECORD RATE 1 ms/cm
PVC SANDWICH - 10 mV/cm

(d) IMPACT TEST NO. 12

Figure 4-5. Oscilloscope Records of Acoustical Transducers -- Drop Tests

where

$E_{SE(OC)}$ = open circuit output voltage of sensing element

t = thickness of sensing element

F = force

r = radius of sensing element

3 = first subscript denotes direction of electric field

3 = second subscript denotes direction of strain.

Note that for unity dimensions and force, the piezoelectric g_{33} constant is equal to the open-circuit output $E_{SE(OC)}$.

The experimental charge output Q of the sensing element was obtained using Equation 5.

It was encouraging that six of the sensing element materials produced high piezoelectric activity. Three of the sensing element materials (quartz, electret TFE, electret FEP) had a higher piezoelectric g_{33} constant than did PZT-5A. The experimental value of the g_{33} constant and charge output for the quartz sensing element was reasonably close to the theoretical value.

Experimental results for the piezoelectric g_{33} constant for polyvinylchloride and polyvinylfluoride were in partial agreement with those of Cohen (Reference 18). The result that PVC had higher piezoelectric activity than PVF was in agreement with Cohen. Cohen's values of the piezoelectric g_{33} constant were at least an order of magnitude higher than the values obtained in these tests. However, comparisons between the results presented in Table 4-3 and Cohen's results are difficult to make for three reasons. First, the piezoelectric activity results given in Table 4-3 are based upon outputs at high frequencies (typically greater than 100 kHz) while Cohen's results were based upon outputs at low frequencies (~20 Hz). If the voltage outputs of the sensing elements for lower frequencies (B data in Table 4-2) were tabulated for piezoelectric activity, there would be closer agreement with Cohen's results. Secondly, the experimental setups used to measure the piezoelectric activity of these materials were quite different. Finally, the piezoelectric properties of the untreated samples used by Cohen may have been much different than the untreated materials used for this report.

4.4.3 Direct Impact Gages

Since a number of plastic materials produced substantial piezoelectric activity, two additional types of impact gages were built. Photographs of these gages are shown in Figures 4-6 and 4-7. One of these impact gages, a "polyethylene sheet" gage, consisted of a 30-cm-square sheet of 0.04-mm-thick polyethylene mounted on a wooden frame with two electrical leads attached. Data for drop tests on this gage are given in Table 4-2, Figure 4-5(b) shows the typical output of this gage. The two output signals shown in the figure correspond to the sphere bouncing up off the sheet after the first impact and then impacting on the sheet a second time. The other gage, a polyethylene "sandwich" impact gage consisted of a 30-cm-square sheet of 0.075-mm-thick polytehtylene placed between two 30-cm-square sheets of 2.5-mm-thick aluminum with leads attached to the aluminum sheets. Data for drop tests on this gage are given in Table 4-2.

4.5 PROTOTYPE IMPACT GAGE–BALLISTIC RANGE TEST SERIES 1

In addition to the drop tests of the prototype impact gages, ballistic range tests were carried out at the MDAC Aerophysics Laboratory using light-gas guns. The ballistic range tests were made in five separate series to study five main areas of interest. The first series of impact tests were carried out on a model of the MDAC modular space station (Figure 4-8) with the pressure wall uniaxially stressed to 1.37×10^8 N/m^2 (20,000 psi) in a special jig. The stress was applied to permit observation of the effect of impact under realistic design conditions. Both PZT-5A and polymer electrets were used as sensing elements for the prototype impact gage mounted on the pressure wall. An experimental plastic sandwich gage was installed behind the pressure wall to detect the arrival of debris when the pressure wall was penetrated. In addition to the standard ballistic-range technique of using oscilloscopes to record data during the shot, a midband tape recorder was also used for the following reasons:

A. To record possible acoustical emissions from the target material which could occur after the direct oscilloscope record rate was completed.

B. To provide backup for data recorded on oscilloscopes during the run.

C. To provide playback capability of the data from the shot for possible filtering, amplification, and improved resolution.

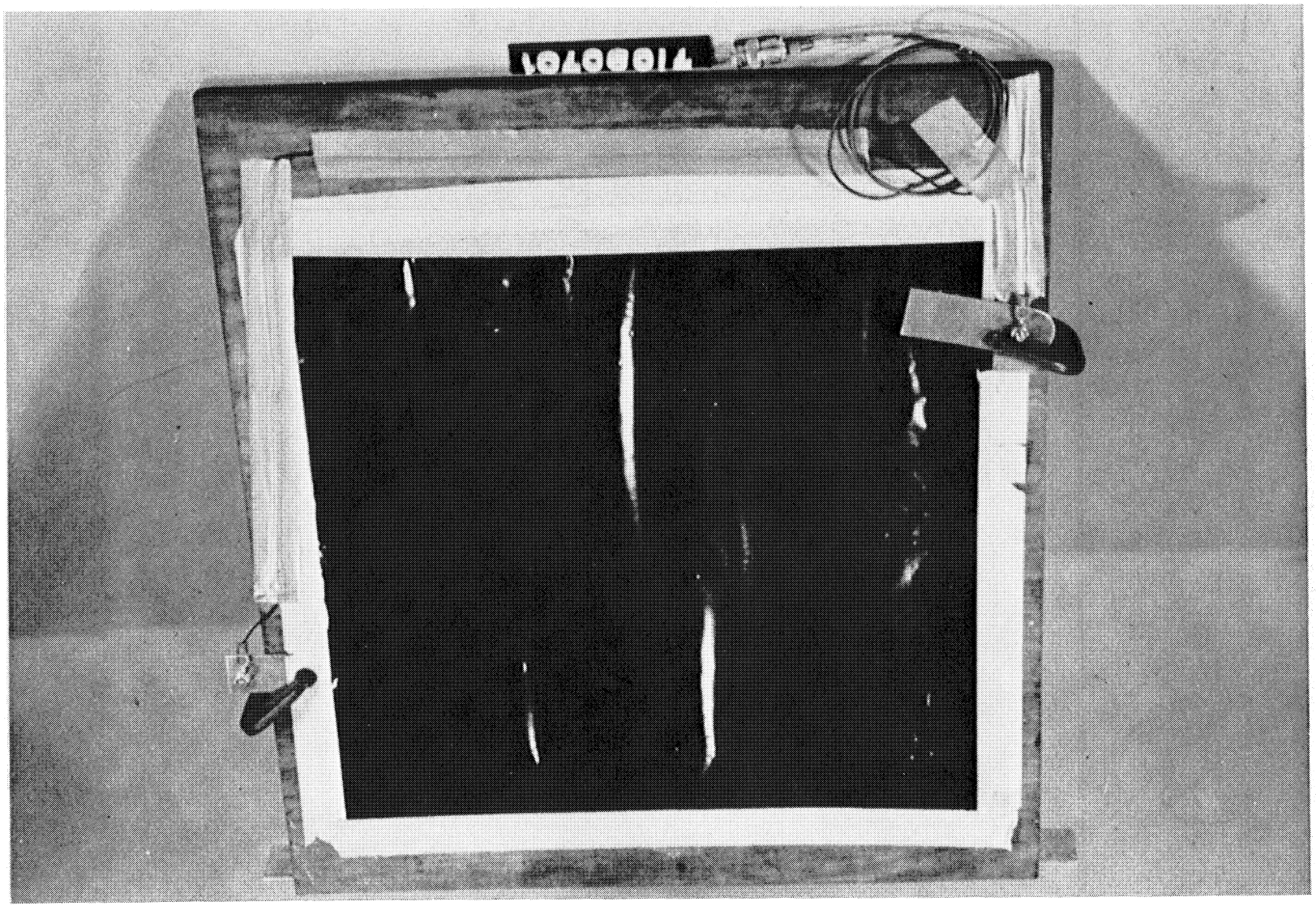

Figure 4-6. Polyethylene Sheet Impact Gage

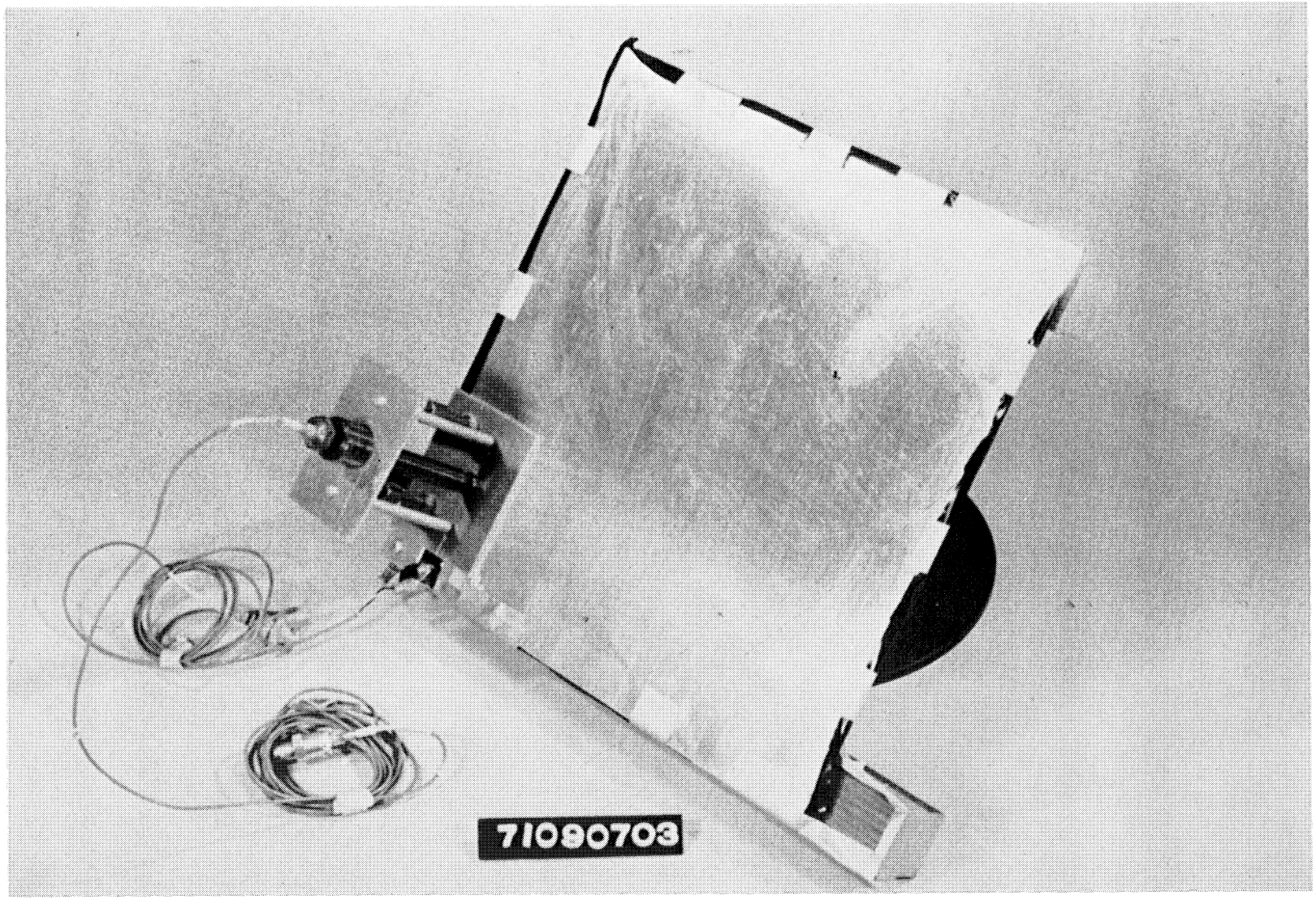

Figure 4-7. Polyethylene Sandwich Impact Gage

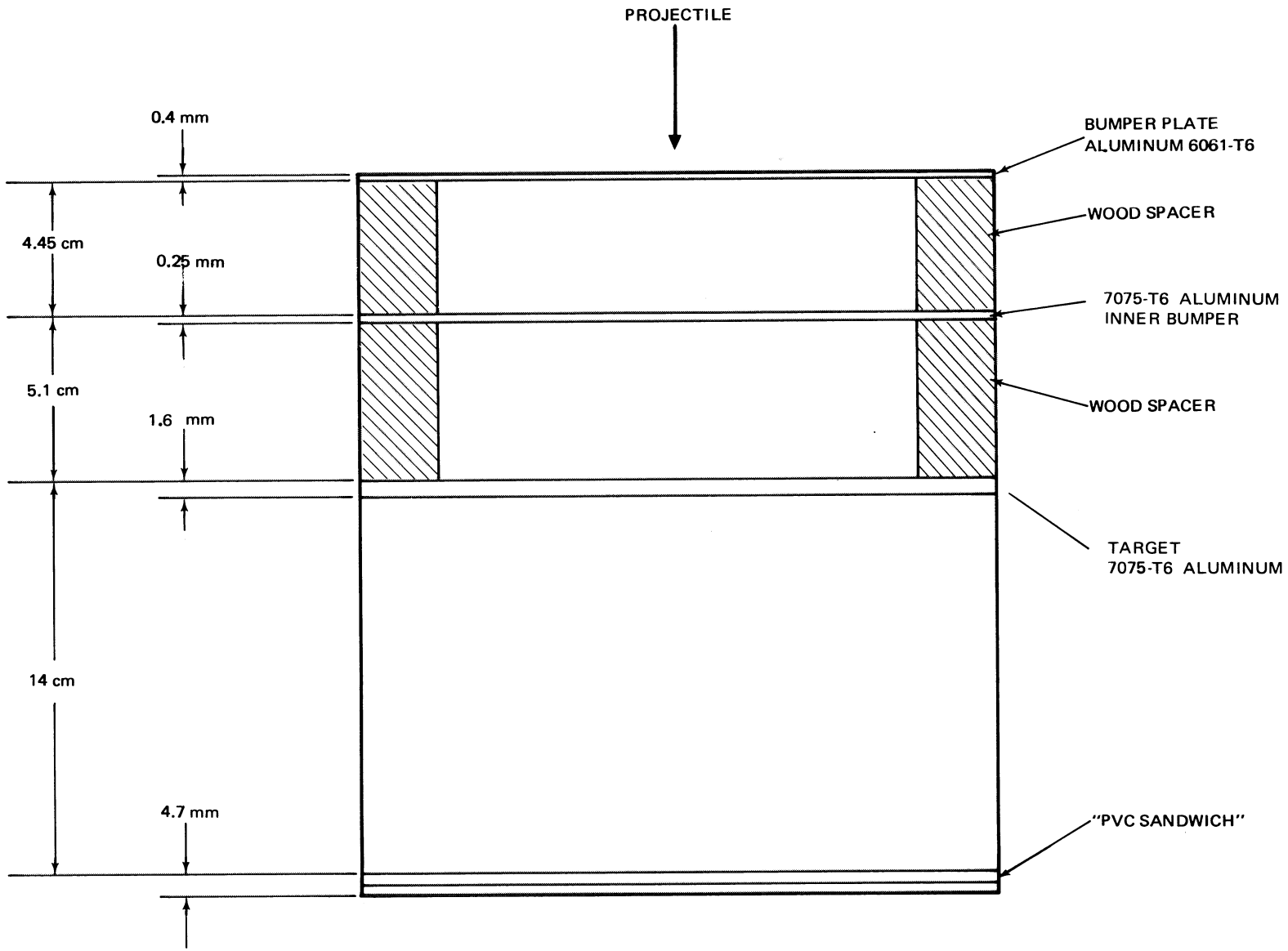

Figure 4-8. Test Setup Run B54-1 - Space Station Model Structure

Two tests were carried out in Series 1. The first (Impact Shot B54-1) at the relatively low projectile velocity of 1.52 km/s was completely successful. The point of impact on the pressure wall was successfully determined by shock-wave time-of-arrival triangulation techniques using three of the prototype gages. The second test (B54-2) was only partially successful in that the projectile broke up during launch. However, the impact of several hypervelocity fragments on the target structure provided valuable information on the performance of the prototype impact gages.

4.5.1 Series 1 Test Details

Small sections of a simulated space station wall with a meteorite bumper and a unique "sandwich" impact gage were installed in a range tank with a pressure maintained at 50 mm Hg and were impacted by a projectile launched from the light-gas gun. Figure 4-8 shows the test setup. The target plate was bolted to a hanging steel wall and stressed to 1.37×10^8 N/m^2. Three of the prototype impact gages, two gages using PZT-5A as the sensing element and one gage used an electret TFE, were mounted on a target sheet of 7075 T6 aluminum, 1.60 mm thick. A bumper plate was installed in front of the target plate. An "in-house" MDAL shock detector was installed on the bumper plate. The "sandwich" impact gage, consisting of a plastic piezoelectric material (polyvinylchloride, 25.4 cm x 25.4 cm x 0.075 mm) sandwiched between two aluminum sheets (25.4 cm x 25.4 cm x 0.234 mm), was installed behind the target panel.

The outputs of the three prototype impact gages, the "sandwich" impact gage, and the MDAL shock detector were recorded on oscilloscopes and a midband tape recorder. Figure 4-9 shows a block diagram of the instrumentation setup. Since the signal from the MDAL shock detector occurs before the signal from the impact gages, the MDAL shock detector was used to trigger the oscilloscope. Photographs of the test setup taken after the shot are given in Figures 4-10 and 4-11. Figure 4-12 shows the oscilloscope records obtained from the oscilloscopes that were used to record the data during the run. A few of the oscilloscope records obtained by playing back tape-recorded impact gage data into an oscilloscope are given in Figure 4-13.

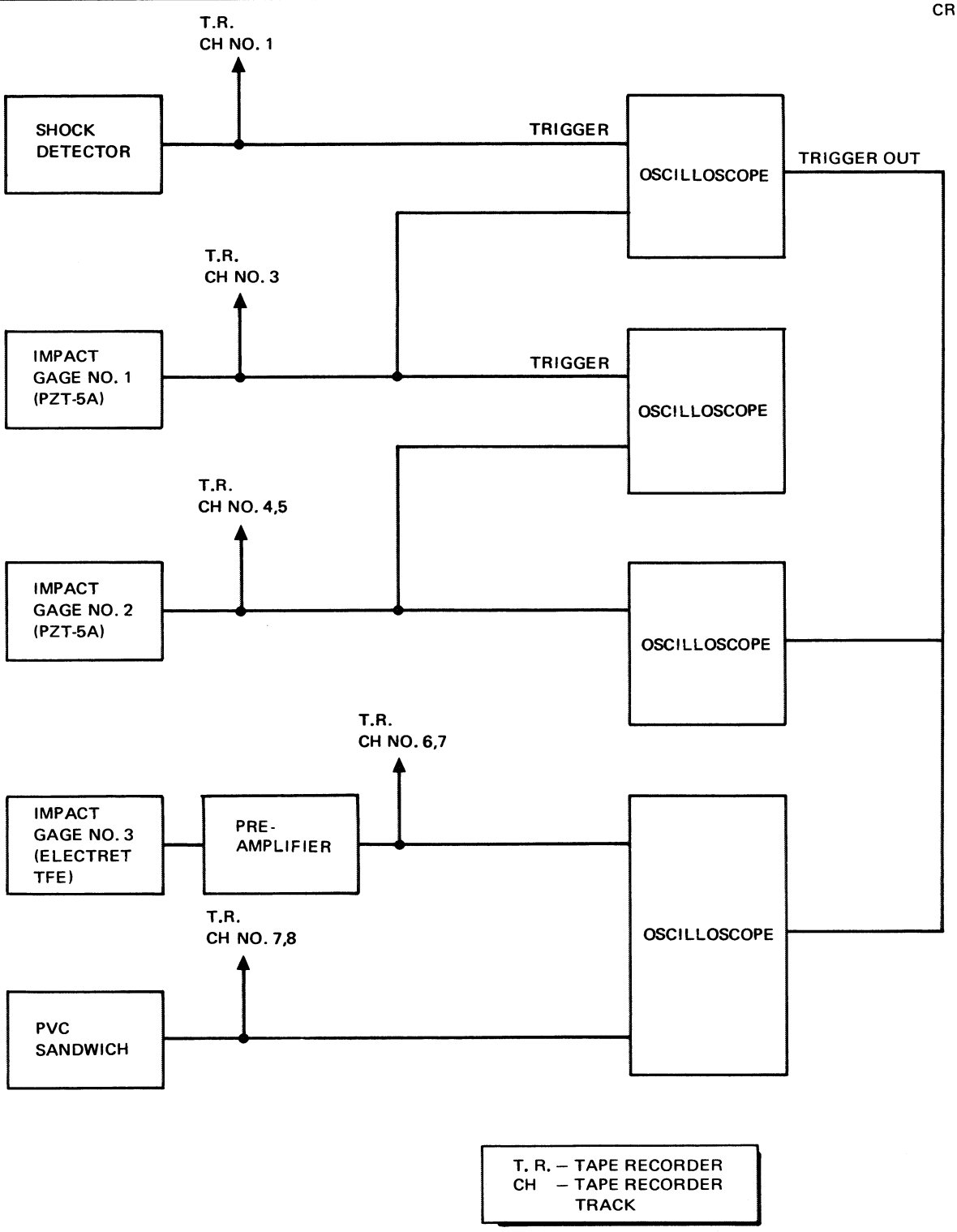

Figure 4-9. Instrumentation Setup Run B54-1 (Ballistic Range)

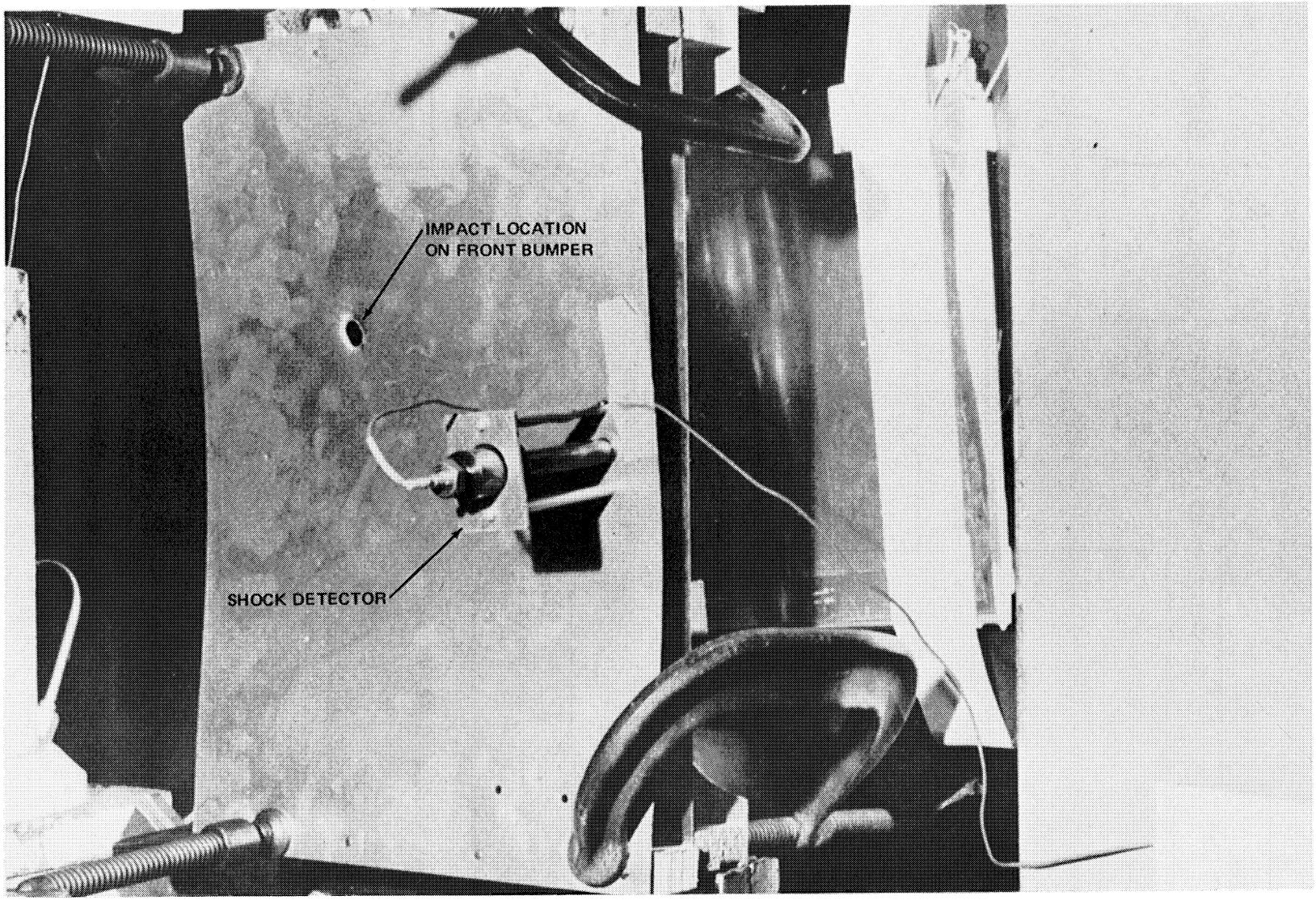

Figure 4-10. Front View of Test Setup Run B54-1(Ballistic Range)

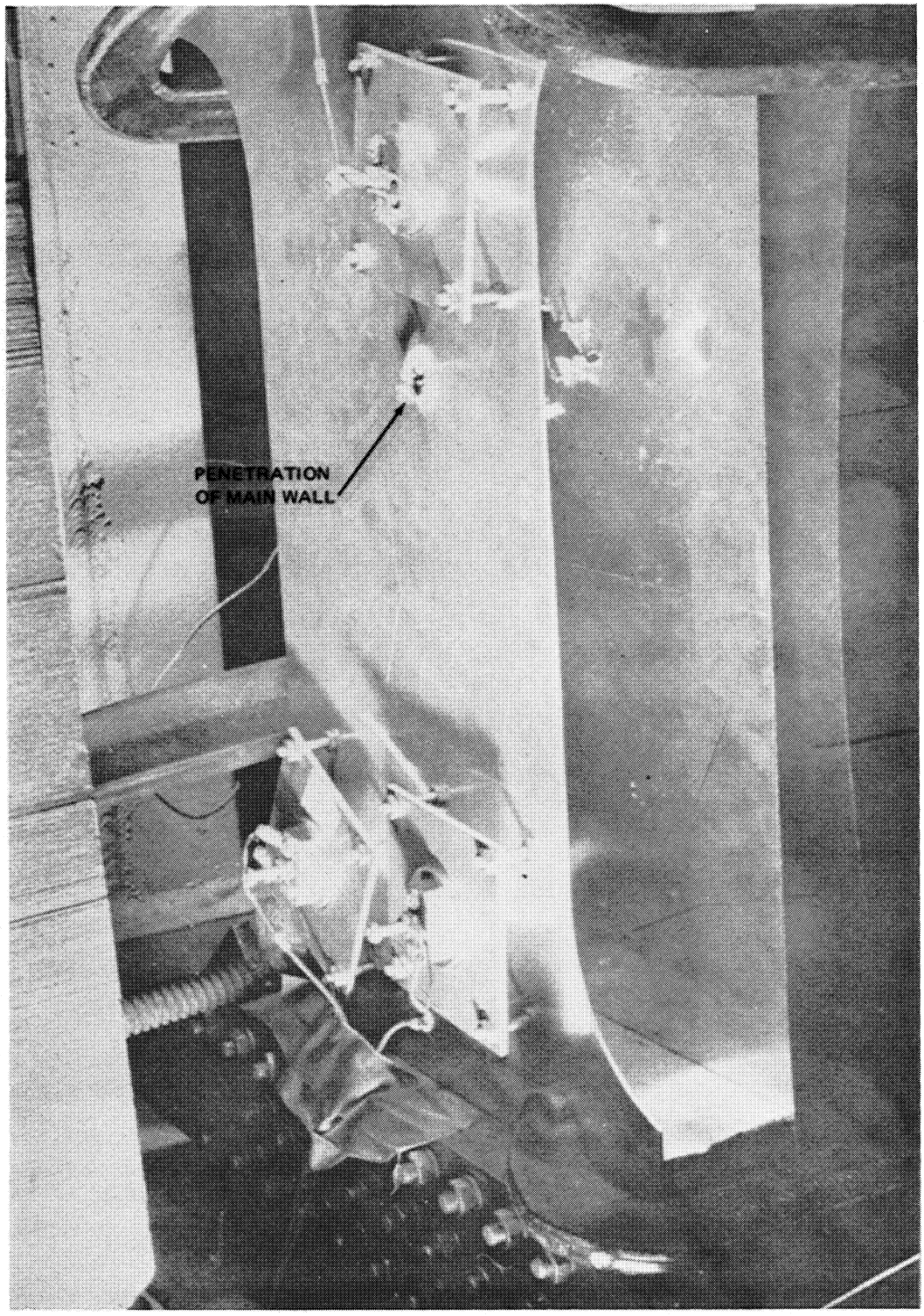

Figure 4-11. Rear View of Test Setup Run B54-1(Ballistic Range)

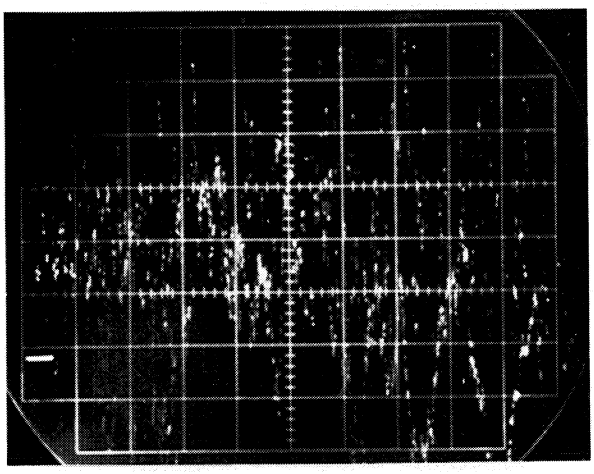

RECORD RATE 50 μs/cm
UPPER TRACE - SHOCK DETECTOR - 200 mV/cm -
LOWER TRACE - IMPACT GAGE NO. 1 (PZT-5A) - 2V/cm
OSCILLOSCOPE TRIGGER - SHOCK DETECTOR

(a)

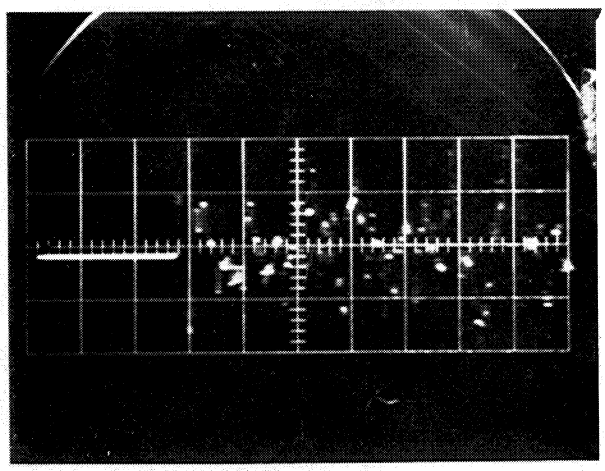

RECORD RATE 20 μs/cm
IMPACT GAGE NO. 2 (PZT-5A) - 2V/cm
OSCILLOSCOPE TRIGGER - SHOCK DETECTOR

(b)

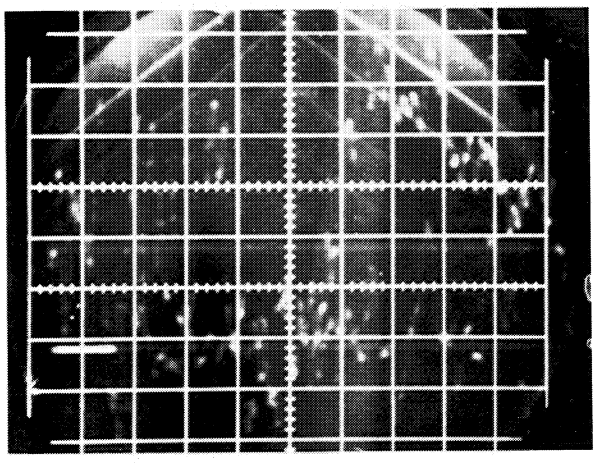

RECORD RATE 20 μs/cm
UPPER TRACE - IMPACT GAGE NO. 1 2V/cm
LOWER TRACE - IMPACT GAGE NO. 2 2V/cm
OSCILLOSCOPE TRIGGER - IMPACT GAGE NO. 1

(c)

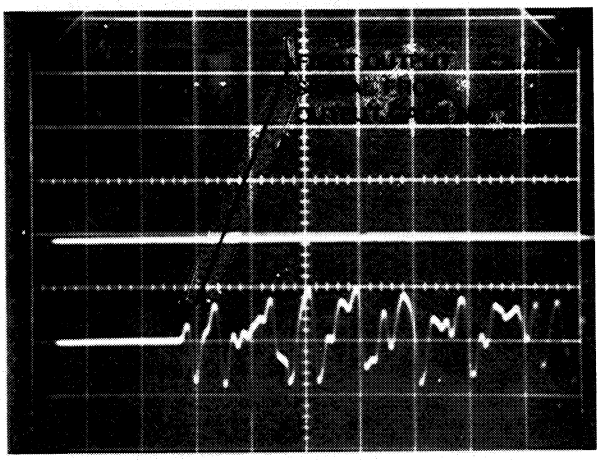

RECORD RATE 20 μs/cm
UPPER TRACE - PVC SANDWICH - 2 V/cm
LOWER TRACE - IMPACT GAGE NO. 3 TFE - 0.2 V/cm

(d)

Figure 4-12. Impact Gage Signals Recorded on Oscilloscope During Run B54-1(Ballistic Range)

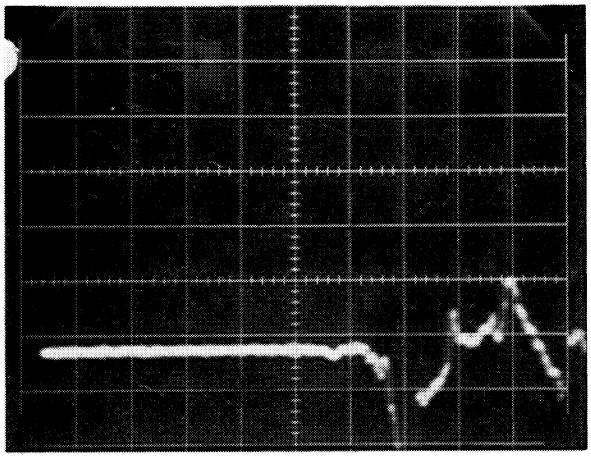

RECORD RATE 50 μs/cm
"PVC SANDWICH" - 0.2 V/cm
OSCILLOSCOPE TRIGGER - SHOCK DETECTOR

(a)

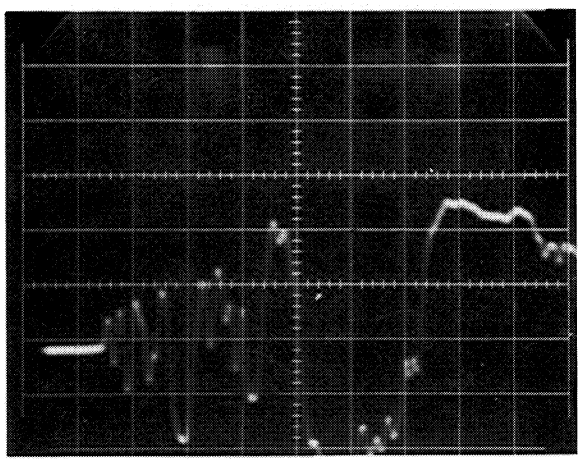

RECORD RATE 20 μs/cm
IMPACT GAGE NO. 1 (PZT-5A) - 1 V/cm
OSCILLOSCOPE TRIGGER - SHOCK DETECTOR

(b)

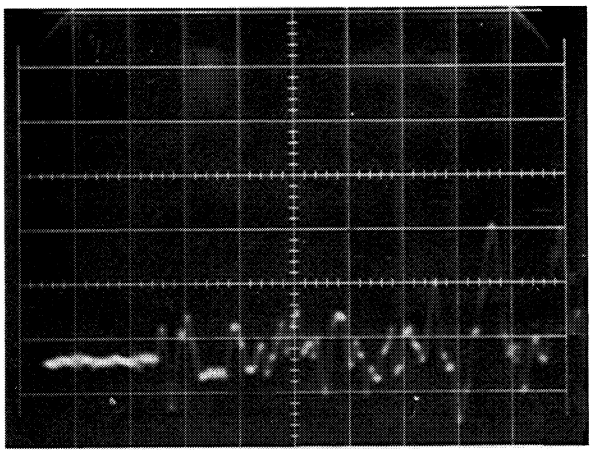

RECORD RATE 20 μs/cm
IMPACT GAGE NO. 2 PZT-5A - 0.1 V/cm
OSCILLOSCOPE TRIGGER - SHOCK DETECTOR

(c)

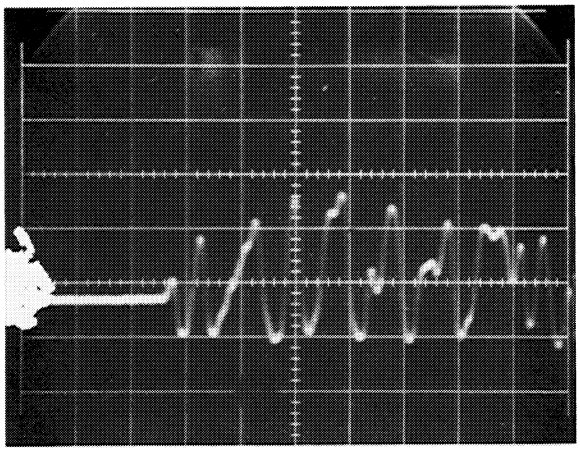

RECORD RATE 20μ/cm
IMPACT GAGE NO. 3 (TFE) - 0.1 V/cm
OSCILLOSCOPE TRIGGER - SHOCK DETECTOR

(d)

Figure 4-13. Oscilloscope Records of Impact Gage Signals Recorded on Tape Recorder During Run B54-1

Test conditions of Shot B54-1 are given in Table 4-4. The triangulation technique of obtaining the impact point from shock arrival times was used. Signal arrival times were based upon the first signal obtained from the three impact transducers. The impact gage with the signal appearing first (Impact Gage No. 1) was used as the reference transducer. The velocity in the target sheet was assumed to be primarily due to the longitudinal wave and was calculated from the difference in the arrival time of the first signal appearing at the No. 1 and 3 input transducers, using the impact location to establish path lengths. Arrival-time difference at the three transducer pairs was converted into path length differences using the velocity in the target sheet (see the Appendix for mathematical derivation of the method). Figure 4-14 shows the set of hyperbolas which were generated from the loci of these three constant distance differences and the impact point (zone)

Table 4-4

TEST CONDITIONS—SERIES 1

Run B54-1		
Velocity:		1.52 km/s
Projectile:		0.5368-gram polyethylene cylinder
Triangulation Data	Signal arrival time at transducer No. 1:	0 μs (Reference)
	Signal arrival time at transducer No. 2:	26 μs
	Signal arrival time at transducer No. 3:	22 μs
	Longitudinal velocity:	0.540 cm/μs
Run B54-2		
Velocity:		6.1 km/s
Projectile:		0.289-gram cylinder
Remarks:		Model broke up—target impacted by hypervelocity fragments.

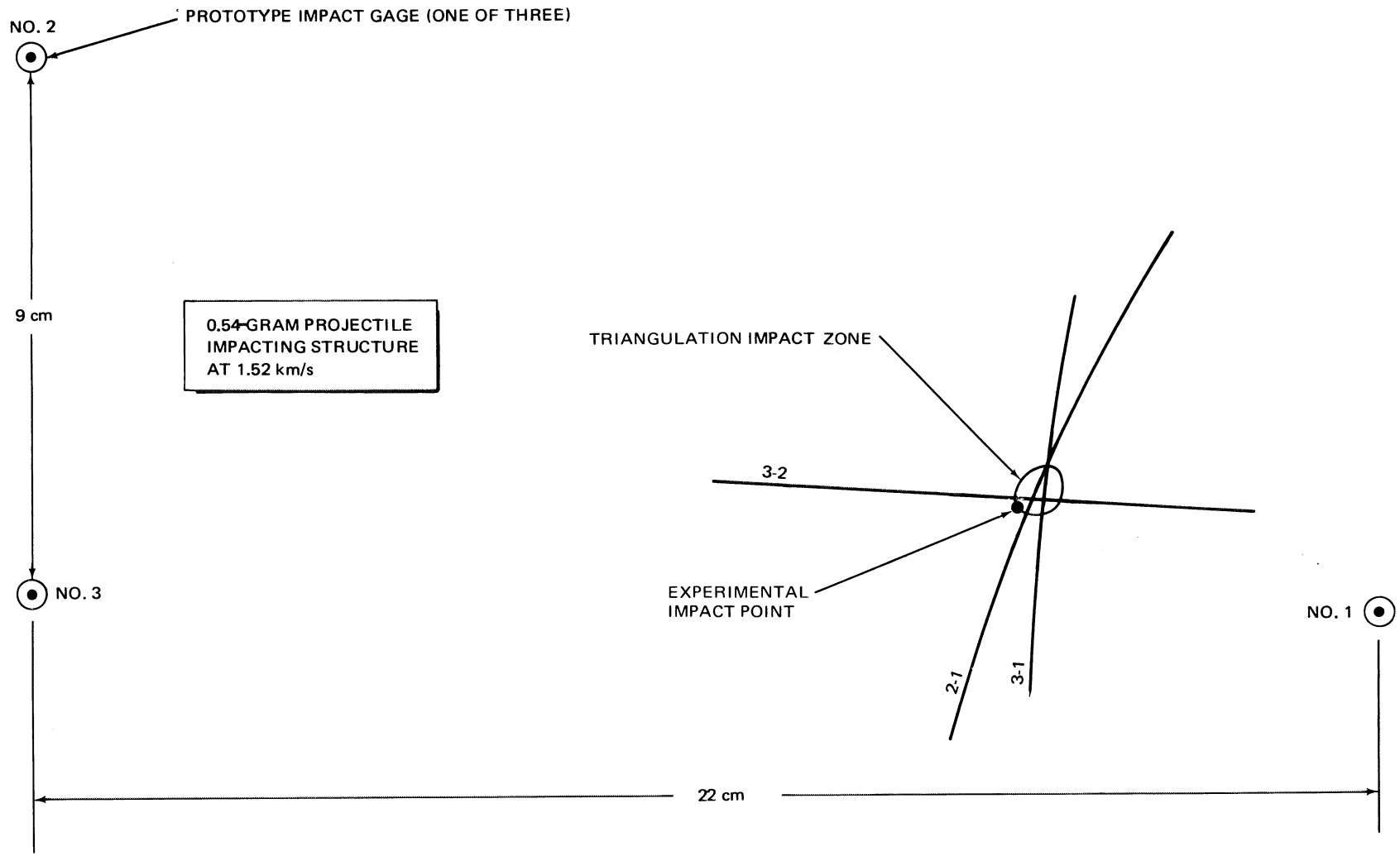

Figure 4-14. Location of Point of Impact by Triangulation Techniques with Three Prototype Impact Gages - Space Station Structure - Test Shot B54-1 (Ballistic Range)

which occurs at the intersection of the hyperbolas (determined by graphical methods). The location of the impact point (triangulation) was extremely accurate. The triangulation impact point was located within 1 cm of the actual impact point. Also the calculated velocity of the longitudinal-type wave agrees closely with the velocity given in Reference 5.

The profile of the signal output of impact gage No. 3, which had a piezoelectric plastic electret TFE as the gage sensing element, was similar to that of the gages with the ceramic piezoelectric PZT-5A.

Although the oscilloscope traces of Figure 4-12, which were obtained during the shot, were adequate to obtain the shock arrival time of the three prototype impact gages, they were not good enough to give a clear profiles of the gage outputs. Oscilloscope records of the playback of tape-recorded data produced excellent profiles.

Figure 4-13(a) shows the oscilloscope record of the output from the "sandwich" impact gage. This record was obtained from the playback of the tape-recorded data. The gage produced outputs when impacted by debris particles. The outputs appeared to correspond with the resultant impacts on the gage front surface.

4.6 IMPACT GAGE-BALLISTIC RANGE TEST SERIES 2

A second series of impact tests was carried out on a model which simulated an unstressed space station wall with a meteorite bumper. Seven different types of impact transducers were mounted on the target and bumper sheets.

Three tests were carried out. Two of the tests (Impact Shots B54-2-7 and B54-2-9) were successful. No projectile hit the target for Impact Shot B54-2-8, rendering the test valueless. Both successful shots were made at a projectile velocity of 6.4 km/s. Test results show that all the impact gages produced useful output signals, although the output of the polyethylene disk impact gage was extremely low. Time-of-arrival pulses from the impact gages indicate good agreement with the impact location assuming a wave velocity in the target sheet of approximately 0.54 cm/μs. The frequency

of the waves generated in the bumper sheet appeared to be about four times higher than those generated in the target sheet.

During these tests, liquid crystal formulations (memory type) were applied to both bumper and main wall sheets as a visual indicator of the location of a hypervelocity impact and transfer of energy to the sheet.

4.6.1 Series 2 Test Details

A target sheet of 6061T8 aluminum, 40.6 by 40.6 by 0.317 cm, with a bumper sheet of 6061T6 aluminum, 0.405-mm-thick, mounted one inch in front of the target sheet was clamped to a hanging steel wall in the range tank. The following impact transducers were mounted on the bumper and target sheets:

A. Impact Gage No. 0 – A piezoelectric PZT-5A ceramic disk* sensing element with 36 AWG leads soldered to the front and rear surfaces was epoxied (Epoxy Patch Kit - Type 10 manufactured by Hysol Company) to the center of the front surface of a 6061T5 aluminum mounting plate, 3.8 by 2.5 by 0.152 cm. The mounting plate was bonded to the front surface of the bumper sheet (Location 0) with contact cement (Eastman 910).

B. Impact Gage No. 1 – Prototype impact gage with a 0.0254-mm thickness and 0.635-cm-dia electret TFE sensing element was mounted on the rear surface of the target sheet (Location 1). It was installed by first drilling four mounting holes in the target sheet and then placing a small aluminum plate on the rear surface of the gage and securing the plate to the target with four 8-32 screws and nuts.

C. Impact Gage No. 2 – Prototype impact gage with a PZT-5A disk sensing element was bonded to the rear surface of the target sheet (Location 2) using a very thin coating of contact cement.

D. Impact Gage No. 3 – Prototype impact gage with an electret FEP sensing element, 0.0254 mm thick and with a 0.635-cm dia, was mounted on the rear surface of the target sheet (Location 3) by

*All PZT-5A disks were 0.317 mm in diameter and 0.635 mm thick, with their negative sides placed on the target and bumper sheets.

using the same mounting technique as the prototype impact gage at Location 1.

E. Impact Gage No. 4 – Mylar tape gage consisting of a 3.81 by 2.54 by 0.154 mm piece of Mylar pressure-sensitive tape (DPM 868) was taped to the rear surface of the target sheet (Location 4). A thin coating of conductive paint (E-KOTE 3040 manufactured by Epoxy Products, Inc.) 1.27 cm in length and 1.27 cm in width was painted on the backside of the Mylar tape. Electrical leads were cemented to the rear side of the aluminum sheet and the Mylar tape with the conductive paint.

F. Impact Gage No. 5 – Polyethylene disk impact gage consisting of a polyethylene disk 0.635 cm in diameter and 0.254 mm in thickness was painted with conductive paint on both sides. Electrical leads (36 AWG) were cemented with conductive paint to both sides of the polyethylene disk. The disk was bonded to the back side of the target sheet (Location 5) with epoxy.

G. Impact Gage No. 6 – Piezoelectric PZT-5A ceramic disk with electrical leads (36 AWG) soldered to both sides was installed on the rear surface (Location 6) of the target sheet. A thin film of ultrasonic grease (Sperry grease No. 50A4084) was placed between the target sheet and the front side of the disk. The disk was held in place by using Mylar pressure-sensitive tape placed on the back side of the PZT-5A disk and the aluminum.

H. Impact Gage No. 7 – Prototype impact gage with a PZT-5A disk-sensing element was mounted on the rear surface of the target sheet (Location 7) using the same mounting technique as the prototype impact gage at Location 1.

I. Impact Gage No. 8 – Electret FEP disk impact gage consisted of an electret FEP disk 0.0259 mm thick and 0.635-cm dia, with electrical leads (36 AWG) cemented to both sides of the disk using conductive paint. A thin film of ultrasonic grease was placed between the front side of the disk and a 6061T5 aluminum mounting place, 3.81 by 2.54 by 0.152 mm. The disk was held in place on the mounting plate by using Mylar pressure-sensitive tape placed on the back side of the electret disk and the aluminum mounting plate.

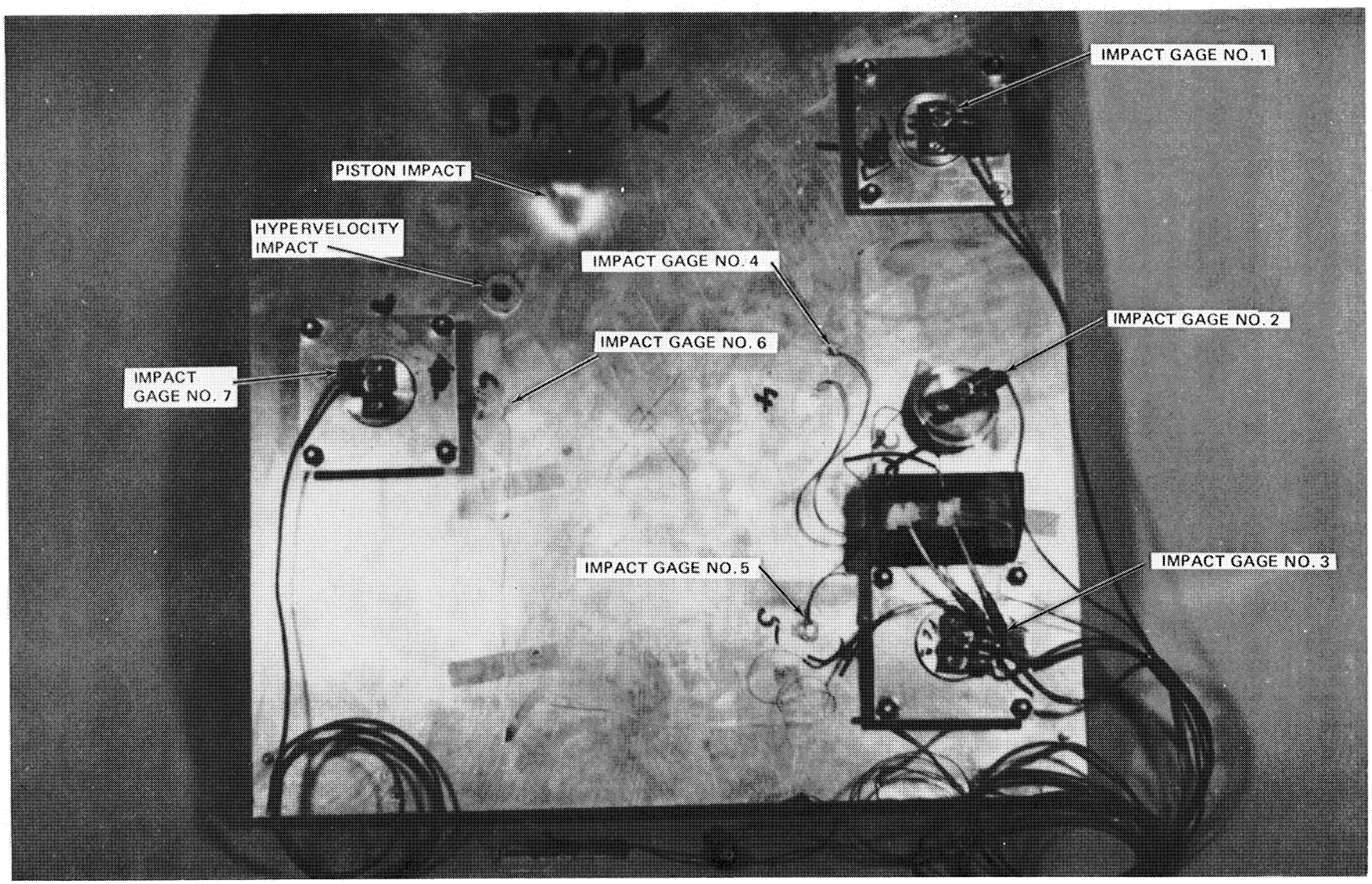

Figure 4-15. Photograph of Rear Side of Target Sheet Taken After Shot B54-2-7

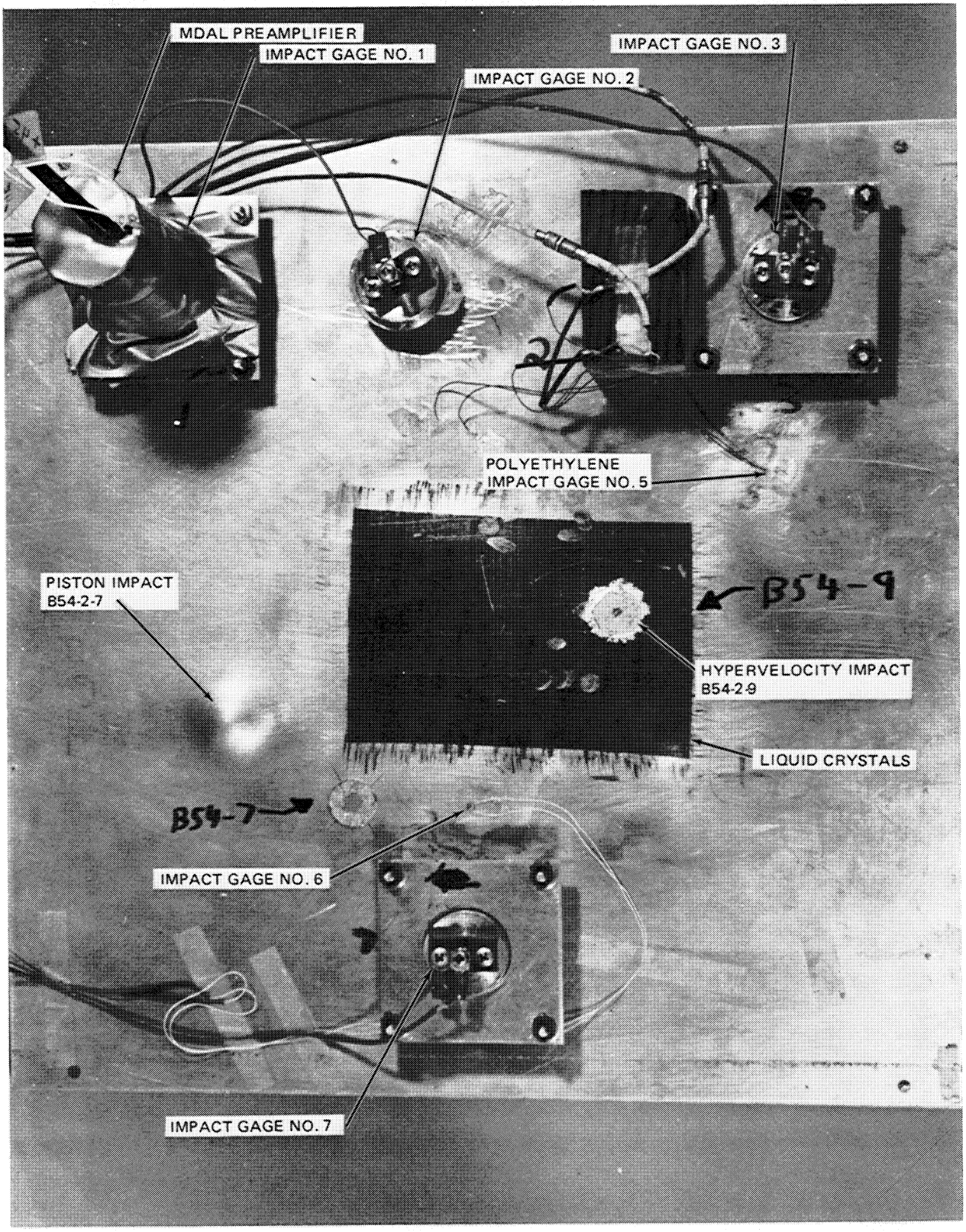

Figure 4-16. Photograph of Rear Side of Target Sheet Taken After Shot B54-2-9

The mounting plate was bonded to the front surface of the bumper sheet (Location 8) with contact cement.

Photographs showing the impact transducers mounted on the target sheet are given in Figures 4-15 and 4-16.

Memory-type liquid crystals with a threshold response of 323K were spray-painted on a portion of the rear surface of the target and bumper sheets for shot B54-2-9. The liquid crystals are shown as the dark rectangular area at the center of the target sheet in Figure 4-16.

Two photocells located 0.61 m apart and approximately 4.55 m upstream of the target were used for projectile velocity measurements. The projectile velocity was calculated by knowing the distance and by measuring the time of transit between the photocells and also between a photocell and the target plate.

The impact gages, photocells, timing markers, and time-zero (gun firing) outputs were recorded on a mid-band type recorder. Four of the impact gage outputs and the photocell outputs were also recorded on three oscilloscopes during the shots. Figure 4-17 shows a block diagram of the instrumentation setup for Shot B54-2-9. Two of the impact gage outputs were conditioned before being tape recorded. A wideband, high-input impedance preamplifier designed by MDAL was installed in a tubular housing and mounted on the back side of the impact gage at Location 1 for Shot B54-2-9. A follower-amplifier* was located approximately 0.6 m from the impact gage at Location 4. The instrumentation setup for Shot B54-2-7 was the same as Shot B54-2-9 except for the following: (1) the follower was connected to Impact Gage No. 3, (2) MDAL preamplifier was not used, and (3) Impact Gage No. 8 was not installed.

*The follower-amplifier had a high-input impedance (10^{11} Ω), unity gain, and a frequency response of 250 KHz for a 2-V peak-to-peak input signal.

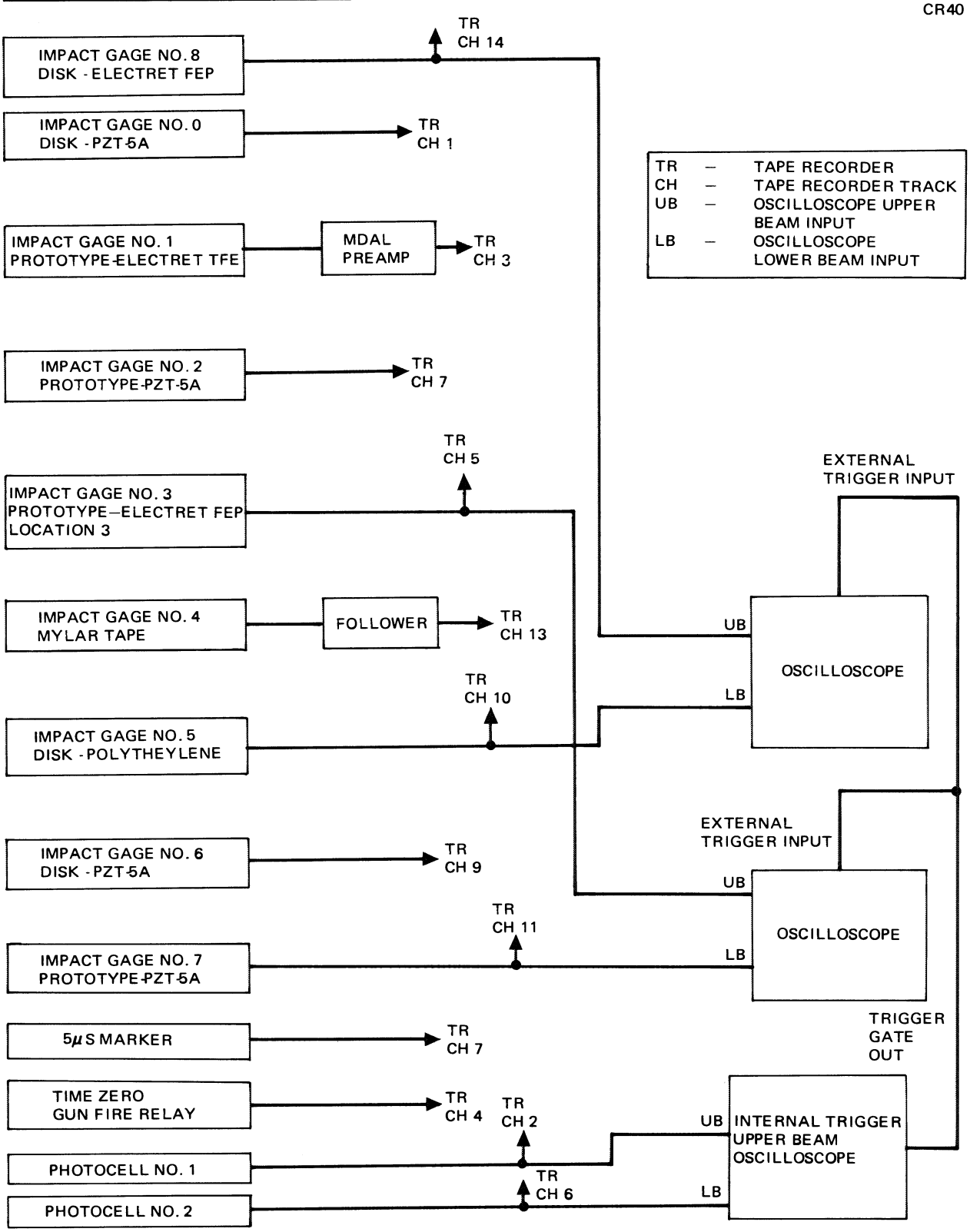

Figure 4-17. Instrumentation Setup Shot B54-2-9

Test conditions for Shots B54-2-7 and -9 are given in Table 4-5. A photograph of the rear surface of the target sheet taken after Shots B54-2-7 and -9 is given in Figures 4-15 and 4-16. A photograph of the front surface of the target sheet taken after Shot B54-2-7 is given in Figure 4-18. The same target sheet was used for both shots. The

Table 4-5

TEST CONDITIONS —SERIES 2

Run Number	B54-7	B54-9
Date	10/15/71	10/21/71
Range Pressure N/m	1.33×10^3	2.8×10^3
Gun Configuration	"B" - 2 Stage	"B" - 2 Stage
H_2 N/m	1.38×10^5	1.38×10^5
Powder (g)	110	110
Piston (g)	420	420
Model	Sphere	Sphere
Material	Al	Al
Diameter (mm)	4.0	3.18
Weight (mg)	92	46.6
Sabot		
Type	Cylinder	Cylinder
Material	Lexan	Lexan
Diameter (cm)	1.27	1.27
Length (mc)	0.765	0.765
Weight (gm)	1.266	1.2110
Velocity Instrumentation	Yes	Yes
Photocell	2	2
Velocity (km/s)	6.4	6.4
Target		
Type	Sheet	Sheet
Material	Al 6061T8	Al 6061T8
Size	0.304 m x 0.304 m x 0.318 cm	0.304 m x 0.304 m x 0.318 cm
Bumper		
Type	Sheet	Sheet
Material	Al 6061T6	Al 6061T6
Size	0.304 m x 0.304 m x 0.405 mm	0.304 m x 0.304 m x 0.405 mm
Spacing (cm)	2.54	2.54

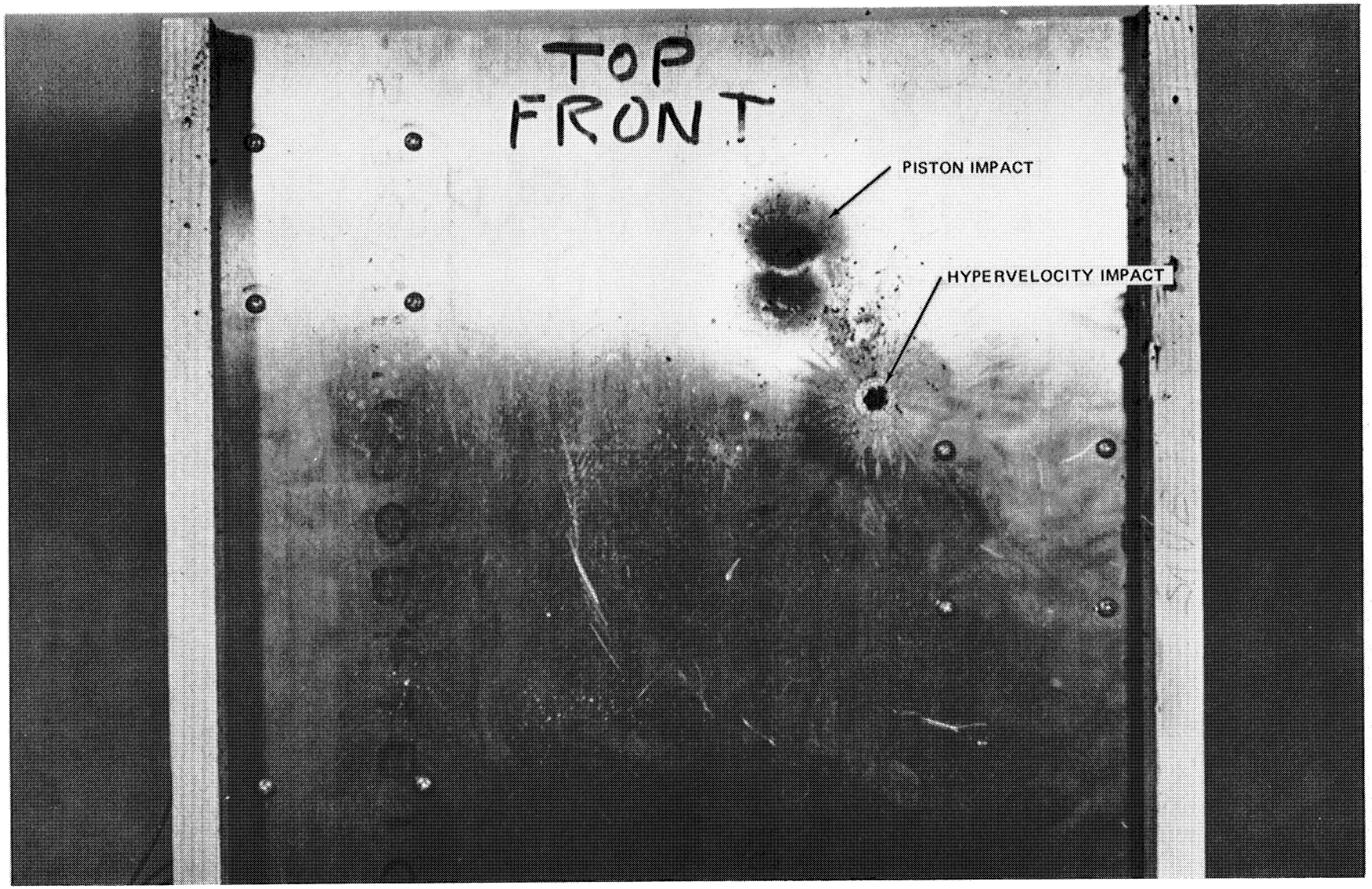

Figure 4-18. Photograph of Front Side of Target Sheet Taken After Shot B54-2-7

bump in the target sheet of Sheet B54-2-7 was caused by the low velocity piston hitting the target plate after the hypervelocity projectile.

Pertinent impact-gage characteristics and test results including the signal arrival times, initial pulse data, and the distance from the impact location for each transducer are given in Tables 4-6 and 4-7. Oscilloscope records of the impact gage output signals which were recorded on a tape recorder and on an oscilloscope during the shots are shown in Figures 4-19 through 4-22. Impact gage output signals occurring approximately 20 microseconds after the initial rise of the impact gage should be disregarded for data analysis. Reflections of the stress waves in the target sheet at the sheet edges, impact location and other sheet discontinuities distort the original stress wave in the sheet.

Output voltages were produced from all the impact gates when impacted by hypervelocity particles, even though the output signal of each impact gage was attenuated (factor of at least ten depending upon gage and external capacities) by approximately 2,000 pF of external capacitance (cable and recording equipment). Attenuation effects of the capacitance loading of the gage output were reduced when the MDAL preamplifier and the follower were inserted between the impact gage and the recording equipment. This can be seen by comparing the pulse amplitudes of Impact Gages 1, 3, and 4 for the shots with and without the amplifier and follower-amplifier installed.

As expected, the highest output signals were obtained from the impact gages with the PZT-5A sensing elements. The disk-type piezoelectric impact gages appeared to have only a slightly lower output than the prototype piezoelectric PZT-5A impact gages. No observable output was obtained from the Mylar impact gage for Shot B54-2-7; the output signal was lower than the data acquisition system noise level. No definite reason can be given for zero output signals from Impact Gages 0 and 2 during Shot B54-2-9. These gages

Table 4-6

IMPACT GAGE TEST RESULTS—SERIES 2
SHOT B54-2-7

Type	Sensing Element	Location	Capacitance[1] (pF)	Distance From Impact (cm)	Cable Cap. ≈(pF)	Pulse[3] Arrival Time (μs)	Pulse[4] Risetime (μs)	Pulse[3] Frequency (kHz)	Pulse[5] Amplitude (MV)	Tape Recorder Gain
Disk	PZT-5A	0 (bumper)	157	19.5	1,500	≈4	≈1.5	250	400	0.27
Prototype	Electret - TFE	1 (target)	66	22.9	1,400	≈34	5	50	2.5	4
Prototype	PZT-5A	2 (target)	172	22.6	1,800	≈32	5	60	800	0.27
Prototype	Electret - FEP	3 (target)	53	29.5	1,600	≈43	≈5	≈50	200	(with Amplifier)
Tape	Mylar	4 (target)	92[2]	16	1,650	(7)	(7)	(7)	<10[7]	3.3
Disk	Polyethylene	5 (target)	27[2]	27[2]	2,200	≈34	≈5	≈50	1	3.3
Disk	PZT-5A	6 (target)	160	4.92	2,050	Reference	≈5	≈40	280	0.25
Prototype	PZT-5A	7 (target)	197	7.85	2,350	5	≈5	50	480	0.17

NOTE:
(1) Includes gage housing capacitance
(2) Gage capacitance includes approximately 0.304 m of 36 AWG leads and BNC connector.
(3) Time selected at the midpoint of the rise of the first output pulse from the impact gage.
(4) Risetime (10 to 90 percent) of the first output pulse from the impact gage.
(5) Frequency of the first output pulse from the impact gage.
(6) Amplitude of first output pulse from impact gage.
(7) Impact gage output lower than data acquisition system noise level.

Table 4-7

IMPACT GAGE TEST RESULTS—SERIES 2
SHOT B54-2-9

Type	Sensing Element	Location	Capacitance[1] (pF)	Distance From Impact (cm)	Cable Cap. ≈(pF)	Pulse[3] Arrival Time (μs)	Pulse[4] Risetime (μs)	Pulse[5] Frequency (kHz)	Pulse[6] Amplitude (MV)	Tape Recorder Gain
Dis'	PZT-5A	0 (bumper)	152	20.	1,500	(7)	(7)	(7)	<200[7]	0.27
Prototype	Electret - TFE	1 (target)	155	20.9	1,600	12	≈5	≈100	250 (with MDAL preamp)	0.7
Prototype	PZT-5A	2 (target)		16.8	1,800	(7)	(7)	(7)	<200[7]	0.27
Prototype	Electret - FEP	3 (target)	≈53	15.2	1,400	28	≈5	≈70	130	7
Tape	Mylar	4 (target)	79[2]	8.90	1,650	1	≈4	≈50	15 (with amp)	3.3
Disk	Polyethylene	5 (target)		8.90	2,200	-3	≈3	≈100	7	7
Disk	PZT-5A	6 (target)	137	10.8	2,050	Reference	≈4	≈80	800	0.33
Prototype	PZT-5A	7 (target)	198	15.2	2,350	12	≈4	≈70	740	0.17
Disk	Electret - FEP	8 (bumper)		20.3	1,900		≈2	≈125	200	6

NOTE: (1) Includes gage housing capacitance.
(2) Gage capacitance includes approximately 0.304 m of 36 AWG leads and BNC connector.
(3) Time selected at midpoint of the rise of the first output pulse from the impact gage.
(4) Risetime (10 to 90 percent) of the first output pulse from the impact gage.
(5) Frequency of the first output pulse from the impact gage.
(6) Amplitude of first output pulse from impact gage.
(7) Impact gage output lower than the data acquisition system noise level.

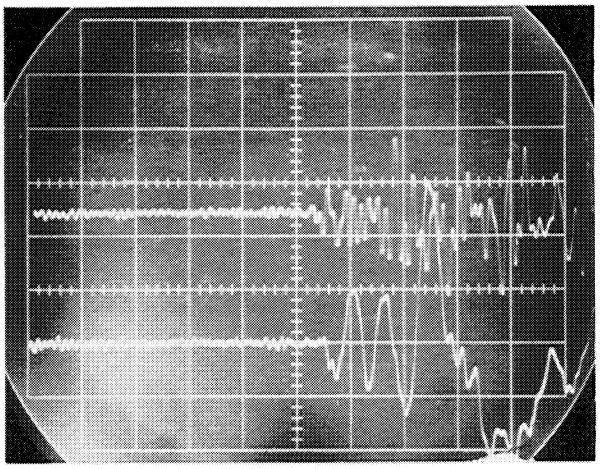

(a)

RECORD RATE: 20μs/cm

UPPER TRACE: DISK IMPACT GAGE NO. 0 (LOCATION 0) ON BUMPER SHEET -0.2 V/cm

LOWER TRACE: PROTOTYPE IMPACT GAGE NO. 7 - PZT-5A ELEMENT (LOCATION 7) -0.2 V/cm

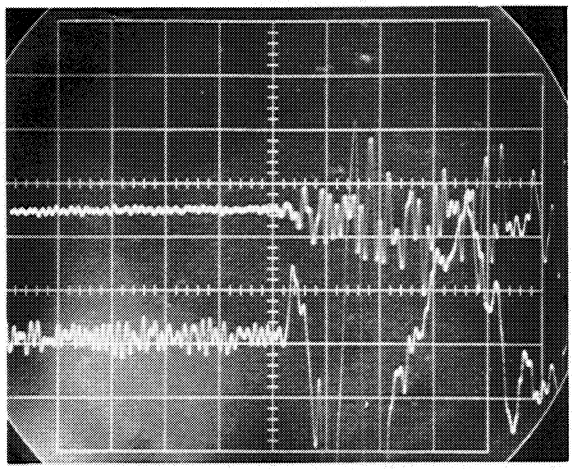

(b)

RECORD RATE 20μs/cm

UPPER TRACE: DISK IMPACT GAGE NO. 0 (LOCATION 0) ON BUMPER SHEET -0.2 V/cm

LOWER TRACE: DISK IMPACT GAGE NO. 6 (LOCATION 6) PZT-5A -0.05 V/cm

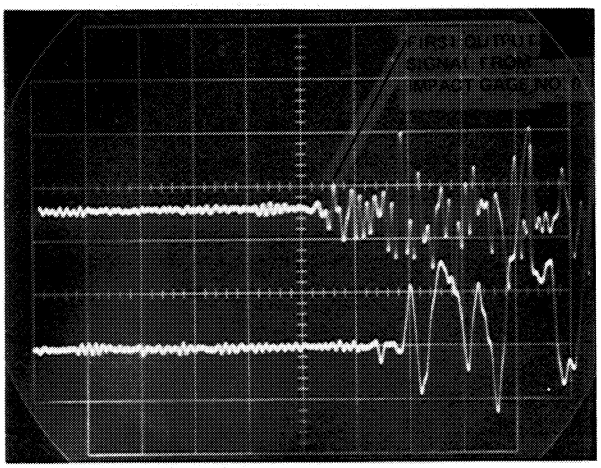

(c)

RECORD RATE 20μs/cm

UPPER TRACE: DISK IMPACT GAGE NO. 0 (LOCATION 0) ON BUMPER SHEET -0.2 V/cm

LOWER TRACE: PROTOTYPE IMPACT GAGE NO. 2 - PZT-5A ELEMENT (LOCATION 2) -0.2 V/cm

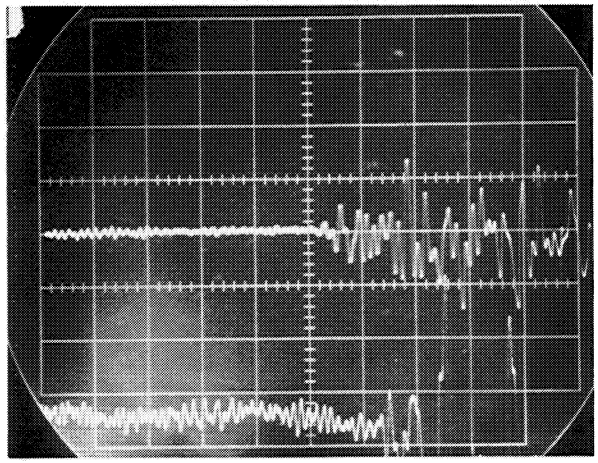

(d)

RECORD RATE 20μs/cm

UPPER TRACE: DISK IMPACT GAGE NO. 0 (LOCATION 0) PZT-5A ELEMENT -0.2 V/cm

LOWER TRACE: PROTOTYPE IMPACT GAGE NO. 3 ELECTRET FEP ELEMENT (LOCATION 3) -0.05 V/cm

Figure 4-19. Oscilloscope Records of Impact Gage Signals Recorded on Tape Recorder During Shot B54-2-7

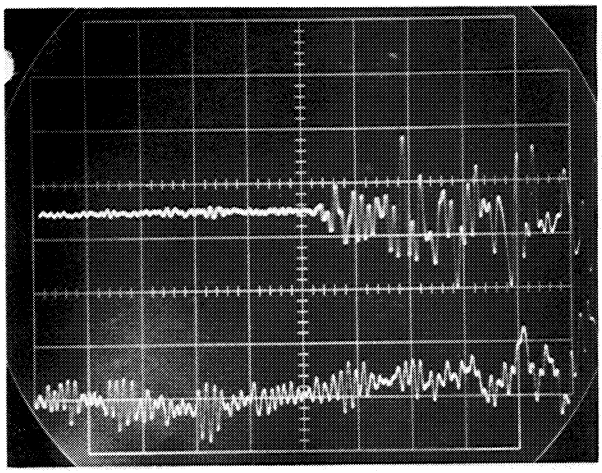

(a)

RECORD RATE: 20μs/cm

UPPER TRACE: PZT-5A DISC IMPACT GAGE NO. 0 (LOCATION 0) -0.2 V/cm

LOWER TRACE: PROTOTYPE IMPACT GAGE NO. 1 (LOCATION 1) ELECTRET TFE-0.05 V/cm

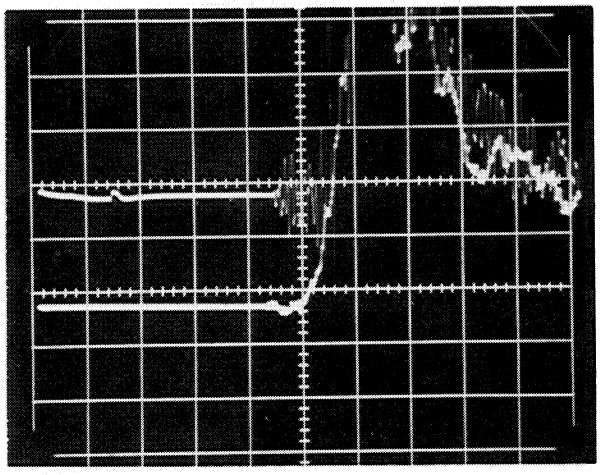

(b)

RECORD RATE: 200μs/cm

UPPER TRACE: PROTOTYPE IMPACT GAGE NO. 1 (LOCATION 1) ELECTRET TFE ELEMENT -0.01 V/cm

LOWER TRACE: POLYETHYLENE DISK IMPACT GAGE NO. 5 (LOCATION 5) -0.01 V/cm

(OSCILLOSCOPE RECORDING DURING SHOT)

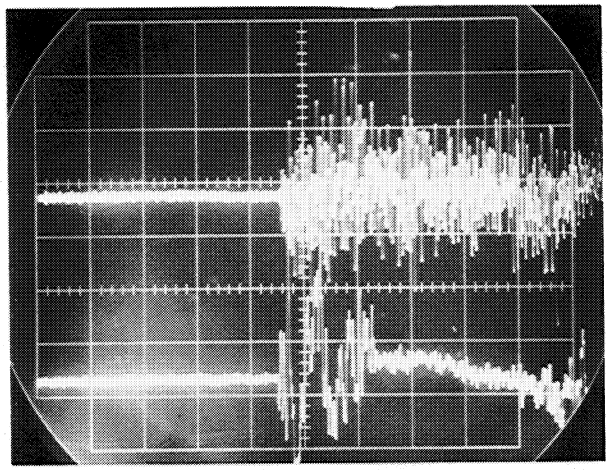

(c)

RECORD RATE: 500μs/cm

UPPER TRACE: PZT-5A DISK IMPACT GAGE NO. 0 (LOCATION 0) - ON BUMPER 0.5 V/cm

LOWER TRACE: PROTOTYPE IMPACT GAGE NO. 7 - PZT-5A ELEMENT (LOCATION 7) -0.2 V/cm

Figure 4-20. Oscilloscope Records of Impact Gage Signals Recorded on Tape Recorder and on an Oscilloscope During Shot B54-2-7

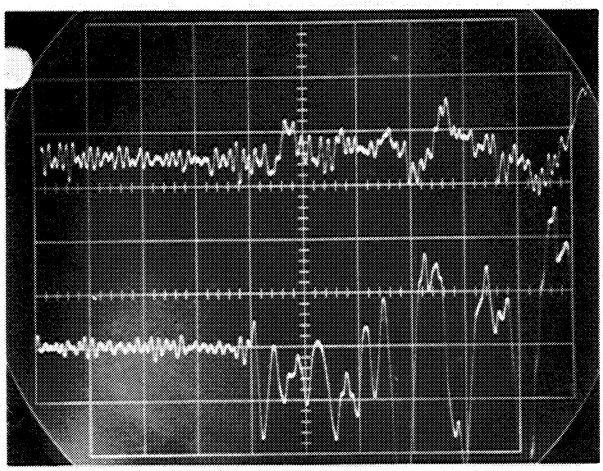

(a)

RECORD RATE 20μs/cm

UPPER TRACE: PROTOTYPE IMPACT GAGE NO. 7 PZT-5A ELEMENT (LOCATION 7) - 50 mV/cm, CH 11

LOWER TRACE: PROTOTYPE IMPACT GAGE NO. 1 - (LOCATION 1) ELECTRET TFE 0.1 V/cm, CH NO. 3

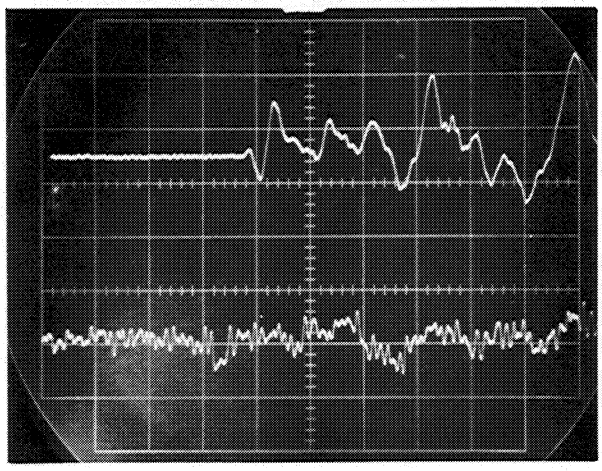

(b)

RECORD RATE 20μs/cm

UPPER TRACE: PROTOTYPE IMPACT GAGE NO. 7 - PZT-5A ELEMENT (LOCATION 7) -0.5 V/cm, CH 12

LOWER TRACE: POLYETHYLENE DISK IMPACT GAGE NO. 5 (LOCATION 5) -0.5% V/cm, CH 10

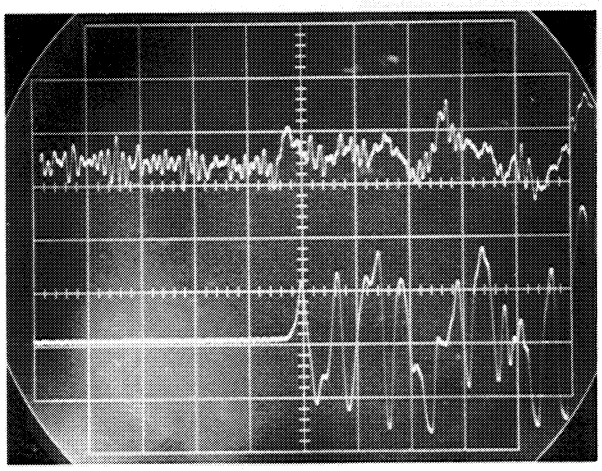

(c)

RECORD RATE 20μs/cm

UPPER TRACE: PROTOTYPE IMPACT GAGE NO. 7 PZT-5A ELEMENT (LOC 7) -0.05 V/cm, CH NO. 11

LOWER TRACE: PROTOTYPE IMPACT GAGE NO. 3 (LOC 3) ELEMENT FEP ELEMENT -1 V/cm, CH 5

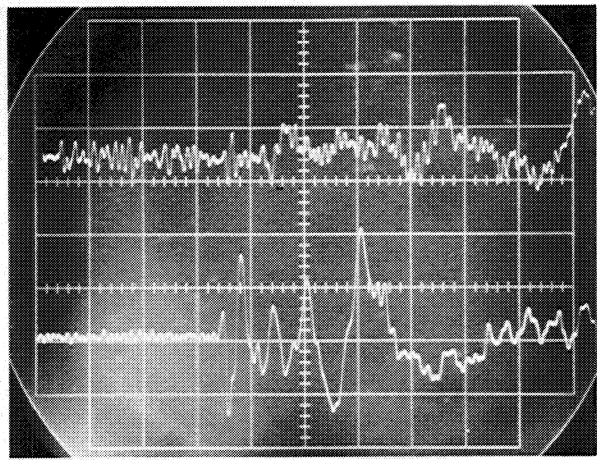

(d)

RECORD RATE 20μs/cm

UPPER TRACE: PROTOTYPE IMPACT GAGE NO. 7 - 50 MV/cm, CH 11

LOWER TRACE: PZT-5A DISK IMPACT GAGE NO. 6 (LOCATION 6) -0.2 V/cm, CH 9

Figure 4-21. Oscilloscope Records of Impact Gage Signals Recorded on Tape Recorder During Shot B54-2-9

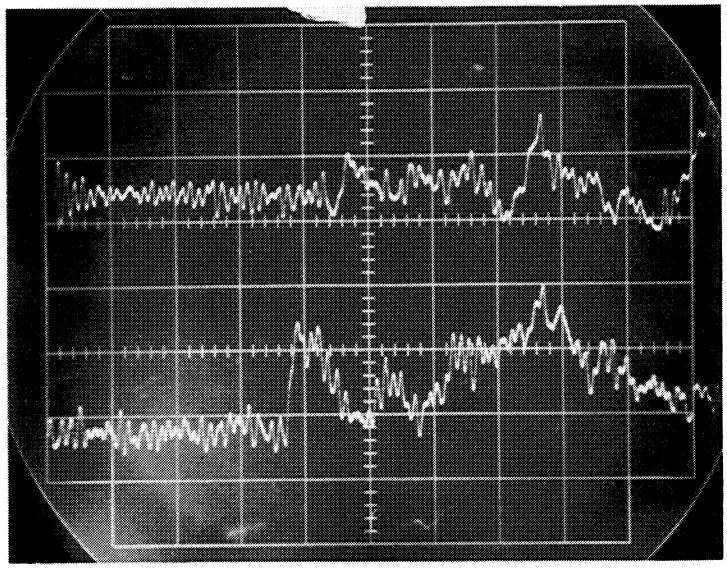

(a)

RECORD RATE 20μs/cm

UPPER TRACE: PROTOTYPE IMPACT GAGE NO. 7 (LOCATION 7) -50mV/cm, CH 11

LOWER TRACE: IMPACT GAGE NO. 4 (LOCATION 4) MYLAR TAPE ELEMENT -50 mV/cm, CH 13

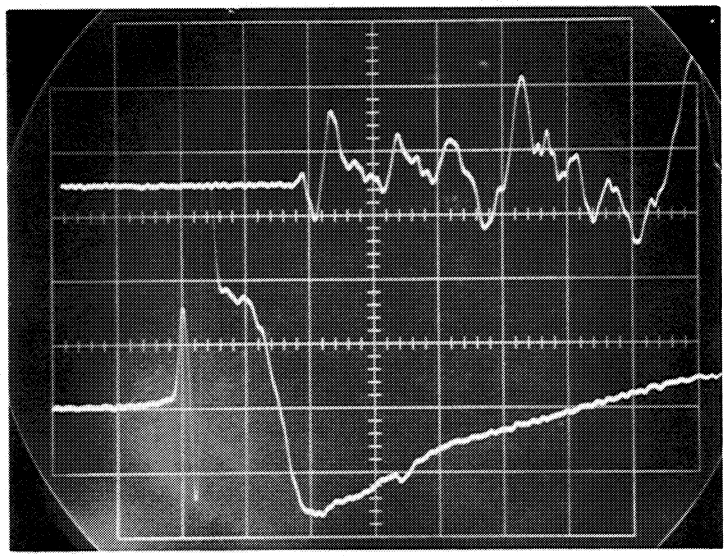

(b)

RECORD RATE 20μs/cm

UPPER TRACE: PROTOTYPE IMPACT GAGE NO. 7 (LOCATION 7) - 0.5 V/cm, CH 12

LOWER TRACE: IMPACT GAGE NO. 8 (LOCATION 8 ON BUMPER) ELECTRET FEP-1 V/cm, CH 14

Figure 4-22. Oscilloscope Records of Impact Gage Signals Recorded on Tape Recorder During Shot B54-2-9

may have fallen off the target prior to the shot since only contact cement held them in place on the target and bumper sheets.

For this test series, a direct readout by triangulation techniques was not employed. Instead, by assuming the velocity of the wave in the target sheet to be 0.54 cm/μs (value reported in Test Series 1) and by using the pulse-arrival time of one of the impact gages as a reference, pulse-arrival times of inidividual gages can be evaluated. The following procedure was used for each impact gage:

A. Subtract the distance from the impact location for the evaluated impact gage from the distance of the impact location for the reference impact gage.
B. Divide the distance obtained in Step 1 by 0.54 cm/μsec to obtain the theoretical pulse arrival time.
C. Compare the theoretical pulse arrival time with the measured value.

Comparison of derived theoretical values of pulse-arrival times with measured experimental values showed good agreement.

Liquid crystal color changes were observed both from the liquid crystals on the bumper sheet and also on the target sheet. The color changed from a light green (ambient condition) to a dark purple in a small circular area approximately 1.27 cm to 1.9 cm from the center of the impact point on the target sheet and a large circular area approximately 1.27 to 3.8 cm from the center of the impact point on the bumper sheet.

4.7 IMPACT-GAGE BALLISTIC RANGE TEST SERIES 3—ACOUSTIC EMISSION TEST

A third test series was carried out at the McDonnell Douglas Aerophysics Laboratory using a light-gas gun on a model similar to the one used in Test Series 1. Hypervelocity impact tests were carried out on a model of the MDAC modular space station (Figure 4-23) with the pressure wall uniaxially stressed to 3.0 x 108 N/m^2, during one test and to 1.37 x 10^8 N/m^2 on another test. The stress was applied to permit observations of the effect of

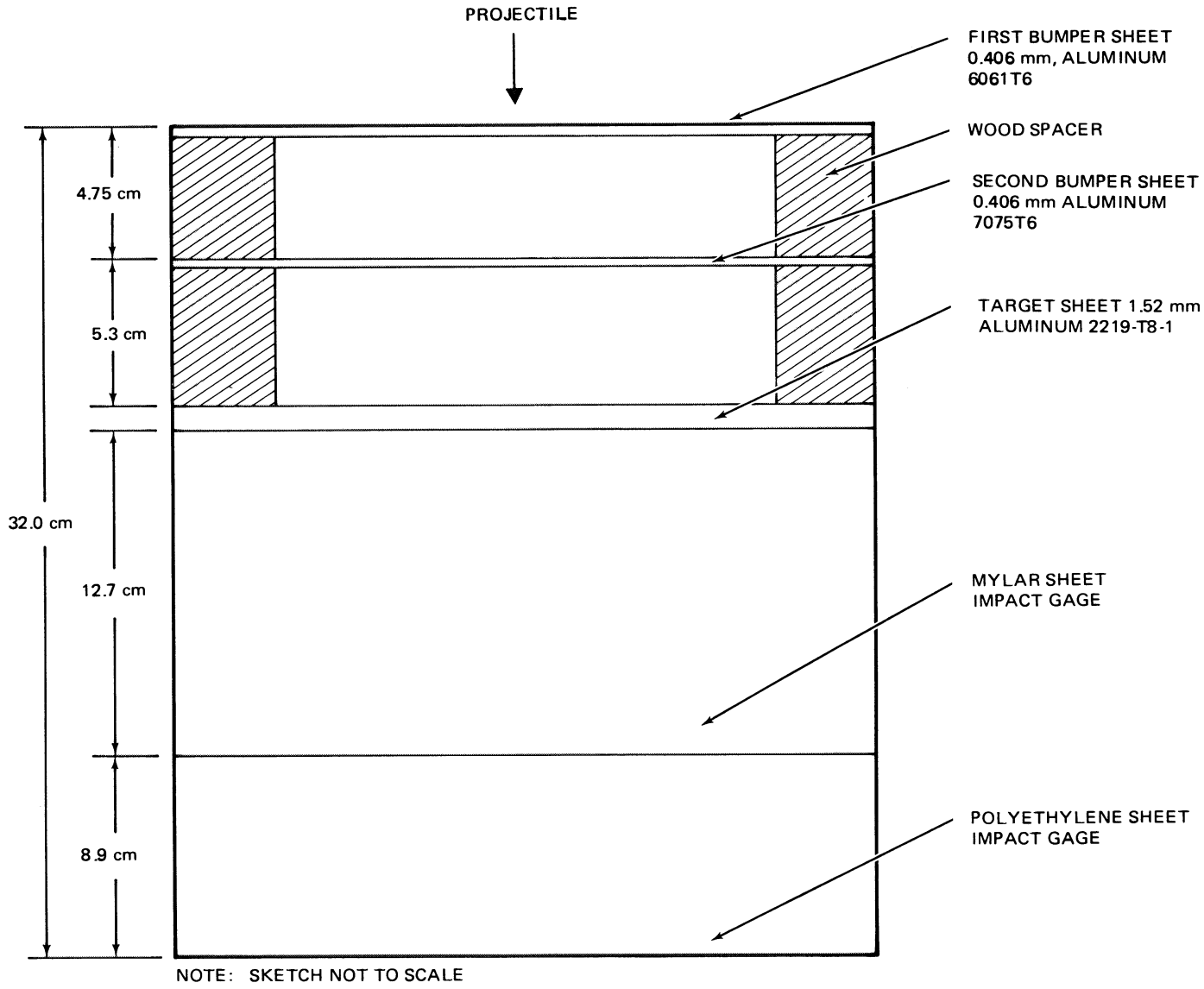

Figure 4-23. Test Setup Shots B54-2-15 and B54-2-16

impact under realistic design considerations. Six different types of impact gages were installed on the multisheet targets. The impact-gage output signals were used to study the response of the impact transducers to acoustical waves generated in the target sheet from the hypervelocity impacts.

Both tests were very successful. Relative voltage outputs of the impact gages resulting from hypervelocity impacts were obtained. Plastic electret impact transducers continued to show promising results during this test series. The point of impact was located very accurately for the stressed target sheet shots, using the impact gages and a triangulation technique. The stress-wave velocity in the stressed targets was found to be about 30 percent greater than in the unstressed targets. However, because of accuracy considerations and the fact that only two shots were made into stressed targets, further experiments would be required to establish the validity of these results. Acoustic emission signals were observed from an impact gage during postshot stressed target tests. The amplitudes of these signals were sufficiently high without amplification to verify the use of the impact gage for both locating hypervelocity impacts and for locating acoustical emissions in flawed areas of a space vehicle structure where a leak or a catastrophic failure could occur.

Liquid-crystal color changes were observed after hypervelocity impacts. This result shows that liquid crystals can be used as a visual indicator of the location of a hypervelocity impact.

4.7.1 Test Details – Impact Shots B54-2-15 and B54-2-16

Two hypervelocity impact shots were made into multisheet targets with stressed pressure walls in the range tank at the McDonnell Douglas Aerophysics Laboratory Ballistic Range. Small sections of a simulated space station wall with meteorite bumpers and two "sheet" impact gages were impacted by a projectile launched from a light-gas gun. Eight impact transducers (five different types) were mounted on the stressed target sheet. These shots were made primarily to find the location of the point of impact on

the stressed target sheet for two stress conditions, using a triangulation technique. In addition, the output signals from the impact gages were used to study the response of the impact transducers to acoustical waves generated in the sheets from the hypervelocity impacts of the debris particles. Attempts were made to monitor acoustic emissions during these shots and after Shot B54-2-16 for various target stress levels. Finally, liquid crystals were used to sense temperature changes on one of the "sheet" impact gages.

A target sheet of 2219-T8-1 aluminum with one bumper sheet of 7075-T6 aluminum, 0.406 mm thick, was mounted 10 cm in front of the target sheet, and another bumper sheet of 6061-T6 aluminum, 0.406 mm thick, was located 5.3 cm in front of the target sheet (Figure 4-23). A Mylar "sheet" impact gage (Location 8) (Figure 4-24) was installed approximately 12.7 cm behind the target sheet. This gage consisted of a Mylar sensing element, a sheet of Mylar approximately 30.4 cm x 30.4 cm x 0.0127 mm which was metalized on the back side, taped to a Plexiglas frame approximately 35.5 cm x 35.5 cm x 0.94 cm with a 7.6-cm border. Aluminum tabs, 2.54 cm square, with electrical leads attached were clamped on opposite sides and ends of the Mylar sheet and the Plexiglas frame. A polyethylene "sheet" impact gage (Location 1) was installed approximately 8.6 cm behind the Mylar "sheet" impact gage. This impact gage was identical to the Mylar "sheet" impact gage except that a polyethylene sheet approximately 30.4 cm x 30.4 cm x 0.037 mm was used as the sensing element instead of the metalized Mylar sheet. The polyethylene "sheet" impact gage was used only for Shot B54-2-15. The following impact transducers were mounted on the target sheets:

A. Impact Gages 1 and 2 – Prototype impact gages with PZT-5A dia* sensing elements were bonded to the rear surface of the target sheet (Location 1 and 2) using a thin coating of Eccobond Epoxy No. 285R (manufactured by Emerson and Cummings Corporation).

*PZT-5A piezoelectric ceramic disks were 0.317 cm in diameter and 0.635 mm thick, with the negative side of the disks placed closest to the target sheet.

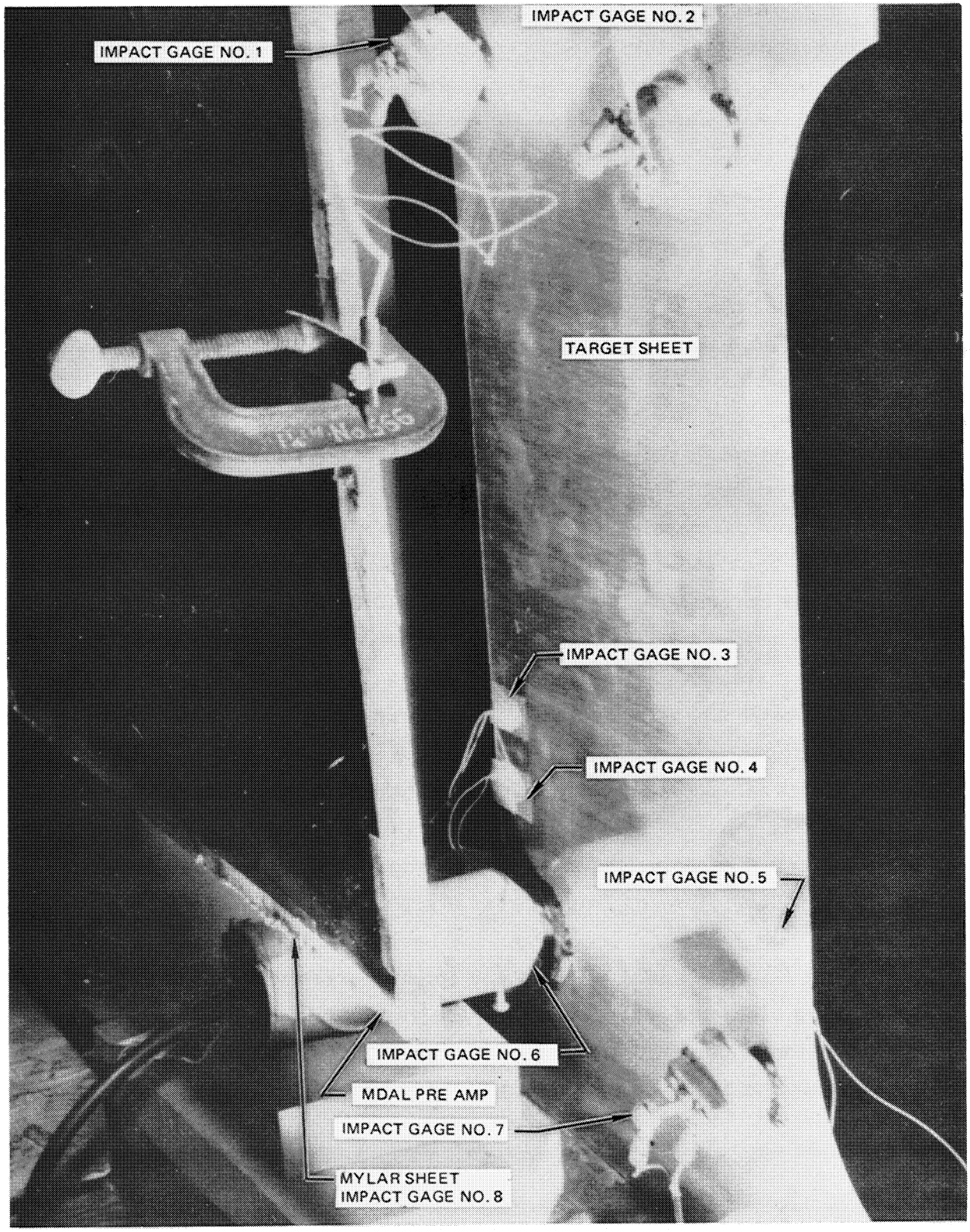

Figure 4-24. Photograph of Rear Surface of the Target Sheet and the Sheet Impact Gage Taken Before Shot B54-2-15

B. Impact Gages 3, 4, and 10 – PZT-5A ceramic disk impact gages consisted of a PZT-5A ceramic disk with electrical leads (36 AWG) soldered to both sides. Two gages were installed on the rear surface (Locations 3 and 4) of the target sheet and one gage on the front surface of the Mylar "sheet" impact gage (Location 10)*. A thin film of ultrasonic grease (Sperry grease 50A4084) was placed between the sheets and the front side of the disk. The disks were held in place using Mylar pressure-sensitive (DPM 868) tape placed on the back side of the PZT-5A disk and the target sheets and the front side of the Mylar sheet.

C. Impact Gage 5 – Mylar tape impact gage consisted of a 3.8 cm x 2.54 cm x 0.140 mm piece of Mylar pressure-sensitive tape placed on the rear surface of the target sheet (Location 5). A thin coating of conductive paint E-KOTE 3040 (manufactured by Epoxy Products, Inc.) 1.27 mm in length and 1.27 mm in width was painted on the back side of the Mylar tape. Electrical leads (36 AWS) were cemented with conductive paint to the rear side of the aluminum sheet and to the section of the Mylar tape which was covered with conductive paint.

D. Impact Gage 6 – Electret TFE prototype impact gage with an 0.635-cm Electret TFE scanning element, 0.0254 mm in thickness and 0.635-cm dia, was bonded to the rear surface of the target sheet (Location 6) using a thin coating of Eastman 910 contact cement.

E. Impact Gage 7 – Electret FEP prototype impact gage with an Electret FEP sensing cement, 0.0254 mm in thickness and 0.635 cm in diameter, was bonded to the rear surface of the target sheet (Location 7) using a thin coating of Eccobond Epoxy type 285R.

The impact transducers were removed from the target sheet after Shot B54-2-15 and placed on a new target sheet at approximately the same location for Shot B94-2-16. The test setup is shown in Figure 4-23. A photograph of the rear surface of the target sheet and the Mylar "sheet" impact gage, which was taken before Shot B54-2-16, is given in Figure 4-24.

*The impact gage at Location 10 was installed only for Shot B54-2-16.

Two photocells located 60.8 cm apart and approximately 13.8 m upstream of the target were used to obtain the projectile velocity. The projectile velocity was calculated by knowing the distance between the photocells and by measuring the time of transit between the photocells. In addition, the projectile velocity between one of the photocells and the target sheet was also obtained by knowing the distance between a photocell and an impact gage sensor on the target sheet and by measuring the transit time between the photocell and the impact gage.

Memory-type liquid crystals with a threshold response of 313K were spray-painted on a 30.4 cm square section of the rear surface of the Mylar "sheet" impact gage for Shot B54-2-16.

All impact gages, photocells, and timing marker signals were recorded on a wide-band (1.5-MHz bandwidth) tape recorder. Two impact-gage signals and two photocell outputs were also recorded on two dual-beam oscilloscopes during the shots. Figure 4-25 shows a block diagram of the instrumentation setup for Shot B54-2-15. The instrumentation setup for Shot B54-2-16 was the same as for Shot B54-2-15 except that the polyethylene "sheet" impact gage was not used and the PZT-5A disc impact gage was installed on the Mylar "sheet" impact gage at Location 10.

A wideband, high input-impedance preamplifier was used to condition the output signals of the impact gage at Location 6. This amplifier was mounted on the back side of the impact gage and is shown in Figure 4-24. A pre-amplifier was used to condition the output signals from the polyethylene "sheet" impact gage and was mounted approximately 0.6 m away from the gage. The output signals from the impact gage at Location 1 were conditioned by a follower located approximately 0.6 m away from the gage. An impedance converter* was used to condition the output of the Mylar tape impact gage and was installed approximately 0.6 m away from the gage.

*Impedance converter has a high input-impedance (5×10^{10} ohms), unity gain, and a frequency response of 500 kHz for a 2-V peak-to-peak input signal.

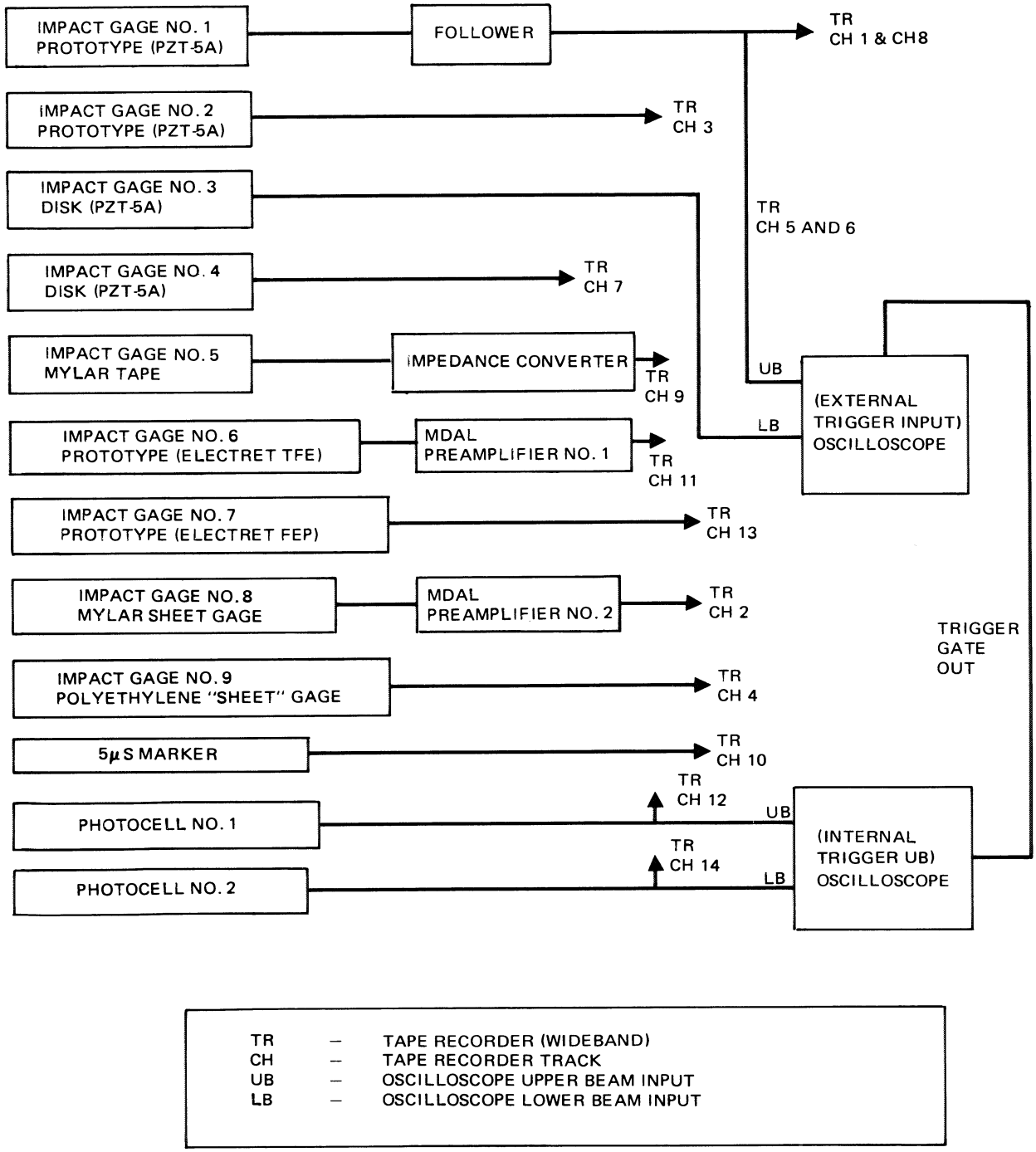

Figure 4-25. Instrumentation Setup for Shot B54-2-15

Test conditions for Shots B54-2-15 and B54-2-16 are given in Table 4-8. The only significant difference between the test conditions for these two shots was that the target was uniaxially stressed to 3.0×10^8 N/m^2 for the first shot and 1.37×10^8 N/m^2 for the second shot. A 0.475 cm diameter aluminum sphere was launched for each shot at a velocity of 7.0 km/s. The tape recorders continued to record for approximately five minutes after each shot in order to record any acoustic emissions which might be occurring immediately after the shot.

Photographs of the target, bumper sheets, and "sheet" impact gages taken after Shot B54-2-15 are shown in Figures 4-26, 4-27, and 4-28 and photographs after Shot B54-2-16 are given in Figures 4-29 and 4-30. Pertinent impact gage characteristics and test results, including signal arrival times, initial pulse data, and the distance from the impact location for each transducer, are given in Tables 4-9 and 4-10. Oscilloscope records of impact gage output signals are shown in Figures 4-31, 4-32, 4-33 and 4-34.

Results for the location of the impact point on the target sheet using a triangulation method were good. The impact points were located within 0.95 cm for Shot B54-2-15 and 1.9 cm for Shot B54-2-16. The previously described triangulation technique of obtaining the impact point from shock-arrival times was used. Figures 4-35 and 4-36 show the set of hyperbolas which were generated from the loci of these constant distance differences and the calculated impact point which occurs at the intersection of the hyperbolas. Note that the location of the impact point by triangulation is less accurate using the sheet velocity of 0.54 cm/μs obtained from previous results. This can be observed in Figures 4-35 and 4-36 where the actual triangulation impact location is given and the triangulation impact location based on an assumed sheet velocity of 0.54 cm/μs is also shown.

The velocity* in the target sheet for Shot B54-2-15 was approximately 0.685 cm/μs and 0.71 cm/μs for Shot B54-2-16. These sheet velocities

*Values reported in the literature for velocities in stressed aluminum sheets (not impacted by hypervelocity impact particles) varied by less than 1 percent from unstressed aluminum. For example, see Reference 3, page 465.

Table 4-8

RUN CONDITIONS—SERIES 3

Shot	B54-2-15	B54-2-16
Date	10-29-71	11-02-71
Run Pressure (N/m^2)	2.53×10^3	2.92×10^3
Gun Configuration	"B" - 2 Stage	"B" - 2 Stage
H_2 (N/m^2)	1.37×10^5	1.37×10^5
Powder (g)	125	125
Piston (g)	200	200
Model		
Material	Al	Al
Diameter (mm)	1.19	1.19
Weight (mg)	157.3	157.3
Sabot		
Type	Cylinder	Cylinder
Material	Lexan	Lexan
Diameter (cm)	1.27	1.27
Length (cm)	0.76	0.76
Weight (gm)	1.3029	1.2964
Velocity Instrumentation	Yes	Yes
Photocell	Yes	Yes
Velocity (km/s)	7.05	7.05
Target (Pressure Wall)		
Type	Sheet	Sheet
Material	Al 2219-T81	Al 2219-T81
Size	1.6 mm thick	1.6 mm thick
Stress (N/m^2)	3×10^8	1.37×10^8
Bumper (First)		
Type	Sheet	Sheet
Material	Al 6061T6	Al 6061T6
Size	0.356 m x 0.356 m x 0.406 mm	0.356 m x 356 m x 0.406 mm
Spacing (cm)	4.76 m	4.76 m
Bumper (Second)		
Type	Sheet	Sheet
Material	Al 7075T6	Al 7075T6
Size	0.356 m x 0.356 m x 0.406 mm	0.356 m x 356 m x 0.406 mm
Spacing (cm)	5.3 cm	5.3 cm

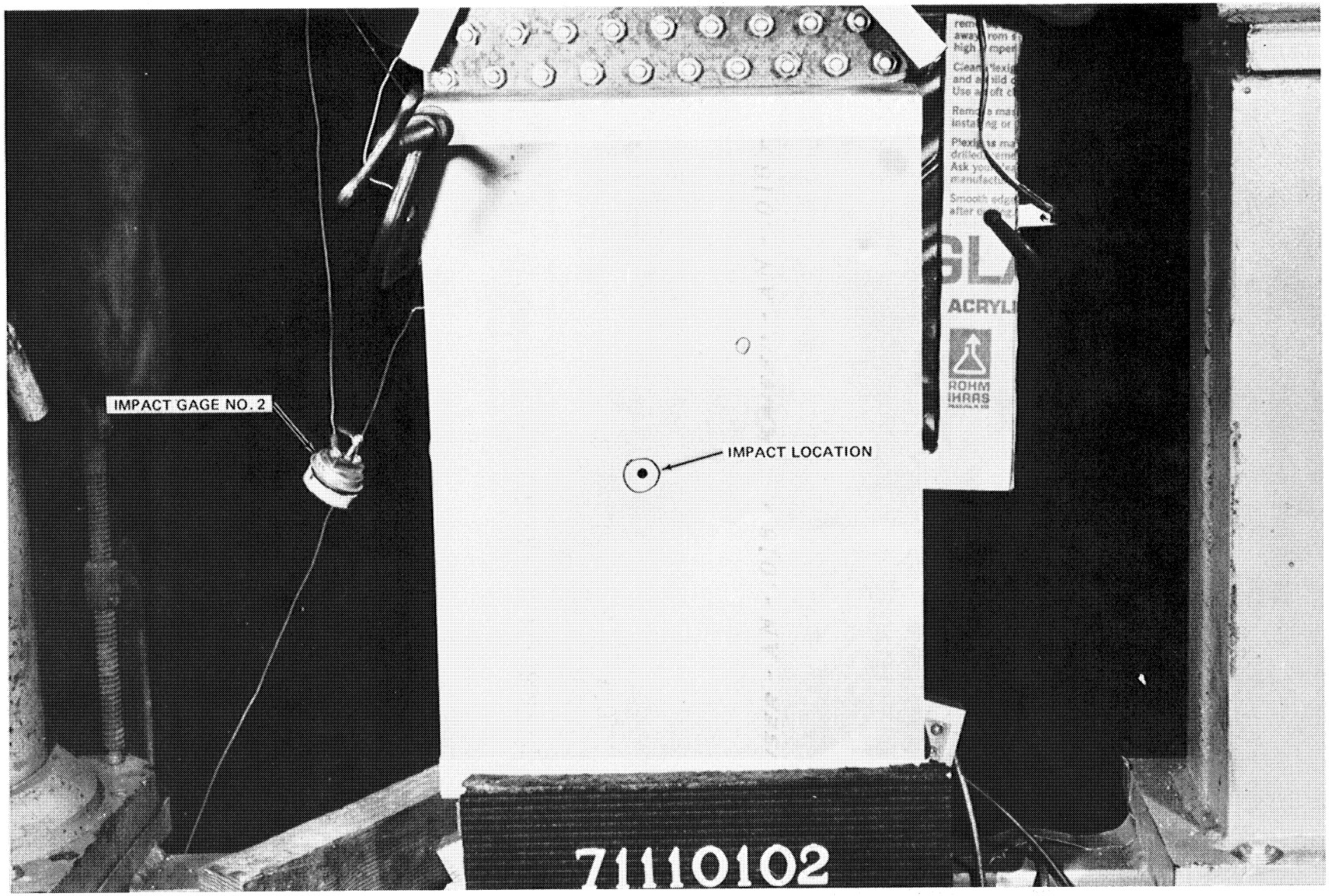

Figure 4-26. Photograph of Front Bumper Sheet Taken After Shot B54-2-15

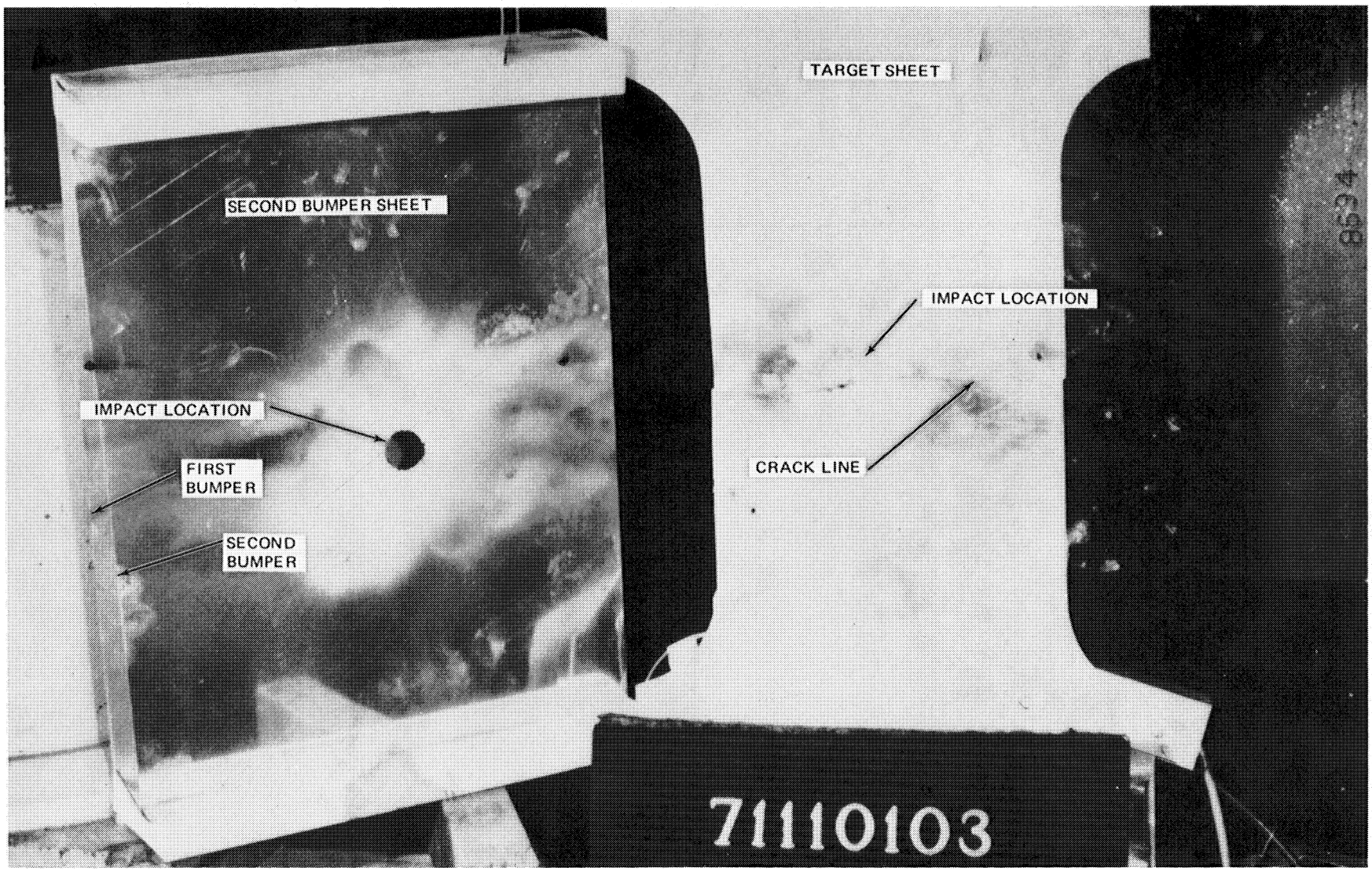

Figure 4-27. Photograph of Rear Surface of Second Bumper Sheet and Front Surface of Target Sheet Taken After Shot B54-2-15

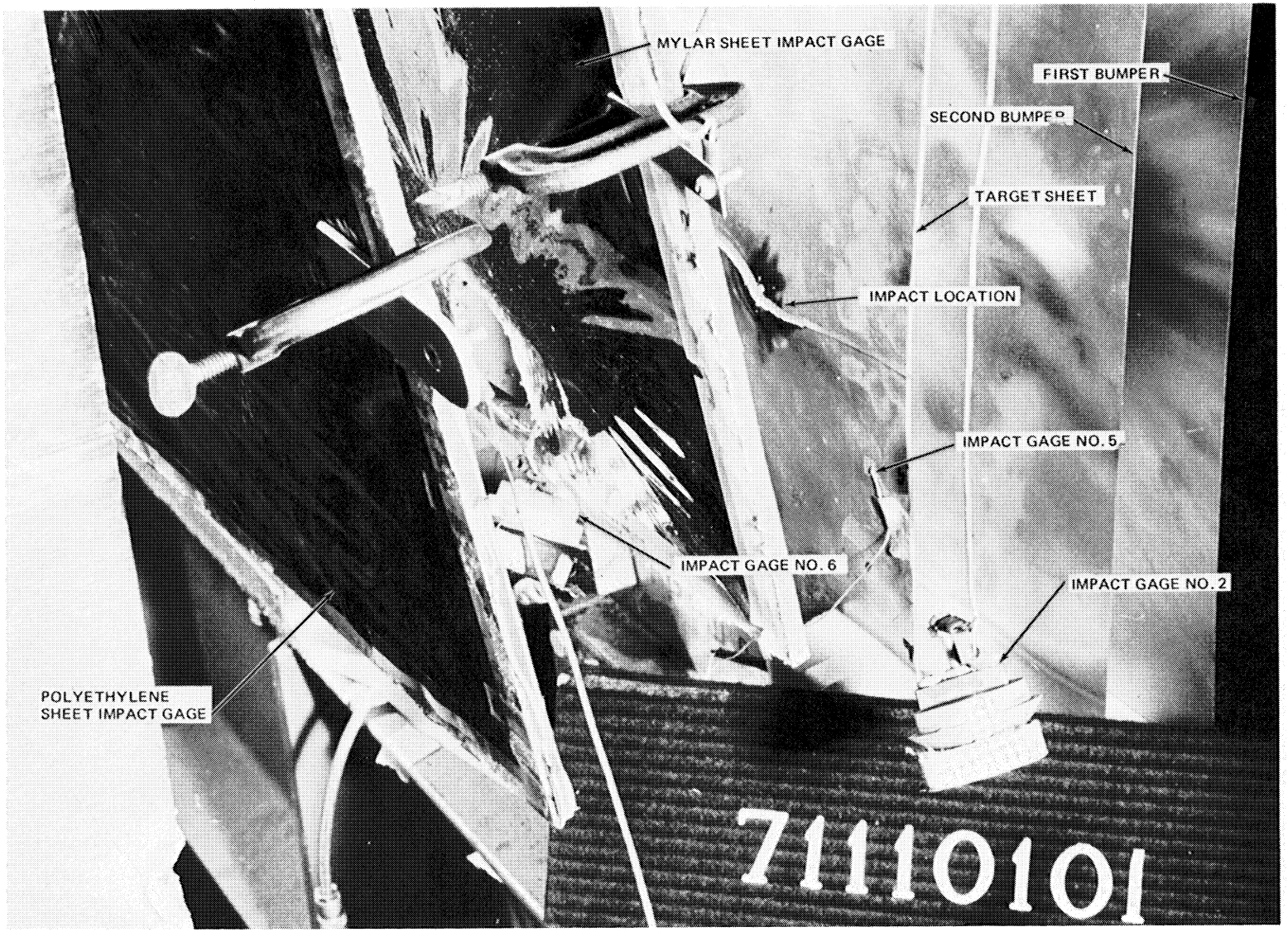

Figure 4-28. Photograph of Rear Surface of Bumper Sheets, Target Sheets, and Sheet Impact Gages Taken after Shot B54-2-15

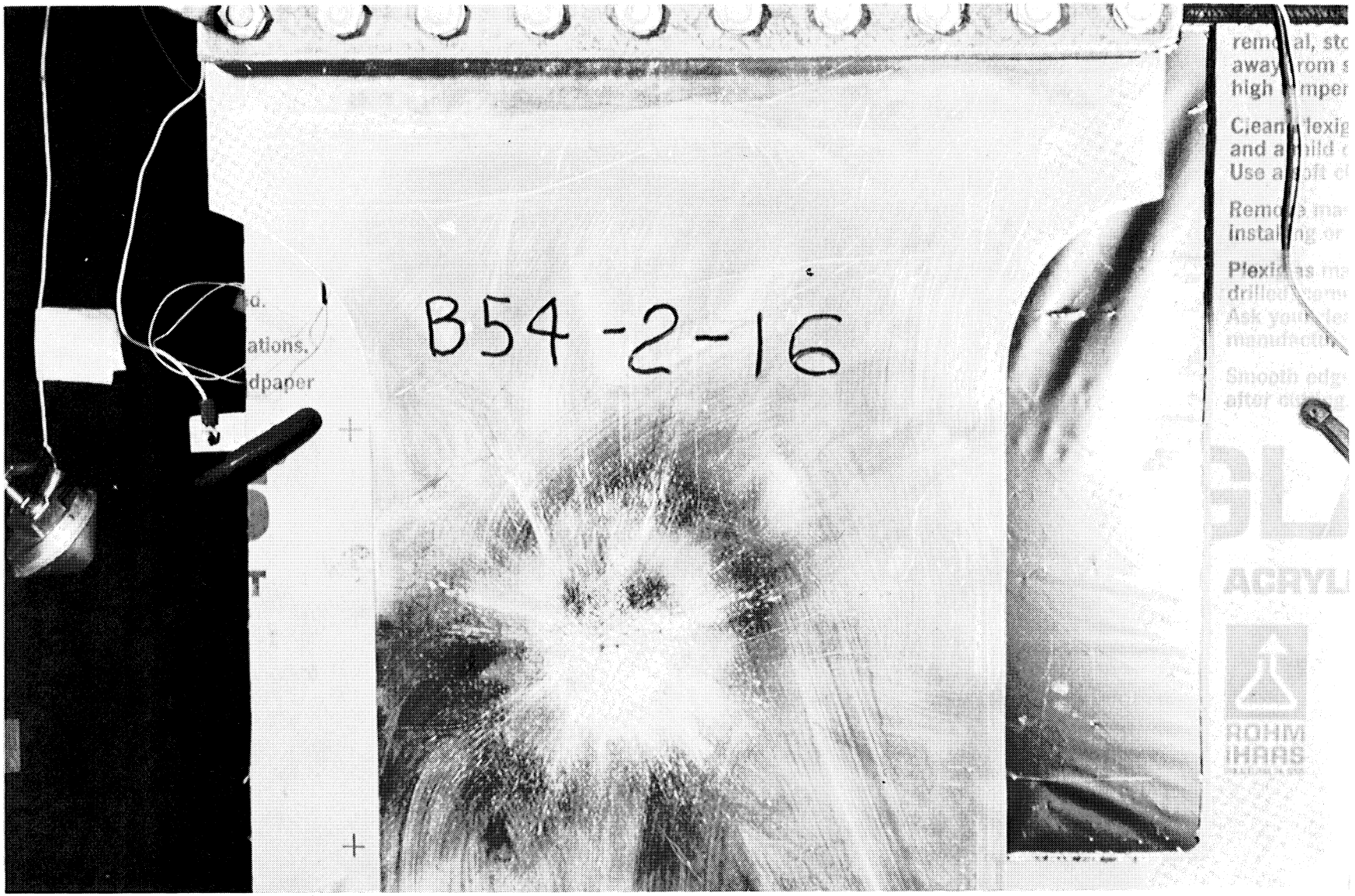

Figure 4-29. Photograph of Front Surface of Target Sheet Taken after Shot B54-2-16

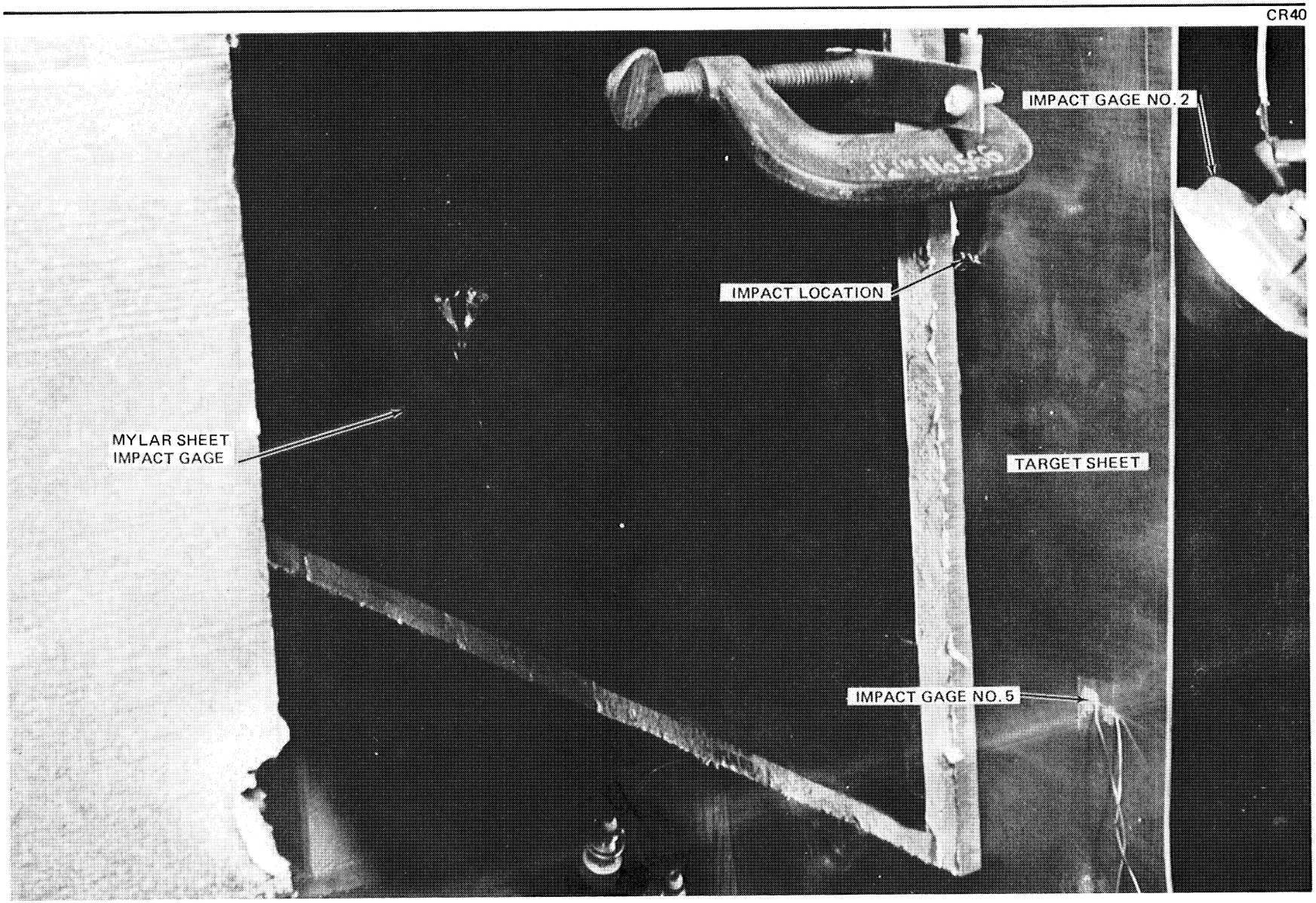

Figure 4-30. Photograph of Rear Surface of Target Sheet and Sheet Impact Gage Taken after Shot B54-2-16

Table 4-9

IMPACT GAGE TEST RESULTS—SERIES 3
SHOT B54-2-15

Gage Type	Sensing Element	Location	Gage[1] Cap (pF)	Preamp	Distance From Impact (cm)	Cable Cap. ≈(pF)	Pulse[3] Arrival Time (μs)	Pulse[4] Risetime (μs)	Pulse[5] Freq. (kHz)	Pulse Amplitude[6] (MV) Actual[7]	Corrected[8]	Tape Recorder Channel	Gain	Remarks
Prototype	PZT-5A	1 (Target)	180	Yes	21.0	1,800	15	2	125	1,000	100	1 8	4 12	
Prototype	PZT-5A	2 (Target)	180	No	20.0	1,820	13	2	160	400	400	3	10	
Disk	PZT-5A	3 (Target)		No	9.85	1,700	-	-	-	-	-	5 6	1 8	Not Connected
Disk	PZT-5A	4 (Target)	≈160	No	10.8	1,800	Reference	1	250	450	450	7	2	
Tape	Mylar	5 (Target)	≈92[2]	Yes	7.64	1,800	-	-	-	-	-	9	8	Slow Response
Prototype	Electret (TFE)	6 (Target)	72	DAL No. 1 Preamp	13.4	2,100	8	3	83	300	12	11	5	
Prototype	Electret (FEP)	7 (Target)	52	No	13.4	2,500	-	-	-	-	-	13	3	No Output
Sheet	Mylar	8	≈500	No	13	2,750	≈34	1	250	18	22	2	22	
Sheet	Polyethylene	9	≈30[2]	DAL No. 2 Preamp	21	4,200	75	2	250	35	0.5	4	12	

NOTE:
(1) Includes gage housing capacitance.
(2) Gage capacitance includes approximately 0.304 m of 36 AW6 leads and BNC connector.
(3) Time selected at the first 10 percent of the first output pulse from impact gage.
(4) Risetime (10 to 90 percent) of the first output pulse from the impact gage.
(5) Frequency (sine wave type cycle) of the first output pulse from the impact gage.
(6) Amplifued of the first output pulse from the impact gage.
(7) Impact gage output lower than the data acquisition system noise level.
(8) Pulse amplitude correction based upon external cable capacitance of 1800 pf and no preamplifier.
(9) Actual pulse amplitude was equal to the signal level recorded at the tape recorder output divided by the tape recorder gain.

Table 4-10

IMPACT GAGE TEST RESULTS—SERIES 3
SHOT B54-2-16

Gage Type	Sensing Element	Location	Gage[1] Cap. (pF)	Preamp	Distance From Impact (cm)	Cable Cap. ≈(pF)	Pulse[3] Arrival Time (μs)	Pulse[4] Risetime (μs)	Pulse[5] Freq. (kHz)	Pulse Amplitude[6] (MV) Measured[9]	Pulse Amplitude[6] (MV) Corrected[8]	Tape Recorder Channel	Tape Recorder Gain	Remarks
Prototype	PZT-5A	1 (Target)	180	Yes	15.88	1,800	2	2	125	800	88	1 8	4 12	
Prototype	PZT-5A	2 (Target)	180	No	12.40	1,820	Reference	3	90	140		13	3	
Disk	PZT-5A	3 (Target)		No	6.25 15.88	1,700	-	-	-	-		5 6	1 8	No output
Disk	PZT-5A	4 (Target)	≈160	No	17.8	1,800	4	1	250	700	700	7	2	
Tape	Mylar	5 (Target)	≈92[2]	Yes	13.34	1,800	1	4	70	17	≈1	9	8	
Prototype	Electret (TFE)	6 (Target)	≈72	DAL No. 1 Preamp	20.96	2,100	12	2.5	100	70	2.8	11	5	
Prototype	Electret (FEP)	7 (Target)	≈52	No	19.69	2,500	10	1.5	120	40	52	3	10	
Sheet	Mylar	8	≈500	No	12.7	4,200	(7)	(7)	(7)	(7)	(7)	4	12	Hit by very small debris particles
Disk	PZT-5A	9 (on Mylar sheet gage)	190	No	12.7 + 6.4	2,750	60	1	>250	10	15	2	22	

NOTE:
(1) Includes gage housing capacitance.
(2) Gage capacitance includes approximately 0.304 m of 36 AW6 Leads and BNC connector.
(3) Time selected at the first 10 percent of the rise of the first output pulse from the impact gage.
(4) Risetime (10 to 90 percent) of the first output pulse from the impact gage.
(5) Frequency (sine wave type cycle) of the first output pulse from the impact gage.
(6) Amplitude of the first output pulse from the impact gage.
(7) Impact gage output lower than the data acquisition system noise level.
(8) Pulse amplitude correction based upon external cable capacitance of 1,800 pF and no preamplifier.
(9) Measured pulse amplitude was equal to the signal level recorded at the tape recorder output divided by the tape recorder gain.

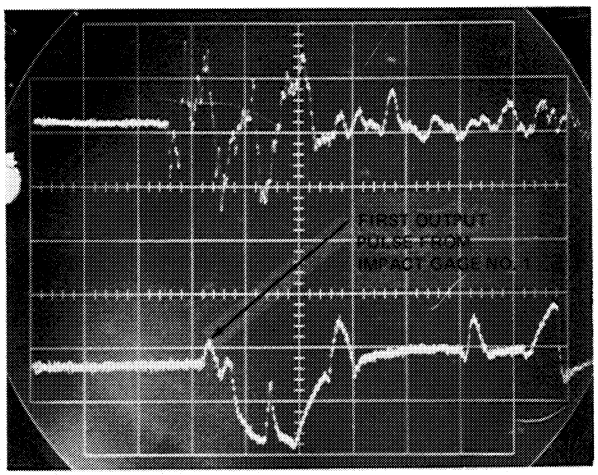

(a)

RECORD RATE 20 μs/cm

UPPER TRACE: PZT-5A DISK IMPACT GAGE NO. 4 (LOCATION NO. 4) 1V/cm, CH 7

LOWER TRACE: PZT-5A PROTOTYPE IMPACT GAGE NO. 1 (LOCATION NO. 1) 1V/cm, CH 1

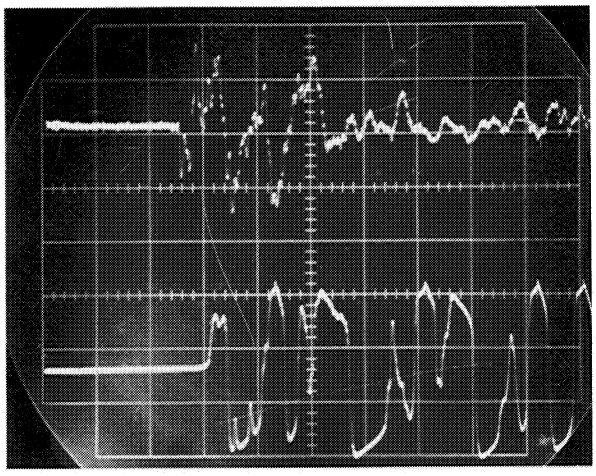

(b)

RECORD RATE 20 μs/cm

UPPER TRACE: PZT-5A DISK IMPACT GAGE NO. 4 (LOCATION NO. 4) 1V/cm, CH 7

LOWER TRACE: PZT-5A PROTOTYPE IMPACT GAGE NO. 2 (LOCATION NO. 2) .5V/cm, CH 3

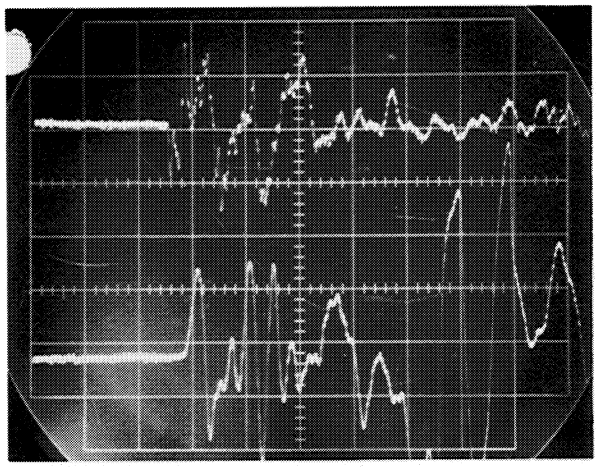

(c)

RECORD RATE 20 μs/cm

UPPER TRACE: PZT-5A DISK IMPACT GAGE NO. 4 (LOCATION NO. 4) - 1V/cm, CH 7

LOWER TRACE: ELECTRET TFE PROTOTYPE GAGE NO. 6 (LOCATION NO. 6) 1V/cm, CH 11

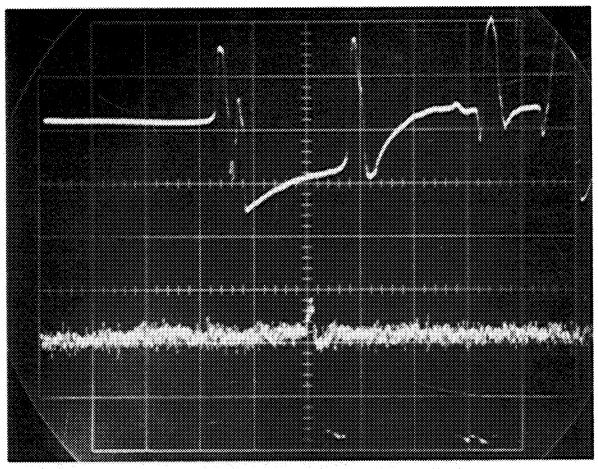

(d)

RECORD RATE 20 μs/cm

UPPER TRACE: PZT-5A PROTOTYPE IMPACT GAGE NO. 1 (LOCATION NO. 1) 0.2V/cm, CH 8

LOWER TRACE: MYLAR SHEET IMPACT GAGE NO. 8 (LOCATION NO. 8) 0.5V/cm, CH 2

Figure 4-31. Oscilloscope Records of Impact Gage Signals Recorded on Tape Recorder During Shot B54-2-15

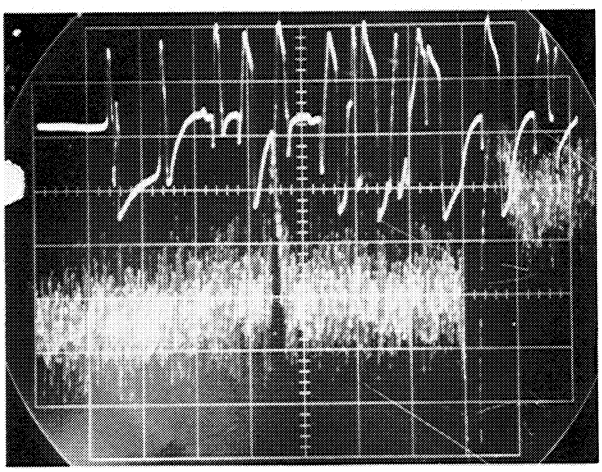

(a)

RECORD RATE 20μs/cm

UPPER TRACE: PZT-5A PROTOTYPE IMPACT GAGE NO. 1 (LOCATION NO. 1) 0.2 V/cm, CH 8

LOWER TRACE: POLYETHYLENE SHEET IMPACT GAGE NO. 9 (LOCATION NO. 9) 0.1 V/cm, CH 4

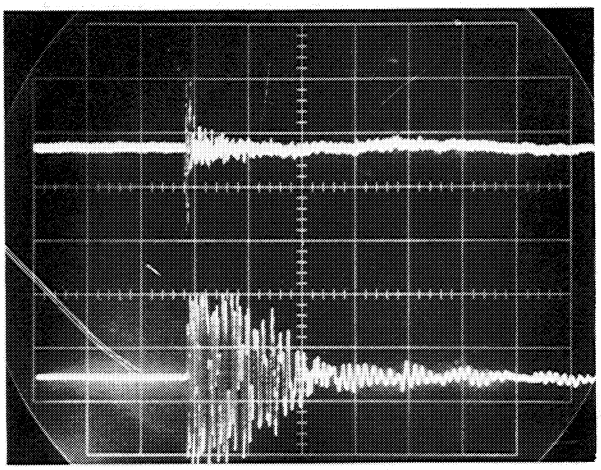

(b)

RECORD RATE 500μs/cm

UPPER TRACE: PZT-5A DISK IMPACT GAGE NO. 4 (LOCATION NO. 4) 1V/cm, CH 7

LOWER TRACE: PZT–5A PROTOTYPE IMPACT GAGE NO. 2 (LOCATION NO. 2) 5V/cm, CH 3

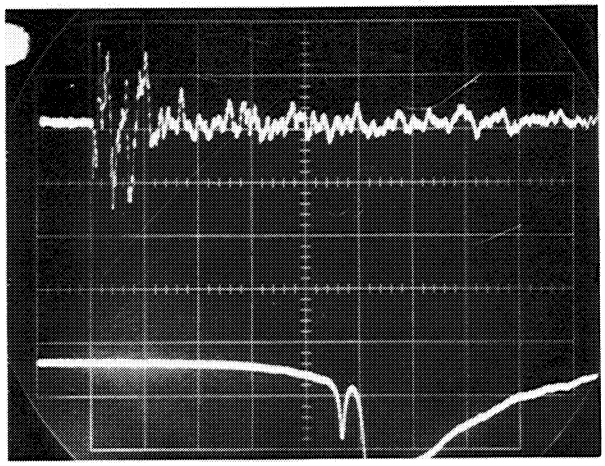

(c)

RECORD RATE 50μs/cm

UPPER TRACE: PZT-5A DISK IMPACT GAGE NO. 4 (LOCATION NO. 4) 1V/cm, CH 7

LOWER TRACE: MYLAR TAPE IMPACT GAGE NO. 5 (LOCATION NO. 5) 1V/cm, ch 9

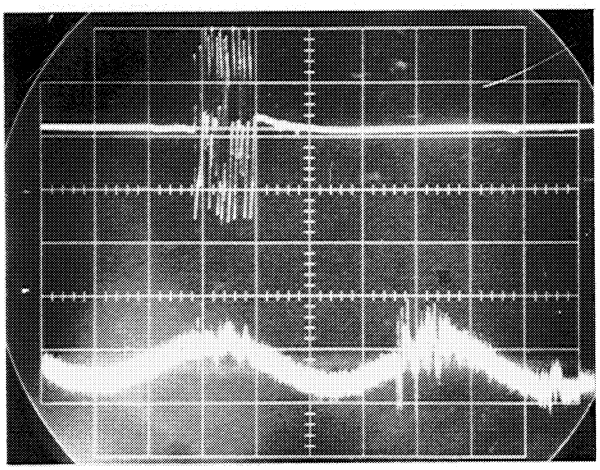

(d)

RECORD RATE 500μs/cm

UPPER TRACE: PZT-5A PROTOTYPE IMPACT GAGE NO. 1 (LOCATION NO. 1) 0.2V/cm, CH 8

LOWER TRACE: MYLAR SHEET IMPACT GAGE NO. 8 (LOCATION NO. 8) 0.5V/cm, CH 2

Figure 4-32. Oscilloscope Records of Impact Gage Signals Recorded on Tape Recorder During Shot B54-2-15

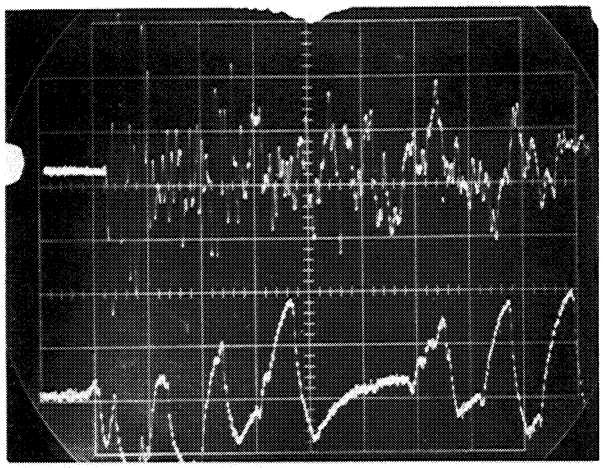

(a)

RECORD RATE 20μs/cm

UPPER TRACE: PZT-5A DISK IMPACT GAGE NO. 4 (LOCATION NO. 4) 1V/cm, CH 7

LOWER TRACE: PZT-5A PROTOTYPE IMPACT GAGE NO. 1 (LOCATION NO. 1) 1V/cm, CH 1

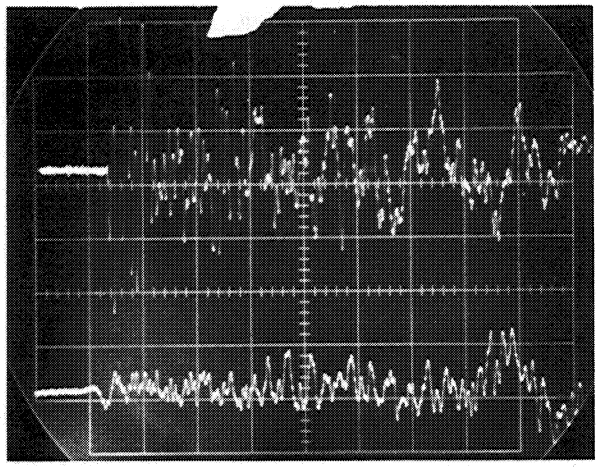

(b)

RECORD RATE 20μs/cm

UPPER TRACE: PZT-5A DISK IMPACT GAGE NO. 4 (LOCATION NO. 4) 1V/cm, CH 7

LOWER TRACE: PZT-5A PROTOTYPE IMPACT GAGE NO. 2 (LOCATION NO. 2) 1V/cm, CH 13

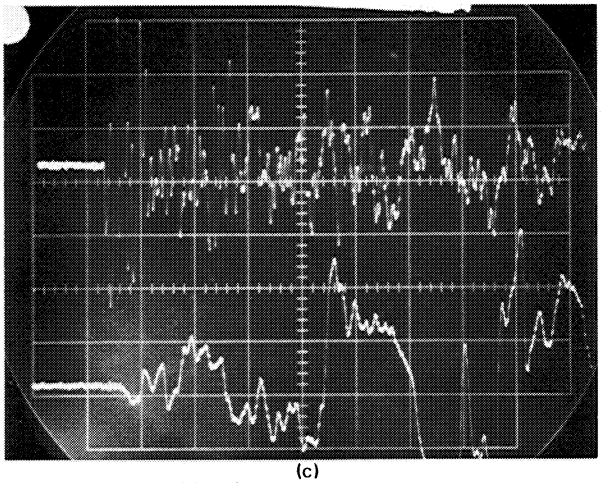

(c)

RECORD RATE 20μs/cm

UPPER TRACE: PZT-5A DISK IMPACT GAGE NO. 4 (LOCATION NO. 4) 1V/cm, CH 7

LOWER TRACE: ELECTRET TFE PROTOTYPE IMPACT GAGE NO. 6 (LOCATION NO. 6) 1V/cm, CH 11

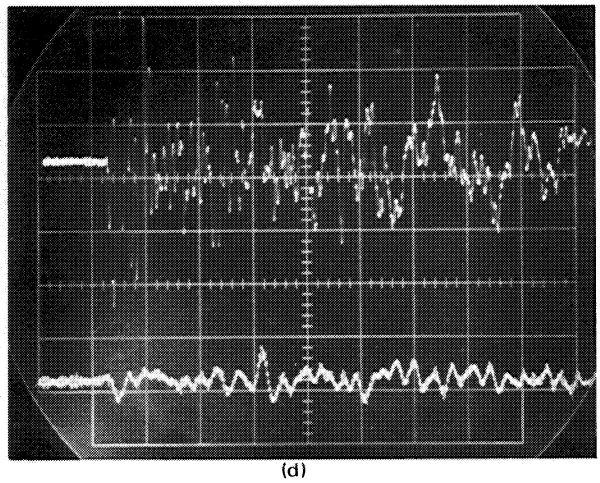

(d)

RECORD RATE 20μs/cm

UPPER TRACE: PZT-5A DISK IMPACT GAGE NO. 4 (LOCATION NO. 4) IV/cm, CH 7

LOWER TRACE: ELECTRET FEP PROTOTYPE IMPACT GAGE NO. 7 (LOCATION NO. 7) 1V/cm, CH 3

Figure 4-33. Oscilloscope Records of Impact Gage Signals Recorded on Tape Recorder During Shot B54-2-16

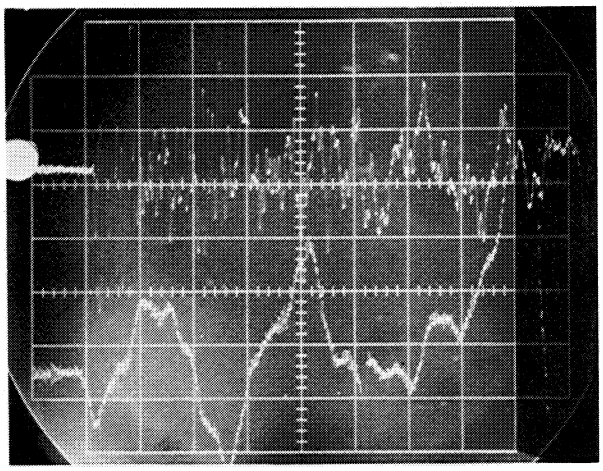

(a)

RECORD RATE 20μs/cm

UPPER TRACE: PZT-5A DISK IMPACT GAGE NO. 4 (LOCATION NO. 4) 1V/cm, CH 7

LOWER TRACE: MYLAR TAPE IMPACT GAGE NO. 5 (LOCATION NO. 5) 0.2V/cm CH 9

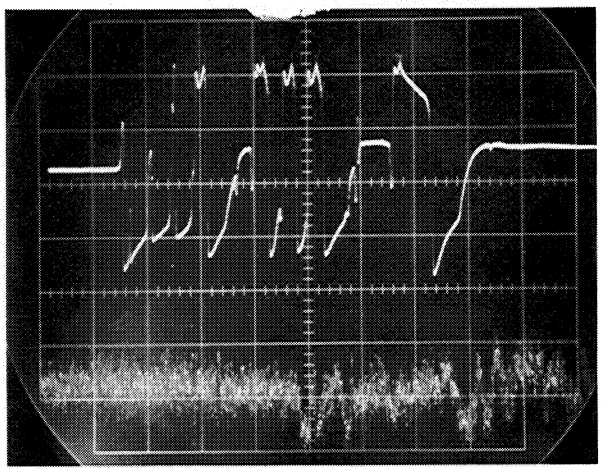

(b)

RECORD RATE 50μs/cm

UPPER TRACE: PZT-5A PROTOTYPE IMPACT GAGE NO. 1 (LOCATION NO. 1) 0.2V/cm, ch 8

LOWER TRACE: PZT-5A DISK IMPACT GAGE NO. 10 (LOCATION NO. 10) 0.2V/cm, CH 2

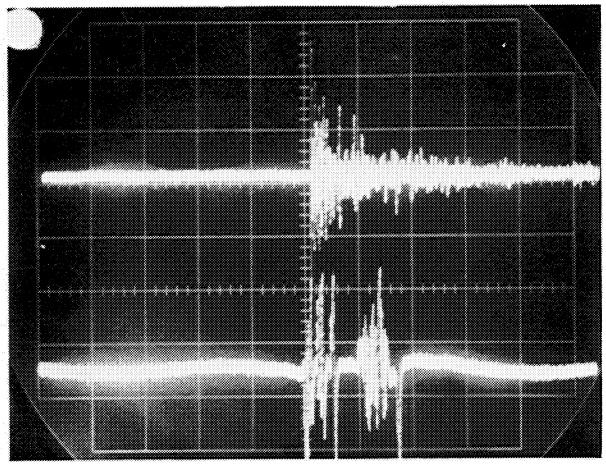

(c)

RECORD RATE 500μs/cm

UPPER TRACE: PZT-5A DISK IMPACT GAGE NO. 4 (LOCATION NO. 4) 1V/cm, ch 7

LOWER TRACE: PZT-5A PROTOTYPE IMPACT GAGE NO. 1 (LOCATION NO. 1) 1V/cm, CH 1

Figure 4-34. Oscilloscope Records of Impact Gage Signals Recorded on Tape Recorder During Shot B54-2-16

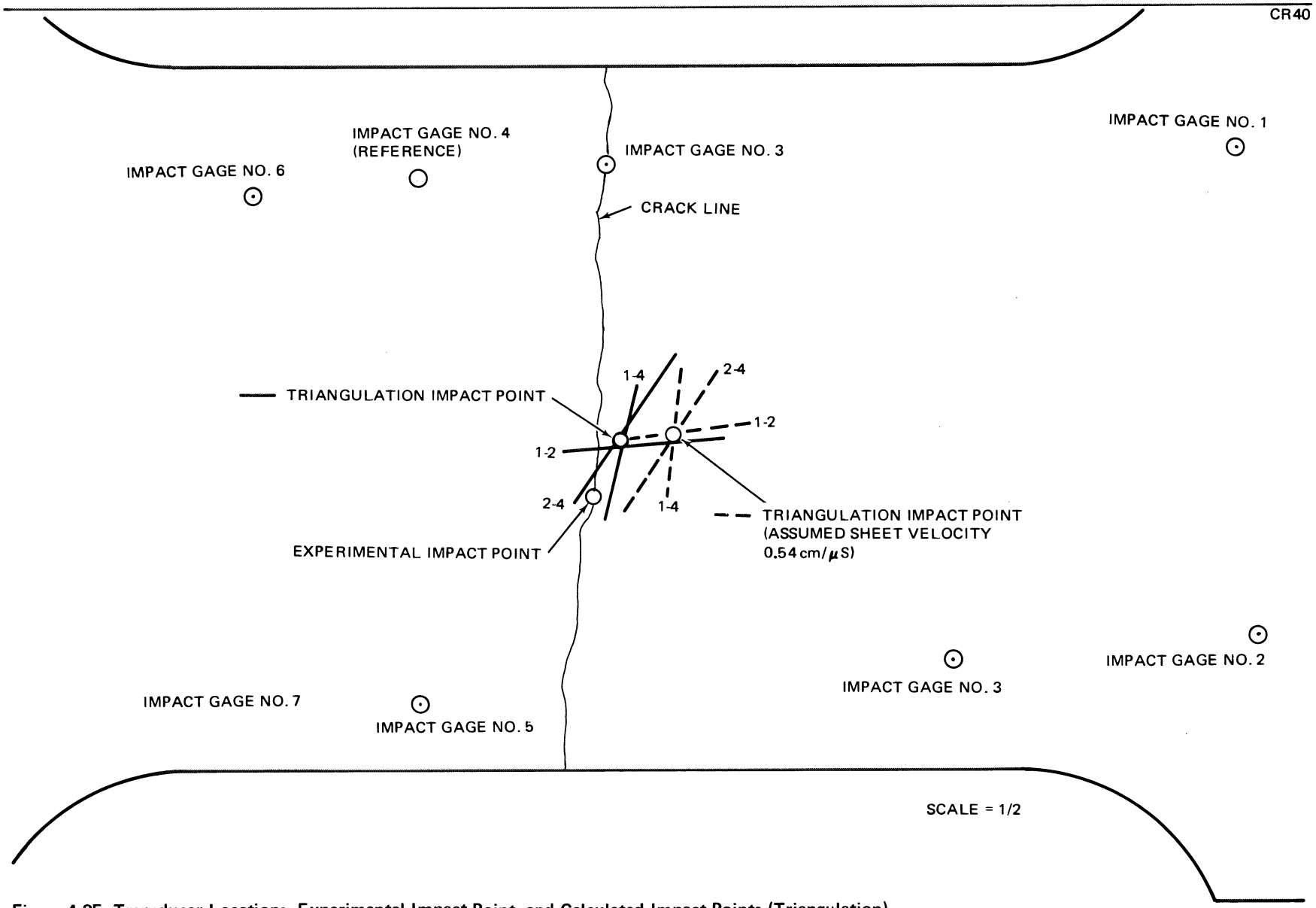

Figure 4-35. Transducer Locations, Experimental Impact Point, and Calculated Impact Points (Triangulation) Shot B54-2-15

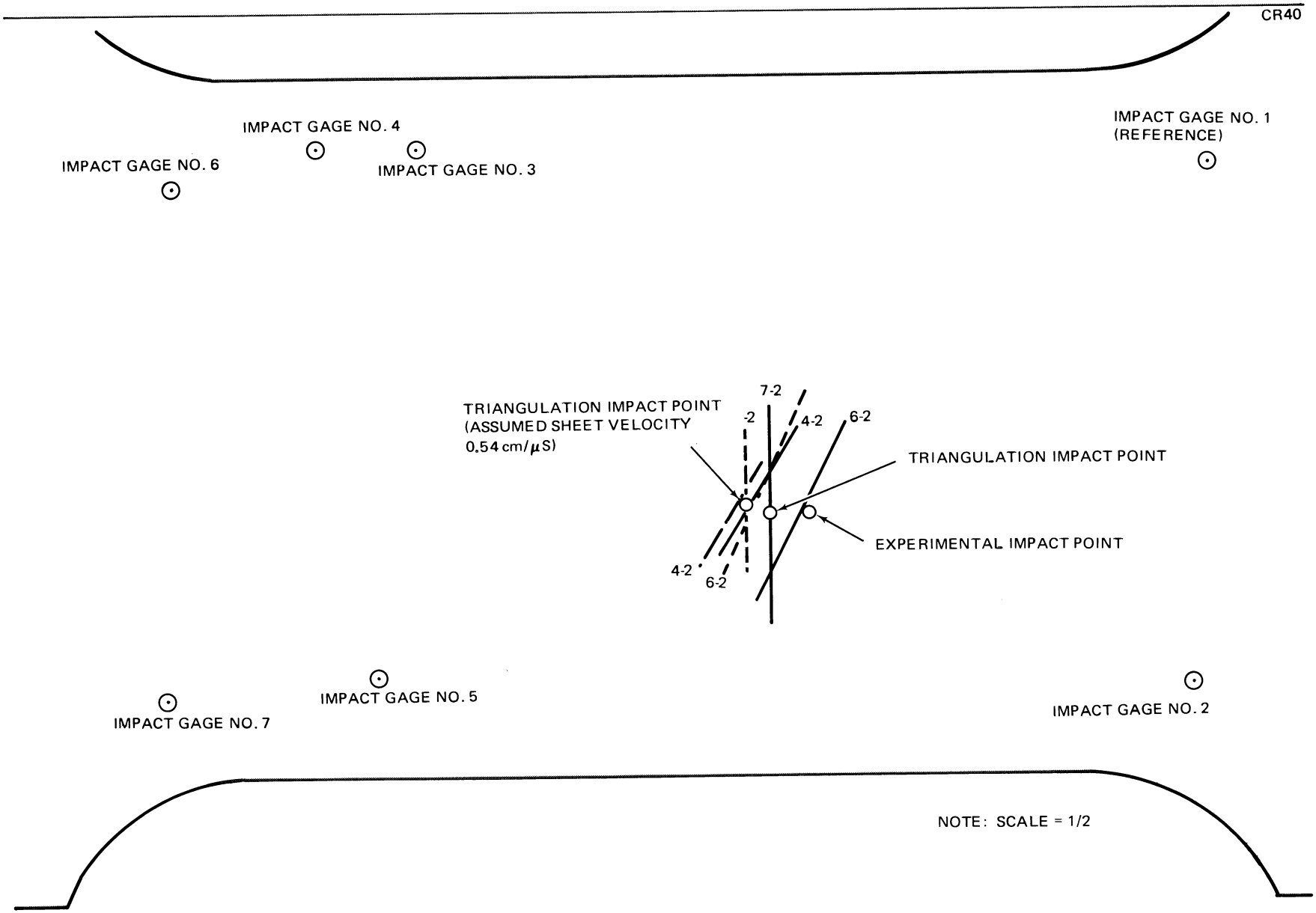

Figure 4-36. Transducer Locations, Experimental Impact Point, and Calculated Impact Points (Triangulation) Shot B54-2-16

were approximately 30 percent higher than the 0.54 cm/μs sheet velocity obtained for previous shots. Two possible explanations can be given for these different velocities. First, the impact location for Shots B54-2-15 and 16 occurred approximately the same distance from all of the impact transducers (within 7.6 cm); this resulted in a maximum time of arrival difference of only 15 microseconds between any two impact gages. Hence, recording equipment inaccuracies and errors in reading of the oscilloscope record of only a few microseconds could cause large differences in the calculated velocity. Secondly, these shots were made under different test conditions.

All of the impact gages except one produced observable output signals during the first 100 microseconds after the hypervelocity impact. However, the Electret FEP prototype gage No. 7 and the Mylar tape gage No. 5 produced no output during Shot B54-2-15 because of damages to electrical leads during installation. The Mylar "sheet" gage No. 8 produced no observable output during Shot B54-2-16 because only a few small debris particles impacted on its Mylar sensing element with no penetration. Correspondingly, the gage output signals were too low to be distinguished from the data acquisition system noise. No definite reason can be given for no output signal from the PZT-5A disk gage No. 3 during Shot B54-2-16.

The highest pulse-amplitude signals from the impact gages on the target sheet were obtained from PZT-5A disk impact gage No. 4. The amplitude of its initial pulse was only slightly higher than the PZT-5A prototype impact gage for Shot B54-2-15, but significantly higher for the next shot. The initial pulse amplitude of the impact gages on the target sheet, based upon the descending order of output*, are as follows:

A. PZT-5A disk gage No. 4
B. PZT-5A prototype gage No. 2
C. PZT-5A prototype gage No. 1
D. Electret FEP prototype gage No. 7
E. Electret TFE prototype gage No. 6
F. Mylar tape gage No. 5

*Output voltages are corrected for an equivalent external cabling capacitance of 1800 picofarads and the removal of the amplifiers.

One significant result was that the initial pulse amplitude of the electret FEP prototype gage No. 7 was only slightly lower than the pulse amplitudes of PZT-5A prototype gages.

The initial pulse frequencies of the impact transducers were approximately the same for both shots. The initial pulse frequencies of the target sheet gages ranged from 70 to 290 kHz. These frequencies are only rough estimates and can be misleading because the actual initial pulses (see Figures 4-31 through 4-34) were not pure sine waves but combinations of various frequencies depending upon the impact transducer and the acoustical waves in the sheet. Playback of the tape recorded data into wave-analyzing devices such as a spectrum analyzer (displays amplitude versus frequency) would allow study in more detail of the resultant waves in the target sheets generated by hypervelocity impacts.

A color change from light green (ambient condition) to dark purple (greater than 313K temperature condition) was observed from the liquid crystals on the rear surface of the Mylar "sheet" impact gage after Shot B54-2-16. The color change occurred in a spherical pattern approximately 12.7 cm in length and 7.6 cm in width and was centered directly behind the hypervelocity impact on the target sheet.

4.7.2 Acoustical Emission Experiment

Attempts were made to monitor acoustic emissions from the stressed target sheets which might occur after the hypervelocity impact. The tape recorder continued to record for five minutes after the shots were made and the oscilloscopes were set to very high sensitivities and placed in the continuous display mode. No obvious acoustic emissions were observed.

Shot B54-2-15 was made with the target sheet stressed to 3.0×10^8 N/m^2. The photograph in Figure 4-27 shown the catastrophic failure of the target sheet which occurred from the hypervelocity impact. No obvious acoustic emissions were observed from the signals outputs of the impact gages on the target sheet either before the shot while the target sheet was stressed or after the hypervelocity impacts of the debris particles. The output signals from two of the target sheet impact gages are shown in Figure 4-32(b) for a

few milliseconds after the hypervelocity impact. Note that no obvious acoustical emission pulses are present.

For Shot B54-2-16, the only test condition which was different from the previous shot was that the target sheet was stressed to only 1.37×10^8 N/m^2. The hypervelocity impact of the debirs particles caused only a small hole (approximately 1.57 mm dia) in the target sheet. This can be seen from the photographs of the target sheet in Figures 4-29 and 4-30. No definite acoustic emission signals were observed from the signal outputs of the impact gages on the target sheet either before the shot, while the target sheet was stressed, or after the hypervelocity impacts of the debris particles. However, a few large output signals were produced from the PZT-5A disk Impact Gage 4 and the PZT-5A prototype gage No. 1 which were not produced in the previous shot (see Figure 4-34(c)). These signals could have been caused by acoustic emissions.

Following Shot B54-2-16, a test was set up to find out if acoustic emission could be observed on the target sheet under static conditions after the target sheet had been impacted by hypervelocity debris particles. The instrumentation setup and the transducers installed on the new target sheet were the same as for Shot B54-2-16 except that Impact Gage 7 was not installed and the ultrasonic amplifier was used to amplify the signal from the PZT-5A disk Impact Gage 4. The amplifier was installed approximately 3 m away from the gage. The target sheet from Shot B54-2-16 was maintained at a stress level of 1.37×10^8 N/m^2. Impact Gages 1, 2, and 3, which were knocked off the target sheet after Shot B54-2-16 were epoxied on the sheet. The stress level on the target sheet was increased in four steps until catastrophic failure of the target sheet occurred. Signal outputs of the impact gates were recorded on the tape recorder, and a few of the gage outputs were also monitored on oscilloscopes which were set to very high sensitivities and placed in the continuous display mode.

The following results were obtained:

Stress (N/m^2)	Acoustic Emission Pulses
1.37×10^8	zero
1.37×10^8 to 1.65×10^8	zero
1.65×10^8 to 2.17×10^8	two in two minutes
2.17×10^8 to 3.0×10^8	approximately ten in two minutes
3.0×10^8 to 3.1×10^8	large number of acoustic emissions which rapidly increased in occurrence just before catastrophic failure
3.1×10^8	catastrophic failure

An oscilloscope record of an acoustic emission which occurred when the target sheet was stressed at approximately 3.02×10^8 N/m^2 is shown in Figure 4-37. The amplitude of the acoustical emission signals at the ultrasonic amplifier input was approximately 35 mV.

A photograph showing the target sheet after catastrophic failure is given in Figure 4-38. The crack line was centered at the center of the hyper-velocity impact location and ran approximately in a horizontal straight line across the sheet. The crack line resulting from the catastrophic failure of the target sheet during Shot B54-2-15 was slightly curved.

4.8 MINIATURE IMPACT GAGE

Miniature impact gages were designed and built based upon the experience gained with the prototype impact gages. One model was constructed to allow a "chip" integrated-circuit amplifier to be installed inside the gage housing as shown in Figure 4-39. The miniature impact gages were designed so that both ceramic and plastic piezoelectrics could be used as gage "sensing" elements. Two other smaller models, constructed for use without an amplifier in the gage housing, are shown in Figure 4-40.

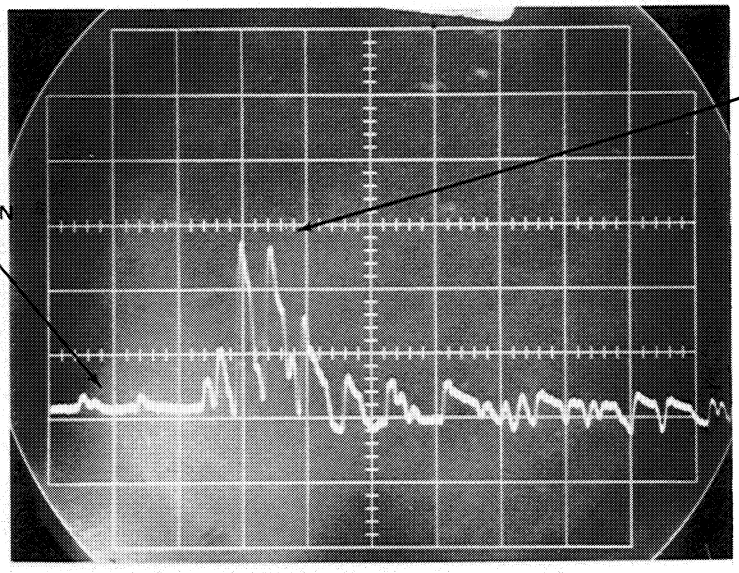

(a)

RECORD RATE 10μs/cm

IMPACT GAGE NO. 4: (ACOUSTICAL EMISSION)

SENSITIVITY: 1V/cm, CH 5

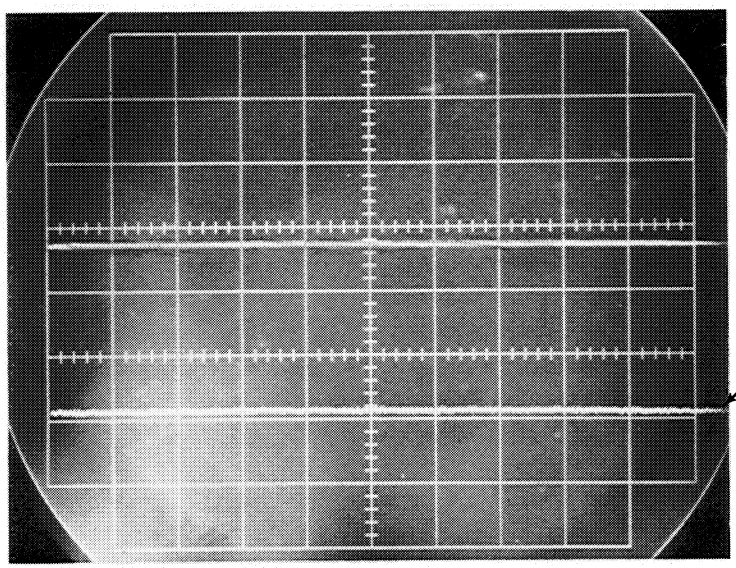

(b)

RECORD RATE 10μs/cm

IMPACT GAGE NO. 4: (ZERO TRACE)

SENSITIVITY: 1V/cm, CH 5

Figure 4-37. Oscilloscope Record of an Acoustical Emission Signal Recorded on Tape Recorder After Shot B54-2-16

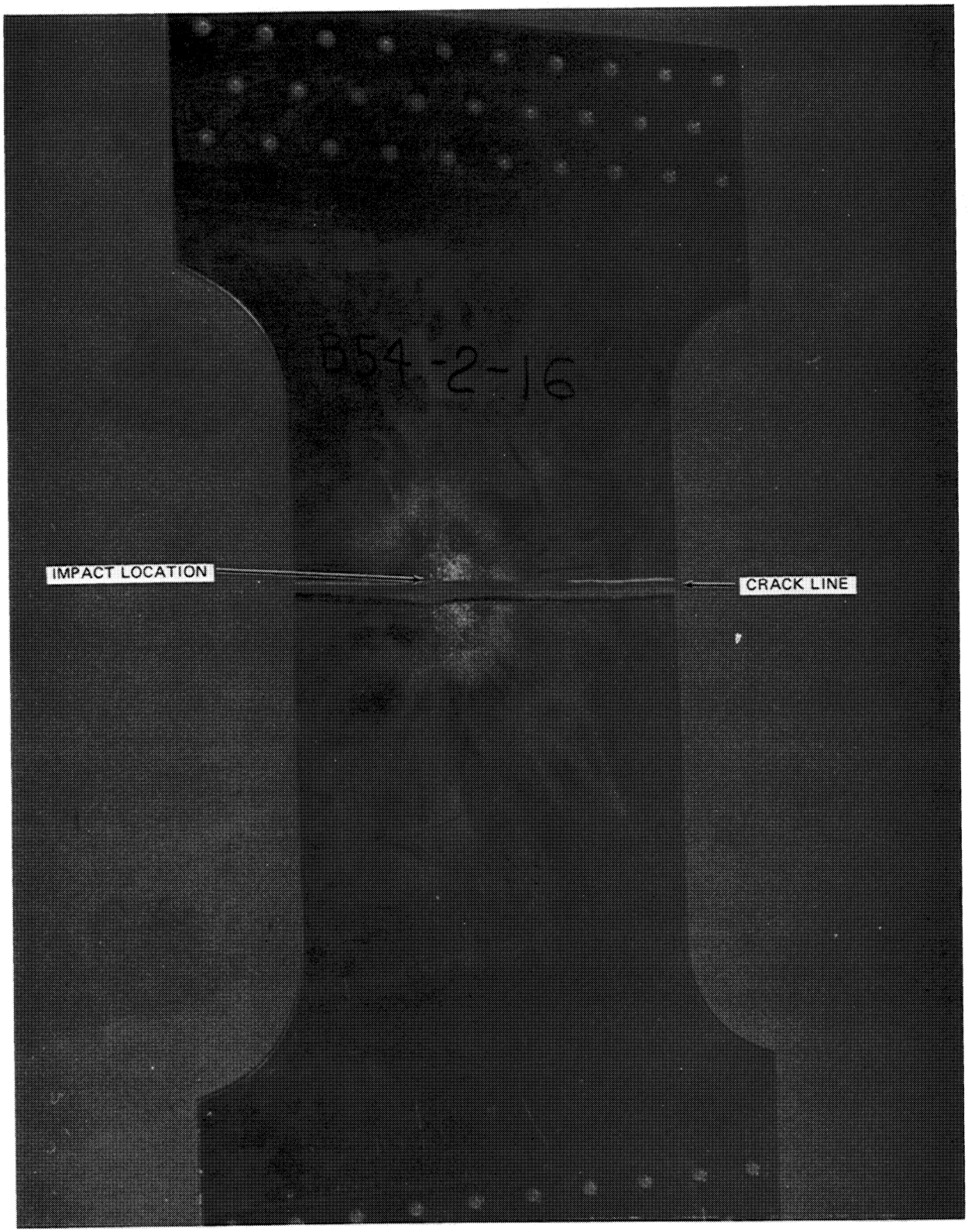

Figure 4-38. Photograph of Target Sheet of Shot B54-2-16 Taken After Target Stressed to 3 x $10^8 N/m^2$

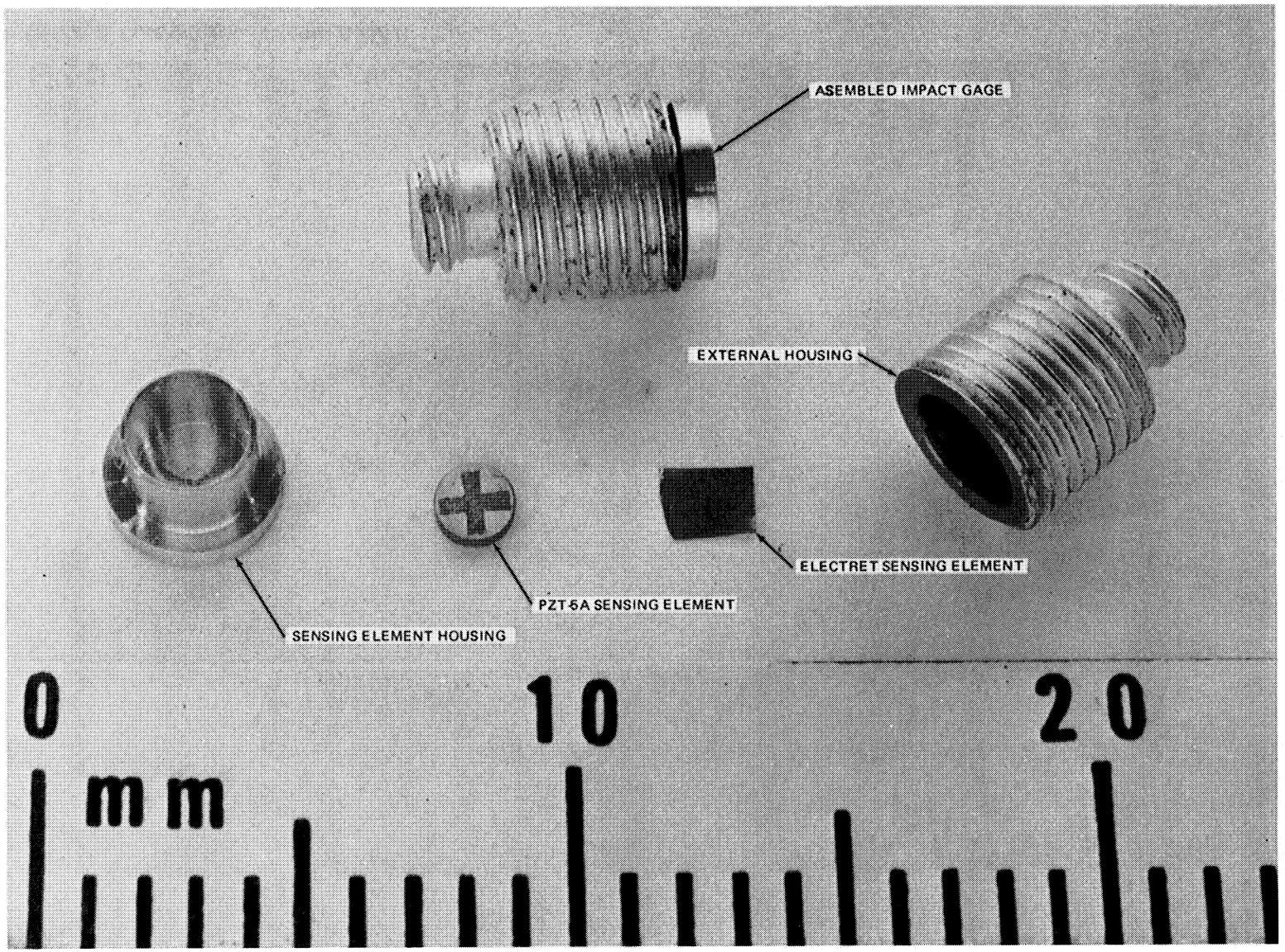

Figure 4-39. Miniature Impact Gage – Model A

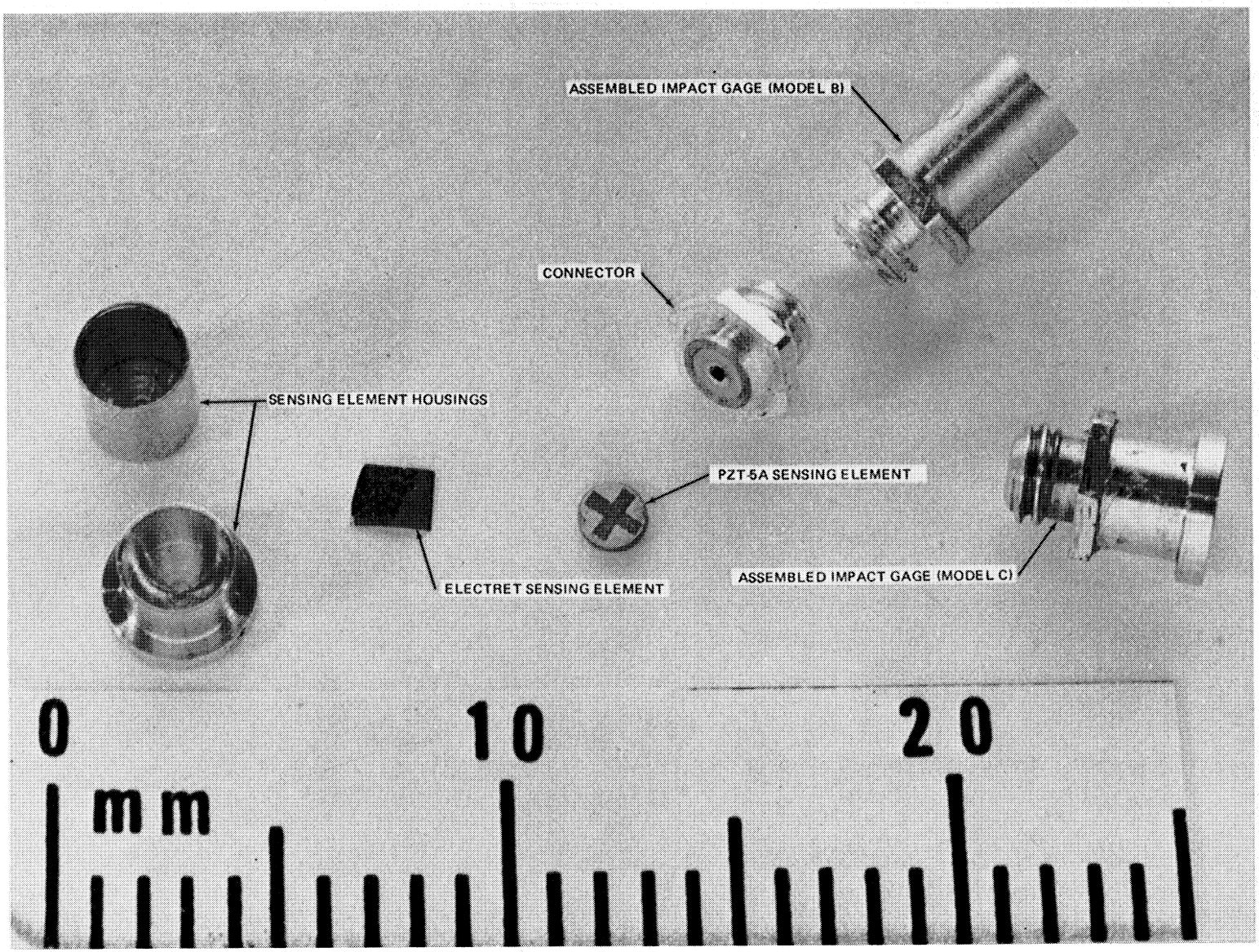

Figure 4-40. Miniature Impact Gages — Models B and C

Basically, the impact gage consisted of a ceramic or plastic piezoelectric sensing element bonded to the inside sensing element housing (aluminum) with conductive epoxy. An electrical lead was attached to the back side of the sensing element with conductive epoxy and then soldered to the center conductor of the external housing (brass). Depending upon the desired frequency response of the gage, the sensing element housing was either encapsulated with a filled epoxy or left unpotted. Then it was bonded to the external housing with conductive epoxy. A standard connector was a part of the external housing. The impact gage was then connected to the data-acquisition system using low noise cable.

One of the impact gages (model A) is shown installed on an isogrid wall structure of a 2.42-m-diameter Delta tank wall structure prior to testing (Figure 4-41).

Miniature impact gages with PZT-5A and Electret FEP sensing elements and "off the shelf" impedance converters connected to the output connector of the impact gages are shown in Figures 4-42(b) and 4-42(d). These impedance converters significantly reduced the attenuation of the impact gage output signal by external cable capacitance. Figures 4-42(a) and 4-42(c) show the output signals of these impact gages for identical acoustic pulses generated on the diaphragm of each impact gage. Although its open circuit output is attenuated by a factor of 2 by the impedance converter, the impact gage with the electret sensing element produced approximately the same output voltage as the impact gage with the PZT-5A sensing element.

4.9 PARAMETRIC TESTS ON IMPACT GAGES—BALLISTIC RANGE TEST SERIES 4 (LARGE SHEET STRUCTURES)

4.9.1 Parametric Tests with Miniature Light-Gas Gun

A fourth series of hypervelocity impact tests were made at the MDAC Aerophysics Laboratory using a miniature light-gas gun. The MDAC miniature light-gas gun shown in Figure 4-43 offered many advantages for impact gage tests on large sheet structures. For parametric studies involving a large number of shots, the mini-gun afforded a low-cost method of accelerating projectiles over a wide range of velocities. Furthermore the gun could be operated in the open laboratory in air as shown in Figure 4-44 or in a

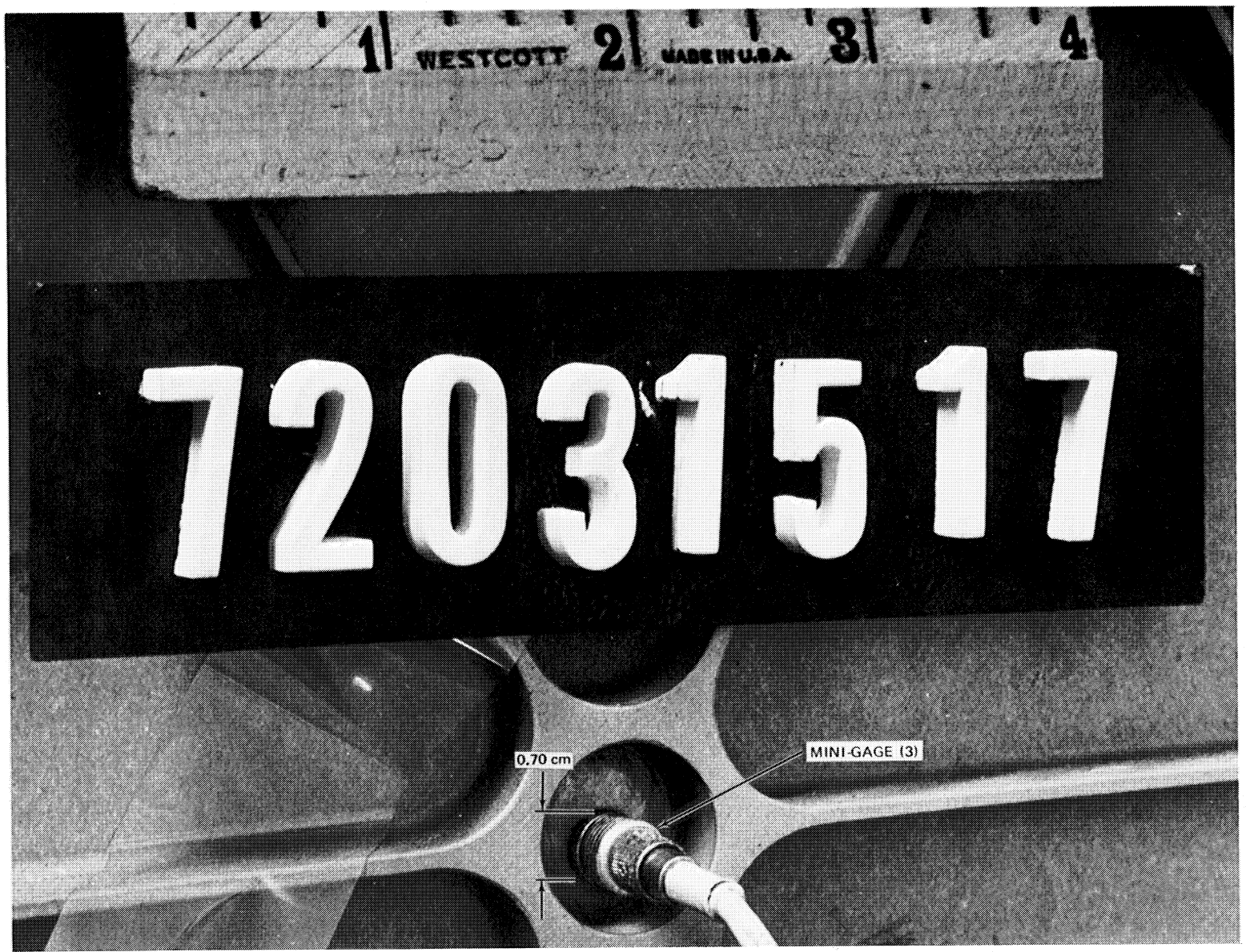

Figure 4-41. Miniature Impact Gage (3) Model A Installed on Isogrid Wall of 8-Foot-Diameter Delta Tank

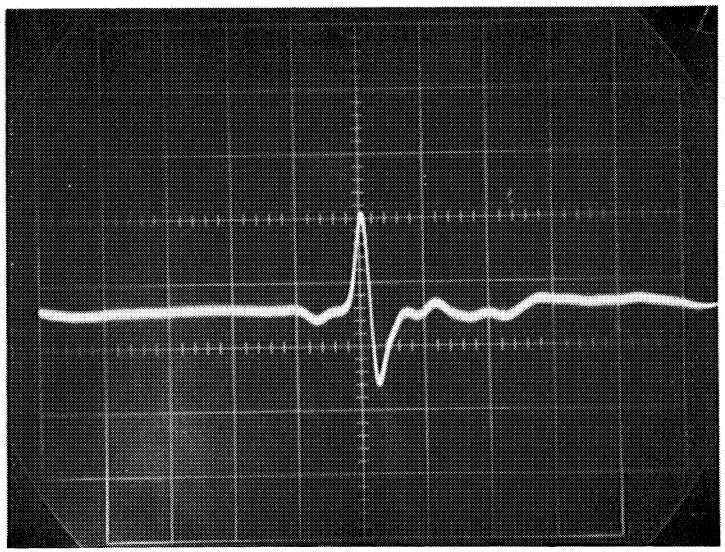

RECORD RATE 20 μs/cm

MINI IMPACT GAGE WITH PZT-5A SENSING ELEMENT - 200 mV/cm

(a)

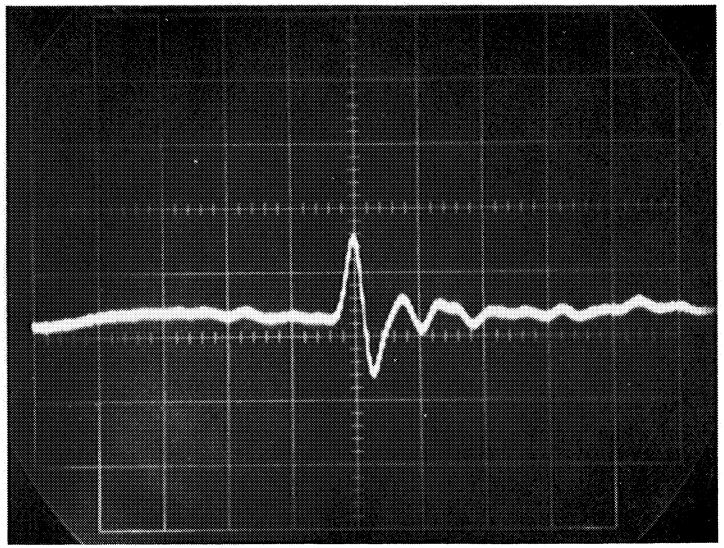

RECORD RATE 20 μs/cm

MINI IMPACT GAGE WITH ELECTRET FEP SENSING ELEMENT - 200 mV/cm

(c)

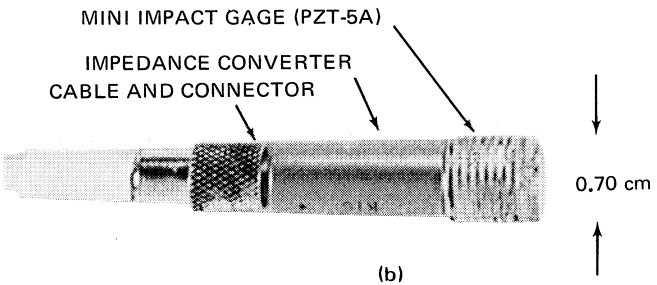

(b)

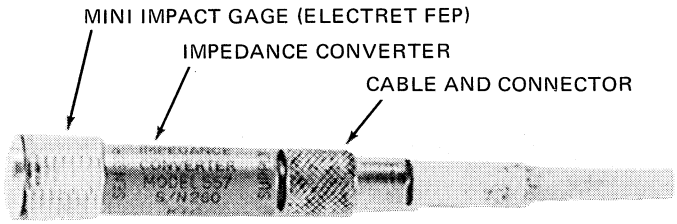

(d)

Figure 4-42. Miniature Impact Gage Output with Impedance Converters for Identical Acoustical Signal Input

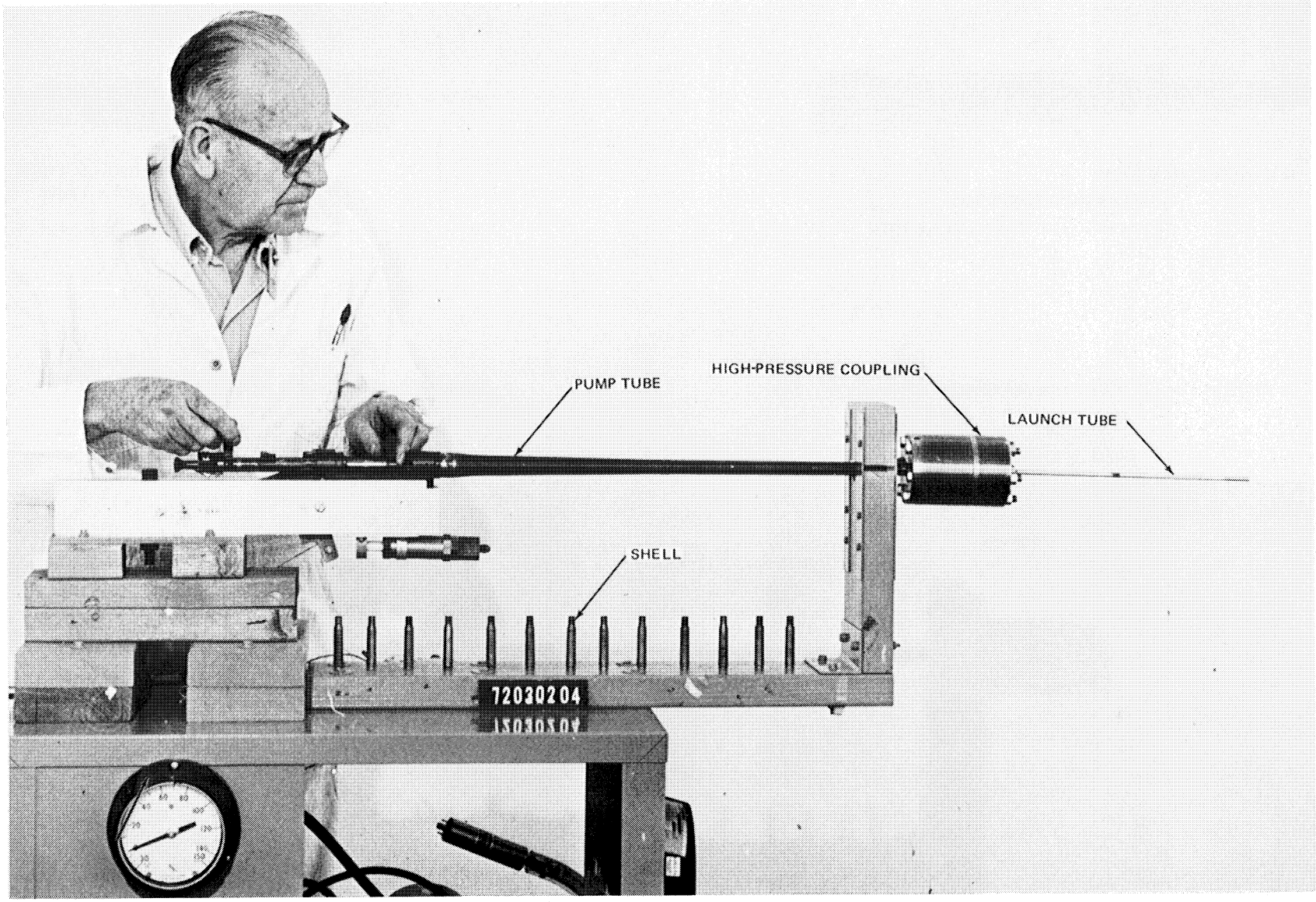

Figure 4-43. Mini-Portable Light-Gas Gun Used for Impact Gage Tests

conventional target chamber. The gun provided flexibility in that it is portable and could be employed under field conditions.

Typical Mini-Gun Performance Parameters are:

A. Projectile - 5 mg 2.3-mm-dia polyethylene cylinder
   Velocity range: Helium - 1 to 6 km/s
   Hydrogen - 1 to 8 km/s

B. Projectile - 12 mg, 3.2-mm-dia polyethylene cylinder
   Velocity range: Helium - 1 to 4.5 km/s
   Hydrogen - 1 to 6 km/s

Impact tests were carried out on two large target sheets of aluminum (3.65m by 1.21m by 1.6 mm) and (3.65m by 1.21m by 0.42 mm). These sheet thickness are characteristics of typical future manned payload carriers. Parametric tests were used to study impact gage signal characteristics as a function of projectile kinetic energy, momentum, and sheet thickness. An impact gage signal processing subsystem was also tested successfully for triangulation predictions of impacts on large structural sheets. Results will be discussed in a later section.

Thirty-six tests were carried out. Of these, only the most pertinent will be discussed. Limited parametric tests to study the relationship of impact gage signal characteristics to projectile energy, momentum, and sheet thickness were carried out for the complex condition of target penetration in order to relate signal output to an actual hole (leak) condition. The test data given in Table 4-11 indicates that signal amplitude is not a simple function of energy or momentum. The stress-wave amplitude is related to the energy transfer to the plate during the interaction process between plate and projectile. As expected, the signal amplitude for penetration of thin sheets (0.42 mm thick) is much smaller than for sheets of thickness 1.60 mm. For very low-velocity impacts such as 8.1 kg ballistic pendulum impacting at 1.60 m/s (test 57-31), signal output was negligible even though a large momentum was imparted to the sheet. This test result suggests a time-dependent function for impact-gage signal amplitude.

Table 4-11

IMPACT GAGE TEST RESULTS—SERIES 4
(LARGE STRUCTURES)

SHOT	PROJECTILE PARAMETERS					IMPACT GAGE			
	Shape	Mass (mg)	Velocity (km/s)	Kinetic Energy (J)	Momentum (kg m/s)	No.	Distance From Impact (cm)	Amplitude (1) (mV)	S.A.T (2) (μs)
B57-18	Polyethylene Cylinder	8	4.7	80	0.0359	1	34.0	4,800	43
						2	213	4,200	370
						D	213	200	370
						E	8.9	8,000	Reference
B57-23		32	2.82	110	0.091	1	236	800	415
						2	55	9,000	83
						D	54	800	80
						E	9.2	5,000	Reference
B57-24		8	4.7	80	0.0358	1	230	850	392
						2	48.5	11,000	66
						D	47.0	1,000	62.5
						E	11.7	2,500	Reference
B57-28 (3)		8	4.7	80	0.0358	1	232	200	400
						2	56.5	8,800	76
						D	47.2	200	63
						E	17.5		Reference

Table 4-11

IMPACT GAGE TEST RESULTS—SERIES 4
(LARGE STRUCTURES) (Continued)

SHOT	PROJECTILE PARAMETERS					IMPACT GAGE			
	Shape	Mass (mg)	Velocity (km/s)	Kinetic Energy (J)	Momentum (kg m/s)	No.	Distance From Impact (cm)	Amplitude (1) (mV)	S.A.T (2) (μs)
B57-31	Pendulum Polyethylene	8.1 x 10^{3}	1.60 x 10^{-3}	9.4	12.3	1	207	1.5	380
						2	29.5	5.5	
						D	26.6	5.5	54
						E	6.35		Reference
B57-36 (4)	Polyethylene Cylinder	8	4.7	80	0.0358	1	27.3	750	35
						2	91		152
						D	25.4	700	32
						E	7	1,000	Reference

(1) Peak-to-peak amplitude of second output pulse from impact gage
(2) S.A.T - Signal arrival time at impact gage
(3) 4-in. dia. hole cut from the aluminum sheet between the impact point and impact gage (D)
(4) Test shot using 0.406-mm-thick target sheet

The point of impact on the pressure wall was successfully determined within a few inches by shock wave time-of-arrival triangulation techniques using impact gages as far as 2.43m from the point of impact. However, when a test shot was made with impact gages separated from the impact location by a large cutout, the point of impact was successfully located but with a location error of approximately 0.3m. The frequency of the initial output pulses of the impact gages for waves generated in the sheets for high projectile velocity impacts decreased linearly for increasing sheet thickness. This result agrees with previous test results and suggests that the first stress waves generated in the thin sheets and sensed by the impact gages are symmetrical type Lamb Waves.

4.9.2 Test Details - Large Sheet Structures

Large sheets of 6061T6 aluminum (3.65m by 1.21m by 1.6 mm) and (3.65m by 1.21m x 0.42 mm) were installed in the gun room at the MDAC Aerophysics Laboratory and were impacted by projectiles launched from the miniature light-gas gun. Figure 4-44 shows the test setup. The aluminum sheets were supported by thin metal strips clamped to the ceiling and to the top edge of the sheets. The following four types of impact transducers (total of eleven impact gages) were mounted on the target sheets:

A. Impact Gages 1, 2, and 3 - Prototype impact gages with PZT-5A disk* sensing elements. Impact Gages 2 and 3 were bonded to the front surface of the target sheet using a thin coating of Eccobond Epoxy No. 285R, and Impact Gage 1 was bonded to the target sheet using a thin coating of Epoxy Patch Kit.

*PZT-5A piezoelectric ceramic disks were 0.317 cm in diameter and 0.635 mm thick with the negative side of the disk placed closest to the target sheet.

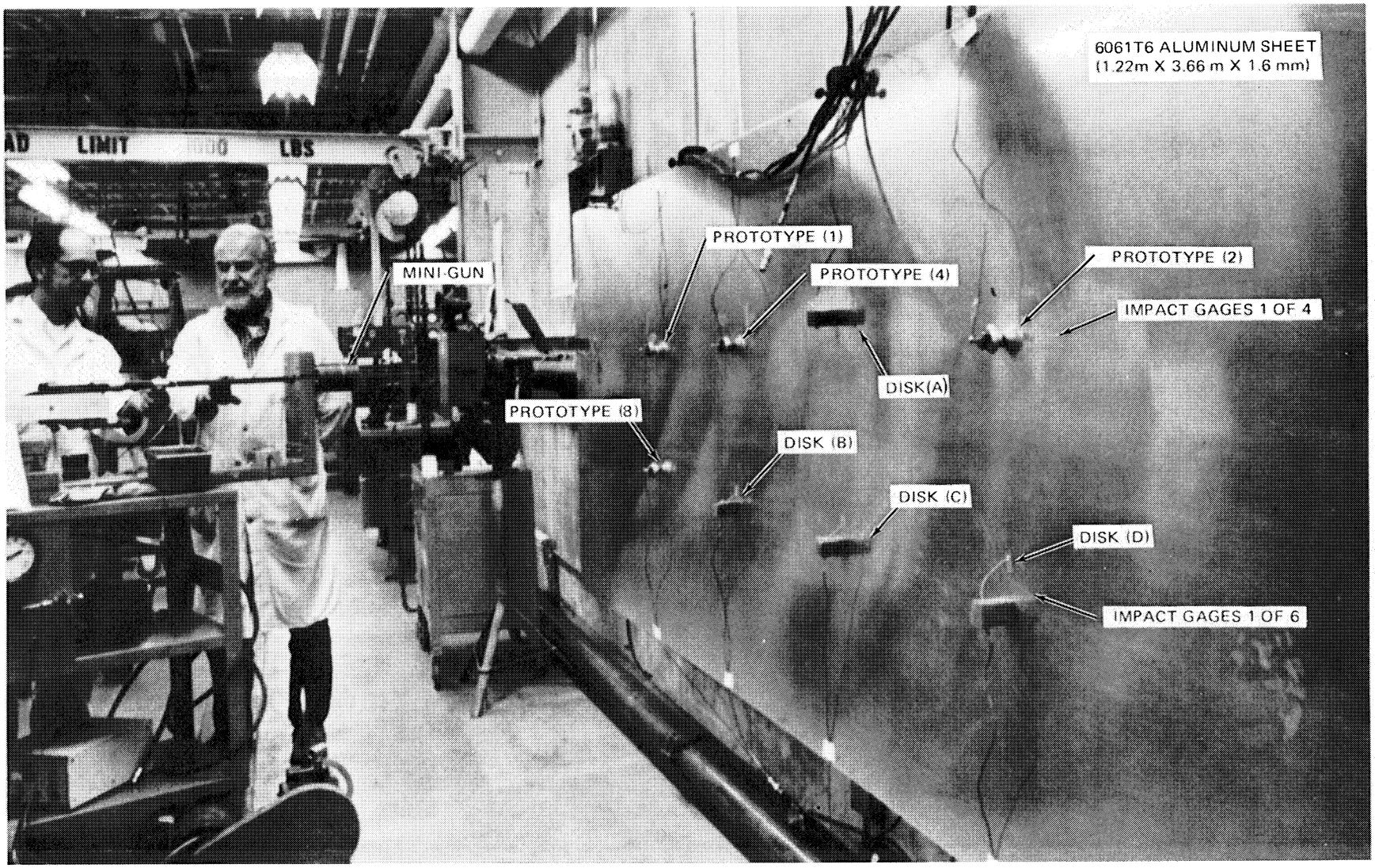

Figure 4-44. Test Setup of Impact Gage Triangulation Experiment on Large Area Wall Structure

B. Impact Gage 4 - Prototype impact gage with Electret-FEP sensing element, 0.0254-mm thickness and 0.635-cm diameter was bonded to the front surface of the target sheet using a thin coating of Eccobond Epoxy No. 285R.

C. Impact Gages A, B, C, D, AB, and E - PZT-5A ceramic disk impact gages consisted of a PZT-5A ceramic disk with electrical leads (36AWG) soldered to both sides. All gages except AB were installed on the front surface of the target sheet. Impact Gage AB was installed on the back side of the sheet directly opposite to Impact Gage A. A thin film of ultrasonic grease (Sperry grease No. 50A4084) was placed between the sheets and the negative side of the disk. The disks were held in place using Mylar pressure-sensitive tape (DPM 868).

D. Impact Gage (MINI-1) - Mini-impact gage with a PZT-5A sensing element and backed with epoxy was installed on the target sheet using a thin coating of Eastman 910 contact cement.

Figure 4-45 shows the locations of the impact gages on the 1.6-mm-thick target sheet. Eight of the above impact gages were installed for the test shots on the 0.42-mm-thick target sheet. Impact gage locations are shown in Figure 4-46. A prototype and a mini-impact gage were bonded to the target sheet using a thin coating of Eastman 910 contact cement.

In addition to hypervelocity impacts on the target sheets from projectiles launched from a miniature light-gas gun, low-velocity high-kinetic energy impact tests were made on the sheet using a ballistic pendulum projectile. Figure 4-47 shows a photograph of the 8.1 kg projectile which was suspended from the ceiling with safety wire.

The impact gages, timing markers, and time-zero (gun firing) outputs were recorded on a wide-band (1.5 MHz) tape recorder. Six of the impact gages were also recorded on three oscilloscopes during the test shots.

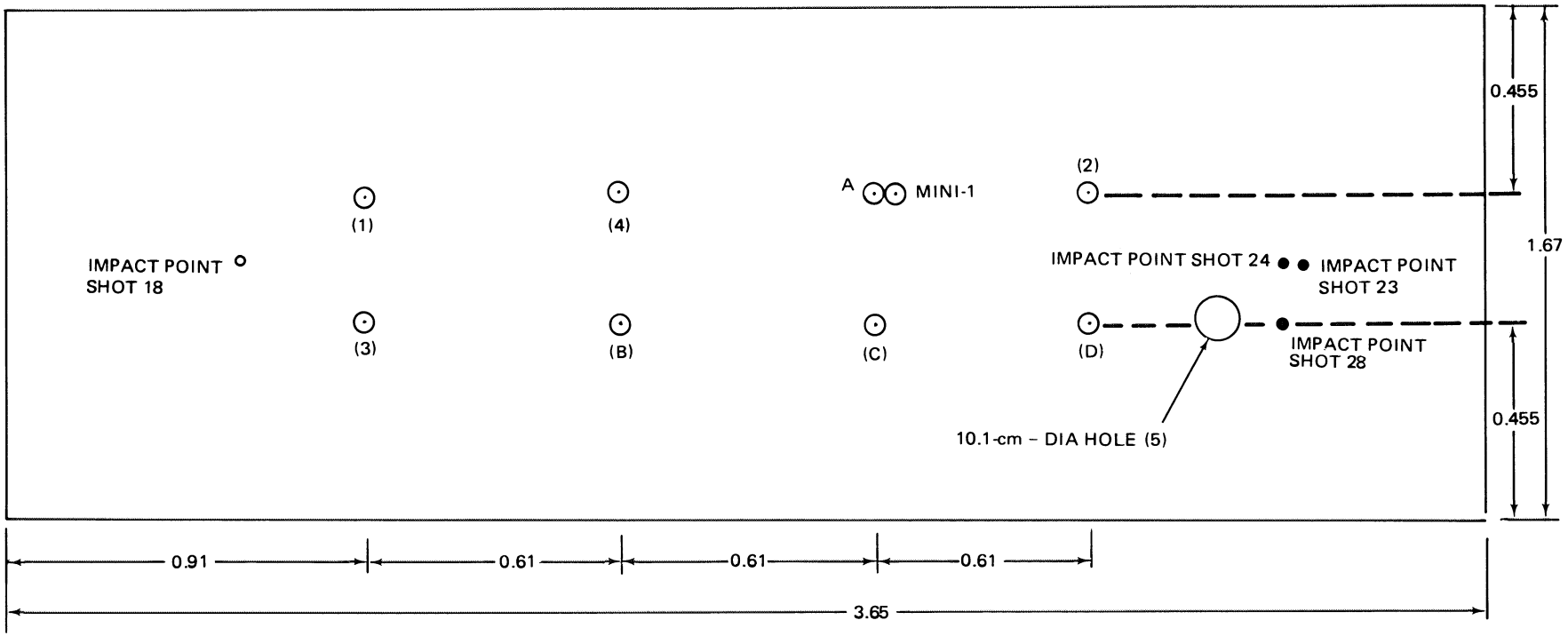

NOTES:
1. ⊙ IMPACT GAGE LOCATION
2. ALL DIMENSIONS IN METERS
3. IMPACT GAGE (AB) LOCATED ON OPPOSITE SIDE OF SHEET AT SAME LOCATION AS IMPACT GAGE (A)
4. 10.1-cm-DIA HOLE MADE IN SHEET FOR TEST SHOT B57-28

Figure 4-45. Impact Transducer Installation on Large Aluminum Sheet (1.6 mm Thick) for Triangulation Experiments Test B57

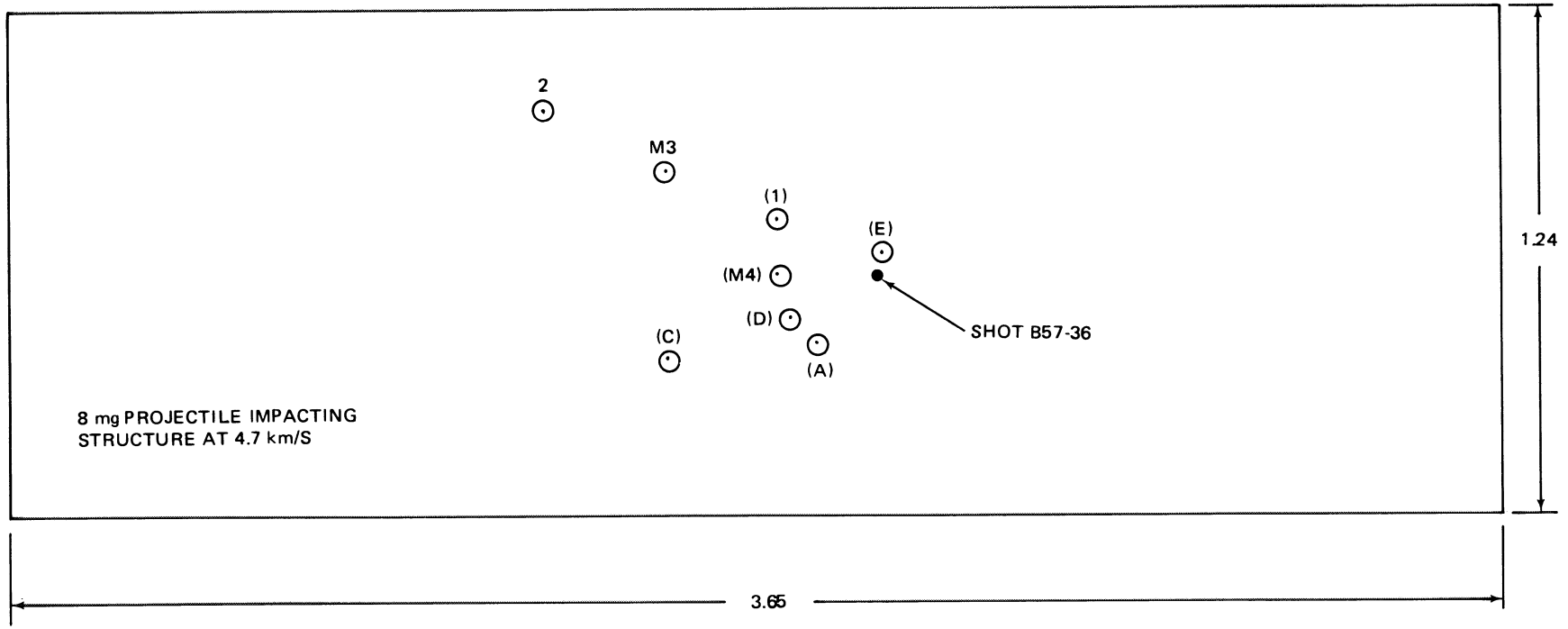

NOTES: 1. ⊙ IMPACT GAGE LOCATION
2. ALL DIMENSIONS IN METERS

Figure 4-46. Test Setup Shot B57-36 (Ballistic Range)

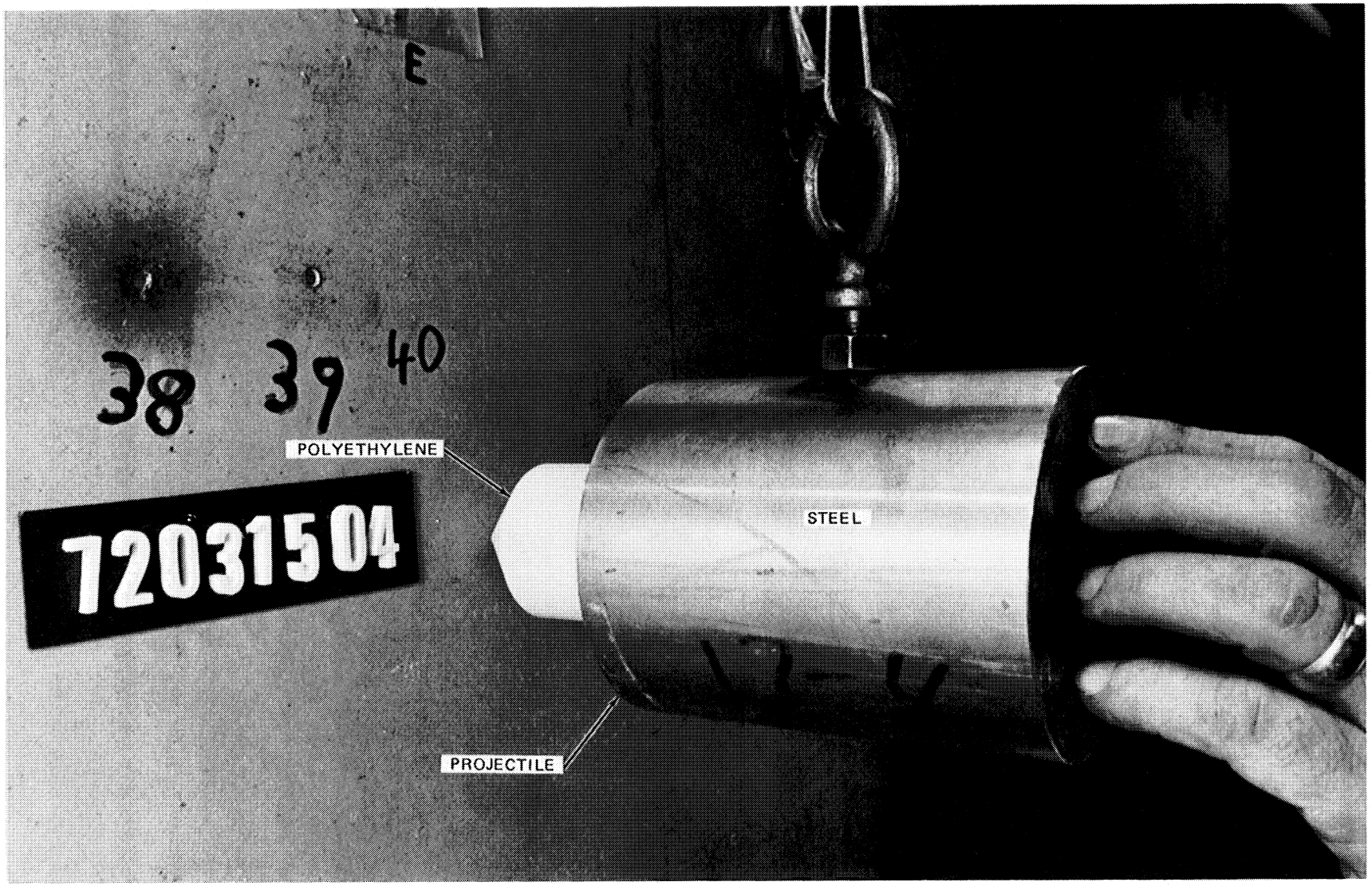

Figure 4-47. Projectile used for Ballistic Pendulum-Type Impacts on Large Target Sheet

Test conditions and pertinent data from a few of the impact gages are given in Table 4-11 . Figure 4-48 shows typical oscilloscope records obtained from the output of the impact gages. A plot of impact gage output voltage and distance from the point of impact is given in Figure 4-49. The attenuation of the output signal of the three plotted impact gages appears to be approximately 12 percent for each 0.3-m increase in distance from the impact location.

Figures 4-50 and 4-51 show typical results obtained for locating the point of impact using triangulation techniques. The point of impact (triangulation) was located exactly at the impact point for Test Shot B57-24 for the smooth 1.6-mm-thick sheet. For one of the test shots (B57-28), a 10.1-cm-dia hole (a practical worst-case condition) was cut out of the 1.6-mm-thick sheet on a center line between the projectile impact point and impact gage D. The center point of the cutout was approximately 15.3 cm from the impact point and 33 cm from impact gage D. The calculated point of impact (triangulation) was located but with a location error of approximately 0.3m.

A plot of initial pulse frequency of the three impact gages and sheet thickness is given in Figure 4-52.

4.10 IMPACT GAGE TESTS ON DELTA TANK STRUCTURE - BALLISTIC RANGE TEST SERIES 5

The final series of hypervelocity impact tests were carried out using the miniature light-gas gun on a realistic wall structure featuring an integrally machined isogrid wall, and the large welded section of the test structure provided a realistic worst-case wall structure for triangulation predictions of impact locations.

Four tests were carried out and the results were extremely successful. The point of impact on the wall was successfully determined by shock wave triangulation techniques. Impact points were located within a few inches of the actual impact point. Ballistic pendulum type impacts, which simulated a worst case of internal cabin impacts, produced no measurable output from the impact gages. There was a high attenuation of impact gage output voltages with increasing distance from the impact point as compared to test shots

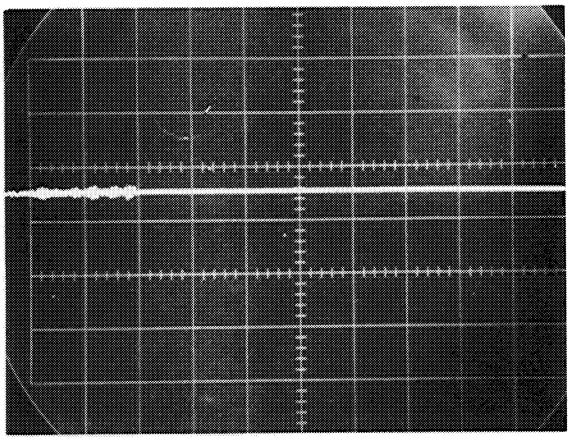

(a)

RECORD RATE: 20 μs/cm

SHOT B57-23 - 2V/cm

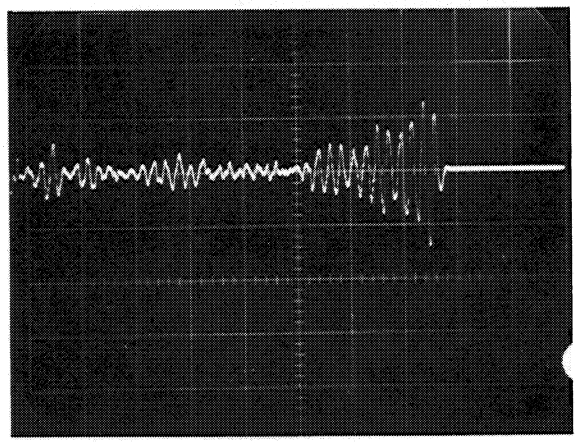

(b)

RECORD RATE: 50 μs/cm

SHOT B57-24 - 1V/cm

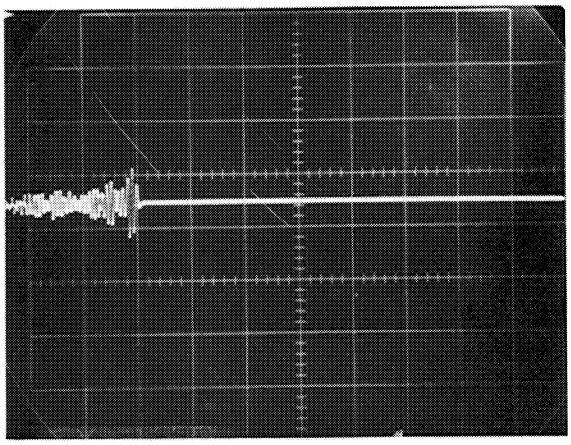

(c)

RECORD RATE: 50 μs/cm

SHOT B57-18 - 1V/cm

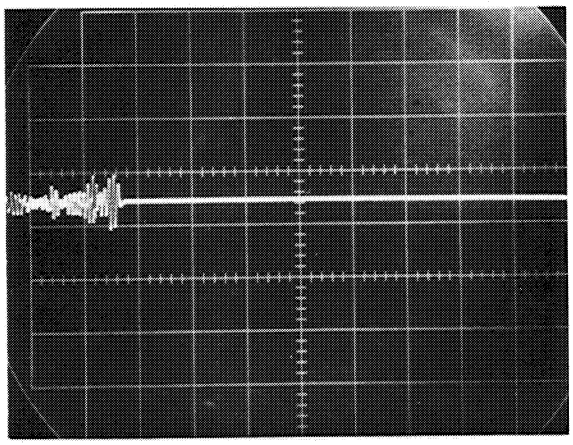

(d)

RECORD RATE: 50 μs/cm

SHOT B57-28 - IV/cm

Figure 4-48. Oscilloscope Records of Impact Gage (1) Signals Recorded on Oscilloscope During Test Shots B57-18, B57-23, B57-24, and B57-28

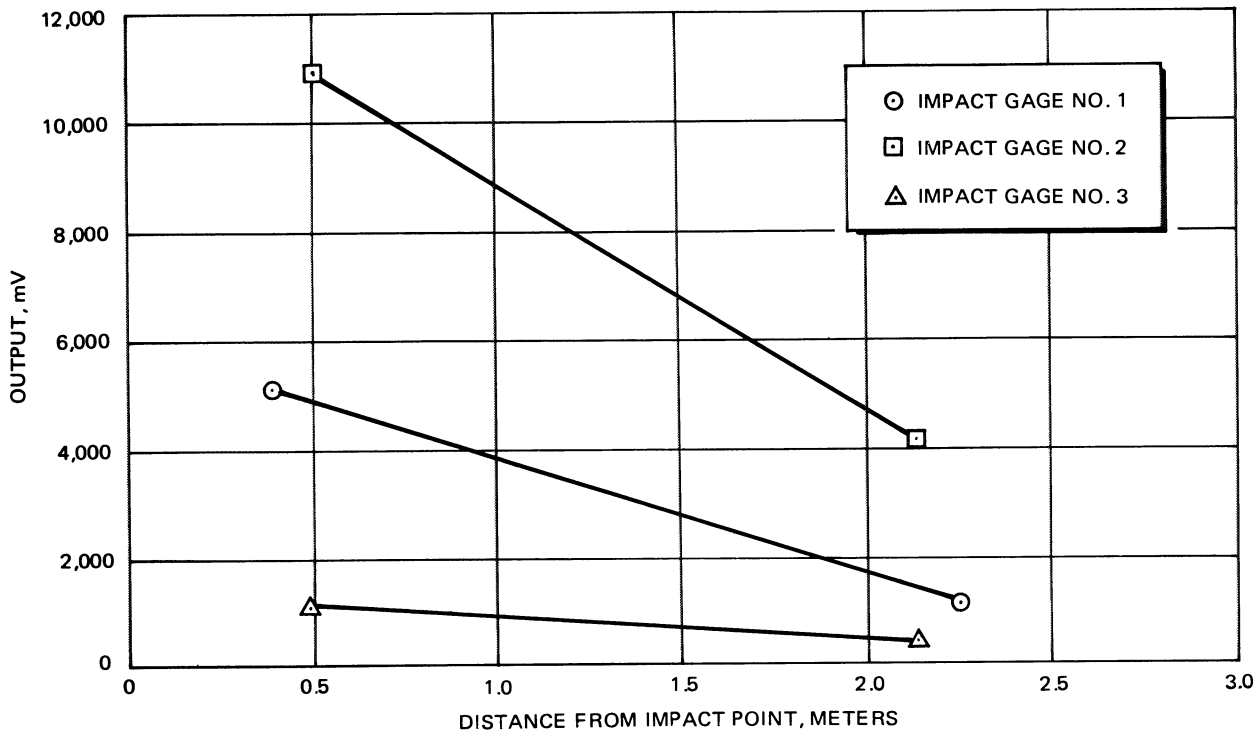

Figure 4-49. Output Voltage and Distance from Impact Location for Three Impact Gages — Impact Shots B57-18 and B57-24

on a smooth-surfaced test structure, however, signal level was adequate for stress-wave detection.

4.10.1 Test Details - Test Shorts B57-38, 39, 41

A 3.65m by 1.67m by 1.65 mm section of an 2.43-m dia Delta tank wall structure with an integrally machined isogrid structure was installed in the gun room at the MDAC Aerophysics Laboratory. It was impacted by projectiles launched from a light-gas gun and a ballistic pendulum projectile. Figure 4-53 shows the test setup using the light-gas gun, while Figure 4-54 shows the test setup using the ballistic pendulum. Photographs of the inside surface of the Delta structure with the impact gages installed are given in Figures 4-55 and 4-56. Note the large welded section (8.9 cm in width and 0.635 cm thick) of the Delta structure shown in Figure 4-56. The ribs of the isogrid wall structure are 11.2 cm by 0.32 cm by 0.95 cm and are 10.2 cm apart. The holes of the isogrid wall structure are 1.9 cm in diameter, 0.95 cm deep, and separated from adjacent holes by 11.4 cm.

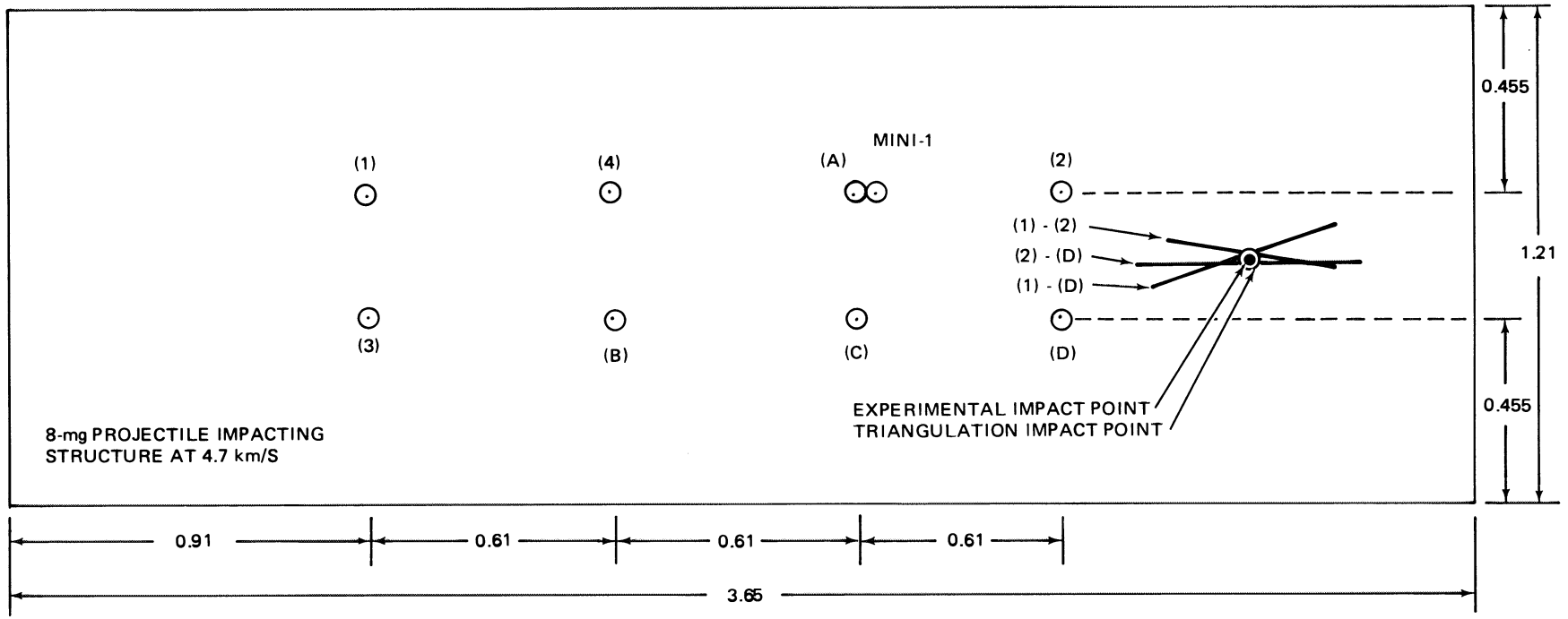

NOTES: 1. ⊙ IMPACT GAGE LOCATION
2. ALL DIMENSIONS IN METERS
3. IMPACT GAGE (AB) LOCATED ON OPPOSITE SIDE OF SHEET AT SAME LOCATION AS IMPACT GAGE (A)

Figure 4-50. Location of Point of Impact by Triangulation Techniuqe Using Three of the Impact Gages - Space Station Structure - Test Shot B57-24 (Ballistic Range)

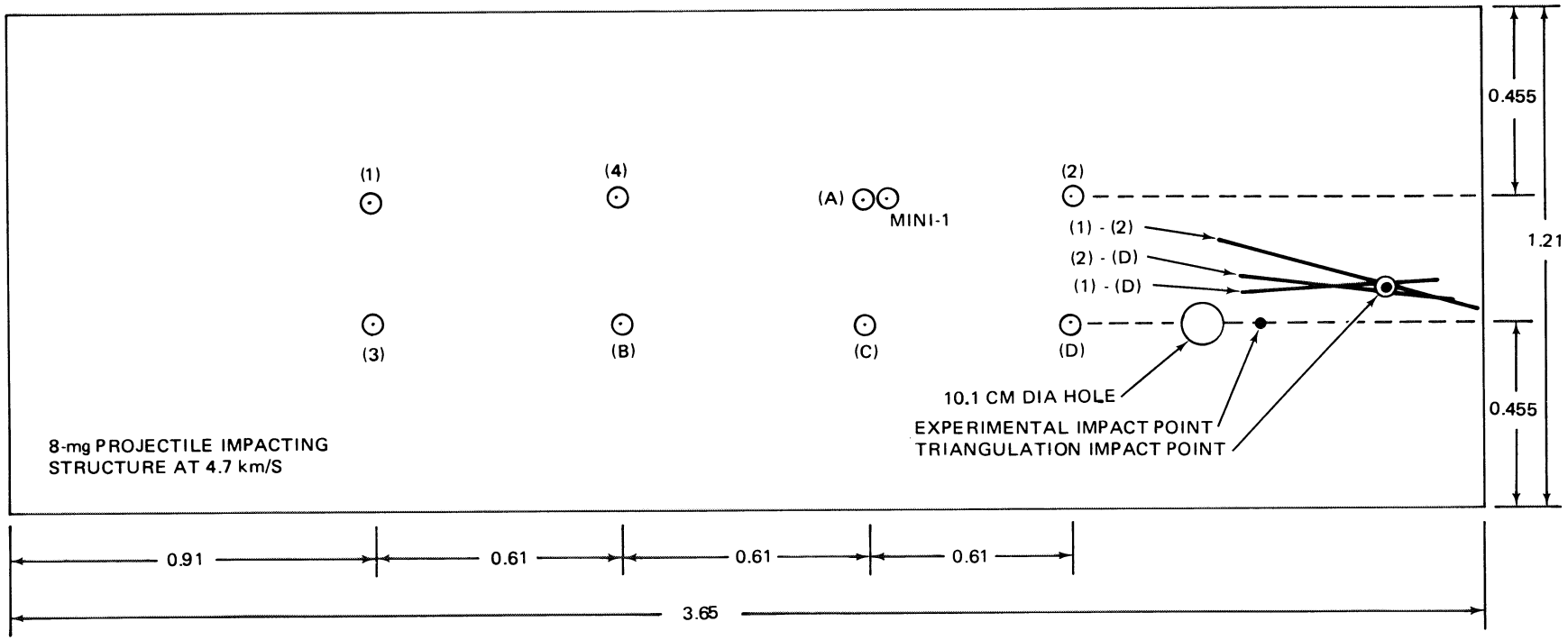

NOTES: 1. ⊙ IMPACT GAGE LOCATION
2. ALL DIMENSIONS IN METERS
3. IMPACT GAGE (AB) LOCATED ON OPPOSITE SIDE OF SHEET AT SAME LOCATION AS IMPACT GAGE (A)

Figure 4-51. Location of Point of Impact by Triangulation Technique Using Three of the Impact Gages - Space Station Structure - Test Shot B57-28 (Ballistic Range)

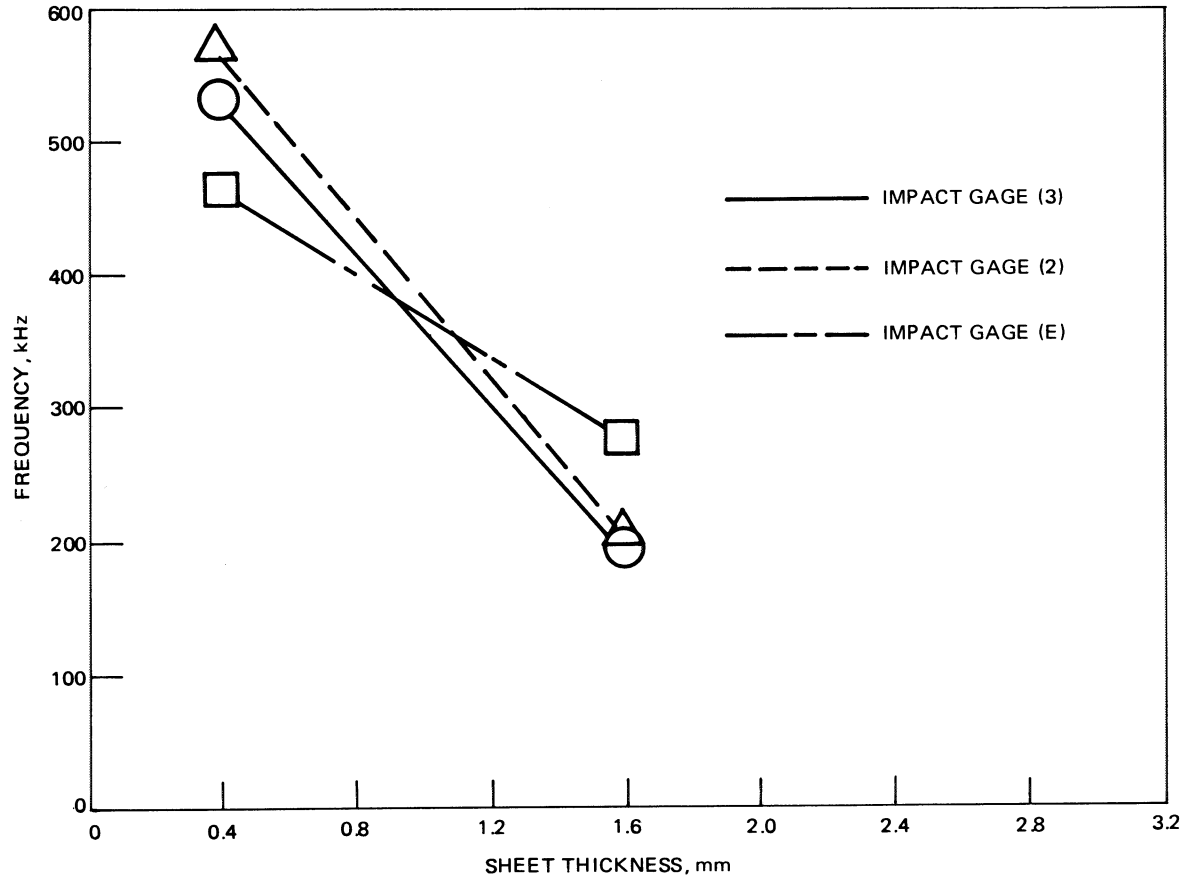

Figure 4-52. Impact Gage Output Frequency for Projectile Impacts Into Aluminum Sheets of Two Thicknesses - Test Shots B57-36 and B57-24

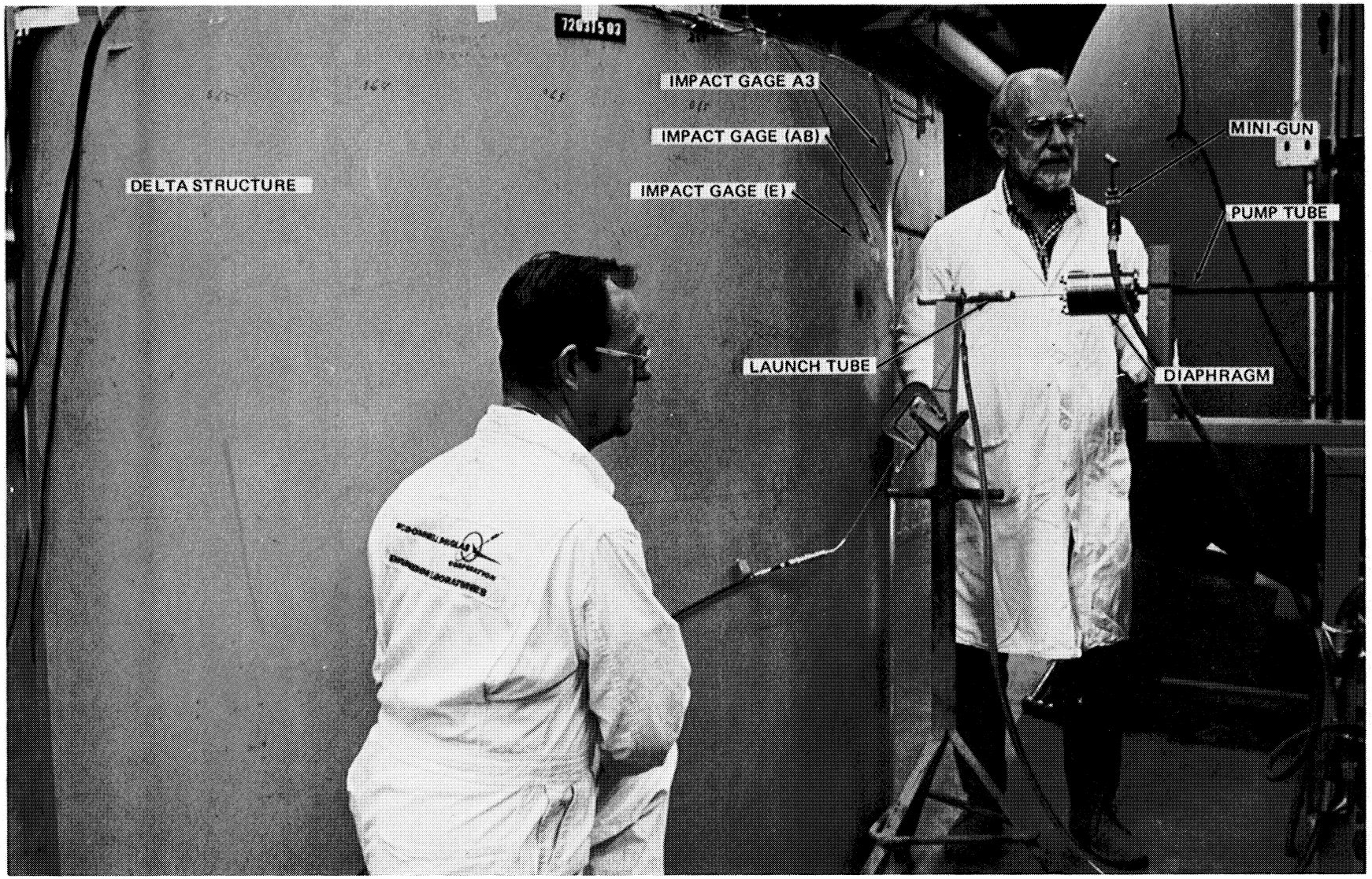

Figure 4-53. Test Setup of Front Surface of Delta Structure Test Shot B57-40

Figure 4-54. Test Setup of Front Surface of Ribbed Delta Structure - Test Shot B57-41

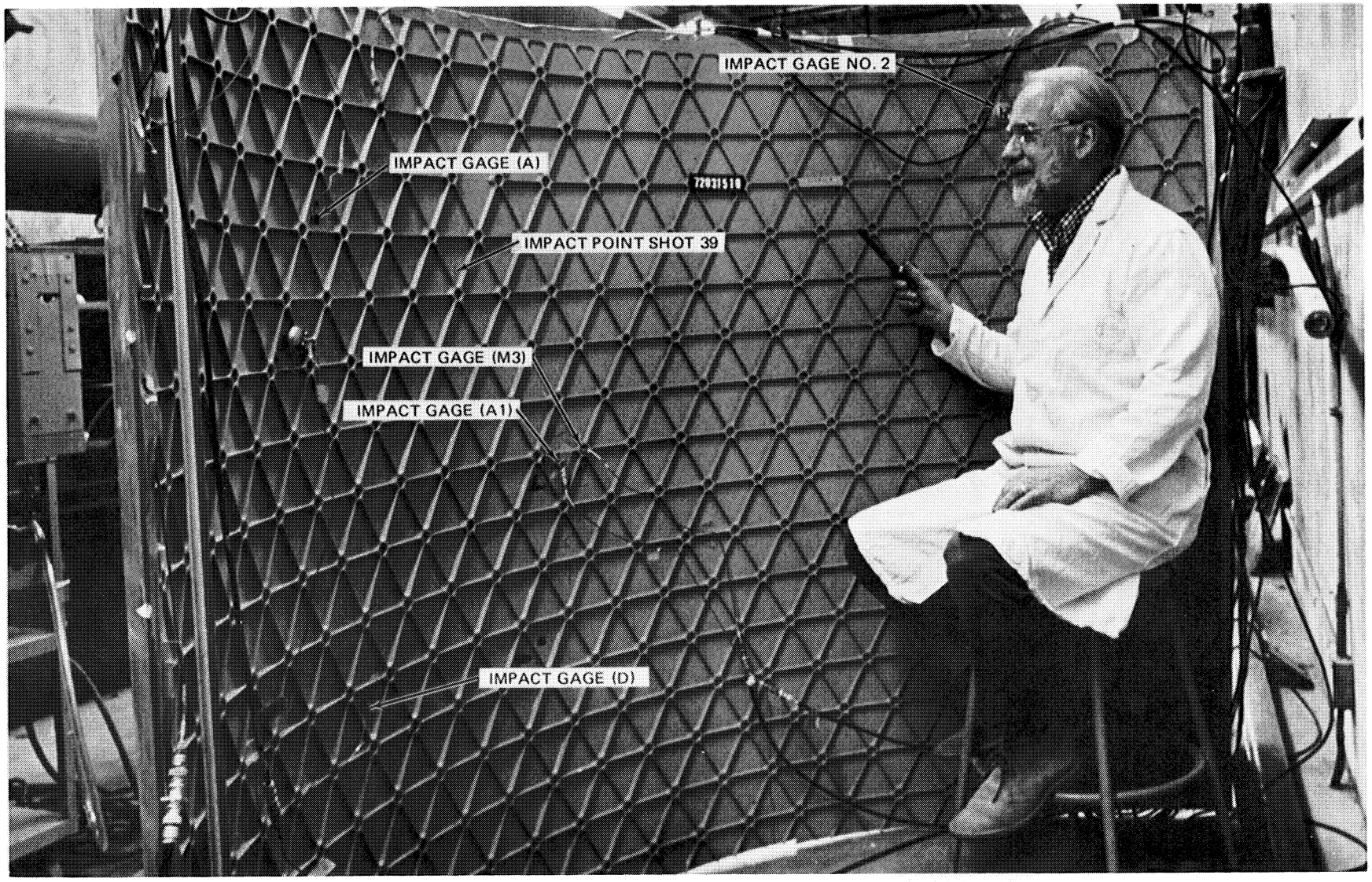

Figure 4-55. Test Setup of Inside Surface of Ribbed Delta Structure - Test Shot B57-39

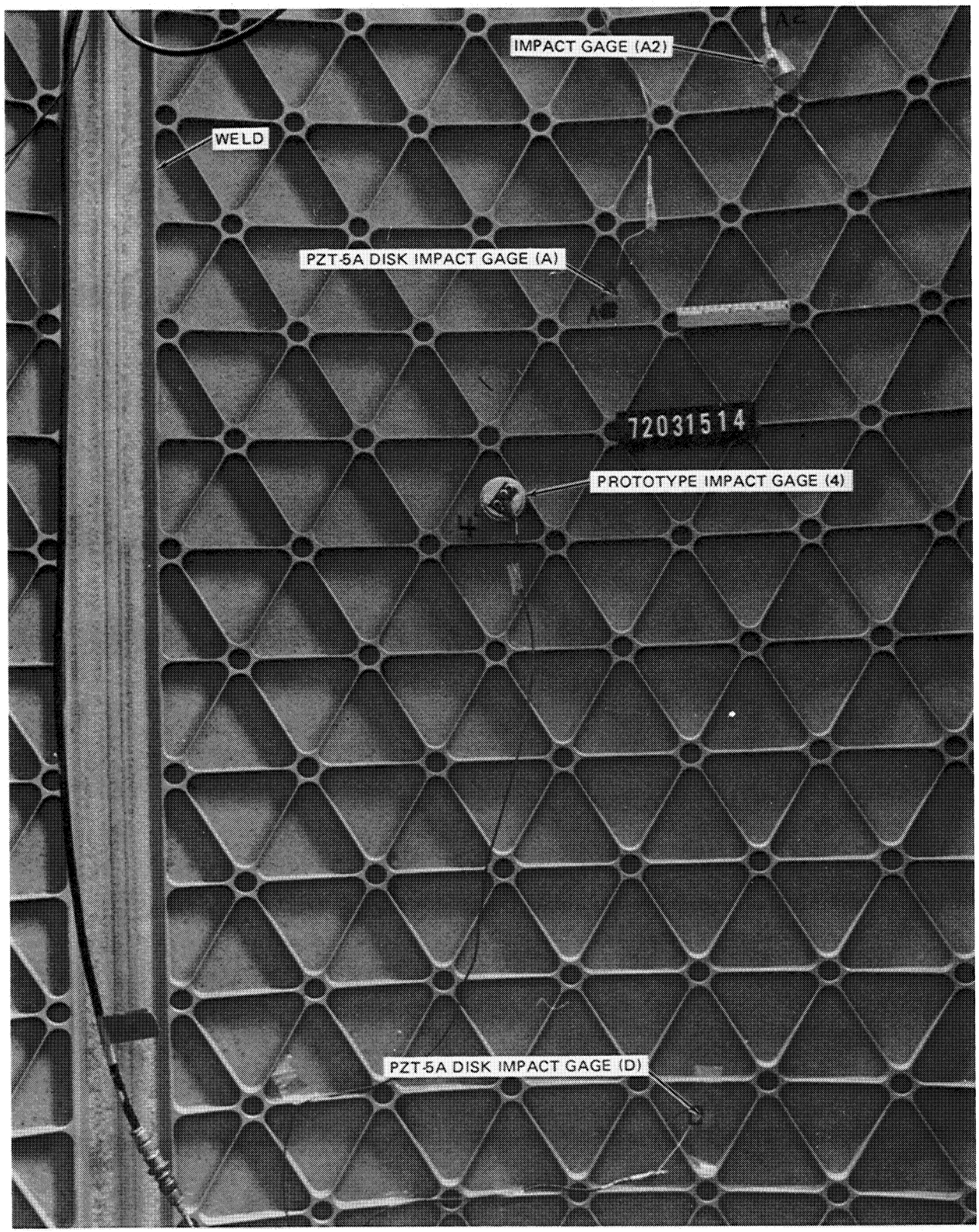

Figure 4-56. Partial Section of Rear Surface of Isogrid Structure of Delta Tank - Test Shot B57-39

Most of the impact gages (1, 2, 3, 4, A, AB, C, D, E) were used for the parametric test shots and will not be described here. Two new mini-gages were installed (M3 and M4). A commercial acoustical transducer was installed at location A1 and used for comparison purposes. All prototype and mini impact gages were bonded to the Delta wall structure using a thin film of Eastman 910 contact cement. The search unit was installed by using a thin film of ultrasonic grease (Sperry grease No. 50A 4084) between the Delta structure and the search unit and taping the unit to the wall using Mylar pressure sensitive tape. Figure 4-56 shows the locations of the impact gages on the Delta structure.

The impact gages, timing markers, and time-zero (gun firing) outputs were recorded on a wide-band (1.5 MHz) tape recorder. Six of the impact gages were also recorded on three oscilloscopes during the test shots.

Test conditions and pertinent data from a few of the impact gages are given in Table 4-12. Typical oscilloscope records obtained from the output of the impact gages are given in Figures 4-57 and 4-58.

Results obtained by locating the point of impact using triangulation techniques (method discussed in a previous section) were excellent. The point of impact (triangulation) was located (see Figures 4-59 and 4-60) only a few centimeters from the actual point of impact for test Shots B57-37 and 39. There was a high attenuation of the impact-gage output voltage with increasing distance from the impact point as compared to test shots on the smooth-surfaced test structures. For example, the output of impact gage D located a distance of 76.2 cm for shot B57-38 from the impact point was approximately fifteen times lower than the impact-gage output obtained for the same distance from an impact point for the test shots on the 1.6 mm-thick aluminum sheets during Test Series 4.

The ballistic pendulum-type impacts on the Delta structure produced no measurable output from the impact gages.

Table 4-12

IMPACT GAGE TEST RESULTS—SERIES 5 (DELTA TANK WALL STRUCTURE)

Shot	Projectile					Impact Gage			
No.	Shape	Mass (mg)	Velocity (km/s)	Kinetic Energy (J)	Momentum (kg m/s)	No.	Distance from Impact (cm)	Amplitude[1] (mV)	S. A. T.[2] (μs)
B57-38	Polyethylene Cyliner	8	4.7	80	0.0359	1	120	40	220
						2	126	30	229
						D	76	80	128
						E	7.6	10,000	Reference
B57-39	Polyethylene Cylinder	24	2.82	12.9	0.0684	1	114	20	203
						2	137	20	242
						D	75.5	50	125
						E	7.6	12,000	Reference
B57-41	Pendulum Polyethylene	8.1×10^{3}	1.6×10^{-3}	9.4	12.3	1	107	< 1	
						2	147	< 1	
						D	76	< 1	
						E	7.6	< 1	

[1] Peak-to-peak amplitude of second output pulse from impact gage - impact gage external cabling capacitance was typically 1,500 pf.

[2] S. A. T. Signal arrival time at impact gage.

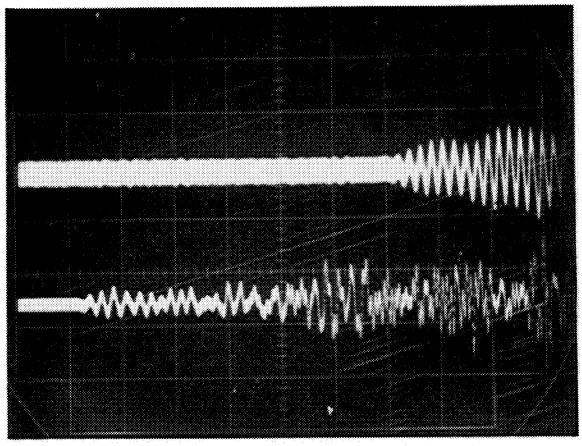

(a)

RECORD RATE: 20 μs/cm

UPPER TRACE: PZT-5A PROTOTYPE IMPACT GAGE (2) - 50 mV/cm

LOWER TRACE: PZT-5A DISK IMPACT GAGE (D) - 200 mV/cm

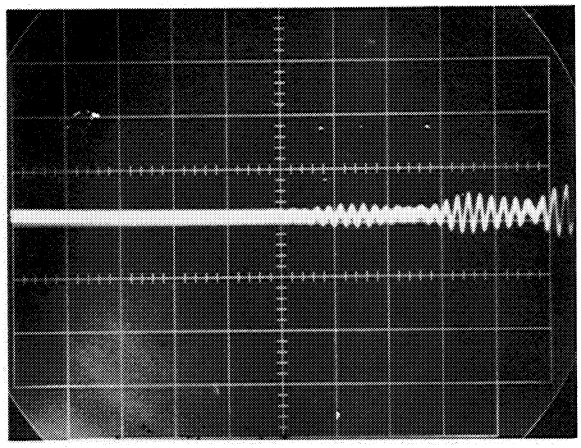

(b)

RECORD RATE: 20 μs/cm

PZT-5A PROTOTYPE IMPACT GAGE (1) - 100 mV/cm

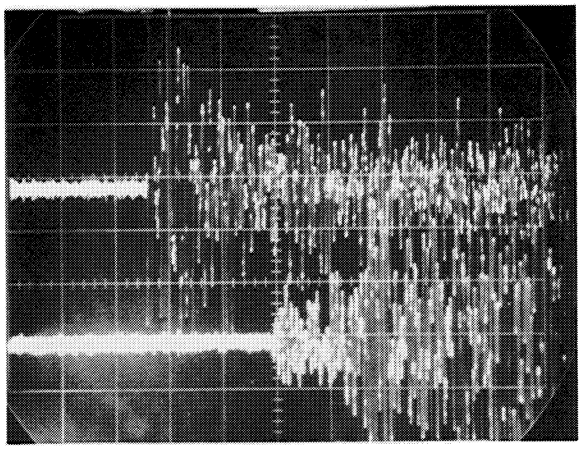

(c)

RECORD RATE: 50 μs/cm

UPPER TRACE: PZT-5A DISK IMPACT GAGE (E) -500 mV/cm, CH 6

LOWER TRACE: PZT-5A DISK IMPACT GAGE (D) - 500 mV/cm, CH 8

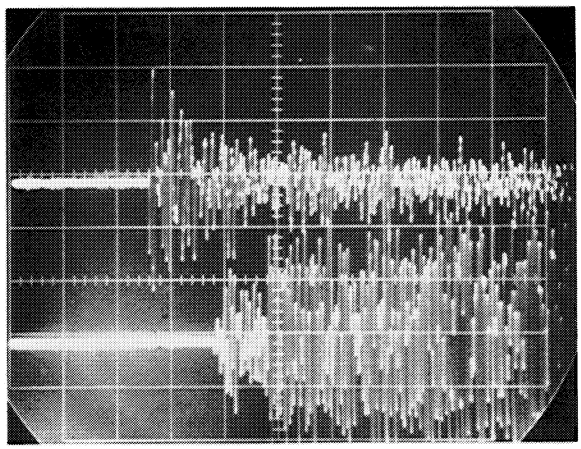

(d)

RECORD RATE: 50μs/cm

UPPER TRACE: PZT-5A DISK IMPACT GAGE (E) - 1 V/cm, CH 6

LOWER TRACE: MINI IMPACT GAGE (M3) - 1V/cm, CH 12

Figure 4-57. Oscilloscope Records of Impact Gage Signals Recorded on Oscilloscope and a Tape Recorder During Shot B57-39

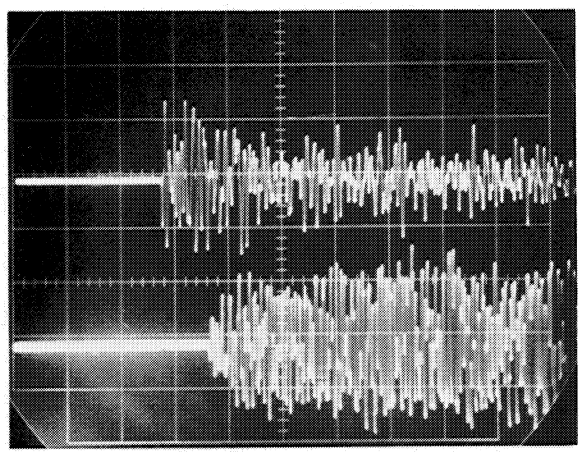

(a)

RECORD RATE - 50μs/cm

UPPER TRACE: PZT-5A DISK IMPACT GAGE (E) - 2 V/cm, CH 7

LOWER TRACE: PZT-5A DISK IMPACT GAGE (A) 5 V/cm, CH 11

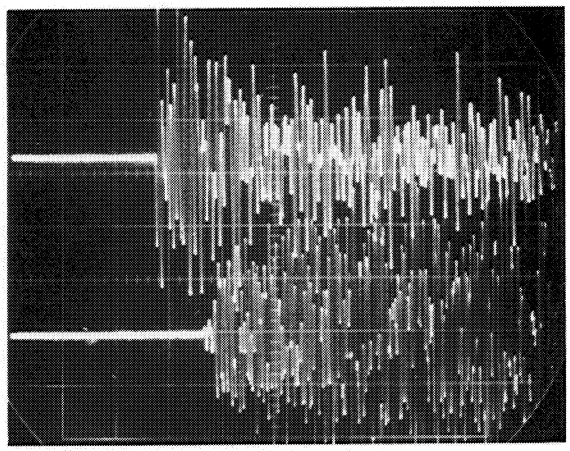

(b)

RECORD RATE - 50μs/cm

UPPER TRACE: PZT-5A DISK IMPACT GAGE (E) - 1 V/cm, CH 7

LOWER TRACE: PZT-5A DISK IMPACT GAGE (A-B)- 2 V/cm, CH 13

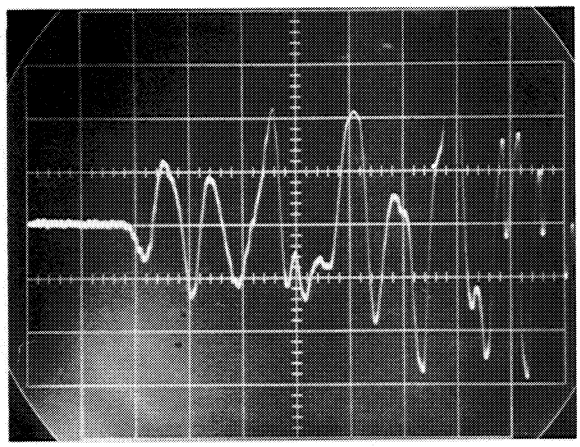

(c)

RECORD RATE -5μs/cm

PZT-5A DISK IMPACT GAGE (A) - 2 V/cm, CH 11

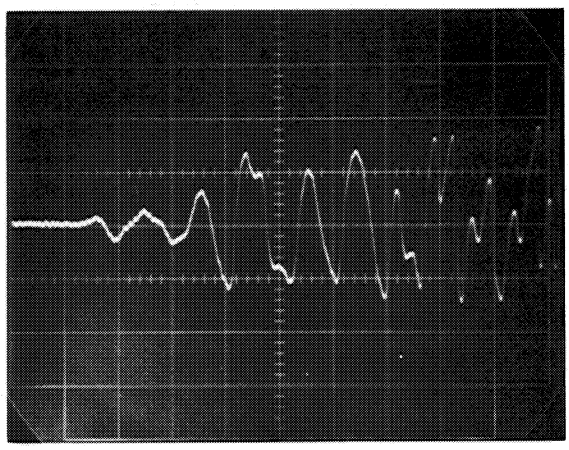

(d)

RECORD RATE - 5μs/cm

PZT-5A DISK IMPACT GAGE (A-B) - 2 V/cm, CH 13

Figure 4-58. Oscilloscope Records of Impact Gage Signals Recorded on Tape Recorder During Shot B57-39

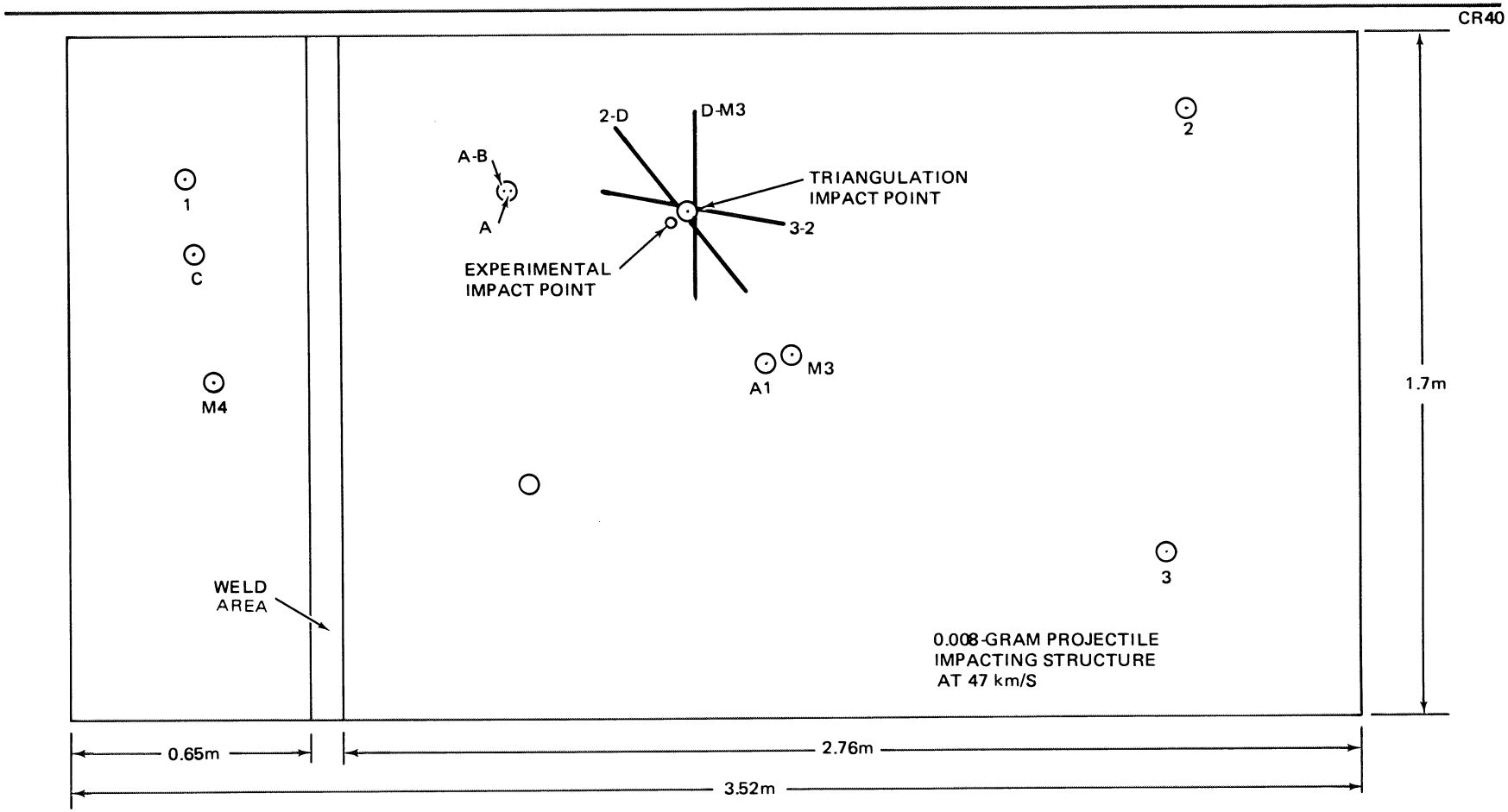

NOTE: 1. DELTA TANK RIBS AND IMPACT GAGE (E) ARE NOT SHOWN
2. ⊙ IMPACT GAGE LOCATION
3. ALL DIMENSIONS IN METERS

Figure 4-59. Location of Point of Impact by Triangulation Using Four of the Ten Installed Gages - Delta Tank Structure - Test Shot B57-38 (Ballistic Range)

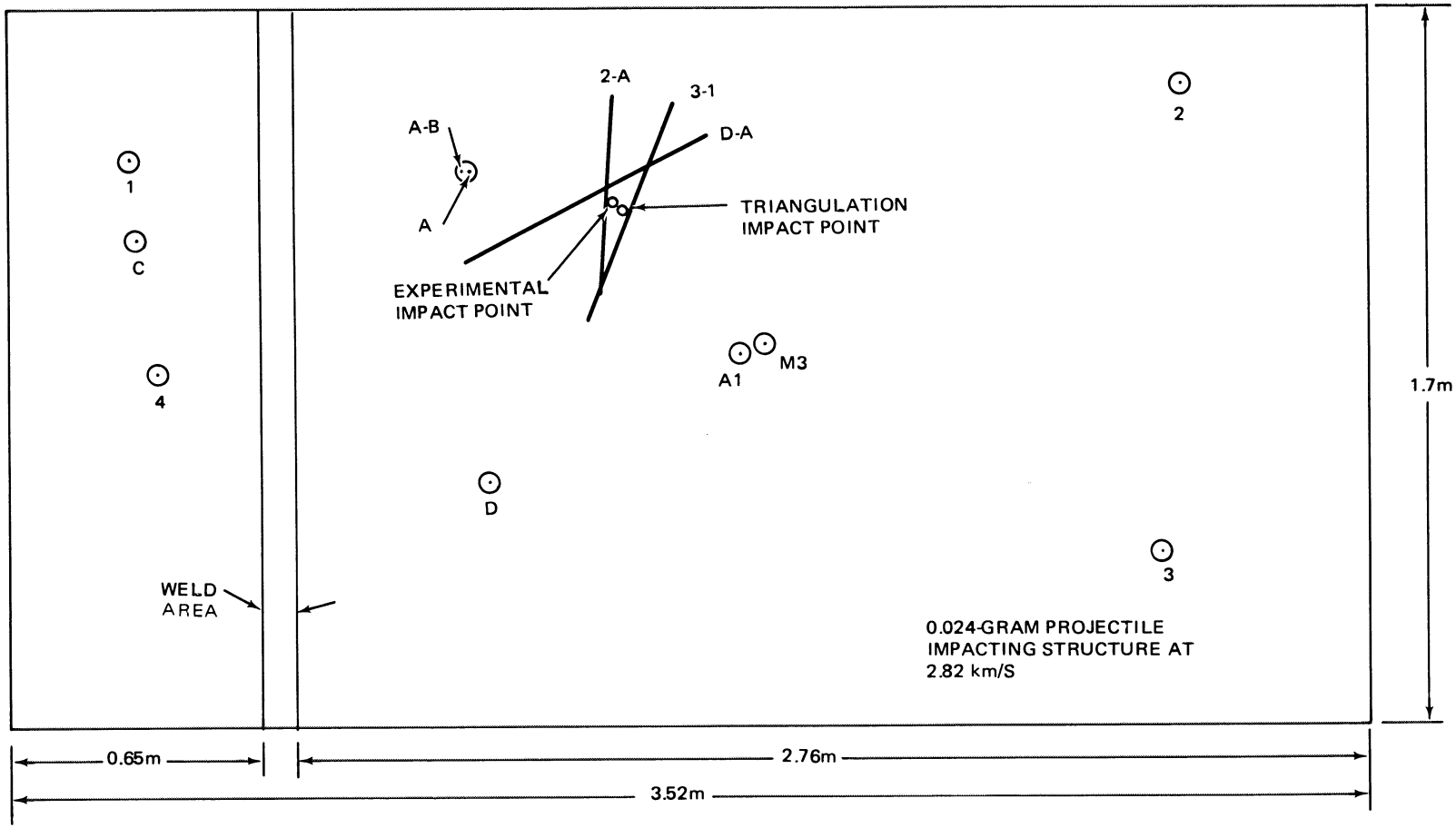

NOTES:
1. DELTA TANK RIBS AND IMPACT GAGE (E) ARE NOT SHOWN
2. ⊙ IMPACT GAGE LOCATION
3. ALL DIMENSIONS IN METERS

Figure 4-60. Location of Point of Impact by Triangulation Techniques Using Five of the Ten Installed Impact Gages - Delta Tank Structure - Test Shot B57-39 (Ballistic Range)

4.11 ACOUSTICAL EMISSION SIMULATION TESTING OF IMPACT GAGES

In addition to hypervelocity impact tests and drop tests, an acoustical emission simulation test set (Reference 21) was also used to test the impact gages. The device is shown in Figure 4-61. A current pulse* from the pulser unit is used to energize a thin-wire magnetostrictive transducer. A pulse with a center frequency of 100 kHz propagates as an extensional wave to the end of the lead-in wire. A sound pulse is received by the structure when the lead-in wire is pressed to the structure surface. This unit can be used for acoustic emission experiments and many other tests.

One application of this test set has been to check that the impact gages are operating properly. Figure 4-62 shows this device being used to check impact gage (AB). Note that the impact gage response to the acoustic emission pulses can be seen in the oscilloscope display.

The acoustic emission test set was also used to study both the pulse distortion as a function of distance along the structure and the wave velocity in test structures. Figure 4-63 shows the output of PZT-5A disk impact gage C and prototype Impact Gage 1 when these impact gages were installed on the Delta structure (Figure 4-64) and the lead-in wire was placed 9.5 mm below PZT-5A disk impact gage C. These impact gages were located 20.5 cm apart. For a similar test, with impact gage C replaced by mini-gage 4, and the impact gages installed on a 1.6-mm-thick aluminum sheet, the output of Impact Gage 1 was much higher [Figure 4-63(c)].

Figures 4-63(a) and 4-63(b) show the response of mini-gage 4 with a PZT-5A sensing element and mini-gage 5 with an electret FEP sensing element when the lead-in wire was placed directly on the front face of the impact gages.

---

*0.5 A, 3 μs duration, 60-Hz repetition.

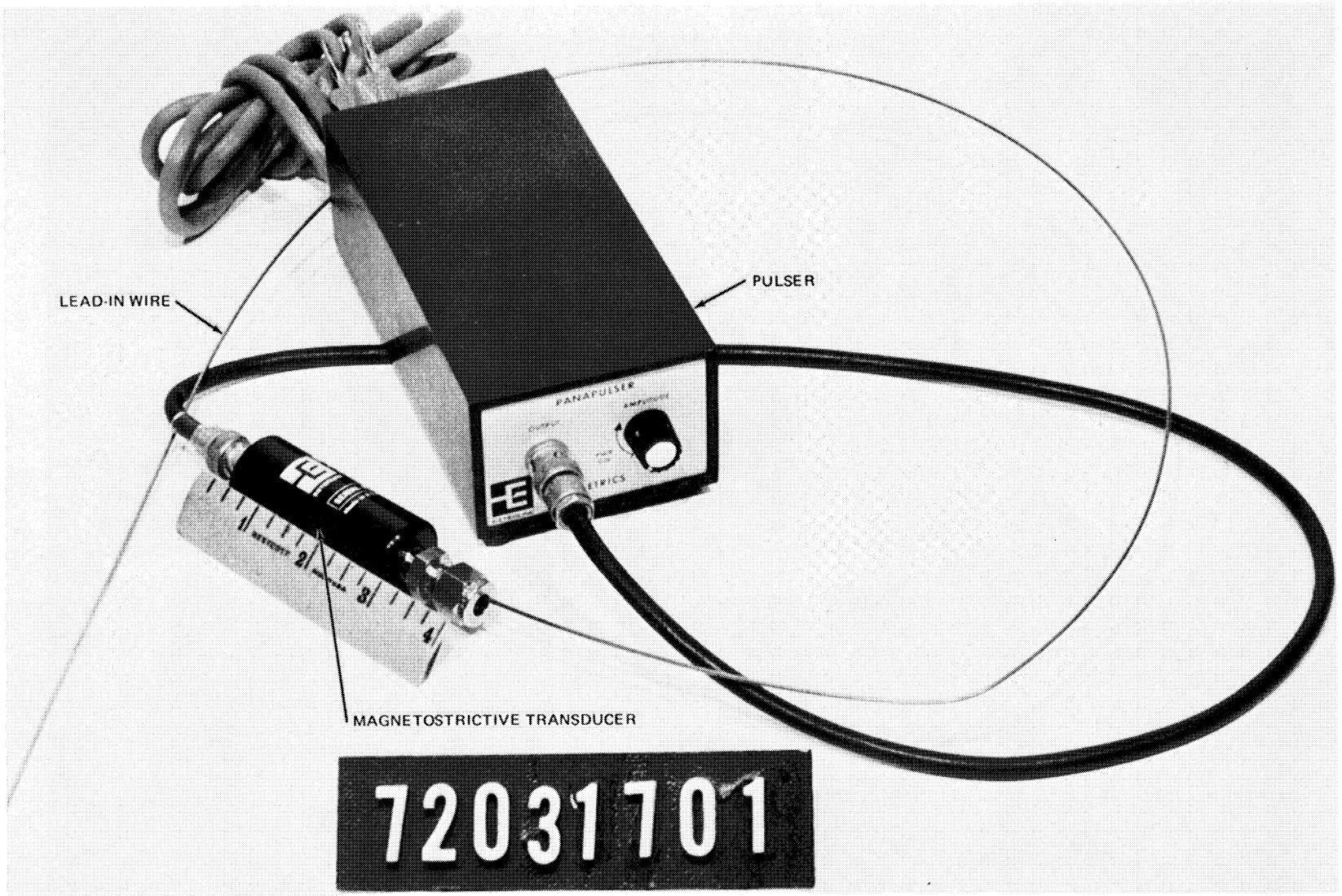

Figure 4-61. Acoustic Emission Test Set

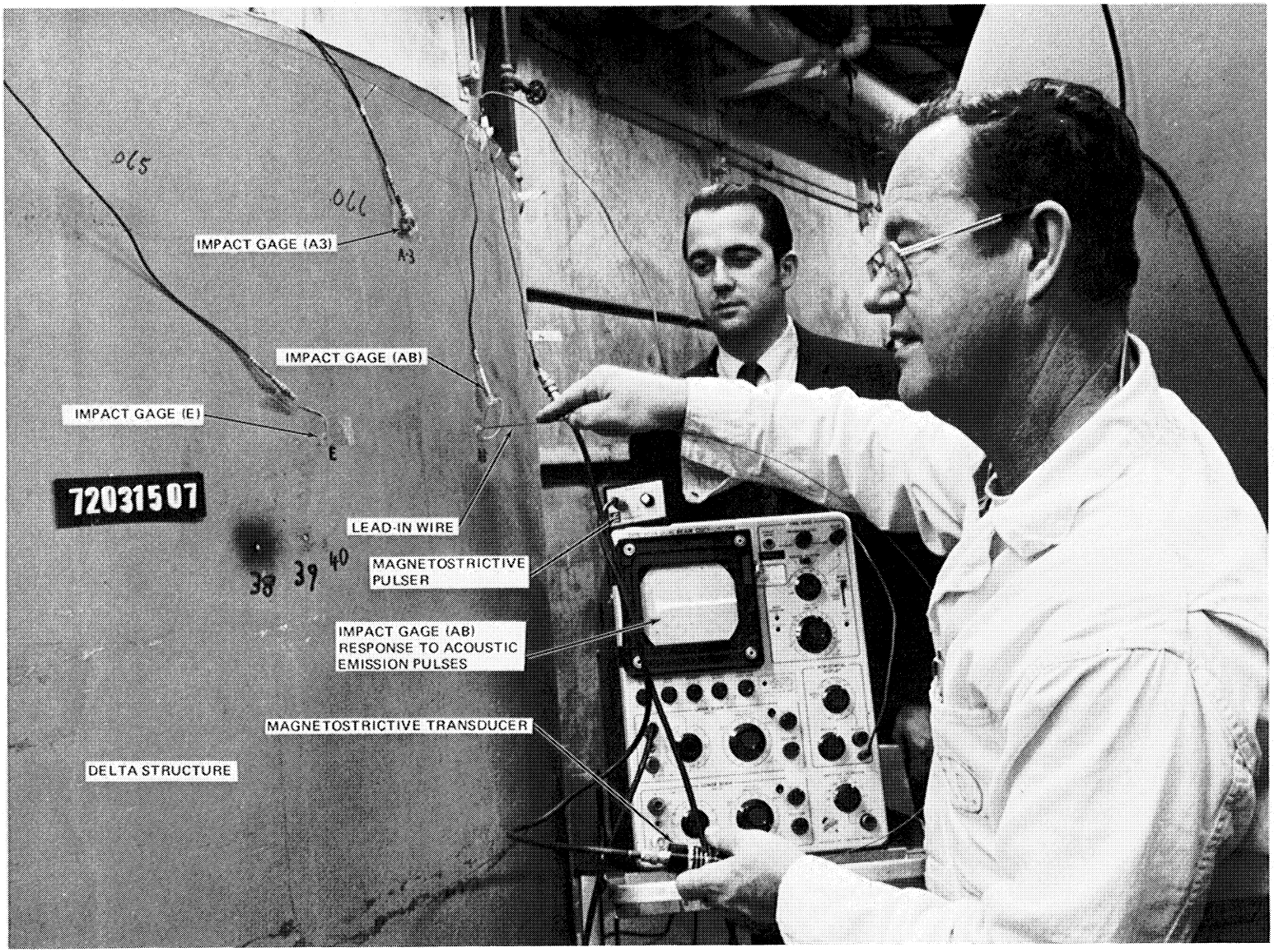

Figure 4-62. Acoustic Emission Simulation Test Set used to Test Impact Gages on a Partial Section of a Delta Tank

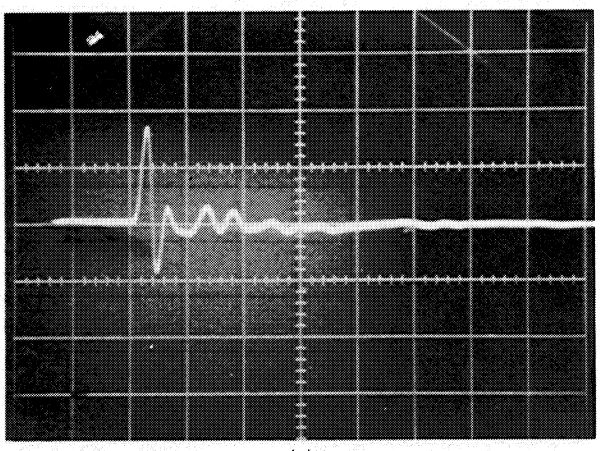

(a)

RECORD RATE - 20μs/cm

SENSITIVITY: 2 V/cm

MINI-GAGE (4): PZT-5A SENSING ELEMENT

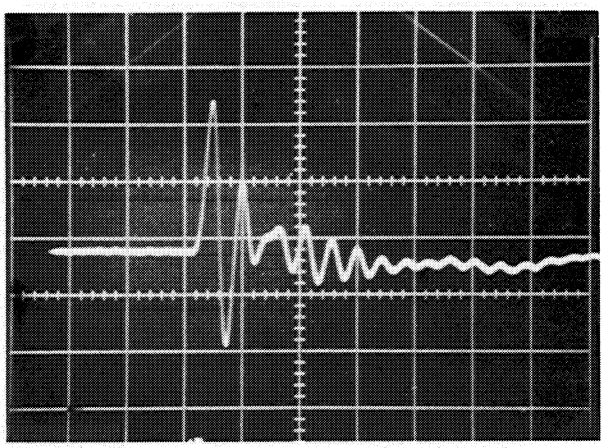

(b)

RECORD RATE - 20μs/cm

SENSITIVITY: 10 mV/cm

MINI-GAGE (5): ELECTRET FEP SENSING ELEMENT

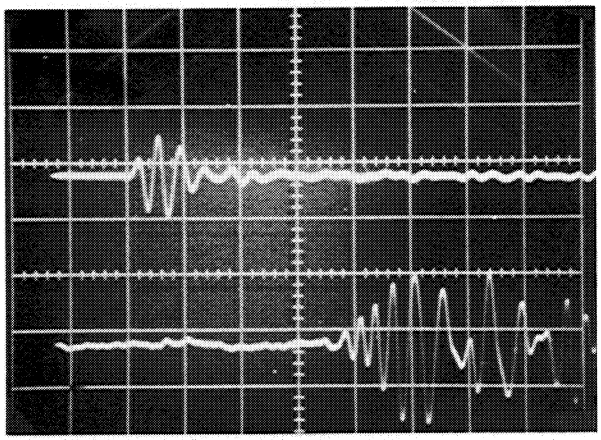

(c)

RECORD RATE - 20μs/cm

UPPER TRACE: MINI-GAGE (4), 50 mV/cm

LOWER TRACE: PROTOTYPE IMPACT GAGE (1) - PZT-5A, 0.5 mV/cm

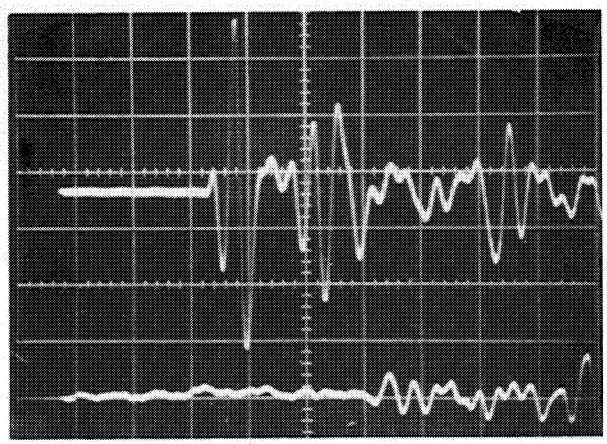

(d)

RECORD RATE - 20μs/cm

UPPER TRACE: DISK IMPACT GAGE (3) - 5 mV/cm

LOWER TRACE: PROTOTYPE IMPACT GAGE (1) - 0.2 mV/cm

Figure 4-63. Impact Gage Output Signals for Acoustic Emission Simulation Pulses

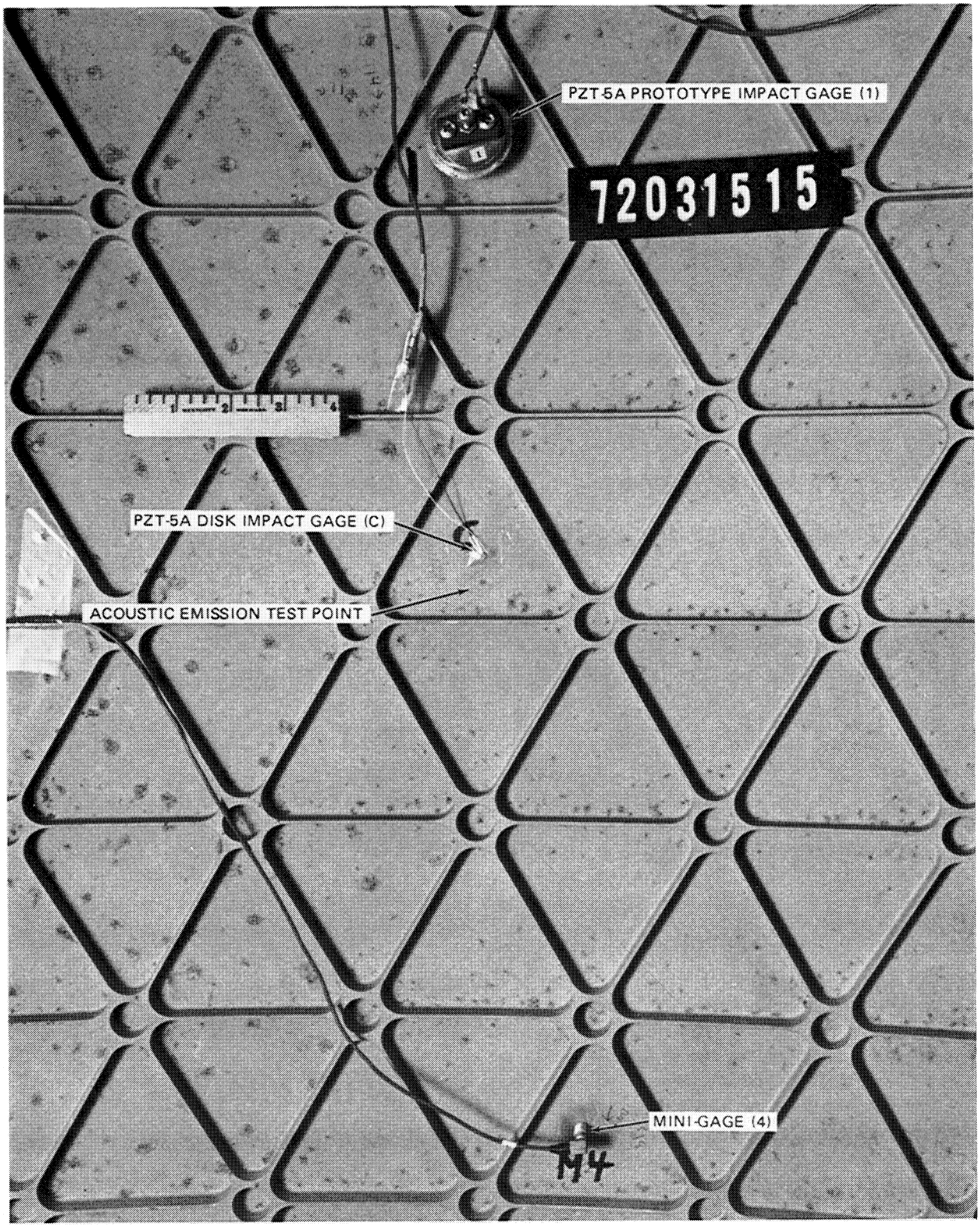

Figure 4-64. Partial Section of Inside of Isogrid 2.44-Meter-Diameter Delta Tank Structure with Impact Gage

4.12 DUAL-FUNCTION IMPACT LOCATION SYSTEM

4.12.1 Preamplifier

To allow study of low-level acoustic phenomena such as acoustic emission, a transducer preamplifier was designed and fabricated. The design objective was to allow the output of a transducer to be transmitted through a long cable without distortion, attenuation, or degradation of signal-to-noise ratio. The preamplifier (Figure 4-65) consists of a low-noise field-effect transistor input stage and an emitter follower line driver. Printed circuit board construction was used. The amplifier transforms the input impedance of 2 MΩ to less than 100 Ω on the output with a voltage gain of 2.3 dB. Thus, the output signal as received is virtually independent of the connecting cable length or characteristics. The preamplifier was designed to have a frequency response flat from 30 kHz to well over 1 MHz. Because of high-frequency limitations of the available test equipment, performance could only be verified from 30 to 600 kHz. Insertion of an 8m cable had no measurable effect on the output signal. The input diode D1 does not conduct when the signal level is low, but clamps the input when a large signal as caused by a meteoroid impact appears. This clamping action protects the input transistor.

CR40

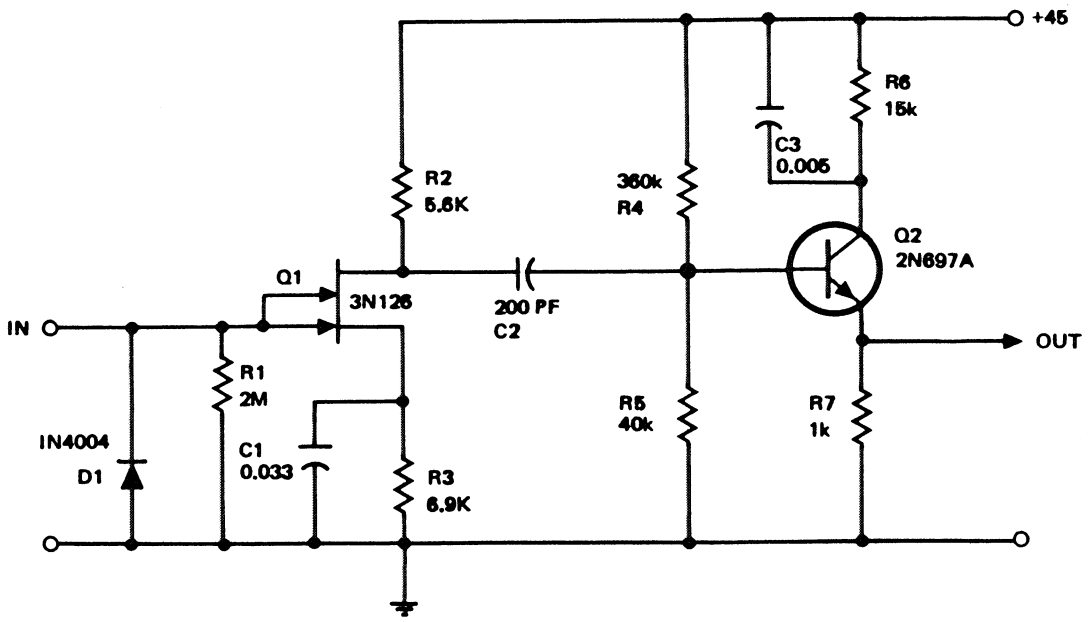

Figure 4-65. Preamplifier/Driver for Impact Location System

4.12.2 Ultrasonic Amplifier

The ultrasonic amplifier (Figure 4-66) consisting of four high-gain (23-dB) stages followed by a line driver stage, was fabricated and checked out. The extremely high overall gain (92 dB) and wide bandwidth led to an oscillation problem which was eliminated by additional power supply decoupling and more chassis ground points. Since the amplifier has an output noise level of 500 mV, no further amplification would be of use unless the bandwidth were greatly reduced. This amplifier was used to investigate acoustic emission phenomena.

4.12.3 Impact Triangulation System

The block diagram for the impact triangulation system designed, built, and tested in breadboard form is shown in Figure 4-67. The breadboard without the acoustic emission amplifiers is shown in Figure 4-68. Circuit details are shown in Figures 4-69 and 4-70. The system essentially consists of a series of one-shot multivibrators each connected to one impact transducer.

Upon receipt of an impact signature, each multivibrator produces a unique (preset pulse width) out. This pulse is generated by an SN 74121 TTL integrated circuit. Continual triggering is prevented by a NAND gate logic circuit utilizing the SN 7400 quadruple NAND integrated circuit. A single reset signal enables all channels. The outputs of all channels are summed with a 741 operational amplifier and fed to a single display with a common time base. The packaged breadboard will have adjustments as shown in Figure 4-71. The operating principles are illustrated in Figure 4-72. The wave originating from the impact point arrives at the Impact Gage 2 first, causing channel 2 to produce its characteristics output pulse and start the recording device. The fact that the wave arrives at Gages 1 and 3 close together does not cause ambiguous data as the summing amplifier adds the output channel signals. (Different pulse heights could also be used to identify each channel.) Figure 4-73 shows the actual operation of the system using three of the four channels of the breadboard unit.

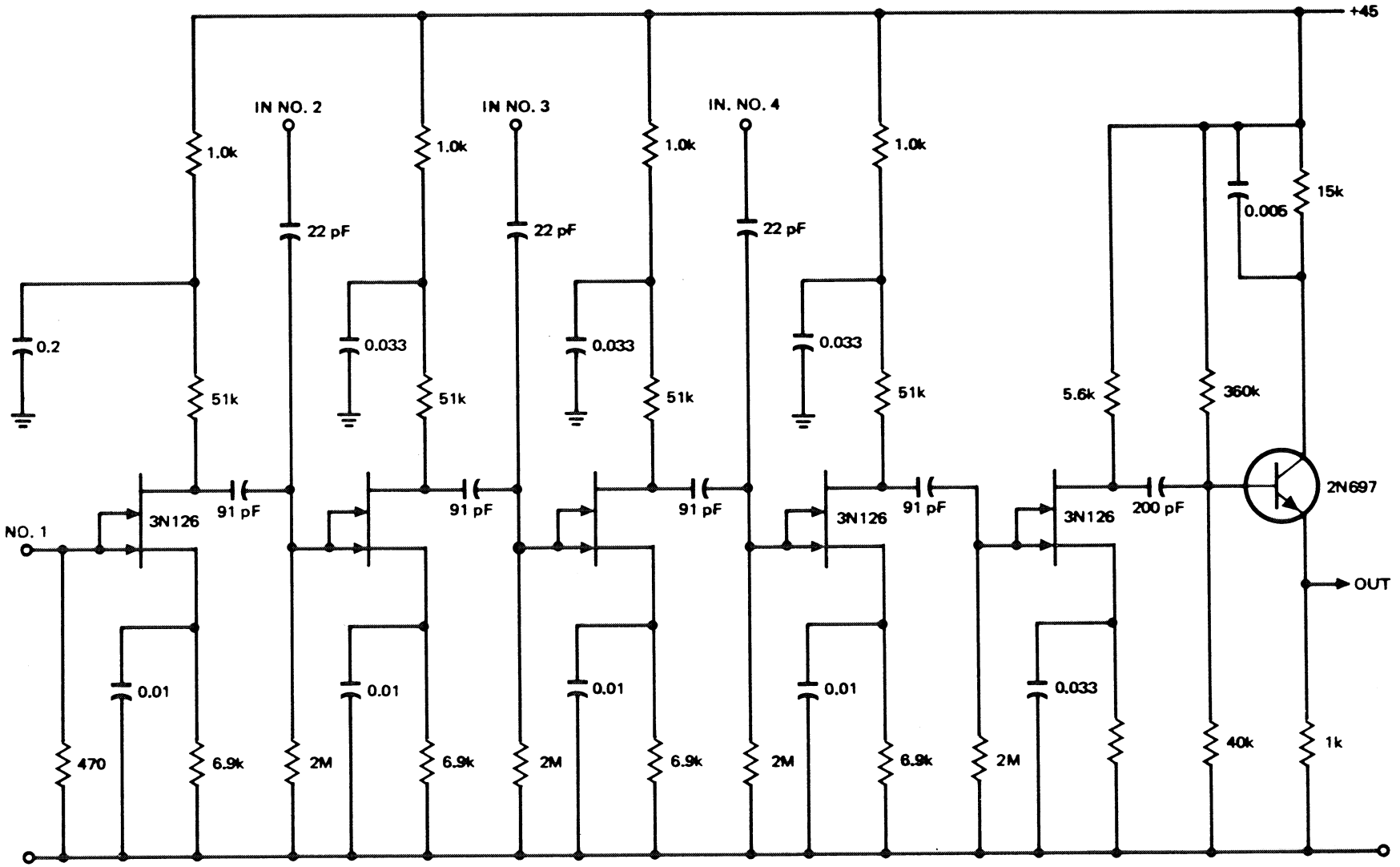

Figure 4-66. Main Amplifier for Impact Location System

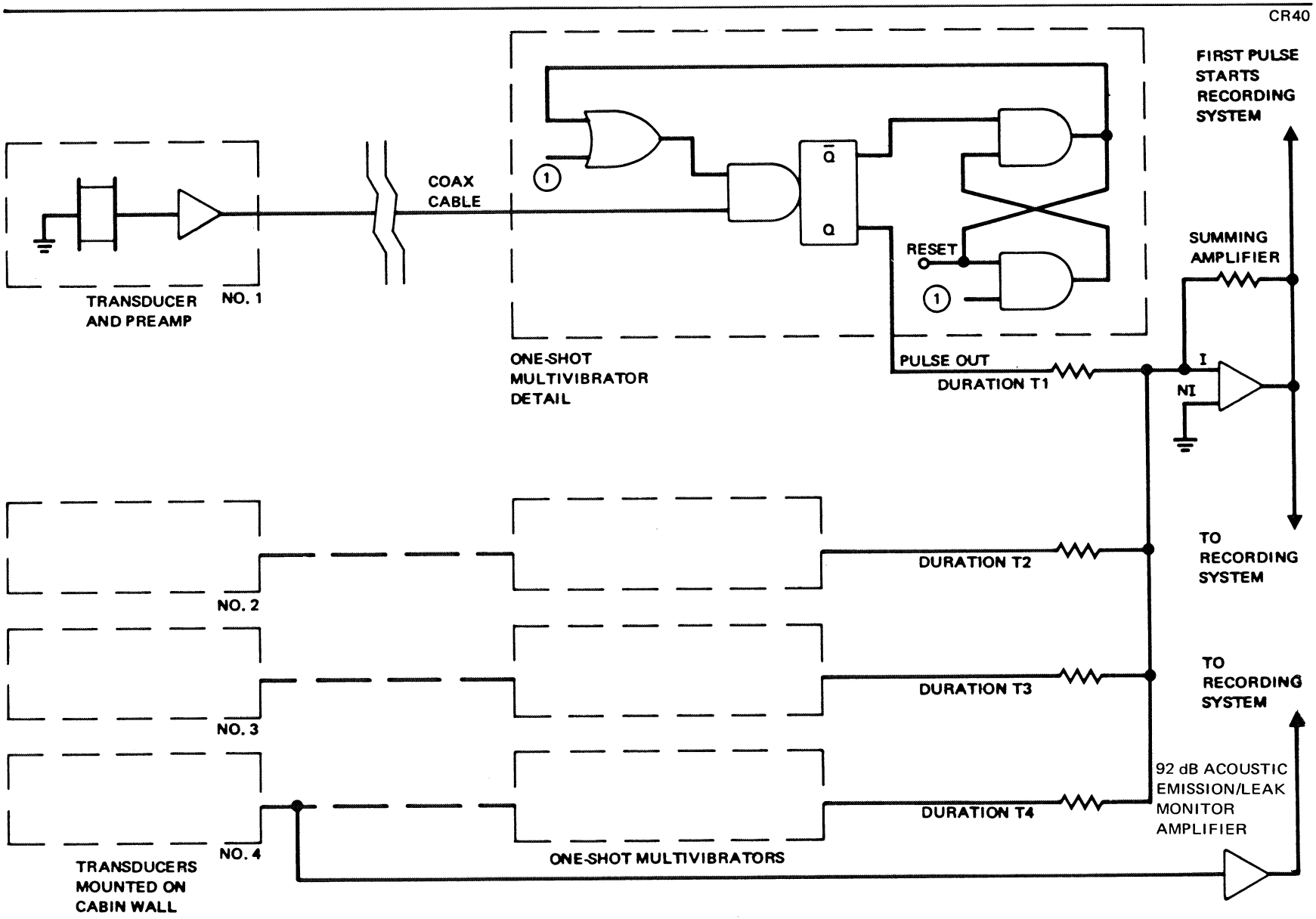

Figure 4-67. Impact Location System

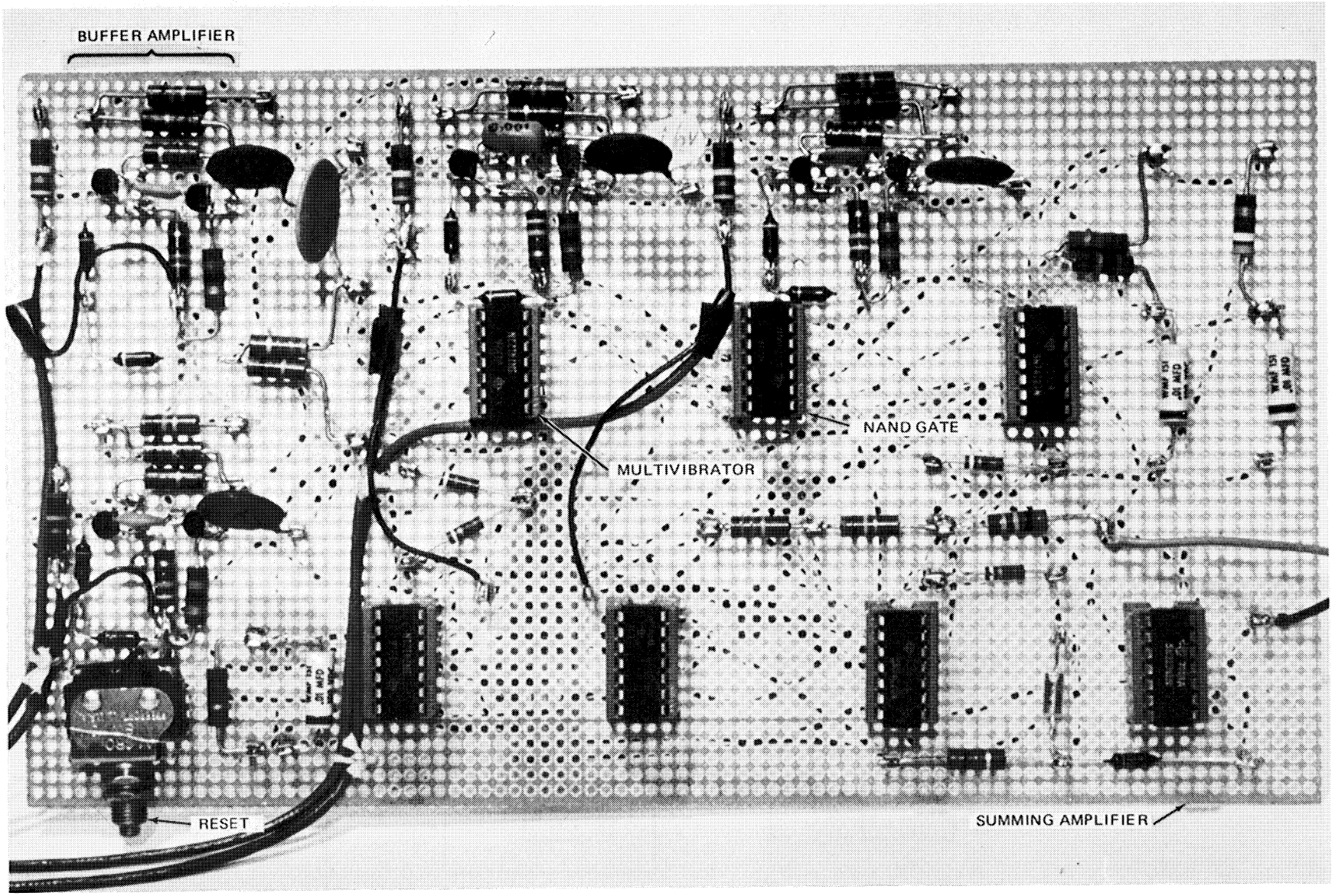

Figure 4-68. Impact Gage Multiplexing System Breadboard

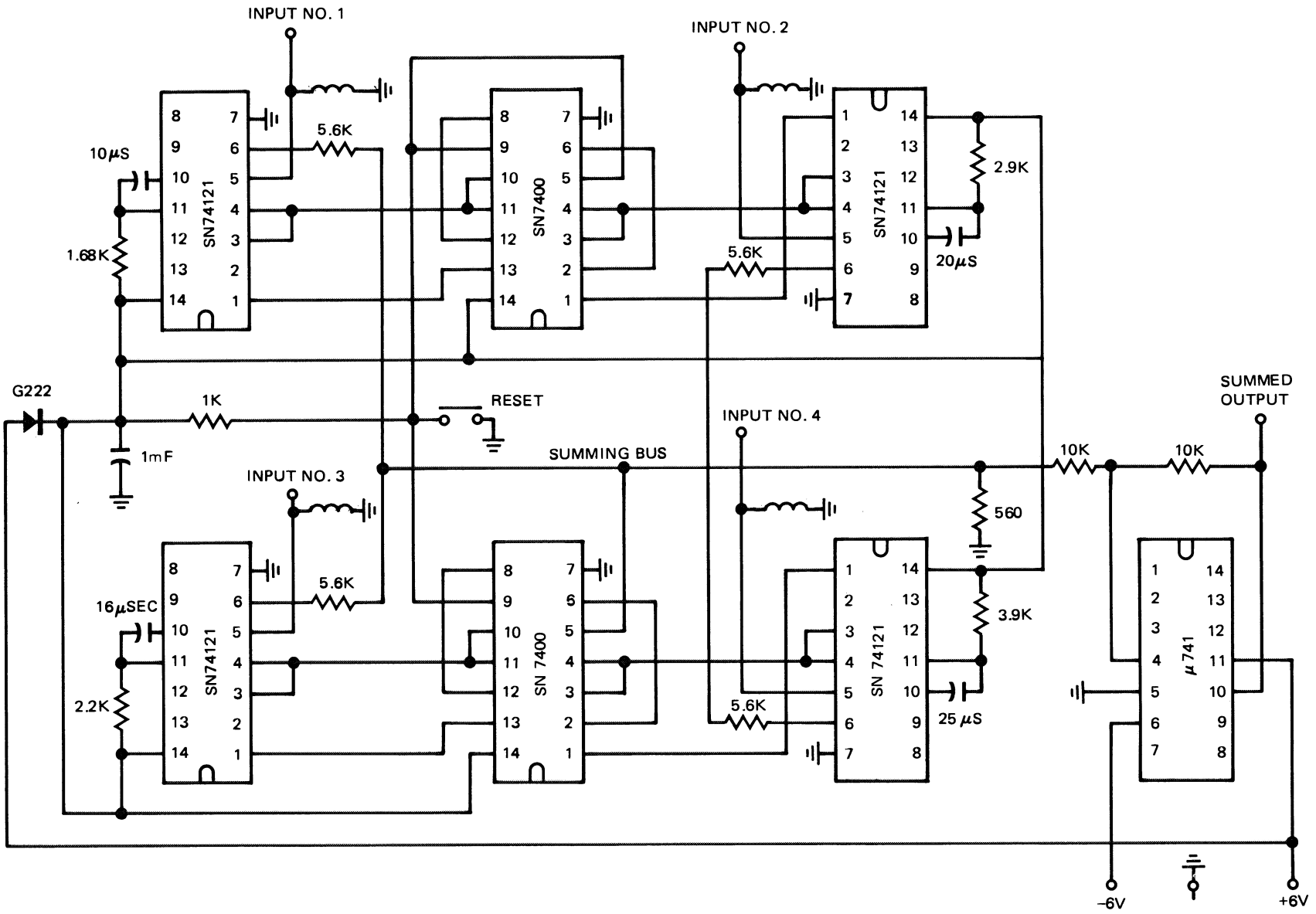

Figure 4-69. Impact Gage Multiplexing System - Circuit Details

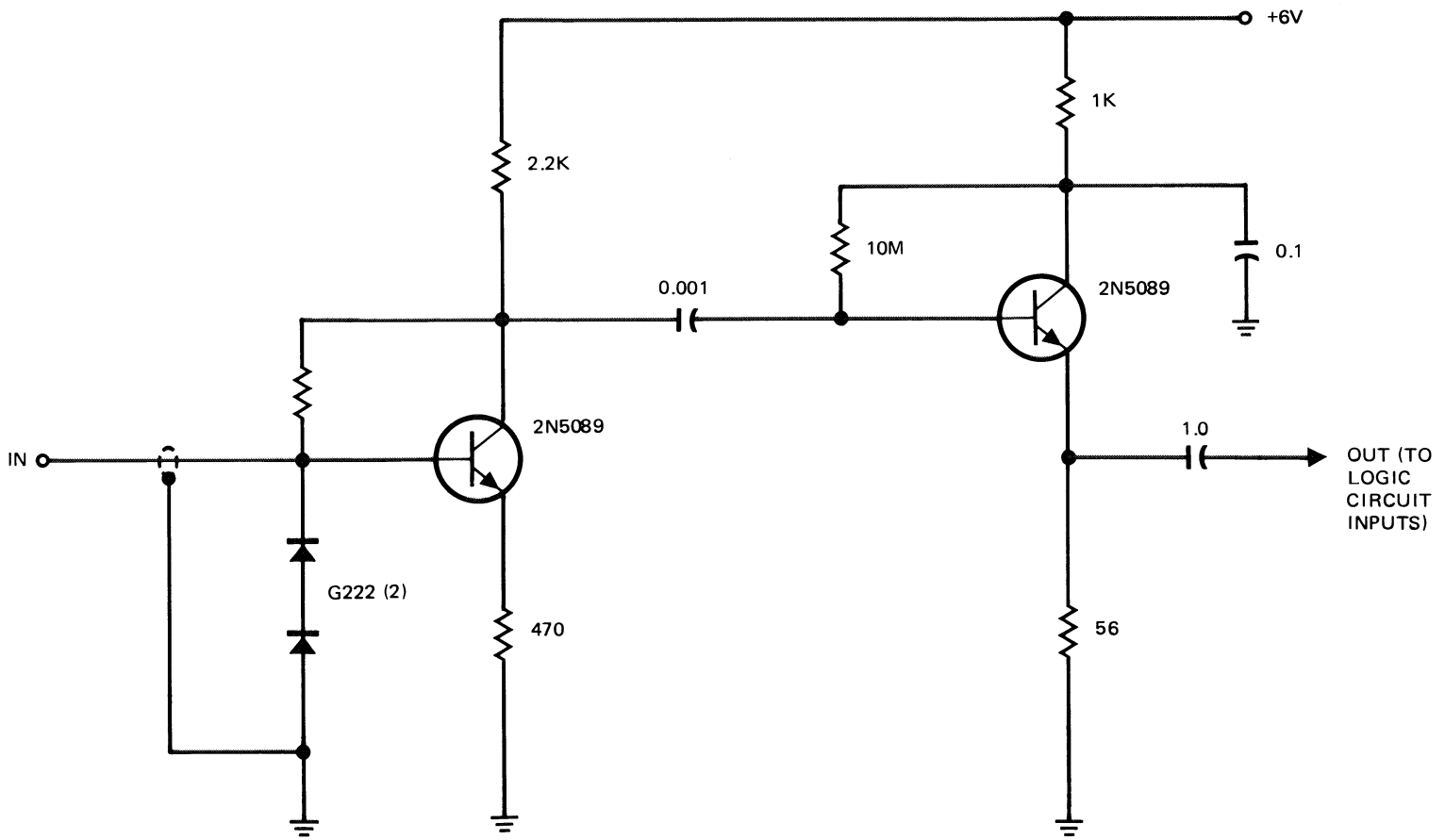

Figure 4-70. Impact Gage Multiplexing System-Buffer Amplifier Circuit Detail

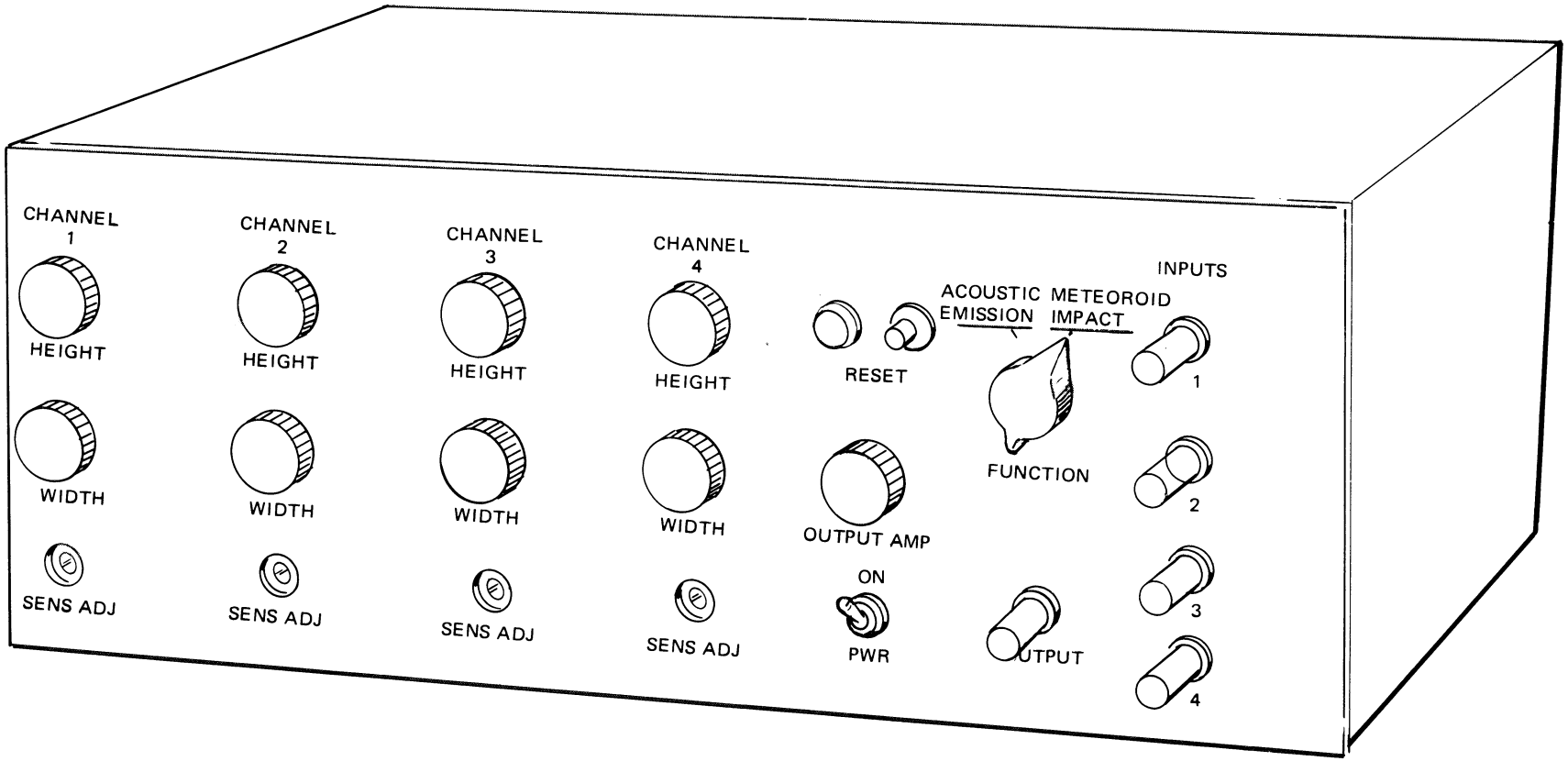

Figure 4-71. Meteoroid Damage Triangulation Subsystem

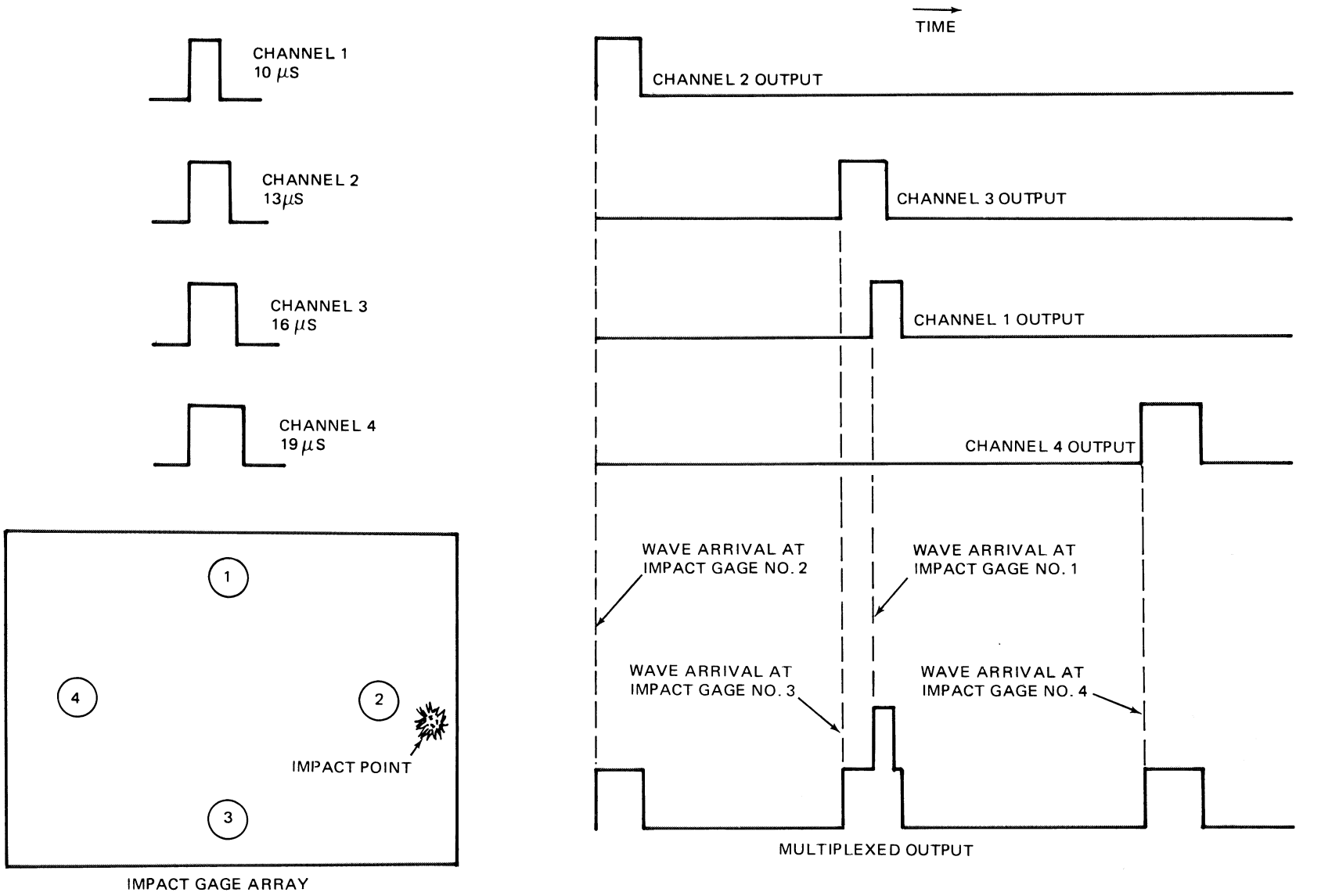

Figure 4-72. Impact Gage Multiplexing System Operation

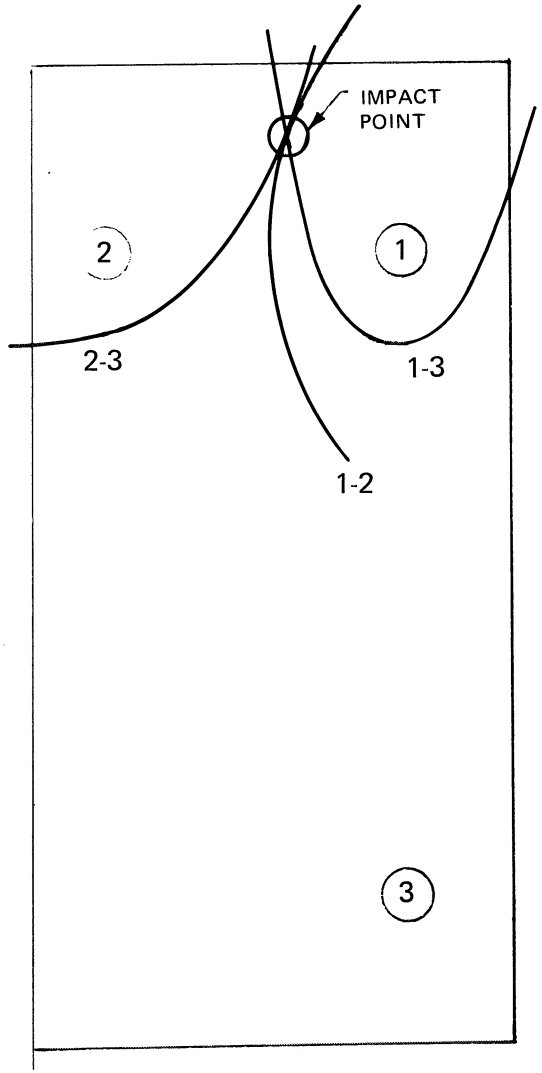

IMPACT GAGE ARRAY AND
TRIANGULATING HYPERBOLAS

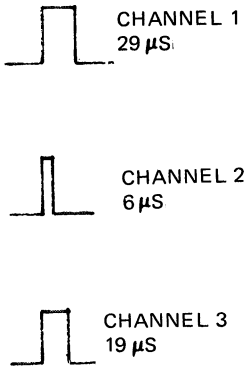

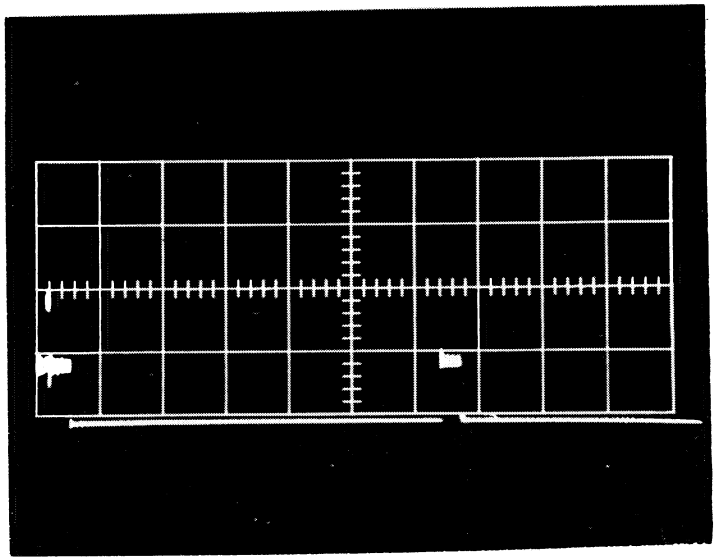

50 μS/cm

MULTIPLEXER OUTPUT (B57-6)

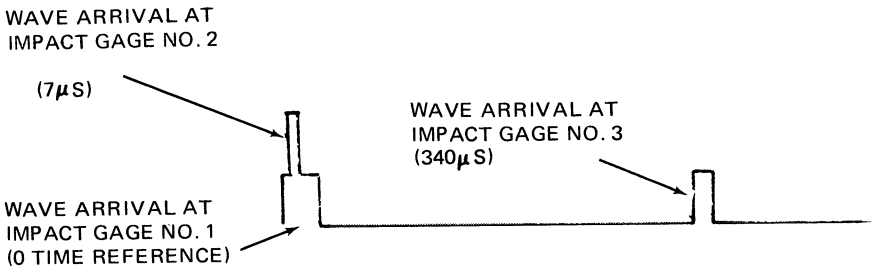

Figure 4-73. Meteoroid Impact Triangulation — Experimental Results — Test Shot B57-6

The information obtained from the B-57 program in which a large number of tests were performed simulating meteoroid impacts on realistic structures with holes and ribs suggests significant improvements can be made in the electronics. For one thing it appears the wide band amplifiers were over-designed, and a frequency response of 200 to 800 kHz is adequate for both impact triangulation and acoustic emission triangulation. Further, it has been shown that transducers specifically designed for this application can produce acoustic emission signals at a millivolt level instead of at the micro-volt level. Thus the signal-to-noise ratio becomes much less critical. There are two implications of this information. The first is that a very small integrated circuit preamplifier can be incorporated into the miniaturized impact gage (Mini-Gage). The milliwatt power used to supply it can be sent through the same line as the signal. Thus no additional cabling would be required. The second implication is that a separate acoustic emission amplifier is not required. The present buffer amplifier can be a high gain amplifier with a fast AGC loop. Acoustic emission pulses would generate triangulation signals in the same manner as the present impact system. Thus constant monitoring and triangulation for micro crack formation is feasibile. In event of a meteoroid impact, the strong AGC voltage would provide information that a hit had occurred. The magnitude of the AGC voltage could be used to record the energy imparted by the impact. Summing the voltages from a number of channels would take into account the possibility a low-energy-impact near an individual gage causing a large AGC voltage to appear in one channel. The system is illustrated in Figure 4-74.

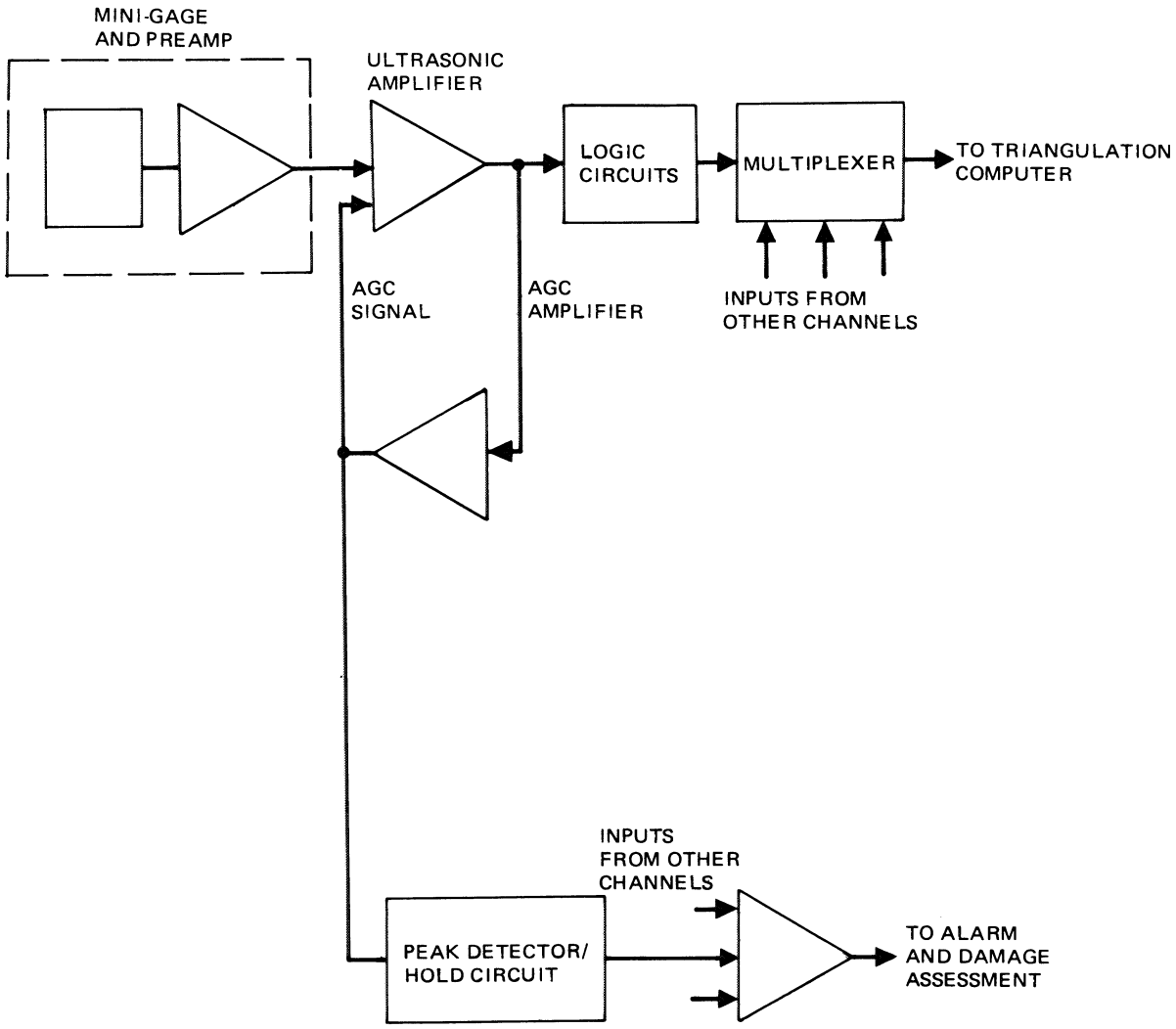

Figure 4-74. Proposed Dual-Function Impact Gage Damage Assessment System

Section 5
CONCLUSIONS

Experimental results obtained in this program indicate that all three leak detection/location techniques for overboard leakage are feasible for integration into a damage control system for Space Stations.

5.1 SEAL LEAK DETECTOR

For the detection of overboard leakage past seals, the thermal conductivity method using thermistors in a Wheatstone bridge circuit proved to be the only method capable of meeting the objective of a detection sensitivity of 10^{-4} scc/s or better. In fact, the thermistor detector far exceeded this objective by exhibiting a sensitivity of 1×10^{-8} scc/s. This sensitivity allows measurement of the normal permeation of cabin atmosphere through the elastomer seal. A baseline signal is then established which could be checked on an intermittent or continuous basis. Thermistor sensors are small, rugged, low in power requirements, and can readily be integrated into a damage control system. Further, it was demonstrated in the breadboard development that the signal output can be presented in a direct digital read-out of leak rate which can be coupled with an audio alarm to trigger at any preset leak rate level.

The capacitance sensor for detecting moisture leaking past a seal did not demonstrate the design objective sensitivity of 1×10^{-4} scc/s in the state of development achieved in this program. However, the method has potential for significant improvement. The capacitance sensor is a flexible detector and can be applied to flange-type seals with minimal design changes in the flange. Furthermore, capacitance thin-film sensors can be applied to both overboard and onboard seal leaks of fluids.

5.2 ACTIVE ULTRASONICS-LAMB WAVE TECHNOLOGY

The application of Lamb wave technology is feasible for the remote detection and location of leaks (or precursor damage modes) in space cabin walls having realistic structural features such as ribs, feed-throughs, viewports and hatches.

Lamb waves are sensitive to very small-sized flaws anywhere within the wall thickness. Grain structure effects are significant for Lamb wave technology and must be taken into account in designing a transducer array detection system.

Considerations of an array system indicate that transmit-receive methods will prove more valuable than pulse-echo techniques for use in remote active ultrasonic leak detection and location in integrally stiffened wall structures.

5.3 IMPACT GAGE

Triangulation techniques based on the shock wave time-of-arrival to an impact gage array from the point of impact have demonstrated over a wide range of velocities for a variety of wall structures the successful prediction (within a few centimeters) of the point of impact. The success of the technique has been verified for plain aluminum sheets and integrally ribbed large-area sheets.

Low-velocity impacts that may accidently occur on the inner wall surface of the space cabin can readily be discriminated against.

Miniature impact gages demonstrated efficient performance in array tests for both ballistic and hypervelocity impact.

Plastic electrets show considerable promise for application as transducers for impact gages. Impacts directly on a plastic film may be used for sensing and locating the impact.

The fluorocarbon electrets show particular promise for a wide variety of applications in impact technology.

A breadboard impact gage signal processing subsystem successfully demonstrated that by using multiplexing techniques, output signals can be provided for direct calculation of the point of impact.

It was demonstrated that acoustic emission signals can be detected with the miniature impact gage. Impact and acoustic emission signals can be processed with electronic units having a frequency response from 50 to 800 kHz using different multiplexing techniques.

The dual-function passive ultrasonic gage sensing both impacts and acoustic emission signals is judged feasible based on the test results obtained in this program.

Section 6
RECOMMENDATIONS

All three leak detection and location concepts studied experimentally in this program are recommended for further development. Future work should reflect the impact of realistic parameters as derived from design studies of future manned Earth-orbital systems.

6.1 SEAL LEAK DETECTOR

The thermal conductivity technique should be applied to realistic static and dynamic seals. Design of the thermal conductivity cell should be implemented to improve response time and reduce the weight from the current 140 to about 25 g, within a size configuration of 0.5 cm-diameter by about 3 cm long. A standard set of thermal conductivity cells should be developed to cover specific leak detection ranges ranging from <0.001 to >1.0 kg/day. Finally, a prototype detector should be integrated into available hardware to run some real-time tests. Integration into critical make-or-break seals such as hatch seals should also be carried out on a test basis.

Further work should be carried out on the capacitance sensor to improve detection sensitivity. Several design approaches merit implementation. These include: (1) use of multiple plates, (2) use of electrolyzed gold on Teflon as an electrode/insulator combination, and (3) decrease thickness of dimenthylsilicone films to increase basic capacitance.

6.2 ACTIVE ULTRASONICS-LAMB WAVE TECHNOLOGY

To develop the potential of Lamb wave technology for damage control applications, additional work should be performed in the area of flaw detection on integrally stiffened panels, and new study areas should be pursued. The following research and development areas are recommended.

- The development of a triangulation breadboard where the Lamb wave modes and the operating parameters are optimized for use on a multiple-rib integrally stiffened panel.
- The development of omnidirectional transducers and of transducer array concepts so that a permanently mounted leak location system can be tested on a multiple-ribbed panel.
- Thorough investigation of Lamb-wave propagation and flaw detection on weldments, and studies to determine the feasibility of passing Lamb waves from membrane sections to weldment sections of integrally stiffened structures.
- Further flaw detection studies using cracks and other real damage in integrally stiffened panels to assess the detectability of potential damage modes which could cause space-cabin leakage.
- The development of instrumentation for automating a permanently mounted transducer array, and of techniques for recording the signature of the background pattern received from a simulator test panel.
- Leak location testing in a realistic environment as in a space station simulator to determine the interaction of the environment with the operation of an active ultrasonic damage control system; also determination of the lifetime of bondable couplants used for attaching ultrasonic transducers to a structure.

6.3 IMPACT GAGES

It is recommended that a parametric investigation of impact gage arrays be extended to structures representative of simulators and future manned Earth-orbital systems. Further parametric tests should be carried out on the signal characteristics of impact gages as a function of metallurgical properties of the wall structure, amount of stress present in the wall, and the effects of large cutouts, through-puts, and hatches.

A further study should be carried out on impact transducer signal properties as a function of projectile properties including momentum, energy, and time of interaction with the structure. This parametric investigation should be carried out for both non-penetrating and penetrating impacts of the pressure wall structure. Analysis of such data could lead to a predictive technique which would not only locate the point of impact but also give some information as to the degree of damage.

Additional acoustic emission experiments should be performed on realistic structures for two types of dynamic flaws: (1) crack propagation associated with meteoroid impact and (2) dynamic flaws associated with defects in the structure itself.

The electronics for a dual-function gage for detecting both acoustic emission and impact should undergo an improved design phase incorporating an optimized impact gage with an integrated circuit pre-amplifier. The electronic unit should incorporate an AGC controlled ultrasonic amplifier for acoustic emission which doubles as a buffer amplifier for impacts.

Finally, the logic output of the electronics signal conditioning unit should be designed to interface with prototype information management systems for manned space vehicles.

REFERENCES

1. M. V. Scherb et al., Study of Damage Control Systems for Space Station, NASA CR 111963, October 1971.

2. Withey, D. J., Repair of Leaks in an Aerospace Environment, Report No. ASD-TDR-62-1015, General Electric Co., February 1963.

3. J. and H. Krautkramer, Ultrasonic Testing of Materials, Springer Verlag, New York (1969) p. 10.

4. Frederick, J. R., Ultrasonic Engineering, John Wiley and Sons, Inc., New York, 1965, p. 15.

5. di Novi, R., Lamb Waves - Their Use in Nondestructive Testing, Argonne National Laboratory, Report No. ANL 6630, March 1963.

6. di Novi, R., Status Report on Lamb Waves, Argonne National Laboratory, Report No. ANL-6329, March 1962.

7. Worlton, D. C., Lamb Waves at Ultrasonic Frequencies, AEC Research and Development Report, HW-60662, 1959, p16.

8. Worlton, D. C., Applications of Lamb Waves in Ultrasonic Testing, Symposium on Nondestructive Tests in the Field of Nuclear Energy, ASTM Special Technical Publication No. 223, 1958.

9. Gross, B., "The Electret," Endeavor, vol. XXX, No. 111, p. 115, September 1971.

10. Room and Halkaides, Piezoelectric Transducers, U.S. Patent No. 3,365,593, January 1968.

11. Allison, F. and Hauver, G., Shock-Induced Polarization of Plexiglas and Polystyrene, BLR Report No. 1258, Ballistic Research Labs, Aberdeen Proving Ground, Md. August 1964.

12. Champion, A. R., "Effect of Shock Compression on Electrical Resistivity of Three Polymers," J. of Applied Physics, Vol. 43, No. 5, May 1972, p.2216.

13. Zook, J. D. and Liu, S. T., "Piezoelectric Effect in Teflon Cable," J. of Applied Physics, Vol. 43, No. 3, March 1972, p.1304.

14. Sessler G.M. and West J.E., "Production of High Quasi-permanent Charge Densities on Polymer Foils by Application of Breakdown Fields, J. of Applied Physics, Vol. 43, No. 3, March 1972, p. 922.

15. Edelman, Roth, and Grisham, "Electrical Generation of Motion in Elastomers," Shock and Vibration Bulletin 39, February 1969, Naval Research Lab., Washington, D.C.

16. Edelman, Grisham, Roth, and Cohen, "Improved Piezoelectric Effect In Polymers," J. of Acoustical Society of America, Vol. 48, No. 5 1970, p. 1040.

17. Cohen and Edelman, "Direct Piezoelectric Effect in Polyvinylchloride Films" J. of Applied Physics, February 1971, p. 893.

18. Cohen and Edelman, "Piezoelectric Effect in Oriented Polyvinylchloride and Polyvinylfluoride," J. of Applied Physics Vol. 42 No. 8 P. 3072, July 1971.

19. Fukada, E. and Nishiyama, K., "Piezoelectric Properties in Polarized Polyvinylfluoride, Japanese J. of Applied Physics, Vol. 11 No. 1, January 1972, p. 36.

20. Kawai, H., The Piezoelectricity of Poly (Vinylidene Fluoride) Japan. J. App. Physics, Vol. 8, (1969), p. 975.

21. Fowler, F.A., "Acoustic Emission Test Set," Materials Research and Standards, MTRSA, Vol. 11, No. 3, p 35, March 1971.

Appendix

TRIANGULATION TECHNIQUE FOR LOCATING POINT OF IMPACT

Consider a meteoroid impact at an unknown point P in a plane containing three impact gages: A, B, and C (Figure A-1). Assume the longitudinal wave radiates from the impact point at a constant velocity C. If the time of impact is T_o, and the wave arrival at gage A is T_A, the time from impact to gage A output is D/C, where D is the distance of A from the impact point.

Mathematically

$$T_A - T_o = \frac{D}{C} = \frac{1}{C}\sqrt{(x_i - x_a)^2 + (y_i - y_a)^2} \tag{1}$$

Similarly, for gage B

$$T_B - T_o = \frac{1}{C}\sqrt{(x_i - x_b)^2 + (y_i - y_b)^2} \tag{2}$$

The unknown variables are x_i, y_i, and T_o. Subtracting equation (1) from equation (2) and multiplying both sides by C yields

$$(T_B - T_A)\,C = \sqrt{(x_i - x_b)^2 + (y_i - y_b)^2} - \sqrt{(x_i - x_a)^2 + (y_i - y_a)^2} \tag{3}$$

The right side of this quadratic equation represents the difference in distance between transducer B to any impact point and transducer A to the same impact point. Equation (3) is of the form of a hyperbola which is defined as a curve for which the differences of the distances of any point on it from two fixed points (the foci) is a constant ($L_1 - L_2 = K$).

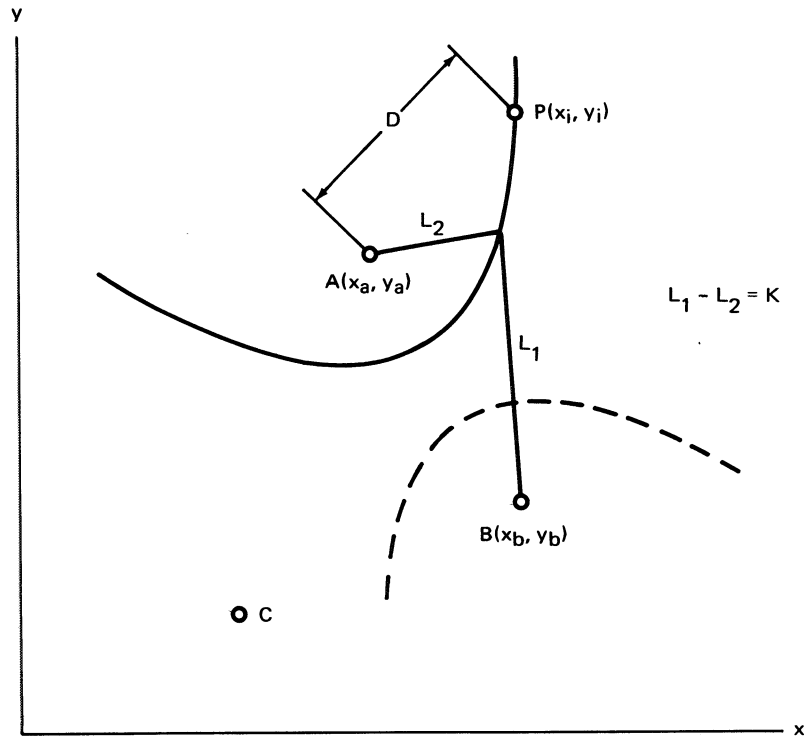

Figure A-1. Triangulation Technique for Locating Point of Impact

In this case, the foci are impact gages A and B. Shown as a broken curve in Figure A-1 is the second branch that is generated by using negative values of the radicals in equation (3). This branch is a trivial solution to the problem.

In a similar manner, a second hyperbola derived from $T_C - T_A$ will intersect the first hyperbola in two places. A unique solution defined by the intersection of a third hyperbola derived from $T_C - T_B$ will determine the point of impact.

The solution may be obtained by mathematical or graphical techniques.

In application to information management systems for space stations, the impact point would be located by a computer solution of three simultaneous equations.